Iron Mediated Reduction Schemes for Dinitrogen and Carbon Dioxide

Thesis by

Caroline Thalia Saouma

In Partial Fulfillment of the Requirements for the Degree of

Doctor of Philosophy

California Institute of Technology

Pasadena, California

2011

(Defended January 5, 2011)

Acknowledgements

The time I has spent in graduate school, at Caltech then MIT then back at Caltech again, have been quite memorable, and there are several people that I would like to acknowledge.

I would first like to thank my adviser, Jonas C. Peters. His intensity was evident in all of our interactions, and he always "hung in there" with me, never being satisfied with my work, never letting me slack off (even after shoulder surgery!), and always encouraging me to strive for perfection. I only really appreciated this when I decided that I wanted to pursue a career in academia, and I am glad that he didn't let our "discussions" interfere with his mentoring of me. His office door was always open, and he always took the time to talk– whether it was about science, advice, or anything else– and he showed much kindness and understanding whenever things in my non-chemistry life went awry.

I would also like to thank my committee, Jackie Barton, Mitchio Okumura, John Bercaw, and Doug Rees for all the discussions and feedback that I have received during meetings and examinations. While I was at MIT, I had the opportunity to interact again with my undergraduate adviser, Steve Lippard, who helped strengthen my love of chemistry. I would also like to thank Tim Swager, who was very supportive of the "Metals in Synthesis" (MIS) seminar series that Neal and I started (we were homesick for Caltech, so we decided to bring IOS to MIT).

During my graduate career, I have had the chance to learn many techniques and to interact with many scientists. Larry Henling, Mike Day, and Peter Müller (MIT) all taught me X-ray crystallography, and their enthusiasm for the technique was contagious.

Dave VanderVelde, Scott Ross, Jeff Simpson (MIT), and Anne Gorham (MIT) all helped me with NMR experiments, and they always took time to answer my many questions about the technique or my data. Angelo Di Bilio has also helped me with EPR experiments, and Jay Winkler helped me with resonance Raman experiments.

Our group collaborates with Prof. Brian Hoffman (Northwestern), and I have been fortunate to be involved with this collaboration. Through this, I have gained an appreciation and understanding of ENDOR spectroscopy. This is largely due to the many email correspondences that I have had with one of his graduate students, Adam Kinney, who answered all of my questions about the technique and our data.

When I joined the group, I was immediately surrounded by great coworkers, which became a constant, whether we were in 301 Noyes, the first floor of building 18, or 213A Schlinger.

My classmates in the group, (soon to be) Dr. Val(erie) Scott Kristof, Dr. Alex Miller, and Dr. Jill(ian) Dempsey have to be the best classmates I could have had. Even though they stayed behind at Caltech, they have always been there for me.

My graduate student mentor, Connie Lu (one of my first boxmates!), taught me a lot of lab techniques, was there with me in the orthopedist's office for 4 hours one afternoon when I needed to get my shoulder examined/injected with cortisone (despite her thesis defense being 3 months away), helped me avoid a fiasco in the lab when I was drugged up on anti-inflammatory drugs, gave me a great project to follow-up on, was always helpful with my spectroscopy questions, and continues to be a great friend. Christine Thomas was another senior graduate student, and was a great resource in the group as well as my afternoon swimming buddy back during my first year of graduate

school. Matt Whited made sure that there was always humor in the group office, and Neal Mankad is like my chemistry big brother. Even though I did not overlap with him, Steve Brown has always been supportive of my chemistry, and I appreciated all the feedback and encouragement he gave me.

At Caltech (the first time around), there were many great post docs in the group. Arjun Mendiratta (another initial boxmate!) was a cheerleader, someone who was always excited to see my results. Mark Mehn (my third initial boxmate!) adamantly told me to work on hydrazine, and I am happy I did. Xile Hu has been a great friend since the first day I met him, and Bruce MacKay always kept the group in order.

The current (and more recent) members of the group have also been great to work with. Nate Szymczak and I had a lot of great discussions about our chemistry projects, and he was always there to listen. My boxmates (Sam MacMillan, Seth Mickenberg, John Anderson, and Henry Fong) put up with my ridiculous standards for keeping a good box atmosphere. Dan Suess and I shared a lab at MIT, and we soon discovered that we have the same taste in music (which is fortunate, as we always had an ipod hooked up to speakers!). Kenny Lotito and Charles McCrory are great chatters in the group office, always there for a conversation over coffee. The rest of the group– Yunho Lee, Ayumi Takaoka, Charlene Tsay, Alicia Chang, Marc-Etienne Moret, and Hill Harmon– have all contributed to making the Peters group a great place to work, and I wish everyone in the group (past and present) the best of luck with their scientific endeavors.

Outside of the Peters' group, several friends within the Caltech chemistry department have made my time at Caltech enjoyable— from our xtalography dinner club (Alex, Jill, Katy Muzikar, Sean Kedrowski) to my housemates (Val and Suz Golisz), and

members of the Bercaw and Gray groups, several of which have also taken the time to help me with specific experiments.

At MIT, I balanced chemistry with rowing, and it is no coincidence that my chemistry picked up when I began to seriously train. One of my coaches, Bob Eldridge, gave me the confidence to pursue my rowing dream, and that confidence eventually transcended into my chemistry. The members of the MIT rowing club and the Riverside Boatclub (particularly the HPG women) were great teammates and friends. Stef Sydlik was my chemistry rowing buddy, and we spent countless hours at the boathouse together— training, rehabbing, and venting about chemistry.

Finally, I would like to thank my family, for always being there for me. My big brother Richard and his wife Betsy, and my little sister Sophie, my dad Victor, and my mom Rhéa, have all been very supportive of me. My Mom in particular— no matter how sick she was, she was there for me, whether it was on the phone or by sending me a month's worth of homemade frozen dinners after shoulder surgery. In addition, she was (and continues to be) an inspiration for me.

Abstract

Several mono- and diiron species that coordinate N_xH_y ligands have been prepared and studied, to serve as structural, spectroscopic, and/or reactivity mimics to intermediates to an alternating reduction scheme for N_2 (i.e., M^n-N≡N → M^n-HN=NH → M^n-H_2N-NH_2 → M^n + 2 NH_3). The reaction between [PhBP$^R_3$]FeMe ([PhBP$^R_3$] = (PhB(CH_2PR_2)$_3^-$; R = Ph, CH_2Cy) and hydrazine affords {[PhBP$^R_3$]Fe}$_2$(μ-η^1:η^1-N_2H_4)(μ-η^2:η^2-N_2H_2). In one instance (R = Ph), the stepwise oxidation of coordinated hydrazine to diazene, and diazene to dinitrogen is achieved, giving {[PhBP$^{Ph}_3$]Fe}$_2$(μ-η^1:η^1-N_2H_2)(μ-η^2:η^2-N_2H_2) and {[PhBP$^{Ph}_3$]Fe}$_2$(μ-NH)$_2$, respectively.

As an extension to this work, a family of complexes which feature the same auxiliary ligands (i.e., [PhBP$^{CH2Cy}_3$]Fe(OAc)), that are all iron(II), and that only differ in the oxidation state of the nitrogenous ligand has also been prepared: {[PhBP$^{CH2Cy}_3$]Fe(OAc)}$_2$(μ-N_2), {[PhBP$^{CH2Cy}_3$]Fe(OAc)}$_2$(μ-N_2H_2), {[PhBP$^{CH2Cy}_3$]Fe(OAc)}$_2$(μ-N_2H_4), and {[PhBP$^{CH2Cy}_3$]Fe(OAc)(NH_3).

To determine whether similar species could be isolated at a single iron site, the coordination chemistry of the more crowded "[PhBP$^{mter}_3$]Fe" fragment was investigated and compared to that of the "[PhBP$^{Ph}_3$]Fe" scaffold. Treatment of [PhBP$^{mter}_3$]FeMe with hydrazine generates the unusual 5-coordinate hydrazido complex, [PhBP$^{mter}_3$]Fe(η^2-N_2H_3), which features an Fe=N π bond. Both 5- and 6-coordinate iron complexes that coordinate hydrazine were also synthesized, and the oxidation of these hydrazine and hydrazido(-) species was explored. In most instances, oxidation results in

disproportionation of the N_2H_y ligand, and $[PhBP^{R}_3]Fe(NH_3)(OAc)$ (R = Ph, *m*ter) is isolated.

A 5-coordinate diiron diazene redox pair of complexes, $\{[PhBP^{Ph}_3]Fe(CO)\}_2(\mu\text{-}\eta^1\text{:}\eta^1\text{-}N_2H_2)^{0/-}$ was also prepared and studied. The electronic structure of the Fe-NH-NH-Fe core in these complexes is unusual in that it features a highly activated diazene ligand, which is unprecedented for mid-to-late transition metals. Combined structural, spectroscopic, and computation studies indicate that there is much π-covalency within the Fe-NH-NH-Fe core, which has a similar electronic structure as butadiene.

With regards to CO_2 reduction, the ability of iron(I) to mediate the one- and two-electron reductions of CO_2 was explored. The reaction between $[PhBP^{CH2Cy}_3]Fe(PCy)_3$ and CO_2 is solvent dependent, with oxalate formation to generate $\{[PhBP^{CH2Cy}_3]Fe\}_2(\mu\text{–}\eta^2\text{:}\eta^2\text{–oxalato})$ being favored in THF, and decarbonylation to give $\{[PhBP^{CH2Cy}_3]Fe\}_2(\mu\text{-O})(\mu\text{-CO})$ occurring exclusively in MeCy. Studies aimed at understanding this unusual solvent-induced selectivity are presented.

Table of Contents

List of Figures

List of Tables

List of Abbreviations and Nomenclature

$\{^{31}P\}$	phosphorous-31 decoupled
°	degrees, a measure of angle
°C	degrees Celsius
^{1}H	hydrogen-1
^{13}C	carbon-13
^{15}N	nitrogen-15
^{31}P	phosphorus-31
Å	Angstrom, 10^{-10} m
A_x	EPR coupling constant where X is the nucleus coupling to the unpaired electron
Ad	1-adamantyl
Anal. Calcd.	elemental analysis calculated
Ar	aryl substituent
atm	atmosphere
ave	average
B3LYP	Becke three-parameter function with Lee-Yang-Parr correlation
$BArF_{24}$	tetra(3,5-di(trifluoromethyl)phenyl)borate
bpy	2,2'-bipyridine
br	broad
^{n}Bu	n-butyl
^{s}Bu	*sec*-butyl

^{t}Bu	*tert*-butyl
C_3, C_s	Schoenflies symmetry designations
ca.	circa
CCD	charge-coupled device
CCDC	Cambridge Crystallographic Data Centre
CH_2Cy	cyclohexylmethyl
cm	centimeter(s)
cm^{-1}	inverse centimeters or wavenumbers
cm^3	cubic centimeters
Cp	cyclopentadienyl
Cp^*	pentamethylcyclopentadienyl
Cy	cyclohexyl
CV	cyclic voltammogram
d	doublet
d^n	d-electron count of n-electrons for a transition metal
dbabh	2,3:5,6-dibenzo-7-aza bicycle[2.2.1]hepta-2,5-diene
D_{calc}	calculated density
dd	doublet of doublets
deg	degrees
DFT	density functional theory
dmpe	1,2-bis-(dimethylphosphino)ethane
DMeOPrPe	1,2-bis[(methoxypropyl)phosphino]ethane
dt	doublet of triplets

E	an atom or functional group forming a metal-ligand multiple bond
ENDOR	electron nuclear double resonance
EPR	electron paramagnetic resonance
equiv	equivalents
ESEEM	electron spin echo envelope modulation
eV	electron volt
EXAFS	extended X-ray absorption fine structure
F_c	calculated structure factor
Fc/Fc^+	ferrocene/ferrocenium
F_o	observed structure factor
fw	formula weight
g	gram(s)
g	g-factor
G	Gauss
GC/MS	gas chromatography mass spectrometry
GHz	gigahertz
h	hour(s)
H	applied magnetic field
HAT	hydrogen atom transfer
HOMO	highest occupied molecular orbital
Hz	hertz
I	intensity
I_n	nuclear spin of atom n

IR	infrared
$^{n}J_{AB}$	coupling constant between nuclei A and B over n bonds (NMR)
K	degrees in Kelvin
kcal	kilocalories
kHz	kilohertz
KIE	kinetic isotope effect
L	dative ligand for a transition metal
lN_2	liquid nitrogen
LUMO	lowest unoccupied molecular orbital
lut	lutidinium
m	multiplet
M	concentration in molarity
M	general transition metal
m-	meta position of an aryl ring
Me	methyl
MeCy	methylcyclohexane
Mes	2,4,6-trimethylphenyl
Me-THF	2-methyl tetrahydrofuran
2,5-diMe-THF	2,5-dimethyl tetrahydrofuran
mg	milligram(s)
MHz	megahertz, 10^6 Hertz
min	minute(s)
mL	milliliter(s)

mm	millimeter
mmol	millimole(s)
MO	molecular orbital
mol	mole(s)
*m*ter	3,5-*meta*-terphenyl
m_s	intrinsic spin quantum number
NHE	normal hydrogen electrode
$[NN^{H3}{}_3]^{3-}$	tris[(N'-tert-butylureaylato)-N-ethyl)]aminato
nm	nanometer(s)
NMR	nuclear magnetic resonance
OEP	octaethylporphyrin
OTf	$-OSO_2CF_3$
OAc	$-OCOCH_3$
p-	*para* position of an aryl ring
PESTRE	pulse-endor-saturation-recovery
Ph	phenyl
$[PhBP^R{}_3]$	$[PhB(CH_2PR_2)_3]^-$
$[PhBP^{tBu}{}_2(pz)]$	$[PhB(CH_2P^tBu_2)_2(pyrazolyl)]^-$
$[PhB(RIm)]^-$	$[PhB(1\text{-}R\text{-}2\text{-}ylidene)_3]^-$
ppm	parts per million
^{i}Pr	*iso*-propyl
py	pyridine
pz	pyrazole

$pz^{R,R'}$	pyrazole substituted at the 3 and 5 positions, respectively
q	quartet
R	general alkyl or aryl substituents
R_1	R-factor (XRD)
Ref	reference
RF	radio frequency
rRaman	resonance Raman
rt	room temperature
s	second(s)
s	singlet
S	spin
(SiP^R_3)	$(2\text{-}R_2PC_6H_4)_3Si^-$
SOMO	singly occupied molecular orbital
SQUID	superconducting quantum interference device
sqrt	square root
t	triplet
T	anisotropic coupling in between electronic and nuclear spin
TBP	trigonal bipyramidal
T_d	tetrahedral symmetry
TEMPO	2,2,6,6-tetramethylpiperidine-1-oxyl
TEMPOH	1-hydroxy-2,2,6,6-tetramethylpiperidine
THF	tetrahydrofuran
THF-d_8	tetrahydrofuran-d_8

$TIMEN^{R}$	tris-[2-(3-R-imidazol-2-ylidene)ethyl]amine
tmeda	tetramethylethylenediamine
TMG_3tren	1,1,1-tris{2-[N^2-(1,1,3,3-tetramethylguanidino)]ethyl}amine
tolyl	$-C_6H_4CH_3$
Tp'	general hydrotris(pyrazolyl)borate ligand
TPB	$(^{i}Pr_2PC_6H_4)_3B$
$Tp^{R,R'}$	hydrotris(3-R,5-R'pyrazolyl)borate
UV-vis	ultraviolet-visible
VT NMR	variable temperature nuclear magnetic resonance
wR^2	weighted R-factor (XRD)
X	monoanionic atom or group, e.g., halide
XAS	X-ray absorption spectroscopy
XRD	X-ray diffraction
xyl	2,6-dimethylphenyl
χ	magnetic susceptibility
δ	chemical shift
δ	isomer shift
ΔE_Q	quadrupole splitting
Δ_π	crystal-field splitting
ε	extinction coefficient in M^{-1} cm^{-1}
κ^n	hapticity in σ-bonded ligands
η^n	hapticity in π-bonded ligands

λ	wavelength
λ_{max}	wavelength of maximum absorption
μ	absorption coefficient (XRD)
μ-A	bridging atom
μ_B	Bohr magnetons
μ_{eff}	effective magnetic moment
μL	microliter(s)
μmol	micromole(s)
ν	frequency
ω	omega (XRD)
φ	phi (XRD)
π	bonding interaction that has a nodal plane including the internuclear axis
π^*	anti-bonding interaction with a node that is perpendicular to the internuclear axis
σ	bonding interaction that contains the internuclear axis with no nodes
σ^*	anti-bonding interaction with a node along the internuclear axis

Dedication

This work is dedicated to my mom, Rhéa Elizabeth Abdunnur-Saouma.

Chapter 1: M≡E and M=E Complexes of Iron and Cobalt that Emphasize Three-Fold Symmetry (E = O, N, NR)

1.1 Introduction

Multiply bonded species of the late transition metals (M≡E and M=E, where E = O, N, NR, CR) have been postulated as key intermediates in many synthetic and enzymatic transformations.[1] These transformations include, for example, olefin epoxidation and aziridination,[2] C-H bond oxygenation and amination,[3] and e^-/H^+ transfer processes related to nitrogen fixation.[4] The diverse multi-electron reactivity exhibited by such species is in part attributed to their multiple bond character, and there has hence been much interest in understanding the electronic structures and reactivity patterns of such species.[5]

The molecular orbital (MO) picture of complexes of the type C_{4v}- $L_5M(E)$ was developed in the classic study of the d^1 vanadyl ion (VO^{2+}) by Ballhausen and Gray (Figure 1.1).[6] This MO picture stressed a large splitting of the t_{2g} orbitals ($\Delta_\pi \approx 13{,}000$ cm^{-1}), arising from the presence of a strongly π– donating oxo ligand, and the presence of a V≡O triple bond. As a consequence, complexes of the type $L_nM(E)$ should feature *bona fide* multiple bond character, and hence electronic stability, when M(E) π* orbitals are vacant or only partially filled,[1a] regardless of local symmetry.

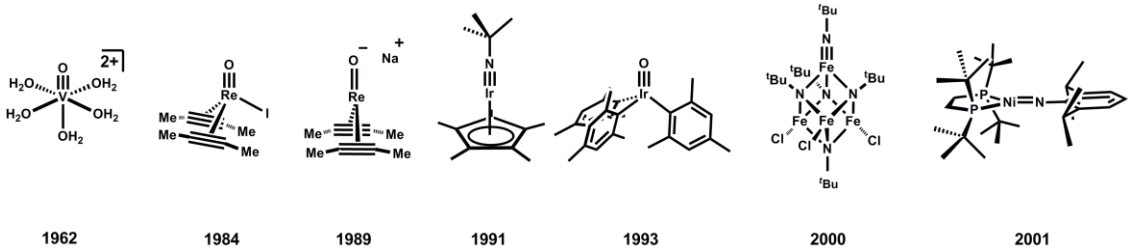

Figure 1.1. Examples of M≡E and M=E species, with year of publication noted

With this generalization in mind, there are at present three well-identified pathways to achieve a reasonable degree of electronic stability in an M≡E or M=E interaction (also abbreviated as M(E)). The most straightforward and hence historically most familiar way is to preserve a low d-electron count at the metal. For a prototypical 6-coordinate metal center that features one terminal multiply bonded ligand $L_5M(E)$, the σ^* and π^* bonding interaction results in the destabilization of four orbitals of d-parentage. It is therefore not surprising that high-valent early transition metals that feature d^0, d^1, or d^2 electron counts have historically dominated the literature of terminal $L_5M(E)$ complexes.[7] To a first-order approximation, the π-bond order decreases from 2 to 3/2, 1, and ½ as the d^3, d^4, and d^5 configurations are respectively populated. Such an approach is of course not limited to complexes of four-fold symmetry. The high stability of complexes such as trigonal bipyramidal (TBP) $\{(Me_3SiNCH_2CH_2)_3N\}V(O)$[8] and tetrahedral $(^iPr_2N)_3Cr(N)$[9] drives home this point. A second means of achieving electronic stability in M(E) species constitutes using a combination of ligands that are both σ donating and π-accepting. Synergism in this context can in principle, via orbital mixing, serve to stabilize d-electrons that would otherwise be destabilized via a strong π^* interaction. Such a scenario has been used, for example, to offer an explanation for the unanticipated stability of the d^6 $L_5Pt(O)$ species prepared by Hill and coworkers.[10] A third mode of achieving electronic stabilization for multiply bonded species is to remove donor ligands from the central metal under consideration. This provides a distinct electronic structure that may be able to accommodate a higher number of d-electrons, so long as those electrons do not fill strongly destabilized orbitals. For example, under three-fold symmetry, both 4- and 5-

coordinate species can accommodate M(E) species with diverse d-electron configurations (Figure 1.2).[1f,5f,11]

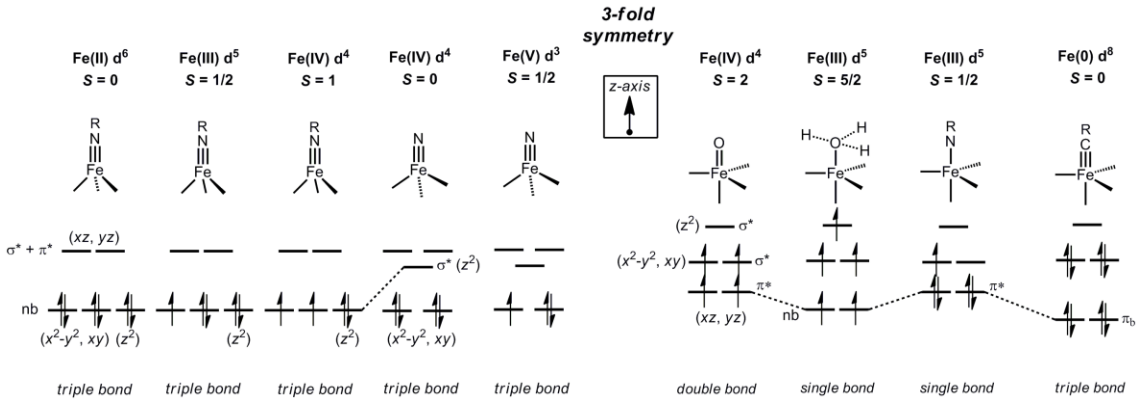

Figure 1.2. Qualitative d-orbital splitting diagrams for L_3-Fe(E) and L'L_3-Fe(E) structure types discussed throughout the review. The diagram is meant as a guide to the discussion in the text. The relative ordering of the orbital energies for the lower-lying *e* set (xy, x^2-y^2) and the a_1 orbital (z^2) is not implied for L_3Fe(NR) structures, and are arbitrarily set as degenerate, for simplicity.

Synthetic entry to M(E) complexes featuring higher d- electron counts first surfaced about 25 years ago when Mayer and Tulip isolated and characterized an intriguing Re(O)I(MeC≡CMe)$_2$ complex (Figure 1.1).[11a] This was the first well-characterized terminal M(E) multiple bond linkage for a complex formulated as d^4. The Re-O bond distance of 1.697(3) Å in Re(O)I(MeC≡CMe)$_2$ is similar to that of higher valent Re(O) complexes,[12] suggesting that the π* orbitals are not populated. To achieve such stabilization, the Re adopts a distorted geometry that can be crudely described as tetrahedral, with approximate three-fold symmetry about the Re-O bond.[13] The two electron reduction of a related complex, Re(O)I(PhC≡CPh)$_2$, furnished an equally interesting d^6, 3-coordinate [Re(O)(PhC≡CPh)$_2$][Na] species.[11c] In this latter complex, partial population of π* orbitals is presumed to cause elongation of the Re-O bond to

1.756(3) Å, a destabilization that leads to a more reactive metal center (Figure 1.1). At a similar time, Meyer and coworkers identified the interesting intermediate-spin, d^4 ruthenium oxo species $(bpy)_2(py)Ru(O)^{2+}$.[14] Again, partial population of π^* orbitals was presumed to give rise to a more reactive Ru(O) linkage.

By establishing the viability of high d-count structures featuring M(E) bonds, these studies anticipated the possibility that M≡E and M=E complexes of the mid-to-late transition metals might be more generally accessible. Such species would be expected to exhibit the highest degree of kinetic stability for third row ions, and it is hence not surprising that about 15 years ago the groups of Bergman and Wilkinson isolated a d^6 iridium(III) imido complex,[15] and a d^4 iridium(V) oxo complex, respectively (Figure 1.1).[16] Wilkinson's d^4 oxo owes its stability to the fact that its four d-electrons reside in largely non-bonding orbitals that are orthogonal to the Ir-O bond vector. As a consequence of its pseudotetrahedral geometry, its higher energy combined σ^*/π^* orbitals are unfilled.

Until about ten years ago it had been commonly held that, owing to their propensity to populate intermediate and high spin states, first row ions that feature multiply bonded ligands would be highly reactive and hence far more difficult to isolate and thoroughly characterize.[1a,17] However, this has turned out not to be the case. For example, the ferrocene-like electronic structure of Bergman's Cp*Ir(N^tBu) imide closely resembles that of the isolobal pseudotetrahedral $L_3Co(NR)$ and $L_3Fe(NR)$ imides that are reviewed herein (Figure 1.2). Similarly, while the electronic structure of Wilkinson's d^4 iridium oxo was not described at the time of its synthesis, its relative stability predicted

the electronic stability of pseudotetrahedral iron nitrides of the type d^4 $L_3Fe(N)$ (Figure 1.2).

Indeed, over the past ten years, there have been several reports of Fe,[1f,5f,18] Co, [19] and Ni[20] complexes that feature multiply bonded ligands, in both high- and low-spin configurations. In many instances, the coordination number and hence symmetry of the species has been reduced. From these reports a general picture of the electronic structures and reactivity patterns of such complexes is emerging. This article reviews the development of terminal M(E) species of cobalt and iron with a specific emphasis on complexes that reside in local three-fold symmetry. Hillhouse,[20b,21] Holland,[22] and Warren[19d] have advanced the field of 3-coordinate M(E) species in approximate C_{2v} symmetry, though a discussion of these systems is beyond the scope of this review.

1.2 The L_3M-X Structure Type

1.2.1 Electronic Lessons Learned from Pseudotetrahedral Cobalt(II)

Prior to delving into a discussion of M(E) species of iron and cobalt, it is instructive to first consider the electronic structures of pseudotetrahedral L_3Co^{II}-X species, as they provide an important lesson with respect to the stabilization of $L_3M(E)$ species. Our group has extensively studied a family of low-spin, high-spin, and spin-crossover complexes of the type L_3Co^{II}-X,[23] in which the L_3 donor ligand is the anionic tris(phosphino)borate ligand, $[PhBP^R_3]$ ($[PhBP^R_3] = [PhB(CH_2PR_2)_3]^-$; R = Ph, ^{i}Pr).[24] The electronic structure model we proposed to account for the magnetic properties of these pseudotetrahedral d^7 ions provided a useful guide to further consider the stability (or

instability) of other d-electron configurations for related structure types, especially where the terminal ligand would be multiply bonded to the metal center.

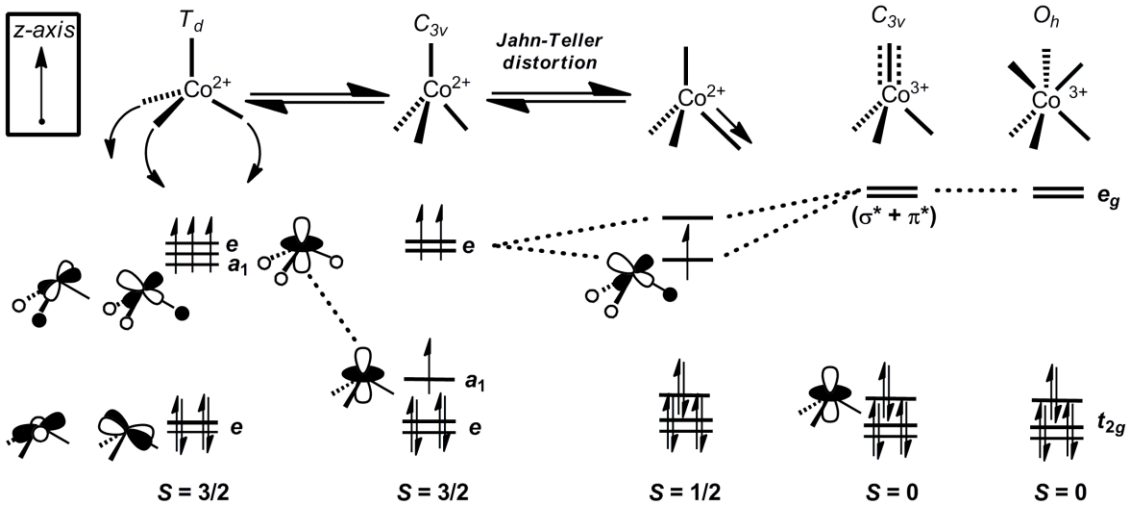

Figure 1.3. Qualitative d-orbital correlation diagram that summarizes the electronic relationships discussed in the text regarding 4-coordinate L_3-Co-X species

Prior to the characterization of low-spin $[PhBP^{Ph}_3]Co^{II}$-X complexes, all of the 4-coordinate cobalt(II) systems known to exhibit low-spin ground state configurations were classified as square planar.[25] Ions of approximate tetrahedral geometries, whether of nearly perfect T_d symmetry, or species more appropriately described as pseudotetrahedral, distorted tetrahedral, or trigonal bipyramidal had been, without exception, classified as high-spin.[26] A similar situation existed for the well-documented cases of iron(II) and nickel(II) ions. These latter systems had been reported to populate high-spin electronic configurations when approximately tetrahedral (S = 2 and S = 1, respectively), and low-spin configurations when square planar.[27]

The familiar tetrahedral ligand-field for divalent cobalt ions places three degenerate orbitals, the *t* set, at a significantly higher energy than a nonbonding *e* set

(Figure 1.3). This splitting is not generally large enough to enforce a low-spin configuration, and hence a high spin S = 3/2 electronic configuration is typically observed. Lowering the symmetry, whether to C_3, C_s, or C_1, does not typically have a large effect on the relative arrangement of the d-orbitals; the splitting of the degenerate t set is generally small by comparison to the pairing energy that would be required to achieve a low-spin configuration. A strong axial distortion, whereby the angles between three of the ligands decrease to well below 109.5^o (as would be enforced by a tripodal ligand), stabilizes the orbital of a_1 symmetry (in C_{3v}) from the upper set. When the ligand-field splitting becomes unusually large, which will be the case for highly covalent, strongly σ–donating and possibly π-accepting L_3 donor sets, a low-spin ground state configuration can be attained (Figure 1.3).[23]

The d-orbital splitting diagram achieved under this scenario recalls the "two-over-three" splitting commonly used to describe octahedral coordination complexes. A low-spin configuration for a pseudotetrahedral d^7 L_3M-X system is thus expected to exhibit a stabilizing Jahn-Teller distortion, away from three-fold symmetry, to split the upper e set. This distortion attenuates a σ antibonding interaction between a phosphine donor and the metal centered SOMO, and is similar to that observed in pseudo-octahedral low spin d^7 ions. Such a distortion is evident in the solid-state structures of numerous low-spin [PhBP$^R_3$]Co-X complexes that have been characterized,[23c] representative examples of which are shown in Figure 1.4. The generality of this phenomenon has been probed by comparing the structural and magnetic data for a series of [PhBP$^R_3$]Co-X complexes. Subtle electronic and steric changes, both within the immediate coordination sphere and well removed from it, have been found to affect the spin-state.

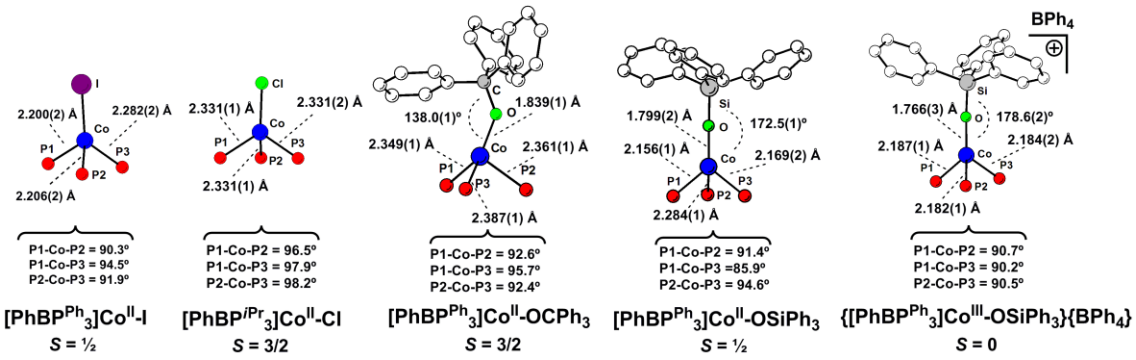

Figure 1.4. Select structural data for a series of pseudotetrahedral [PhBP$^{R}_{3}$]Co-X species that feature both high- and low-spin ground-states

The electronic structure depicted in Figure 1.3 suggested that removal of a single electron from pseudotetrahedral L_3Co^{II}-X systems might give rise to an S = 0 ground state, particularly if significant π donation from the X-type linkage would complement the σ-donor character of the tripodal L_3 scaffold. The complex {[PhBP$^{Ph}_{3}$]Co^{III}-OSiPh$_3$}{BPh$_4$} provided one such case, and clearly illustrated the close electronic structure relationship that exists between the trigonal ligand-field of 4-coordinate L_3Co^{III}-X complexes and the conventional ligand-field of octahedral L_6Co^{III} species.

Around the time that we were developing the MO description of L_3Co^{III}-X complexes, Lee and coworkers reported a tetranuclear iron cluster that featured an Fe(NR) terminal linkage.[28] The iron that coordinates the terminal imido functionality in this system resides in a pseudotetrahedral geometry. Despite the low synthetic yield of the tetranuclear iron cluster (1—2%), they were able to characterize it by several spectroscopic techniques, including X-ray crystallography. Also, Hillhouse and coworkers reported the isolation of a structurally distinct, 3-coordinate nickel imide in 2001 (Figure 1.1).[20b] These two results, combined with our electronic structure

description for 4-coordinate L_3M-X systems, suggested that a variety of d-electron configurations (i.e., d^3, d^4, d^5, d^6) might be electronically stabilized by strong π-bonding at mid-to-late first row transition ions (Figure 1.2).

1.2.2 Pseudotetrahedral $L_3Co(NR)$ Species

Intrigued by the possibility that $L_3M(E)$ species might prove sufficiently stable to isolate, our group began to systematically explore the synthetic feasibility of accessing such complexes. Given our observation that low-spin cobalt(II) systems supported by tris(phosphino)borate ligands were accessible, cobalt(III) seemed like a good place to begin. The soft, polarizable phosphine donors of [$PhBP^R_3$] ligands provided straightforward access to monovalent cobalt(I) precursors of the type [$PhBP^{Ph}_3$]Co^I-L.[19a] Subsequent two-electron [NR] group transfer from an organic azide to cobalt proved a reliable means of generating terminal cobalt(III) imides. This reaction manifold moreover exposed for the first time the viability of a $Co^{III/I}$ two-electron redox couple.

Access to [$PhBP^R_3$]Co^I-L precursors could be accomplished in a two-step sequence starting from a [$PhBP^R_3$]Co^{II}-X precursor via addition of the donor L ligand followed by reduction (Scheme 1.1).[19a,24b] In our initial report, treatment of green [$PhBP^{Ph}_3$]Co^{II}-I with PMe_3 afforded the red 5-coordinate cobalt(II) complex, [$PhBP^{Ph}_3$]Co^{II}(I)(PMe_3). Reduction by sodium/mercury amalgam then provided the desired bright green cobalt(I) precursor, [$PhBP^{Ph}_3$]Co^I-PMe_3, as a d^8 S = 1 species (the two unpaired electrons populate nearly degenerate σ* orbitals of $d_{xz/yz}$ parentage). Treatment of [$PhBP^{Ph}_3$]Co^I-PMe_3 with two equivalents of N_3(*p*-tolyl) resulted in N_2

extrusion and successful formation of the red and diamagnetic terminal imide [PhBP$^{Ph}_3$]Co^{III}(N-*p*-tolyl) (Scheme 1.1). Two equivalents of N_3(*p*-tolyl) are required in this reaction because one equivalent serves to oxidize PMe_3 to PMe_3=N(*p*-tolyl).

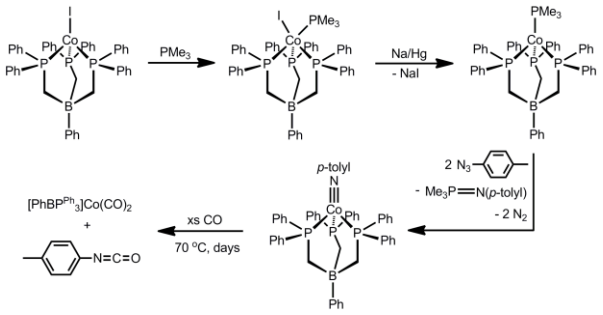

Scheme 1.1.

Table 1.1. Select metrical parameters for pseudotetrahedral L_3Co^{III}(NR) complexes

Complex	Co-N bond length (Å)	N-C bond length (Å)	Co-N-C angle (°)	Displacement of Co from L_3 plane (Å)	Ref
[PhBP$^{Ph}_3$]Co(N*p*-tolyl)	1.658(2)	1.367(2)	169.5(1)	1.23	19a
[PhBP$^{Ph}_3$]Co(N^{t}Bu)	1.633(2)	1.442(2)	176.7(1)	1.24	29
[PhBP$^{iPr}_3$]Co(N*p*-tolyl)	1.667(2)	1.315(3)	173.2(2)	1.21	24b
[(TIMEN^{mes})Co(N*p*-OMeC$_6$H$_4$)][BPh$_4$]	1.675(2)	1.386(4)	168.7(2)	0.90	19b
(Tp^{tBu,Me})Co(N^{t}Bu)	1.660(3)	1.449(5)	179.4(3)	1.20	30
(Tp^{tBu,Me})Co(NAd)	1.655(2)	1.441(3)	178.3(2)	1.196	31
[PhB(^{t}BuIm)$_3$]Co(N^{t}Bu)	1.659(3)	1.463(5)	179.7(3)	1.17	19c

The solid-state structure of [PhBP$^{Ph}_3$]Co^{III}(N-*p*-tolyl) revealed a very short Co-N bond distance of 1.658(2) Å, establishing the presence of significant multiple bond character at the *Co-N*R linkage.[19a] The relatively linear Co-N-C angle of 169.51(2)^o indicated sp-hybridization at the imide N-atom, establishing two π-bonds between the cobalt and nitrogen atoms (Table 1.1). Such a [PhBP$^{Ph}_3$]Co^{III}≡N(*p*-tolyl) bonding

description is consistent with the qualitative d-orbital splitting scenario described above, and was corroborated by DFT calculations.[32] Hence, three low-lying orbitals of dz^2, dxy, and dx^2-y^2 parentage (a_1 + e) accommodate six electrons, whereas the σ and π antibonding orbitals of dxy and dyz parentage lie at higher energies (Figure 1.3).

Of interest with respect to chemical reactivity was our observation that, despite the high kinetic stability of [PhBP$^{Ph}_3$]Co(N-*p*-tolyl), it was possible to release the imide functionality from cobalt to a nitrene acceptor, thereby regenerating cobalt(I).[19a] For example, addition of CO to of [PhBP$^{Ph}_3$]Co^{III}≡N-*p*-tolyl released the free isocyanate O=C=N(*p*-tolyl), whilst generating the 5-coordinate dicarbonyl, [PhBP$^{Ph}_3$]Co^{I}(CO)$_2$ (Scheme 1.1). This reaction, and the analogous release of carbodiimides by addition of C≡NR, have since become a useful diagnostic probe for the presence of imides coordinated to late transition metals.[18h,22c,33] Additionally, it suggested the viability of a catalytic M$^{III/I}$ redox loop (*vide infra*).

Around the time that our studies of [PhBP$^{R}_3$]Co(NR) species were underway, Theopold and coworkers were exploring conceptually related transformations at substituted tris(pyrazolyl)borate (Tp') ligated cobalt(I) precursors in the hope of gaining evidence for terminally bonded cobalt imide and oxo functionalities.[31,34] Whereas they ultimately established the fidelity of the L$_3$Co^{III}(NR) framework for certain (Tp') and NR functionalities, early studies exposed radical degradation pathways. For example, addition of Me_3SiN_3 to (Tp^{tBu,Me})Co(N$_2$) ((Tp$^{R,R'}$)$^-$ = hydrotris(3-R,5-R'-pyrazolyl)borate) resulted in formation of cylometallated, 5-coordinate (HB(pz)$_2$(κ^2-pz'))Co(NHSiMe$_3$) (Scheme 1.2).[34b] This product in all likelihood formed via H-atom transfer (HAT) from a ligand C-H bond to *in situ* generated (Tp^{tBu,Me})Co^{III}(NSiMe$_3$). This idea found merit in

the reactivity patterns of isolable (Tp')Co(NR) species (*vide infra*). An example of such a species is (Tp^{tBu,Me})Co^{III}(NAd), prepared by treatment of (Tp^{tBu,Me})Co(N_2) with AdN_3 (Scheme 1.2).[31,34a] The metrical parameters of the imide functionality in (Tp^{tBu,Me})Co^{III}(NAd) (Co-N = 1.655(2) Å, Co-N-C = 178.3(2)^o) are highly similar to those of [PhBP$^R_3$]Co^{III}(NR) species, establishing their closely related electronic structures (Table 1.1). (Tp^{tBu,Me})Co^{III}(NAd) exhibits a low-spin d^6 electronic configuration, and hence is diamagnetic even at room temperature in solution. For example, (Tp^{tBu,Me})Co^{III}(NAd) has a well resolved ^{13}C NMR spectrum. But (Tp') is a weaker field ligand than [PhBP$^R_3$], which may afford thermal access to open-shell states that would in part explain the propensity of (Tp')Co^{III}(NR) derivatives to display H-atom abstraction behavior. For example, gentle heating of solutions of (Tp^{tBu,Me})Co^{III}(NAd) resulted in partial insertion of the nitrene into a ligand C-H bond (Scheme 1.2).

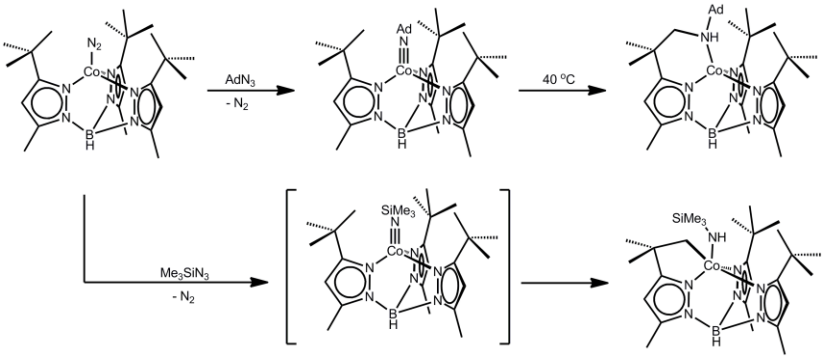

Scheme 1.2.

Meyer and Hu extended the generality of the $L_3Co^{III}{\equiv}NR$ motif and underscored its stability in preference to a 5-coordinate, trigonal bipyramidal $L'L_3Co^{III}$(NR) structure type using a flexible tris(carbene)amine scaffold, which features a hemi-labile amine donor at the axial position.[19b] Once again, oxidative group transfer to cobalt(I) proved the

synthetic method of choice. For example, addition of *p*-tolylazide to trigonal pyramidal [(TIMEN^{xyl})Co][Cl] led to the terminal imide complex [(TIMEN^{xyl})Co(N-*p*-tolyl)]Cl (TIMEN^{R} = tris-[2-(3-R-imidazol-2-ylidene)ethyl]amine; xyl = 2,6-dimethylphenyl) (Scheme 1.3). The solid-state structure of the imide complex clearly established the absence of an interaction between the d^6 cobalt center and the amine N-donor of the (TIMEN^{xyl}) ligand (the Co-N_{ax} distance is 4.01 Å). Accordingly, complexes of the type [(TIMEN^{R})Co(NAr$^{R'}$)]Cl are low-spin, and feature similar metrical parameters to the cobalt imides described above. Were there an appreciable interaction between the apical N-donor and the cobalt center, a triplet ground state would instead be expected (see discussion below for 5-coordinate d^6 L'L_3M(E) species). Despite the clear preference for a low-spin ground state, these [(TIMEN^{R})Co^{III}(NAr$^{R'}$)]Cl imide complexes are thermally unstable and undergo nitrene insertion into one Co-carbene bond at room temperature (Scheme 1.3). This transformation may be facilitated by the flexible ligand scaffold, as nitrene transfer is accompanied by coordination of the axial amine. Hence, it is cautioned that the reactivity patterns in such systems are not easily correlated with observed ground spin states.

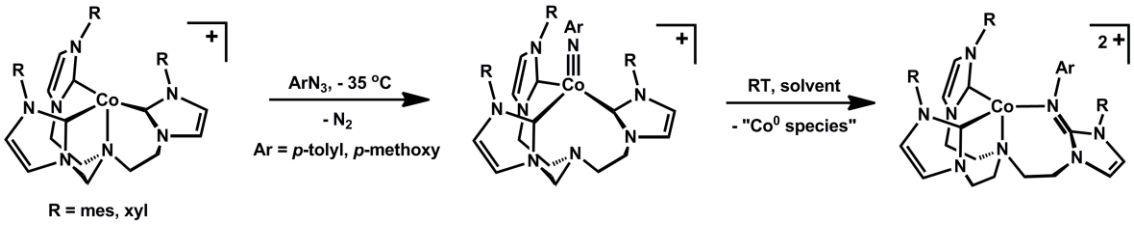

Scheme 1.3.

Another cobalt(III) imide system worth noting in the present context comes from Smith and coworkers.[19c] Using sterically encumbering tris(carbene)borate ligands that are

isomers of the ubiquitous tris(pyrazolyl)borates, they have prepared structurally related $L_3Co^{III}(NR)$ species such as $[PhB(^tBuIm)_3]Co(N^tBu)$ ($[PhB(RIm)_3]$ = $[PhB(1\text{-}R\text{-}2\text{-}ylidene)_3]^-$). As for tris(pyrazolyl)borate derivatives, vertical bulk is readily accomplished with these ligands, yet they differ by virtue of a stronger ligand field conferred by the carbene donors.[35] The cobalt(III) imides derived from these platforms are electronically similar to those already described (Table 1.1). Their method of synthesis provided a noteworthy distinction, however (Scheme 1.4). H-atom abstraction from the cobalt(II) amide precursor, $[PhB(^tBuIm)_3]Co(NH^tBu)$, was accomplished by addition of 2,4,6-tri(*tert*-butyl)phenoxy radical to furnish the d^6 cobalt(III) imide, $[PhB(^tBuIm)_3]Co^{III}(N^tBu)$. This strategy is related to the stepwise oxidation/deprotonation protocol first employed by Hillhouse and Mindiola to prepare a terminal nickel(II) imide.[20b] Worth noting is that in all instances, these cobalt(III) imides lack reversible redox couples. Though this is perhaps intuitive for a reduction event, as a d^7 cobalt(II) species would populate a high-lying orbital, the reason why oxidation to a d^5 cobalt(IV) species is not accessible is less obvious (Figure 1.3).

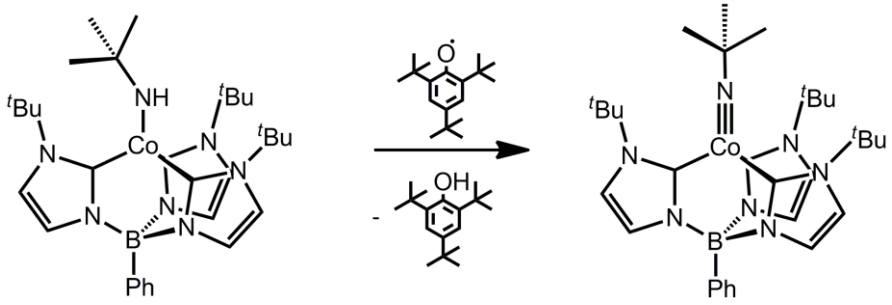

Scheme 1.4.

1.2.3 Pseudotetrahedral $L_3Fe(NR)$ Species

With the aforementioned '[$PhBP_3$]Co' chemistry as a backdrop, our group was eager to explore whether related $L_3Fe(NR)$ species could be generated and thoroughly characterized. Whereas terminal imido complexes of ruthenium and osmium had been known for many years,[36] terminally bonded iron imido complexes were essentially unknown. As noted already, Lee and coworkers had provided the singular exception to this statement in 2000 with the low-yielding synthesis of a tetranuclear iron cluster, $\{ClFe\}_3\{N^tBuFe\}(\mu^3\text{-}N^tBu)_4$, that featured a terminal *Fe-N*^{t}Bu linkage (Fe-N = 1.635(4) Å, Fe-N-C = 178^o).[28]

We were fortunate to find that, akin to the mononuclear $L_3Co(NR)$ systems, iron(III) imides of the type [$PhBP^R_3$]Fe(NR) were synthetically accessible via two-electron oxidative group transfer to iron(I) precursors.[18h,24b,29,37] Again, access to well-defined iron(I) synthons was therefore necessary. Despite the paucity of iron(I) complexes at the outset of our studies,[38] such species proved readily accessible by reduction of [$PhBP^R_3$]Fe^{II}-X precursors in the presence of a coordinating L ligand (e.g., L = PR_3 or N_2). For example, we initially reported that the sodium/mercury amalgam reduction of the yellow and high-spin (S = 2) complex [$PhBP^{Ph}_3$]FeCl in the presence of PPh_3 afforded monovalent, orange and high-spin (S = 3/2) [$PhBP^{Ph}_3$]Fe(PPh_3).[18h] As for the related cobalt system, addition of two equivalents of *p*-tolylazide generated the desired terminal d^5 imide species [$PhBP^{Ph}_3$]Fe(N-*p*-tolyl), in addition to Ph_3P=N(*p*-tolyl) (Scheme 1.5). Of particular interest to us was the low-spin ground state of [$PhBP^{Ph}_3$]Fe(N-*p*-tolyl), further buttressing the electronic structure picture that we had

forwarded to account for the low-spin d^7 L_3Co^{II}-X and d^6 and L_3Co^{III}(NR) systems reviewed above.

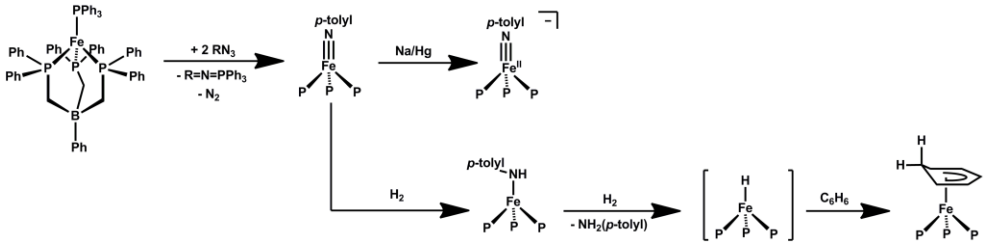

Scheme 1.5.

Table 1.2. Select metrical parameters for pseudotetrahedral $L_3Fe(NR)$ complexes

Complex	Oxidation State	Fe-N bond length (Å)	N-C bond length (Å)	Fe-N-C angle (°)	Displacement of Fe from L_3 plane (Å)	Ref
$\{ClFe\}_3\{N^tBuFe\}(\mu^3\text{-}N^tBu)_4$	4+	1.635(4)	--	178.6(3)	--	28
$\{[PhBP^{Ph}_3]Fe(NAd)\}\{N^nBu_4\}$	2+	1.651(2)	1.434(3)	178.6(1)	1.24	18i
$[PhBP^{Ph}_3]Fe(NAd)$	3+	1.641(2)	1.428(3)	176.3(2)	1.32	18i
$[PhBP^{Ph}_3]Fe(N$*p*-tolyl)	3+	1.658(3)	1.383(3)	170.0(2)	1.31	18h
		1.661(3)	1.374(3)	167.3(2)	1.29	
$[PhBP^{Ph}_3]Fe(N^tBu)$	3+	1.635(1)	1.442(2)	179.2(1)	1.29	29
$[PhBP^{iPr}_3]Fe(NAd)$	3+	1.638(2)	1.438(3)	176.0(2)	1.27	24b
$[PhBP^{CH2Cy}_3]Fe(NAd)$	3+	1.622(4)	1.433(6)	176.3(3)	1.24	37
$[PhB(mesIm)_3]Fe(NCPh_3)$	3+	1.654(3)	1.473(4)	177.7(3)	1.20	18c
$[PhB(P^{tBu}_2)(pz)]Fe(NAd)$	3+	1.626(8)	1.33(3)	176(1)	1.27	18j
		1.634(8)	1.59(3)	170(1)	1.26	
$\{[PhB(P^{tBu}_2)(pz)]Fe(NAd)\}\{BArF_{24}\}$	4+	1.61(1)	1.44(2)	174(1)	1.13	18j
$[PhB(P^{tBu}_2)(pz^{Me,Me})]Fe(NAd)$	3+	1.647(8)	1.45(1)	172.2(6)	1.22	18j
		1.652(8)	1.44(1)	172.4(6)	1.23	
$\{[PhB(P^{tBu}_2)(pz^{Me,Me})]Fe(NAd)\}\{BArF_{24}\}$	4+	1.634(4)	1.456(6)	176.3(3)	1.11	18j
$[PhB(mesIm)_3]Fe(NAd)$	3+	1.625(5)	1.441(7)	177.0(3)	1.13	18e
$\{[PhB(mesIm)_3]Fe(NAd)\}\{BPh_4\}$	4+	1.618(3)	1.439(5)	176.8(3)	1.15	18e

As for the cobalt(III) imides, iron(III) imides containing a variety of ancillary organic groups have proven accessible using this methodology (Table 1.2). These iron(III) imides are generally highly colored and exhibit intense low-energy absorptions that can be assigned as imide-to-iron(III) charge-transfer bands.[29] As would therefore be expected, substitution of an alkylimide for an arylimide greatly reduces the intensity of these transitions, while also increasing the energy at which they are observed. Consistent with this observed blue-shift, the vibrations that are predominantly associated with *Fe*-*N*-R stretching character are observed around 1100 cm^{-1} for alkylimides and near 960 cm^{-1} for arylimides. While the alkylimides *Fe*-*N*-R stretching mode can be very crudely approximated as a harmonic oscillator, the latter arylimides feature strongly vibrationally coupled *Fe*-*N*-C_{ipso} and Fe-*N*-C_{ipso} modes that cannot be decoupled. The d-orbital electronic structures of these iron(III) imides are well described using arguments originally developed for Cp_2Fe^+ by Gray and coworkers.[39]

Akin to the cobalt(III) imides, nitrene transfer to CO also proved to be facile for the iron(III) [$PhBP^R_3$]Fe(NR) imides.[18h] For instance, addition of one atmosphere of CO to [$PhBP^{Ph}_3$]Fe^{III}(N-*p*-tolyl) resulted in formation of O=C=N-*p*-tolyl and [$PhBP^{Ph}_3$]$Fe^{I}(CO)_2$. Alternatively, addition of C≡N^{t}Bu released the carbodiimide ^{t}BuN=C=N(*p*-tolyl). We were moreover able to show that the addition of N_3(*p*-tolyl) to [$PhBP^{Ph}_3$]$Fe^{I}(CO)_2$ regenerated [$PhBP^{Ph}_3$]Fe(N-*p*-tolyl), forming the basis for a catalytic nitrene transfer cycle.[22c]

In addition, the iron imide functionality proved susceptible to hydrogenolysis, a reactivity pattern that Chirik has since reported for a geometrically and electronically distinct iron(III) imide.[18b] Treatment of [$PhBP^{Ph}_3$]Fe^{III}(N-*p*-tolyl) with one atmosphere of

H_2 resulted in complete scission of the Fe-N triple bond, liberating *p*-tolyl-aniline over the course of days at room temperature (Scheme 1.5).[40] The high-spin $S = 2$ anilide species, $[PhBP^{Ph}_3]Fe^{II}$(HN-*p*-tolyl), was observed as a long-lived intermediate and could be isolated. Further exposure to H_2 released H_2N-*p*-tolyl and '$[PhBP^{Ph}_3]Fe(H)$'. The latter hydride species[41] was not observed but inferred from a subsequent benzene insertion reaction to generate $[PhBP^{Ph}_3]Fe(\eta^5\text{-}C_6H_7)$. The solid-state structure of $[PhBP^{Ph}_3]Fe^{II}$(HN-*p*-tolyl) showed an Fe-N-C angle of $127.4(2)^o$ and a Fe-N bond distance of 1.913(2) Å, compared with the respective parameters of 1.658(3) Å and $170.0(2)^o$ for $[PhBP^{Ph}_3]Fe^{III}$(N-*p*-tolyl). These distinct metrical parameters establish sp^2-hybridization at nitrogen, which disrupts the degenerate π bonding manifold of the terminally bonded imide precursor. This disruption in turn leads to a preference for a high-spin configuration, owing to a weakened ligand field.

According to the qualitative d-orbital electronic structure picture we had advanced for these pseudotetrahedral L_3M^{III}(NR) imides (Figures 1.2 and 1.3), we anticipated that iron(II) imides should also be accessible. We were gratified to observe that treatment of $[PhBP^{Ph}_3]Fe$(NAd) with one equivalent of sodium/amalgam, followed by addition of $[^nBu_4N][Br]$, resulted in the clean generation of $\{[PhBP^{Ph}_3]Fe^{II}(NAd)\}\{^nBu_4N\}$.[18i] The metrical parameters of the imide ligand in this d^5 and d^6 redox pair are similar, preserving short Fe-N bonds (approximately 1.65 Å) and near linear Fe-N-C bond angles (Table 1.2). These observations are consistent with a high degree of Fe-N π-bonding. The presence of two strong π-bonds from the imide linkage, along with the strong field tris(phosphino)borate ligands, once again confers the low spin configuration for the iron(II) system. The electronic structure of $\{[PhBP^{Ph}_3]Fe(NAd)\}\{^nBu_4N\}$ was probed by

DFT methods, and is best described by a splitting diagram in which an orbital of $3dz^2$ parentage lies at low energy, close to 3dxy and $3dx^2$-y^2 orbitals that are orthogonal to the Fe-N bond vector. The electronic structure pictures of low-spin $L_3Fe^{II}(NR)^-$, and isoelectronic $L_3Co^{III}(NR)$, are hence closely related to that which was originally elucidated for ferrocene in the classic study by Gray and coworkers nearly four decades ago.[39b,42]

Figure 1.5a plots the visible absorption spectra of select $L_3Fe^{II}(NR)^-$ and $L_3Co^{III}(NR)$ species. If one uses the spin-allowed optical transition assignments (two $^1A_{1g} \rightarrow {}^1E_{1g}$ and one $^1A_{1g} \rightarrow {}^1E_{2g}$) for Cp_2Fe and Cp_2Co^+ as a basis to assign the optical transition assignments for d^6 $L_3Fe(NR)^-$ and $L_3Co(NR)$, then one derives a splitting Δ_1 of ca. 1 eV between the lowest nonbonding xy/x^2-y^2 *e*-set and the z^2 a_1 orbital (Figure 5b). This splitting is substantially smaller than the splitting Δ_2 of ca. 2 eV between the a_1 orbital and the highest-lying xz/yz *e*-set that is strongly σ^* and π^* in character. The splitting Δ_1 is not anticipated by ground state DFT calculations of d^6 $L_3M(NR)$ imides, which place the a_1 orbital nearly degenerate with the nonbonding *e*-set. It would be of obvious interest to theoretically calculate the optical transitions of d^6 $L_3M(NR)$ imides to further explore this issue.

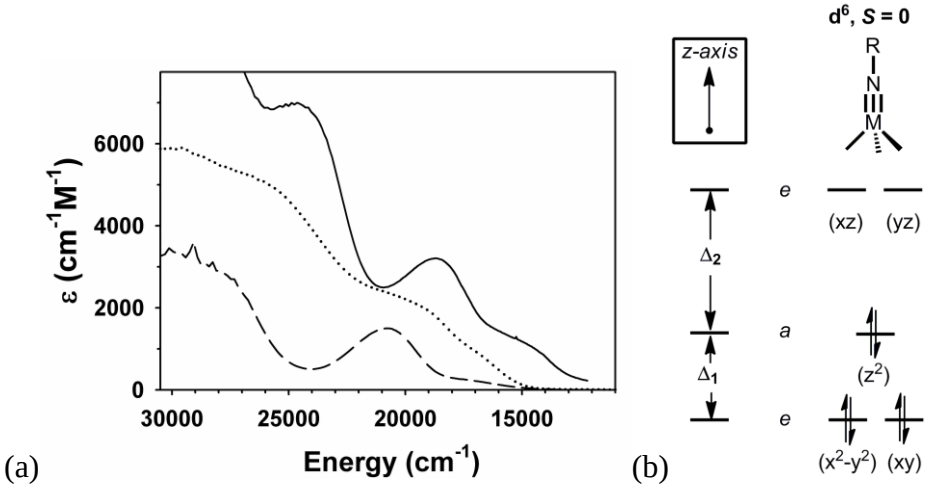

Figure 1.5. (a) Visible absorption spectra of d^6 pseudotetrahedral metal imides. All spectra were recorded at room temperature. (A) $[PhBP_3]Co(NPh)$ (—); (B) $\{[PhBP_3]Fe(NAd)\}^-$ (· · ·) in THF; and (C) $[PhBP_3]Co(N^tBu)$ (— —). (b) d-orbital splitting diagram defining splittings Δ_1 and Δ_2

An obvious progression was to next begin exploring whether the d^4 iron(IV) configuration might also be compatible within the $L_3Fe(NR)$ framework. In parallel with our own studies of $L_3Fe^{III}(NR)$ systems, terminally bonded 6-coordinate iron(IV) oxos had begun to emerge as rigorously isolable species, for example by the groups of Que and Nam.[43] Our initial efforts towards $L_3Fe^{IV}(NR)$ species focused on the one-electron chemical oxidation of $[PhBP^R_3]Fe^{III}(NR)$ precursors, but we were unsuccessful: if an Fe(IV) species was generated in such reaction mixtures, it was not sufficiently long-lived to be detected by the routine characterization methods we adopted. Interrogation of $[PhBP^R_3]Fe^{III}(NR)$ complexes by cyclic voltammetry revealed a chemically irreversible Fe(IV/III) redox couple, contrasting the reversible Fe(III/II) couple that was present at more negative potentials. This observation enforced the notion that $[PhBP^R_3]Fe^{IV}(NR)^+$ species are kinetically unstable, and we thus began to explore related 3-coordinate ligand scaffolds in the hopes of lending a higher degree of stability to the iron(IV) state. One

path of exploration that ultimately proved efficacious was using hybrid scaffolds, whereby one of the phosphine donor ligands was replaced by a pyrazolyl group. To access such ligands, it proved synthetically necessary to decorate the two phosphine donor arms with *tert*-butyl groups, as the intermediate bis(phosphino)boranes, $PhB(CH_2PR_2)_2$, were unstable to dimerization when less encumbering groups were employed.[44] Addition of pyrazole anions to $PhB(CH_2P^tBu_2)_2$ afforded bis(phosphino)pyrazolylborate ligands, abbreviated as $[PhB(P^{tBu})_2(pz^{R,R'})]$ ($pz^{R,R'}$ = pyrazole substituted at the 3 and 5 positions, respectively).

Using a hybrid scaffold of this type, we found that low-spin terminal iron(III) imides could be readily generated, as for the complexes $[PhB(P^{tBu})_2(pz)]Fe(NAd)$ and $[PhB(P^{tBu})_2(pz^{Me,Me})]Fe(NAd)$.[18j] The cyclic voltammograms of these species were distinct from those of tris(phosphino)borate congeners, in that now the Fe(III/II) couple was irreversible, but the Fe(III/IV) couple was quasi-reversible or reversible at room temperature depending on the scan-rate. Chemical oxidation of these iron(III) imides with $[Cp_2Fe][BArF_{24}]$ ($BArF_{24}$ = tetra(3,5-di(trifluoromethyl)phenyl)borate) afforded the bright green iron(IV) imides $\{[PhB(P^{tBu})_2(pz)]Fe^{IV}(NAd)\}\{BArF_{24}\}$ and $\{[PhB(P^{tBu})_2(pz^{Me,Me})]Fe^{IV}(NAd)\}\{BArF_{24}\}$, the former of which was very thermally unstable (Scheme 1.6). The Fe-N bond distance in $\{[PhB(P^{tBu})_2(pz^{Me,Me})]Fe^{IV}(NAd)\}\{BArF_{24}\}$ is 1.634(4) Å and the Fe-N-C angle is $176.2(3)^o$, similar to that of all of the pseudotetrahedral iron(III) imides we had characterized. This is consistent with removal of an electron from an orbital that is orthogonal to the *Fe-N*Ad bond vector, and a $(dz^2)^2(dxy)^1(dx^2\text{-}y^2)^1(dxz)^0(dyz)^0$ electronic configuration (Figure 1.2). Solution Evans method and DFT data were consistent with

this $S = 1$ electronic structure picture. Curiously, upon oxidation, the distance between the iron center and the plane defined by the donor atoms of the tripodal ligand (N-P-P) decreased by ca. 0.11 Å to 1.11 Å. This decrease results in slightly longer Fe-P_{ave} bond distances (ca. 0.03 Å) in the iron(IV) imide compared to the iron(III) congener, which might result in a net decrease of π backbonding from iron into ligand σ* orbitals of appropriate symmetry. This hypothesis is consistent with the observation that the average Fe-P distance decreases by ca. 0.1 Å when neutral [PhBP^{Ph}_3]Fe^{III}(NAd) is reduced by one electron to {[PhBP^{Ph}_3]Fe^{II}(NAd)}{^{n}Bu_4N}, which presumably leads to a net increase in π backbonding into the phosphine ligand σ* orbitals.[18i]

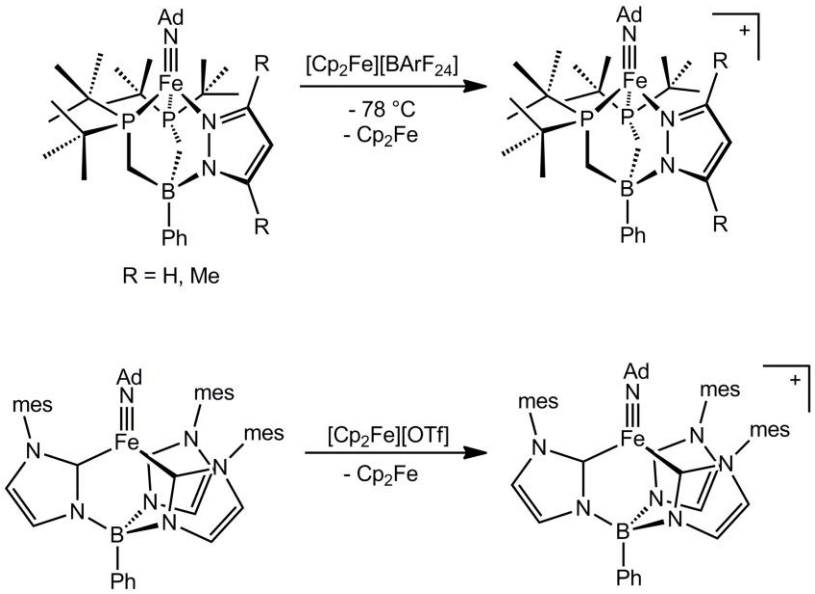

Scheme 1.6.

Smith and coworkers[18e] have recently extended the number of well-characterized iron(IV) imides of the pseudotetrahedral $L_3Fe(NR)$ structure type via the isolation of an intermediate-spin iron(IV) imide, {[PhB$(mesIm)_3$]Fe^{IV}(NAd)}{OTf}, whose electronic

structure is similar to that of {[PhB(P^tBu_2)$_2$($pz^{Me,Me}$)]Fe^{IV}(NAd)}{$BArF_{24}$}. This species was generated by oxidation of the precursor iron(III) imide with [Cp_2Fe][OTf] (Scheme 1.6). The metrical parameters for the core atoms of both the iron(III) and iron(IV) imide congeners are quite similar. For example, the Fe-N_{imide} distances (1.625(4) Å for Fe(III) and 1.618(3) Å for Fe(IV)), the Fe-N-C angle (177.0(3)^o for Fe(III) and 176.8(3)^o Fe(IV)), and the distance between the iron and the plane defined by the tris(carbene) C-donor atoms (1.13 Å for Fe(III) and 1.15 Å for Fe(IV)) change very little. However, the average Fe-C distance increased by 0.04 Å upon oxidation. Again, diminished π backbonding, in this case into σ* orbitals of the tris(carbene) ligand might offer a plausible explanation.

1.2.4 Pseudotetrahedral $L_3Fe(N)$ Species

Well-defined and terminally bound nitrides of iron remain relatively rare. Bridging species are instead often obtained.[1f,45] Nakamoto and coworkers were first to describe the generation of a terminally bonded iron nitride species using an octaethylporphyrin (OEP) supporting ligand framework.[46] They employed a very elegant vibrational analysis to support their assignment. However, the high thermal instability of the (OEP)Fe^V(N) species precluded its further characterization. Wieghardt and coworkers have since characterized low-spin 6-coordinate iron(V)[47] and iron(VI)[48] nitrides using cyclam and cyclam-acetate supporting ligands, respectively. These complexes also exhibit limited thermal stability but have been characterized by a suite of spectroscopic techniques, in addition to having been analyzed theoretically.[49] They populate low-spin

ground states. The S = ½ iron(V) d^3 species appears less stable than the diamagnetic iron(VI) species. The latter d^2 species finds close structural and electronic analogy to the well-established and studied Mn(V) nitride systems.[2d,50]

Our own group's interest in this area focused instead on exploring the feasibility of terminally bonded nitrides under local three-fold symmetry of the type $L_3Fe(N)$. Theoretical analysis suggested to us that replacement of the terminal NR^{2-} ligand by an N^{3-} ligand in systems of this type would strongly destabilize the a_1 orbital of dz^2 parentage that is low-lying in $L_3Fe^n(NR)$ (n = II, III, IV) species (Figure 1.2).[18g] Such destabilization would thereby render d^5 and d^6 configurations comparatively less favorable due to population of a strongly antibonding σ* orbital. By contrast, d^4 and perhaps even lower d-count species might be electronically favored, as there are only two energetically low-lying d-orbitals (dx^2-y^2/dxy). For an iron(IV) species, the predicted electronic configuration is therefore $(xy)^2(x^2\text{-}y^2)^2(z^2)^0(xz)^0(yz)^0$ (Figure 1.6). Such a configuration is similar to Wilkinson's d^4 $Mes_3Ir(O)$ complex. The destabilization of dz^2 relative to the structurally related imides is a consequence of better overlap with the nitrogen sp-hybrid orbital, and a distortion that renders the geometry about the iron center more tetrahedral. The calculated S = 0 $[PhBP^{iPr}_3]Fe(N)$ structure features P-Fe-P angles between 99–101°, whereas these calculated angles for the corresponding imide, S = 0 $\{[PhBP^{iPr}_3]Fe(N^tBu)\}^-$, are between 90–95°, in accord with a wealth of experimental data (Table 1.2). It was therefore incumbent upon us to select an appropriate N-atom transfer agent to test whether an S = 0 nitride would be accessible using the tris(phosphino)borate iron frameworks.

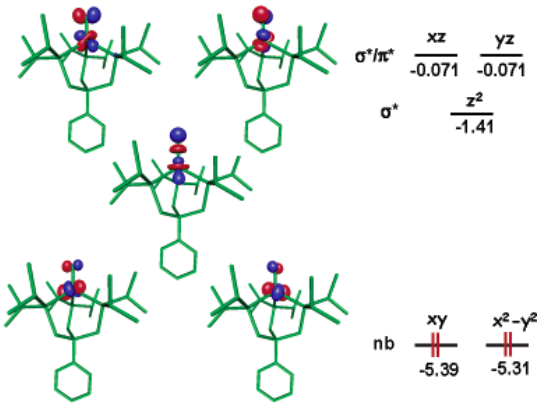

Figure 1.6. Theoretically predicted geometry and electronic structure (DFT, JAGUAR 5.0, B3LYP/LACVP**) for *S* = 0 [PhBP$^{i\text{Pr}}_3$]Fe≡N. Lobal representations correspond to the frontier orbitals (energies in eV). Structural parameters: Fe-P = 2.28, 2.28, 2.29 Å; N-P-Fe = 117, 117, 119°; P-Fe-P = 99, 101, 101°; Fe-N = 1.490 Å. Reprinted with permission from reference 18(g). Copyright 2004 American Chemical Society.

Nitride transfer reactions often occur as two-electron processes that deliver an N-atom while liberating a thermodynamically stable molecule. Azide, N_3^-, is often the reagent of choice owing to its synthetic simplicity and the release of N_2 as a byproduct.[18d,18f,46a,47a,51] N_2 extrusion can occur spontaneously or it can be effected by heating or photolytic means, the latter often being necessary when the resultant nitride is thermally unstable. We found that such protocols were ineffective for generating terminal nitrides with the '[PhBP$^{i\text{Pr}}_3$]Fe' and '[PhBP$^{\text{Ph}}_3$]Fe' frameworks. For example, {[PhBP$^{\text{Ph}}_3$]Fe(N_3)}$_2$ can be prepared and is a thermally stable species. While N_2 extrusion might have been effected by its one-electron reduction to release the d^5 {[PhBP$^{\text{Ph}}_3$]Fe(N)}$^-$ and N_2, any such species appears to be rapidly trapped by "[PhBP$^{\text{Ph}}_3$]Fe$^{\text{I}}$" in solution (iron(I) is generated by kinetically competitive loss of N_3^-

upon reduction) to afford the stable diiron(II) μ-nitride complex [{[PhBP$^{Ph}_3$]Fe}$_2$(μ-N)]$^-$, as shown in Scheme 1.7).[18i]

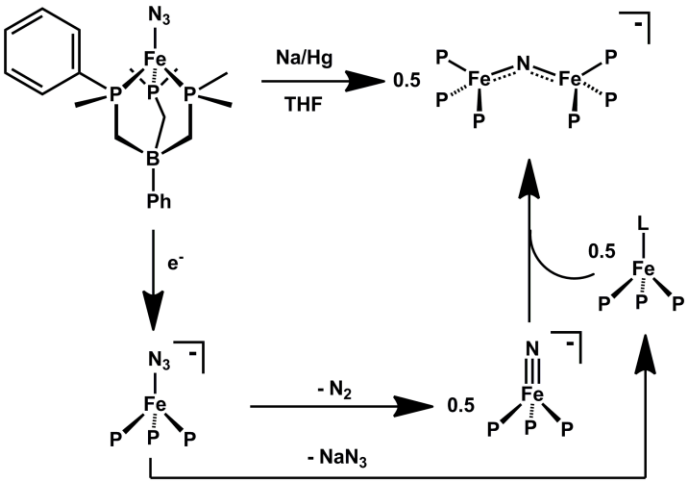

Scheme 1.7.

An alternative approach that proved viable involved use of the N-atom transfer agent Li(dbabh) (dbabh = 1,2:5,6-dibenzo-7-aza bicycle[2.2.1]hepta-2,5-diene). This lithium amide was first used by Cummins and Mindiola to prepare a high-valent chromium nitride.[52] Its utility involves initial formation of a metal amide, M^n-(dbabh), which can thermally release M^{n+2}(N) and one equivalent of anthracene. The utility of this reagent appears to be limited; for example, we have explored its use to install nitride groups at '[PhBP$^R_3$]Mn' and '[PhBP$^R_3$]Ni' systems and in doing so have uncovered alternative reaction manifolds.[53] But to our satisfaction (and relief!), the synthon worked well for '[PhBP$^{iPr}_3$]Fe'.

Using Li(dbabh), the iron(IV) nitride species, [PhBP$^{iPr}_3$]Fe^{IV}(N), can be generated and thoroughly characterized (Scheme 1.8).[18g] Treatment of [PhBP$^{iPr}_3$]FeCl with Li(dbabh) at -35 ^{o}C generated the red and thermally unstable iron(II) amide intermediate,

[PhBP$^{iPr}_3$]Fe^{II}(dbabh). Upon warming to 0 ^{o}C, this intermediate underwent clean first-order decay to release one equivalent of anthracene and the desired diamagnetic product, [PhBP$^{iPr}_3$]Fe(N). Owing to its many spin active nuclei and its diamagnetism, solution NMR characterization of [PhBP$^{iPr}_3$]Fe(N) was straightforward. For example, a diagnostic ^{15}N NMR chemical shift of 952 ppm was observed for the nitride, in accordance with the chemical shift noted for terminal M(N) species.[9,54] The solution IR spectrum showed an Fe-N stretch at 1034 cm^{-1} which is consistent with that of other M(N) species.[55] Upon ^{15}N-labelling, the stretch shifts to 1007 cm^{-1}, in agreement with that calculated (27 cm^{-1}) assuming an Fe-N harmonic oscillator. The Mössbauer spectrum of [PhBP$^{iPr}_3$]Fe(N) was also obtained, and established an isomer shift of δ -0.34 mm/s, and an unusually large quadrupole-splitting parameter, ΔE_Q = 6.01 mms^{-1}.[56] This large quadrupole splitting results from the highly anisotropic electric field gradient that arises from electronic population of dx^2-y^2 and dxy orbitals orthogonal to the B-Fe-N vector, and has proven diagnostic of L_3Fe^{IV}(N) species (*vide infra*). Spontaneous nitride coupling to generate the formal diiron(I) product, {[PhBP$^{iPr}_3$]Fe}$_2$(μ-N$_2$), occured upon concentration or attempts to crystallize [PhBP$^{iPr}_3$]Fe≡N.[18g] We canvassed one other scaffold, '[PhBP$^{CH2Cy}_3$]Fe' (CH_2Cy = cyclohexylmethyl) and successfully generated and characterized [PhBP$^{CH2Cy}_3$]Fe(N) at low temperature.[56] Though nitride coupling does not occur for this latter system, ({[PhBP$^{CH2Cy}_3$]Fe}$_2$(μ-N$_2$) is *not* an accessible species,[37] [PhBP$^{CH2Cy}_3$]Fe(N) proved to be unstable above -50 ^{o}C, and poorly defined degradation pathways frustrated our ability to crystallize this species. Additionally, a short Fe-N bond distance of 1.53(2) Å was obtained for these species by EXAFS.[57]

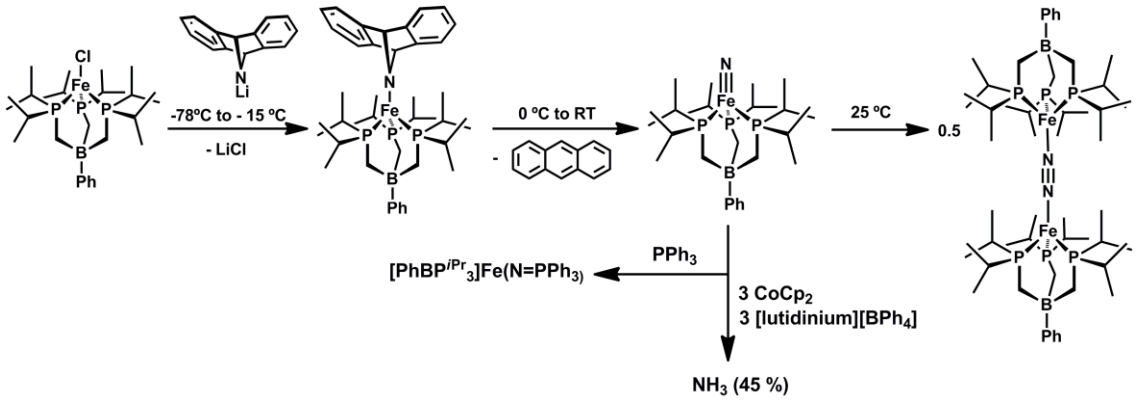

Scheme 1.8.

The respective groups of Meyer and Smith have also targeted terminally bonded iron(IV) nitrides in recent years using the carbene ligand frameworks introduced above. Meyer's 4-coordinate nitrides, $[(TIMEN^{R})Fe(N)][PPh_4]$ (R = mes, xyl), formed via photolysis of 4-coordinate azide precursors, $[(TIMEN^{R})Fe(N_3)][BPh_4]$, proved thermally stable and hence amenable to single-crystal XRD characterization (Scheme 1.9).[18f] Such data revealed an Fe-$N_{nitride}$ bond distance of 1.526(2) Å for $[(TIMEN^{mes})Fe(N)][PPh_4]$ (Table 1.3). This complex represented the first reported terminal iron nitride species to be characterized by X-ray crystallography. Smith's X-ray structure of $[PhB(^{t}BuIm)_3]Fe(N)$ followed soon thereafter.[18d] Meyer's system provided experimental validation that a 4-coordinate $L_3Fe^{IV}(N)$ system is energetically preferred relative to a corresponding 5-coordinate $L'L_3Fe^{IV}(N)$ under local three-fold symmetry, since the apical amine donor does not bind the iron center. The geometry about the iron centers in $[(TIMEN^{R})Fe(N)][PPh_4]$ are close to trigonal pyramidal, with the iron centers ca. 0.54 Å above the plane defined by the three carbene donors. The related $[PhB(RIm)_3]Fe(N)$ system reported by Smith and coworkers was likewise generated via photolysis of

terminal azide precursors. As noted for the calculated structure of [PhBP$^{iPr}_3$]Fe(N), [PhB(^{t}BuIm)$_3$]Fe(N) is somewhat more tetrahedral in structure compared to the corresponding iron(IV) imides (i.e., {[PhB(^{t}BuIm)$_3$]Fe(NAd)}{OTf}), as the average C-Fe-C angle increases from ca. 90^o to ca. 96^o. DFT calculations on the iron(IV) nitrides supported by the three different ligand scaffolds indicate similar electronic structures.[18d,18f,g] Hence, in all three scaffolds the tridentate L_3 donor adopts a geometry such that the a_1 orbital is destabilized to accommodate a favorable d^4 S = 0 $(xy)^2(x^2\text{-}y^2)^2(z^2)^0(xz)^0(yz)^0$ electronic configuration. Note that this electronic structure is distinct from the iron(IV) imides, which adopt an S = 1 ground state due to the fact that the a_1 orbital of dz^2 parentage lies much closer in energy to the nonbonding dxy, $dx^2\text{-}y^2$ *e* set of orbitals (Figure 1.2).

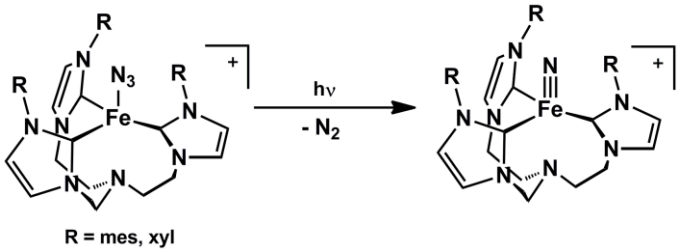

Scheme 1.9.

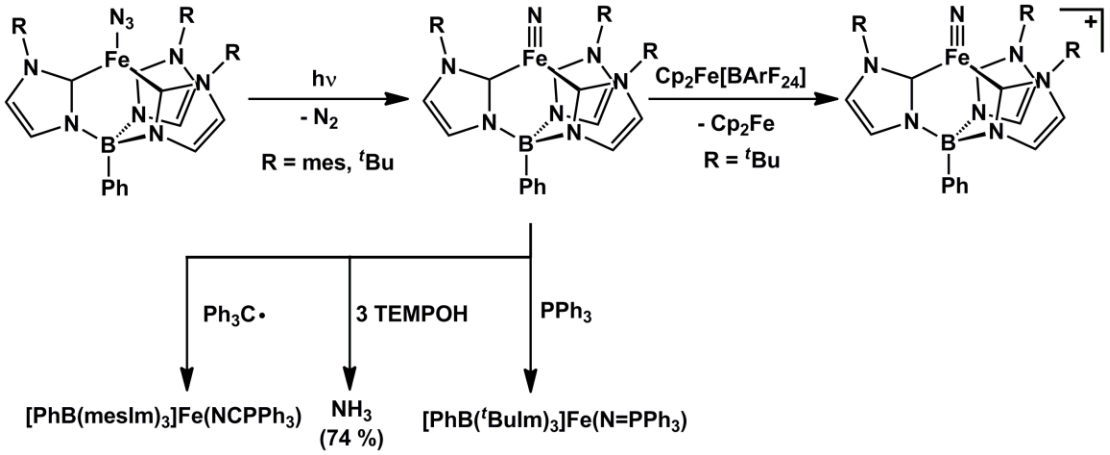

Scheme 1.10.

Table 1.3. Select spectroscopic and structural parameters of pseudotetrahedral $L_3Fe^{IV}(N)$ complexes

Complex	Fe-N stretch $^{14}N/^{15}N$ (cm^{-1})	Fe-N distance (Å)	Displacement of Fe from L_3 plane (Å)	^{15}N NMR chemical shift[a] δ	MB δ (mms^{-1})	MB ΔE_Q δ (mms^{-1})	Ref
$[PhBP^{iPr}_3]FeN$	1034 / 1007	1.51-1.54[b]	--	952	-0.34(1)	6.01(1)	18g,56-57
$[PhBP^{CH2Cy}_3]FeN$	--	1.55[b]	--	929	-0.34(1)	6.01(1)	56-57
$[(TIMEN^{mes})FeN][BPh_4]$	1008 / 982	1.526(2)	0.43	1121	-0.27(1)	6.04(1)	18f
$[(TIMEN^{xyl})FeN][BPh_4]$	--	1.527(3)	0.38	--	--	--	18f
$[PhB(^tBuIm)_3]FeN$	1028 / 999	1.512(1)	0.98	1019	--	--	18d
$[PhB(mesIm)_3]FeN$	--	1.499(5)	1.01	1004	--	--	18c

[a]Referenced to liquid NH_3 at 0 ppm, [b]Obtained by EXAFS.

While the reactivity patterns of these iron(IV) complexes have not been reported in great detail, there are a few transformations worthy of note. Treatment of both $[PhBP^{iPr}_3]Fe(N)$ and $[PhB(^tBuIm)_3]Fe(N)$ with triphenylphosphine effected reductive nucleophilic attack and afforded the corresponding high spin iron(II) phosphiniminato

complexes, [PhBP$^{iPr}_3$]Fe(N=PPh$_3$) and [PhB(^{t}BuIm)$_3$]Fe(N=PPh$_3$), respectively.[18d,18g] Our own group was interested in determining whether the terminal nitride of [PhBP$^{iPr}_3$]Fe(N) could liberate NH_3 on treatment with an e^-/H^+ source, a transformation motivated by a hypothetical Fe-mediated distal scheme for N_2 reduction. It was found that NH_3 could be liberated upon addition of [lutidinium][BPh_4] in the presence of $CoCp_2$, albeit in moderate yield (ca. 45%).[18g] Smith's nitride, [PhB(mesIm)$_3$]Fe(N), was treated with a well-defined H-atom transfer equivalent, TEMPOH, and gave rise to an appreciably higher yield of NH_3 (74%) (TEMPOH = 1-hydroxy-2,2,6,6-tetramethylpiperidine).[18c] The first step of this transformation is thought to occur via H-atom transfer (HAT) from TEMPOH to the nitride, though a protonation/reduction could not be ruled out from the measured free energy of activation. Smith's nitride was also exposed to trityl radical to generate the corresponding iron(III) imide, [PhB(^{t}BuIm)$_3$]Fe(NCPh$_3$). This transformation thereby established another synthetic route to iron imide species.

Perhaps the most interesting reaction to note concerns oxidation of [PhB(^{t}BuIm)$_3$]Fe(N). According to the d-orbital configuration proposed for $L_3Fe^{IV}(N)$ species, d-electron configurations less than d^4 should in principle also show electronic stability. Removal of one electron to generate a d^3 $L_3Fe^{V}(N)$ species is therefore of paramount interest. Such a reaction has very recently been demonstrated using the [PhB(^{t}BuIm)$_3$]Fe(N) precursor. Low temperature oxidation by [Cp_2Fe][$BArF_{24}$] was used to generate the d^3 iron(V) nitride {[PhB(^{t}BuIm)$_3$]Fe(N)}{$BArF_{24}$}, a low-spin species that proved sufficiently stable to isolate and characterize by X-ray crystallography.[58] As should be expected for an $(xy)^2(x^2\text{-}y^2)^1(z^2)^0(yz)^0$ $(xz)^0$ electronic configuration, the Fe-N distance remains virtually unchanged (Fe-N = 1.506(2) Å) relative to its d^4 precursor, and

the iron center remains ca. 1 Å above the L_3 donor plane. Also, {[PhB(^{t}BuIm)$_3$]Fe(N)}{BArF$_{24}$} likewise affords a diagnostic large quadrapole splitting parameter $\Delta E_Q = 4.25$ mms^{-1}.

1.3 Trigonal Bipyramidal (TBP) L'L$_3$-M(E) Structure Types

1.3.1 Orbital Considerations

An interesting question that follows the preceding discussion of L_3M(NR) and L_3M(N) species concerns how the electronic structure rules will vary upon coordination of a fifth ligand in the site *trans* to the multiply bonded ligand E. Such coordination preserves local three-fold symmetry and leads to an L'L_3M(E) structure type, where the L_3 donor set moves into the equatorial plane and L' and E occupy axial sites. Qualitative d-orbital splitting diagrams that provide a starting point for discussing L'L_3M(E) species are shown in Figure 1.7. This electronic picture was introduced in a brief in a review article by Miskowski, Hopkins, and Gray.[59] Assuming a σ-only bonding picture, the dxz/yz *e* set is stabilized by the absence of any σ* interactions with the L'L_3 donor set, which contrasts the strongly destabilized σ* dxz/yz *e* set in pseudotetrahedral L_3M(E) structures. As the E ligand p_x and p_y orbitals are of π symmetry, they can therefore strongly overlap with the dxz/yz *e* set. If these p-orbitals and the dxz and dyz orbitals are each filled with electron pairs, as they would be in a hypothetical species such as $S = 0$ L'L_3Fe^{IV}(N), then a destabilizing π* interaction is present that removes net π bonding at the Fe-N linkage. By contrast, if the ligand E has empty π acceptor orbitals (akin to a CO or NO^+ ligand, for example) then backbonding interactions will occur to stabilize the

dxz/yz *e* set and lead to favorable metal-to-E multiple bonding. A degree of favorable net π-bonding can also be achieved even in the case of π donating ligands such as oxos, imides, and nitrides if only partial population of the dxz/yz *e* set occurs. Perhaps counter-intuitively, the situation can therefore arise where a high-spin d-electron configuration can feature greater multiple bond character than an intermediate- or low-spin configuration for L'L_3Fe(E) structure types (see Figure 1.2 and 1.7). This may be, for example, achieved using supporting ligands that confer a weak ligand field such that a high-spin state is conferred. This scenario directly contrasts that of L_3M(E) species, where high spin configurations will always attenuate the degree of M(E) π bonding. Below we discuss select and pedagogically informative examples of each of these cases, beginning with systems that tend towards low spin configurations.

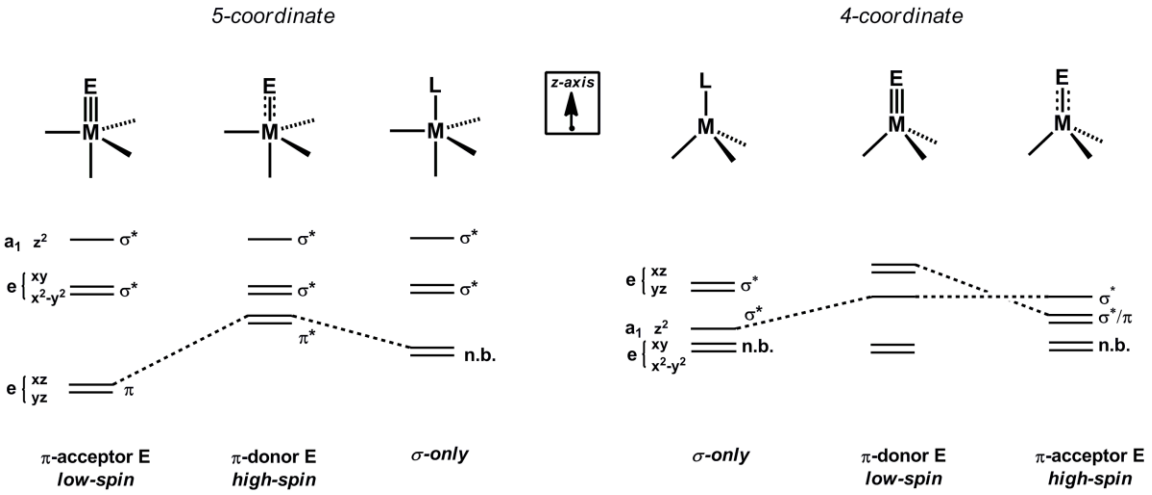

Figure 1.7. Qualitative d-orbital splitting diagrams for 4- and 5-coordinate C_{3v} species, with the anticipated spin-state for each M(E) type noted

1.3.2 Trigonal Bipyramidal L'L_3Fe(NR) Species

The well-studied pseudotetrahedral $L_3Fe^{III}NR$ complexes feature *bona fide* Fe≡NR triple bonds resulting from two highly destabilized, unoccupied $\sigma^*_{L3Fe}\pi^*_{FeN}$ orbitals (Figure 1.2). Introducing a ligand *trans* to the imido group and shifting the Fe into the L_3 plane of a TBP leads in principle to population of the π^*_{FeN} set, thereby obliterating a significant degree of the Fe-N multiple bonding character presumed responsible for the stability of pseudotetrahedral $L_3Fe^{III}NR$ species. Accordingly, until very recently metal-ligand multiply bonded species in TBP configurations of the general type L'L_3M(E), where E is a prototypical π-donor ligand, had been isolated only for d-electron counts of 0 or 1.[5e] TBP systems with higher d-electron counts would be expected to dissociate the apical ligand and distort towards the more stable pseudotetrahedral geometry when accommodating an axial metal-ligand multiple bond, as evident from Meyer's nitrides,[18f] [(TIMEN^R)Fe(N)][BPh_4] and imides,[19b] [(TIMEN^R)Co(NAr)][BPh_4].

To explore a system where such distortion of the axial ligand is prohibited, our group began to study the feasibility of L'L_3Fe(E) species using an anionic tris(phosphino)silyl ligand, $(2\text{-}R_2PC_6H_4)_3Si^-$ ((SiP$^R_3$); R = Ph or ^{i}Pr), as the L'L_3 tetradentate scaffold.[60] These ligands feature a strongly bound silyl donor in the axial position of a TBP, and three tightly chelated phosphine donors in the equatorial plane. Using this ligand scaffold, we have recently mapped the synthetic feasibility of iron imides of the type (SiP$^R_3$)Fe(NR) for direct comparison to [$PhBP_3$]Fe(NR) and related 4-coordinate imides.

In contrast to the [$PhBP^R_3$]$^-$ ligand, which accommodates iron in both high- and low-spin configurations depending on the apically bound ligand (e.g., *S* = 3/2

$[PhBP^{Ph}_3]Fe(PPh_3)$ and S = 1/2 $[PhBP^{Ph}_3]Fe(N^tBu)$) , the $(SiP^R_3)^-$ ligand appears to exclusively enforce low- and intermediate-spin configurations. Hence, 5-coordinate iron(I) d^7 $(SiP^R_3)Fe$-L complexes are S = ½, as for the representative complexes $(SiP^R_3)Fe$-N_2 and $(SiP^R_3)Fe(PMe_3)$. Similarly, iron(II) d^6 complexes of the type $\{(SiP^R_3)Fe\text{-}L\}^+$ and $(SiP^R_3)Fe$-X (L = NH_3, N_2; X = Cl, Me) are invariably intermediate spin S = 1. Removal of an additional electron, as for the complex $\{(SiP^R_3)Fe^{III}\text{-}Cl\}\{BArF_{24}\}$, again results in a d^5, S = 3/2 intermediate-spin configuration.[60-61]

Using a synthetic protocol analogous to that described for the generation of $[PhBP^R_3]M^{III}(NR)$ complexes (M = Fe, Co), we explored the generation of $(SiP^R_3)Fe(NR)$.[33a] Our study showed that $(SiP^{iPr}_3)Fe(NAr)$ species could be generated by addition of arylazides to $[SiP^{iPr}_3]Fe$-N_2, but that they were unstable to subsequent decay pathways (Scheme 1.11). The azide adduct intermediates were more thermally stable and could be isolated for bulky alkyl azide derivatives, for example, $(SiP^{iPr}_3)Fe(\eta^1\text{-}N_3Ad)$. The dominant decay pathway we have discerned for the $(SiP^{iPr}_3)Fe(NAr)$ imide species concerned bimolecular 'NAr' coupling to generate azoarenes ArN=NAr. Such a pathway regenerated $(SiP^{iPr}_3)Fe^I\text{-}N_2$, and hence arylazides could be catalytically degraded to the azoarene byproducts. Chemical trapping experiments were used to further corroborate the presence of the terminal imide moiety. For example, addition of ^{t}BuNC released the carbodiimide ^{t}BuN=C=N-*p*-tolyl and $(SiP^{iPr}_3)Fe(CN^tBu)$. This two electron nitrene transfer is diagnostic of isolable FeNR species (*vide supra*). Also, H-atom trapping by 9,10-dihydroanthracene afforded the d^6 anilide $(SiP^{iPr}_3)Fe(HN\text{-}p\text{-tolyl})$. Related HAT chemistry has been observed in high-spin 4-coordinate FeNR species[62] and invoked in other systems.[17c] The ability of $(SiP^{iPr}_3)FeNAr$ to fascilitate one (HAT), two (nitrene

transfer), and four-electron (azoarene formation) transformations has hence been demonstrated.

Direct detection of S = ½ [SiP$^{i\text{Pr}}_3$]Fe(N-*p*-tolyl) was accomplished using low temperature EPR spectroscopy via *in situ* photolysis of the azide adduct precursor, (SiP$^{i\text{Pr}}_3$)Fe(N$_3$-*p*-tolyl), in a frozen glass[33a] These data, in addition to an accompanying DFT study, placed a majority of the unpaired spin density on iron for (SiP$^{i\text{Pr}}_3$)Fe(N-*p*-tolyl). A distortion away from three-fold symmetry was predicted in the DFT-minimized S = ½ structure. The low-spin configuration seems to be energetically preferred in silico, but was not appreciably lower in energy than the intermediate-spin S = 3/2 species, which also shows a distortion from three-fold symmetry. For comparison, a ruthenium congener, (SiP$^{i\text{Pr}}_3$)Ru(N-*p*-trifluoromethylphenyl), could be prepared, isolated, and thoroughly characterized, including XRD analysis.[63] However, its EPR spectrum suggested an electronic structure distinct from that of (SiP$^{i\text{Pr}}_3$)Fe(N-*p*-tolyl), and combined with accompanying X-ray data and DFT calculations, indicated that (SiP$^{i\text{Pr}}_3$)Ru(N-*p*-trifluoromethylphenyl) is best described as a ruthenium(II) species with an imidyl radical. This may account for its enhanced stability relative to (SiP$^{i\text{Pr}}_3$)Fe(NAr).

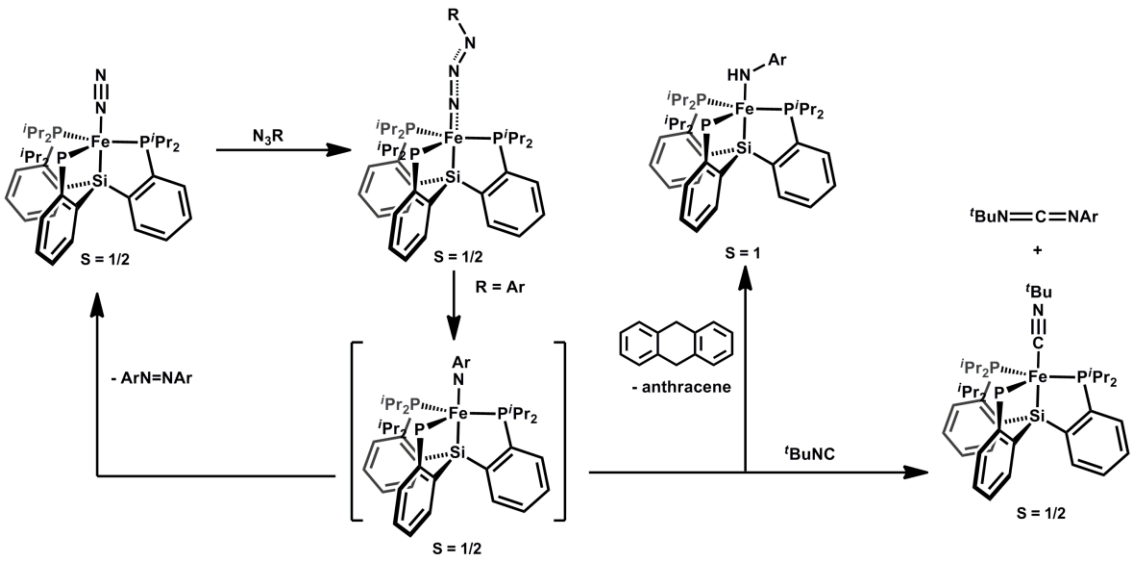

Scheme 1.11.

Very recently our group has explored a ligand closely related to [SiP$^{iPr}_3$], but where the Si-atom is replaced by a B-atom. The tris(phosphino)borane ligand (2-^{i}Pr$_2$PC$_6$H$_4$)$_3$B, was originally introduced by Bourissou and coworkers,[64] and has been abbreviated as TPB (not to be confused with TBP!). We adopt the same convention here. The tris(phosphino)borane TPB ligand might better accommodate the terminal Fe(NR) linkage due to its ability to undergo an axial distortion that would weaken the Fe-B interaction, akin to that observed by Meyer in the tris(carbene)amine ligand scaffold. While studies of (TPB)Fe species are in their early days in our labs, we have determined that the complexes {(TPB)Fe(N$_2$)}$^-$ and (TPB)Fe(N-*p*-MeO-phenyl) can be prepared (Scheme 1.12) and structurally characterized, and that the Fe-to-B bond distance adjusts dramatically to accommodate a π-acidic N$_2$ ligand (2.29 Å in {(TPB)Fe(N$_2$)}{Na(12-crown-4)$_2$}) relative to a π-basic imide ligand (2.61 Å in (TPB)Fe(N-*p*-MeO-phenyl)). Indeed, the latter species is perhaps best formulated as trigonal pyramidal, as the iron sits

0.68 Å above the plane defined by the three phosphine donor ligands. However, a weak Fe-B interaction is indicated by DFT analysis and the triarylborane framework remains pyramidalized in the structure of (TPB)Fe(N-*p*-MeO-phenyl). The iron imide functionality displays similar metrical parameters in the solid-state (Fe-N: 1.668 Å, Fe-N-C: 170.2°) to $L_3Fe(NR)$ species in rigorously 4-coordinate geometries.[65]

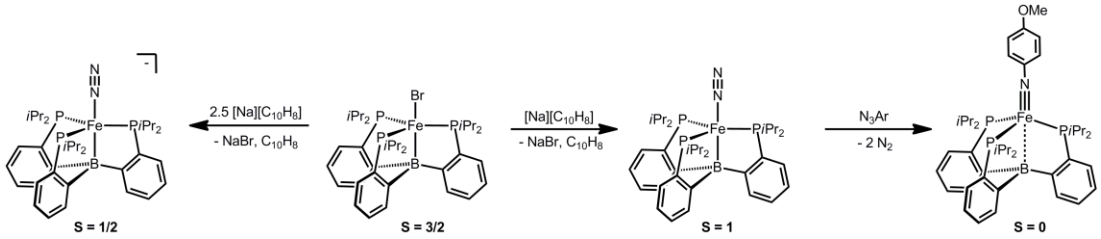

Scheme 1.12.

1.3.3 Trigonal Bipyramidal L'L_3Fe(CR) and L'L_3Fe(N_2R) Species

An alternative means of stabilizing metal-to-ligand multiple bonding in complexes of the L'L_3Fe(E) structure type concerns coordination of a Lewis-acid (e.g., $SiMe_3^+$) to a π-acidic ligand (N_2 or CO), which should in turn enhance its π-acceptor character. This is well illustrated by our group's recent characterization of the terminal carbyne complex (SiP^{iPr}_3)Fe(C-$OSiMe_3$), generated via silylation of the coordinated CO ligand in (SiP^{iPr}_3)$Fe(CO)^-$ (Scheme 1.13).[66] X-ray, Mössbauer, and DFT analysis of this carbyne have established that the iron center is best described as d^8 with two electron pairs strongly backdonating into the carbyne C-atom to afford an Fe-C bond distance of 1.67 Å. The one caveat to this d^8 assignment concerns the presence of a filled Fe-Si σ bonding orbital within the d-orbital energy manifold. This orbital is not shown in Figure

1.2, but if included, suggests that a d^{10} assignment is also plausible. Regardless, in contrast to the Fe-N interaction in the imide species (SiP$^{iPr}_3$)Fe(N-*p*-tolyl), the Fe-C interaction in (SiP$^{iPr}_3$)Fe(COSiMe$_3$) definitely has triple bond character. Hence, one way to circumvent the apparent incompatibility of a high d-electron count within the TBP framework, and an axial metal-to-ligand multiple bond, is to reverse the polarity of the multiply bonded ligand so that it is a π-acceptor rather than a π-donor (Figure 7). Such a situation should thereby lead to stable complexes with high d-counts, and finds analogy in the stability of d^8 FeL$_5$ structure types such as Fe(CO)$_5$.[25]

Using a similar synthetic strategy (i.e., addition of an electrophilic silyl reagent to an Fe(0) precursor), the diazenido complex (SiP$^{iPr}_3$)Fe(N$_2$SiMe$_3$) could likewise be generated.[61] This species is isoelectronic with (SiP$^{iPr}_3$)Fe(COSiMe$_3$) and also features a degree of Fe-to-N multiple bond character. The combined solid-state structure and diamagnetic ground-state suggested that it too can be assigned a low-spin d^8 configuration.

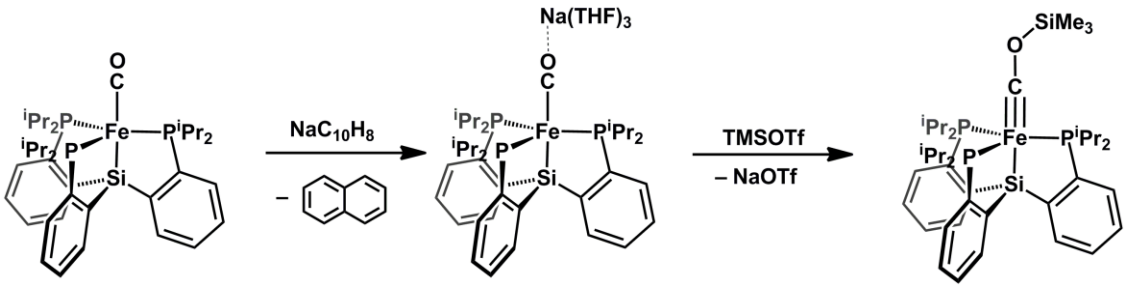

Scheme 1.13.

1.3.4 Trigonal Bipyramidal L'L_3Fe(O) Species

Owing to their postulated mechanistic role in non-heme oxygen activating enzymes, there has been much recent interest in the development of synthetic iron(IV) oxo model species.[1e,67] The S = 2 high spin ground state of the biological non-heme ferryl intermediates is presumed to contribute to their highly reactive nature,[68] and biomimetic analogues that are high-spin have likewise proven comparatively difficult to generate and characterize. The first generation of synthetic non-heme iron(IV) oxo complexes that were thoroughly characterized, including X-ray crystallography, were introduced by Que and Nam and featured local C_{4v} symmetry and intermediate spin S = 1 ground states.[43] These have been thoroughly discussed elsewhere.[1h,69] A descent from four-fold symmetry to three-fold symmetry proved necessary to access well-defined and relatively stable high-spin iron oxo species that feature Fe=O multiple bond character.

Que and coworkers described the preparation of the first synthetic example of a *high-spin* non-heme iron(IV) oxo species.[70] Using the neutral tetrapodal ligand TMG_3tren (TMG_3tren = 1,1,1-tris{2-[N^2-(1,1,3,3-tetramethylguanidino)]ethyl}amine), the trigonal bipyramidal precursor species (TMG_3tren)$Fe^{II}(OTf)^+$ was exploited. Treatment of (TMG_3tren)$Fe^{II}(OTf)^+$ with 2-(*tert*-butylsulfonyl)-iodosylbenzene resulted in the formation of the unusual terminal oxo species (TMG_3tren)$Fe^{IV}(O)^{2+}$ (Scheme 1.14). Its high-spin state was determined by Mössbauer spectroscopy, and further corroborated by XAS and DFT calculations. The high-spin nature of (TMG_3tren)$Fe^{IV}(O)^{2+}$ appeared to contribute to its high degree of thermal instability. A facile intra-molecular self-decay pathway afforded it a half-life of only ca. 30 s at 25 ^oC.[71] The self-decay pathway was thoroughly examined, and the proposed mechanism of decay is shown in Scheme 14.

Kinetic studies on the decay of (TMG$_3$tren)Fe^{IV}(O)$^{2+}$ and (d_{36}-TMG$_3$tren)Fe^{IV}(O)$^{2+}$ revealed a large and primary KIE of 24 at 25 ^{o}C. This isotope effect lent added stability to the deuterated analogue, and allowed for crystals suitable for X-ray data collection to be obtained at -80 ^{o}C. The Fe-O bond distance in (d_{36}-TMG$_3$tren)Fe^{IV}(O)$^{2+}$ was found to be 1.661(2) Å, in agreement with that predicted by DFT and the distance obtained by EXAFS. This bond distance is very similar to that of S = 1 Fe=O species.[18k,43b,72] Taking into account the different d-orbital splitting diagrams under C_{4v} and C_{3v} symmetry this is to be expected, as in both cases the π* orbitals are populated by only two electrons.

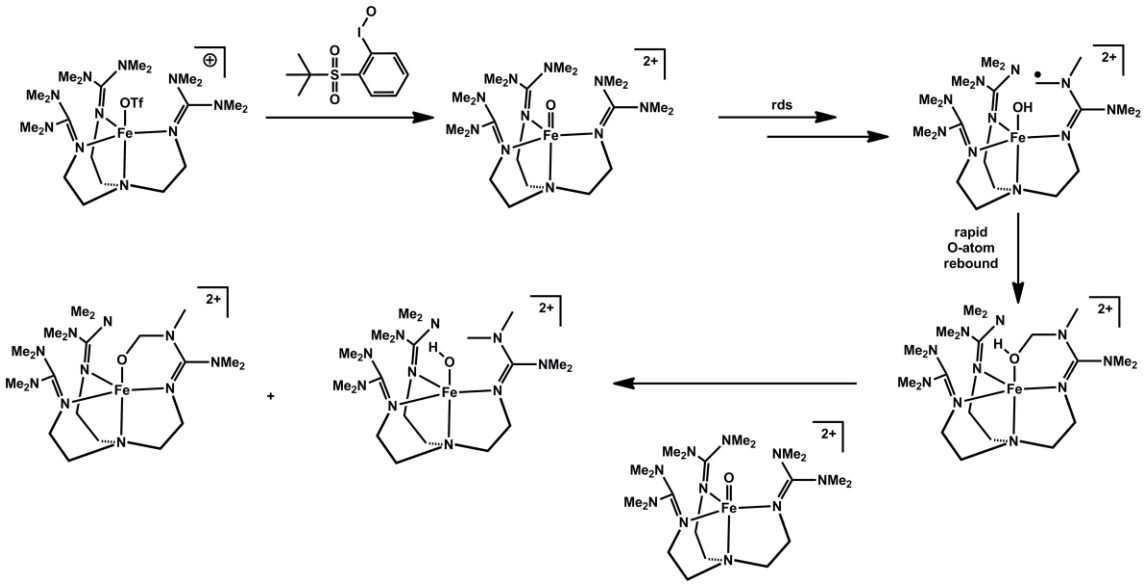

Scheme 1.14.

The group of Borovik has also been able to prepare and isolate 5-coordinate high-spin iron(IV) and iron(III) oxo complexes that reside in local three-fold symmetric environments. With the idea that H-bonding to a terminal oxo ligand may stabilize it, the trianionic, tetrapodal ligand, tris[(N'-tert-butylureaylato)-N-ethyl)]aminato ([NN$^{H3}{}_3$]$^{3-}$ (where H3 indicates the number of H-bond donors) was developed.[73] This ligand scaffold

enforces a TBP geometry, and features three acidic C(O)N*H*(*t*Bu) groups above the plane of the anionic nitrogen donors, which can act as H-bond donors to an oxo ligand.

Treatment of the ligand, $[NN^{H3}{}_3]^{3-}$ with an equivalent of KH, followed by treatment with $Fe(OAc)_2$ and half an equivalent of O_2, afforded the terminal oxo $[NN^{H3}{}_3]Fe^{III}(O)^{2-}$.[74] Its proposed mechanism of formation is shown in Scheme 1.15, which accounts for the additional equivalent of base. This complex is remarkable in that it is high-spin, and yet relatively stable. The solid-state structure of $[NN^{H3}{}_3]Fe^{III}(O)^{2-}$ revealed that the oxo ligand is only 0.04 Å displaced from the plane defined by the three urea nitrogen atoms and supported by H-bonding. The Fe-O bond distance of 1.813(3) Å in $[NN^{H3}{}_3]Fe^{III}(O)^{2-}$ is comparable to those found in $Fe^{III}{}_2(\mu\text{-O})$ complexes,[75] and hence is consistent with partial multiple bond character. This bond distance is however longer than that found in the d^2 $[FeO_4]^{2-}$, which features Fe-O bond distances that range from 1.660(2) to 1.671(2) Å.[76] The stability of $[NN^{H3}{}_3]Fe^{III}(O)^{2-}$ is in part due to the formation of hydrogen bonds, which decreases the covalency in the Fe-O bond and results in elongation of the Fe-O bond.[77]

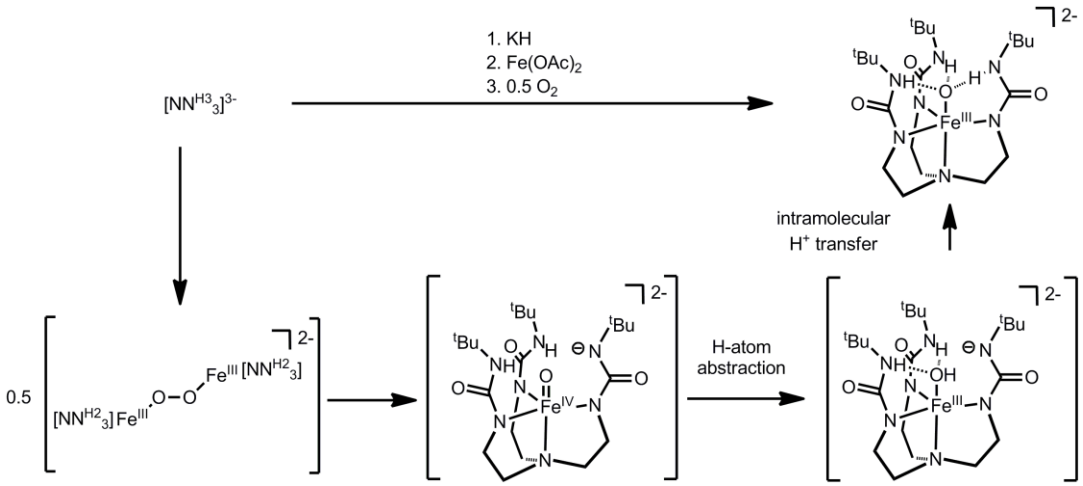

Scheme 1.15.

The iron(III) oxo species displayed modest HAT reactivity to give $[NN^{H3}_3]Fe^{II}(OH)^{2-}$, though the acidity of $[NN^{H3}_3]Fe^{III}(OH)^{-}$ allowed for facile protonation as an alternative reaction pathway.[78] Both the iron(III) oxo and hydroxo species underwent oxidation with $[Cp_2Fe]^{+}$ to generate the S = 2 $[NN^{H3}_3]Fe^{IV}(O)^{-}$ (Scheme 1.16).[79] This latter species was not thermally stable, and underwent H-atom abstraction from solvent to give $[NN^{H3}_3]Fe^{III}(OH)^{-}$ at room temperature, with a half-life of ca. 2.2 hours. The strong NH bond dissociation energy of the urea nitrogen atoms likely precluded intramolecular degradation pathways, which resulted in heightened stability compared to $(TMG_3tren)Fe^{IV}(O)^{2+}$. The solid-state structure of $[NN^{H3}_3]Fe^{IV}(O)^{-}$ was obtained, and showed several discernable differences from its reduced congener. Now, the Fe-O bond distance has decreased by ca. 0.13 Å to 1.680(1) Å, which suggests a similar bonding description to that of $(TMG_3tren)Fe^{IV}(O)^{2+}$ (i.e., two electron population of π^* orbitals). The oxo ligand is 0.262 Å displaced from the plane defined by the three urea H-bonding nitrogen atoms, and vibrational spectroscopy and DFT calculations corroborate the absence of H-bonds interactions with the oxo moiety.[77,79]

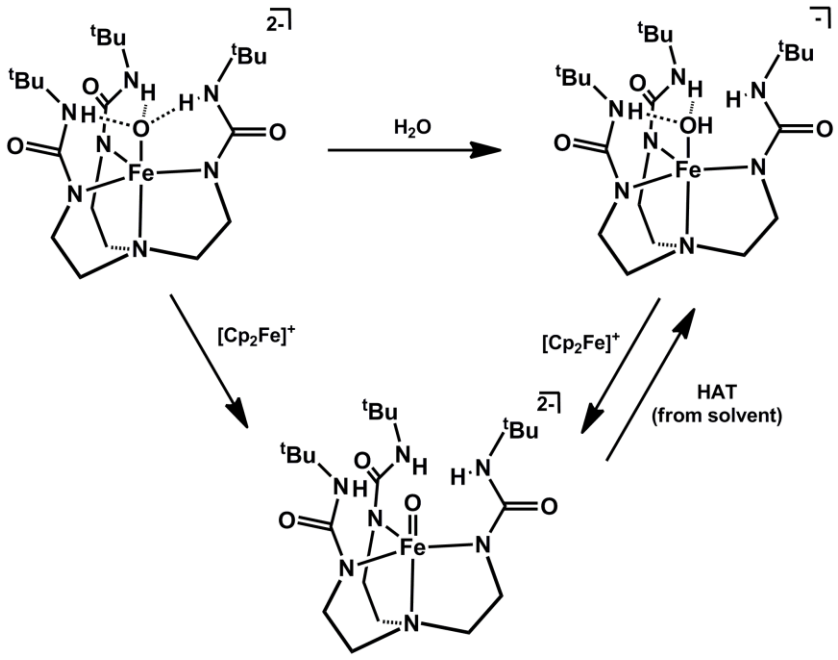

Scheme 1.16.

1.4 Concluding Remarks

1.4.1 Summary

As is hopefully now evident, the field of mid-to-late transition metals that feature metal-to-ligand multiple bonds has emerged as a rich and exciting area of coordination chemistry over the past decade. While the scope of this review has been limited to systems of iron and cobalt that reside in local three-fold symmetry, owing to our own specific expertise and research interests, mid-to-late metals in a host of local geometries and coordination numbers (e.g., linear 2-coordinate, C_{2v} 3-coordinate, C_{4v} 5- and 6-coordinate) have now been demonstrated to be compatible with metal-to-ligand multiple

bonds to terminal imides, oxos, and nitrides. Figure 1.8 displays a few select examples from the recent literature.

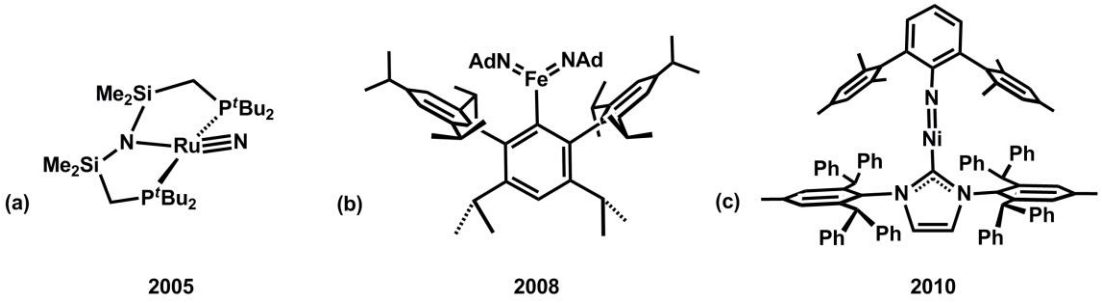

Figure 1.8. Select examples of M(E) species with low coordination numbers. (a) $[(^tBu_2PCH_2SiMe_2)_2N]Ru^{IV}N$,[80] (b) $(Ar)Fe^{V}(NAd)_2$,[18a] (c) $(IAr)Ni^{II}(NAr^*)$.[81]

Pseudotetrahedral iron and cobalt systems of local three-fold symmetry have proven pedagogically informative in establishing how rich the redox chemistry of the $L_3M(E)$ structural unit can be. For example, if one considers pseudotetrahedral iron complexes of the type $L_3Fe(NR)$ and $L_3Fe(N)$, one can now find representative complexes in the formal Fe(2+), Fe(3+), Fe(4+), and Fe(5+) oxidation states where a *bona fide* $Fe{\equiv}N_x$ triple bond is maintained (Figure 1.2). These complexes constitute four spectroscopically distinct d-electron configurations. If one disrupts the π manifold by replacing the N_x ligand by a chemically distinct L donor (e.g., N_2, PMe_3) then one can access Fe(1+) (e.g., $[PhBP_3]Fe(PMe_3)$) and even Fe(0) (e.g., $\{[PhBP_3]Fe(N_2)\}^-$) as spectroscopically distinct species with different d-orbital pictures (d^7 and d^8, respectively). The lesson is a simple one. A pseudotetrahedral L_3Fe-X center can span six formal oxidation states, with six unique d-orbital electronic structures, simply by varying the identity of X! If one moves to iron centers of higher coordination number, one now finds examples of Fe(4+), Fe(5+), and even Fe(6+). Once again, the d-orbital structures

of these species are rich in terms of the spin-states that are accessible and compatible with the multiply bonded ligand. The conclusion is very clear. Whereas a decade ago the chemistry of well-defined iron complexes featuring *bona fide* and terminally bonded imides, oxos, and nitrides, was in its infancy, this area of chemistry, which can span every oxidation state from Fe(2+) to Fe(6+) and a host of spin-states ranging from low- to intermediate- to high-spin, is as rich and perhaps even richer in terms of electronic diversity than that of any other transition element.

1.4.2 Relevance to Small Molecule Activation

As stated in the introduction, multiply bonded species of mid-to-late transition metals are postulated as key intermediates in several synthetic and enzymatic transformations.

With regards to nitrogen fixation, two limiting mechanisms[82] have been proposed to describe the biological reduction of N_2 to NH_3 at the FeMo cofactor of nitrogenase.[82-83] The first, termed distal, involves coordination of N_2 to one or more metal centers, with subsequent addition of protons/electrons to a single nitrogen atom, which releases one equivalent of ammonia and generates a nitride intermediate. Protonation/reduction of the nitride species then releases a second equivalent of ammonia, and regenerates the starting metal species (Scheme 1.17). Such a mechanistic scheme has been shown to be viable at a single molybdenum center.[4a,84] As there is evidence that N_2 reduction occurs at one or more iron centers at the FeMo cofactor,[83,85] there has been much interest in establishing

an analogous iron-based system that can reduce N_2. Many of the Fe(E) (E = N, NR) species described serve as mimics for intermediates in the distal reduction scheme.

The second limiting reduction scheme, termed alternating, also involves initial coordination of N_2 to one or more metal centers. However, the subsequent steps, the addition of protons/electrons, differ, as they are delivered in an alternating fashion to the two nitrogen atoms, such that diazene and hydrazine are intermediates (Scheme 1.17).[82,86] This mechanistic scenario involves little or no oxidation state changes at the metal(s), which contrasts with the distal reduction scheme. Some of the proposed intermediates in this reduction scheme can also feature multiple bonds between the metal and the nitrogenous ligand(s) (i.e., diazenido, hydrazido). This latter reduction scheme has received relatively little attention by synthetic inorganic chemists,[4b] though the realization that diazene[87] and hydrazine[88] are also substrates for the FeMo cofactor of nitrogenase is changing this.

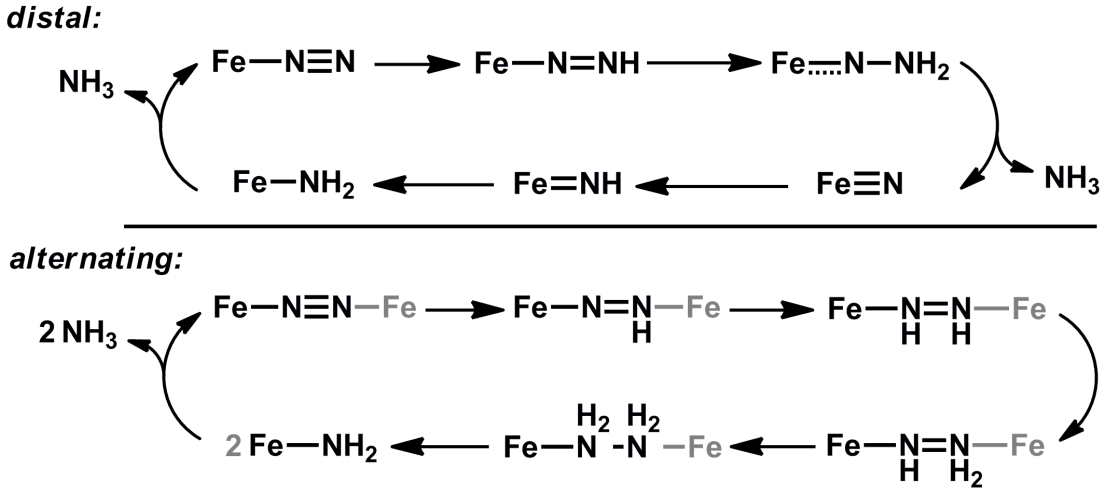

Scheme 1.17.

Another small molecule that is receiving much attention is CO_2, which can be reduced by several mechanisms to give a variety of reduction products, including CO, formate, methanol, and oxalate.[89] Some of these reduction products, as well as proposed intermediates in the reduction chemistry, can also form multiple bonds to a metal center; for example, the two electron reduction of CO_2 often results in decarbonylation, generating oxo species.[90]

1.5 Chapter Summaries

Broadly, Chapters 2–5 focus on synthesizing, characterizing, and interconverting nitrogenous ligands at mono- and diiron centers. These complexes serve as structural, spectroscopic, and/or reactivity mimics for an iron mediated alternating reduction scheme of N_2. Chapter 6 focuses on the iron(I)-mediated reduction of CO_2.

Chapter 2 describes the synthesis and characterization of several 6-coordinate diiron complexes that coordinate N_xH_y ligands in a bridging mode. The reaction between [PhBP$^R_3$]FeMe ([PhBP$^R_3$]$^-$ = PhB(CH$_2$PR$_2$)$_3^-$; R = Ph, CH$_2$Cy) and hydrazine affords {[PhBP$^R_3$]Fe}$_2$(μ-η^1:η^1-N_2H_4)(μ-η^2:η^2-N_2H_2). In one instance (R = CH$_2$Cy), the bridging nitrogen ligands disproportionate to diazene and amides, generating {[PhBP$^{CH2Cy}_3$]Fe}$_2$(μ-η^1:η^1-N_2H_2)(μ-NH$_2$)$_2$. In another instance (R = Ph), the stepwise oxidation of coordinated hydrazine to diazene, and diazene to dinitrogen is achieved, forming first {[PhBP$^{Ph}_3$]Fe}$_2$(μ-η^1:η^1-N_2H_2)(μ-η^2:η^2-N_2H_2) then {[PhBP$^{Ph}_3$]Fe}$_2$(μ-NH)$_2$. This reactivity suggests that the microscopic reverse, dinitrogen reduction to hydrazine, may be feasible at a diiron center.

Chapter 3 discusses a 5-coordinate diiron diazene redox pair of complexes, $\{[PhBP^{Ph}_3]Fe(CO)\}_2(\mu\text{-}\eta^1\text{:}\eta^1\text{-}N_2H_2)^{0/-}$. The electronic structure of the Fe-NH-NH-Fe core is unusual in that it features a highly activated diazene ligand, which is unprecedented for mid-to-late transition metals. These complexes were characterized by XRD, resonance Raman, multinuclear-NMR and EPR spectroscopies, and (in collaboration with Prof. Brian M. Hoffman at Northwestern) ENDOR spectroscopy. Their electronic structures were also investigated by DFT methods. These combined studies indicate that there is much π-covalency within the Fe-N(H)-N(H)-Fe core, and that the electronic structure of the core is similar to that of butadiene and the butadiene anion.

Chapter 4 describes the synthesis and characterization of 5- and 6-coordinate mononuclear iron hydrazido(-), hydrazine, and ammonia species of iron. Treatment of $[PhBP^{m\text{ter}}_3]FeMe$ with hydrazine generates the unusual 5-coordinate hydrazido(-) complex, $[PhBP^{m\text{ter}}_3]Fe(\eta^2\text{-}N_2H_3)$, which features an Fe=N π bond. Reversible coordination of an L-type ligand breaks the π bond and generates $[PhBP^{m\text{ter}}_3]Fe(L)(\eta^2\text{-}N_2H_3)$ (L = N_2H_4 or NH_3). Both 5- and 6- coordinate iron complexes that coordinate hydrazine were also synthesized, and the oxidation of these hydrazine and hydrazido(-) species was explored. In most instances, oxidation results in disproportionation of the N_2H_y ligand, and $[PhBP^{R}_3]Fe(NH_3)(OAc)$ (R = Ph, *m*ter) is isolated. These results contrast with that of the diiron species described in Chapters 2 and 3, and collectively, they underscore the many reaction pathways that are accessible to N_2H_y radical species.

Chapter 5 presents a family of complexes which feature the same auxiliary ligands (i.e., $[PhBP^{CH2Cy}_3]Fe(OAc)$), that are all iron(II), and that only differ in the

oxidation state of the nitrogenous ligand. Thus, {[PhBP$^{CH2Cy}_3$]Fe(OAc)}$_2$(μ-N_2), {[PhBP$^{CH2Cy}_3$]Fe(OAc)}$_2$(μ-N_2H_2), {[PhBP$^{CH2Cy}_3$]Fe(OAc)}$_2$(μ-N_2H_4), and {[PhBP$^{CH2Cy}_3$]Fe(OAc)(NH_3) have all been prepared. These complexes have been thoroughly characterized, and preliminary disproportionation and reduction reactions are described.

Chapter 6 explores the one and two electron reductions of CO_2 that are mediated by iron(I). In coordinating solvents, treatment of [PhBP$^{CH2Cy}_3$]Fe(PR_3) with CO_2 generates the one electron reduction product, {[PhBP$^{CH2Cy}_3$]Fe}$_2$(μ–η^2:η^2–oxalato). In contrast, when the reaction is run in non-coordinating solvents, the two-electron reduction product, {[PhBP$^{CH2Cy}_3$]Fe}$_2$(μ-O)(μ-CO), is exclusively observed. The role that the solvent plays is discussed, as well as the role of the auxiliary ligand. Combined with DFT calculations on the proposed intermediate "Fe-CO_2" species, a mechanistic scheme is proposed, in which reductive coupling of CO_2 ensues from two electronically saturated 19-electron iron centers, and decarbonylation occurs when this electronic configuration cannot be achieved.

Acknowledgements:

This chapter was written jointly with my advisor, Jonas C. Peters. It has been submitted and accepted as a review article for *Coordination Chemistry Reviews* (Sections 1.1 to 1.4.1).

Works Cited:

1. (a) Nugent, W. A.; Mayer, J. M., *Metal Ligand Multiple Bonds*. Wiley & Sons: New York, NY, 1988; (b) Holm, R. H.; Berg, J. M., *Acc. Chem. Res.* **1986**, *19*, 363; (c) Doyle, M. P., *Chem. Rev.* **1986**, *86*, 919; (d) Groves, J. T.; Han, Y.-Z., Cytochrome P450: Structure, Mechanism, and Biochemistry. In *Cytochrome P450: Structure, Mechanism, and Biochemistry*, Ortiz de Montellano, P. R., Ed. Plenum Press: New York, NY, 1995; pp 3; (e) Costas, M.; Mehn, M. P.; Jensen, M. P.; Que, L., *Chem. Rev.* **2004**, *104*, 939; (f) Mehn, M. P.; Peters, J. C., *J. Inorg. Biochem.* **2006**, *100*, 634; (g) Green, M. T., *Curr. Opin. Chem. Biol.* **2009**, *13*, 84; (h) Que, L., *Acc. Chem. Res.* **2007**, *40*, 493.

2. (a) Collman, J. P.; Zhang, X. M.; Lee, V. J.; Uffelman, E. S.; Brauman, J. I., *Science* **1993**, *261*, 1404; (b) Gao, Y.; Hanson, R. M.; Klunder, J. M.; Ko, S. Y.; Masamune, H.; Sharpless, K. B., *J. Am. Chem. Soc.* **1987**, *109*, 5765; (c) Joergensen, K. A., *Chem. Rev.* **1989**, *89*, 431; (d) Groves, J. T.; Takahashi, T., *J. Am. Chem. Soc.* **1983**, *105*, 2073; (e) Li, Z.; Quan, R. W.; Jacobsen, E. N., *J. Am. Chem. Soc.* **1995**, *117*, 5889; (f) Evans, D. A.; Woerpel, K. A.; Hinman, M. M.; Faul, M. M., *J. Am. Chem. Soc.* **1991**, *113*, 726.

3. (a) Müller, P.; Fruit, C., *Chem. Rev.* **2003**, *103*, 2905; (b) Davies, H. M. L.; Hansen, T.; Churchill, M. R., *J. Am. Chem. Soc.* **2000**, *122*, 3063; (c) Davies, H. M. L.; Manning, J. R., *Nature* **2008**, *451*, 417.

4. (a) Schrock, R. R., *Acc. Chem. Res.* **2005**, *38*, 955; (b) Crossland, J. L.; Tyler, D. R., *Coord. Chem. Rev.* **2010**, *254*, 1883.

5. (a) Shaik, S.; Hirao, H.; Kumar, D., *Acc. Chem. Res.* **2007**, *40*, 532; (b) Shaik, S.; Lai, W.; Chen, H.; Wang, Y., *Acc. Chem. Res.* **2010**, *43*, 1154; (c) Cundari, T. R.; Dinescu, A.; Kazi, A. B., *Inorg. Chem.* **2008**, *47*, 10067; (d) Cundari, T. R., *J. Am. Chem. Soc.* **1992**, *114*, 7879; (e) Betley, T. A.; Wu, Q.; Van Voorhis, T.; Nocera, D. G., *Inorg. Chem.* **2008**, *47*, 1849; (f) Berry, J. F., *Comments Inorg. Chem.* **2009**, *30*, 28.

6. Ballhausen, C. J.; Gray, H. B., *Inorg. Chem.* **1962**, *1*, 111.

7. Mayer, J. M., *Inorg. Chem.* **1988**, *27*, 3899.

8. Cummins, C. C.; Schrock, R. R.; Davis, W. M., *Organometallics* **1992**, *11*, 1452.

9. Odom, A. L.; Cummins, C. C.; Protasiewicz, J. D., *J. Am. Chem. Soc.* **1995**, *117*, 6613.

10. Anderson, T. M.; Neiwert, W. A.; Kirk, M. L.; Piccoli, P. M. B.; Schultz, A. J.; Koetzle, T. F.; Musaev, D. G.; Morokuma, K.; Cao, R.; Hill, C. L., *Science* **2004**, *306*, 2074.

11. (a) Mayer, J. M.; Tulip, T. H., *J. Am. Chem. Soc.* **1984**, *106*, 3878; (b) Mayer, J. M., *Comments Inorg. Chem.* **1988**, *8*, 125; (c) Spaltenstein, E.; Conry, R. R.; Critchlow, S. C.; Mayer, J. M., *J. Am. Chem. Soc.* **1989**, *111*, 8741.

12. Rouschias, G., *Chem. Rev.* **1974**, *74*, 531.

13. Mayer, J. M.; Thorn, D. L.; Tulip, T. H., *J. Am. Chem. Soc.* **1985**, *107*, 7454.

14. (a) Moyer, B. A.; Meyer, T. J., *Inorg. Chem.* **1981**, *20*, 436; (b) Moyer, B. A.; Meyer, T. J., *J. Am. Chem. Soc.* **1978**, *100*, 3601; (c) Thompson, M. S.; Meyer, T. J., *J. Am. Chem. Soc.* **1982**, *104*, 4106.

15. Glueck, D. S.; Wu, J. X.; Hollander, F. J.; Bergman, R. G., *J. Am. Chem. Soc.* **1991**, *113*, 2041.

16. Haymotherwell, R. S.; Wilkinson, G.; Hussainbates, B.; Hursthouse, M. B., *Polyhedron* **1993**, *12*, 2009.

17. (a) Jensen, M. P.; Mehn, M. P.; Que, L., *Angew. Chem. Int. Ed.* **2003**, *42*, 4357; (b) King, E. R.; Betley, T. A., *Inorg. Chem.* **2009**, *48*, 2361; (c) Lucas, R. L.; Powell, D. R.; Borovik, A. S., *J. Am. Chem. Soc.* **2005**, *127*, 11596.

18. (a) Ni, C.; Fettinger, J. C.; Long, G. J.; Brynda, M.; Power, P. P., *Chem. Commun.* **2008**, 6045; (b) Bart, S. C.; Lobkovsky, E.; Bill, E.; Chirik, P. J., *J. Am. Chem. Soc.* **2006**, *128*, 5302; (c) Scepaniak, J. J.; Young, J. A.; Bontchev, R. P.; Smith, J. M., *Angew. Chem. Int. Ed.* **2009**, *48*, 3158; (d) Scepaniak, J. J.; Fulton, M. D.; Bontchev, R. P.; Duesler, E. N.; Kirk, M. L.; Smith, J. M., *J. Am. Chem. Soc.* **2008**, *130*, 10515; (e) Nieto, I.; Ding, F.; Bontchev, R. P.; Wang, H. B.; Smith, J. M., *J. Am. Chem. Soc.* **2008**, *130*, 2716; (f) Vogel, C.; Heinemann, F. W.; Sutter, J.; Anthon, C.; Meyer, K., *Angew. Chem. Int. Ed.* **2008**, *47*, 2681; (g) Betley, T. A.; Peters, J. C., *J. Am. Chem. Soc.* **2004**, *126*, 6252; (h) Brown, S. D.; Betley, T. A.; Peters, J. C., *J. Am. Chem. Soc.* **2003**, *125*, 322; (i) Brown, S. D.; Peters, J. C., *J. Am. Chem. Soc.* **2005**, *127*, 1913; (j) Thomas, C. M.; Mankad, N. P.; Peters, J. C., *J. Am. Chem. Soc.* **2006**, *128*, 4956; (k) Rohde, J.-U.; In, J. H.; Lim, M. H.; Brennessel, W. W.; Bukowski, M. R.; Stubna, A.; Münck, E.; Nam, W.; Que, L., *Science* **2003**, *299*, 1037.

19. (a) Jenkins, D. M.; Betley, T. A.; Peters, J. C., *J. Am. Chem. Soc.* **2002**, *124*, 11238; (b) Hu, X.; Meyer, K., *J. Am. Chem. Soc.* **2004**, *126*, 16322; (c) Cowley, R. E.; Bontchev, R. P.; Sorrell, J.; Sarracino, O.; Feng, Y. H.; Wang, H. B.;

Smith, J. M., *J. Am. Chem. Soc.* **2007**, *129*, 2424; (d) Dai, X. L.; Kapoor, P.; Warren, T. H., *J. Am. Chem. Soc.* **2004**, *126*, 4798.

20. (a) Kogut, E.; Wiencko, H. L.; Zhang, L. B.; Cordeau, D. E.; Warren, T. H., *J. Am. Chem. Soc.* **2005**, *127*, 11248; (b) Mindiola, D. J.; Hillhouse, G. L., *J. Am. Chem. Soc.* **2001**, *123*, 4623.

21. Mindiola, D. J.; Hillhouse, G. L., *J. Am. Chem. Soc.* **2002**, *124*, 9976.

22. (a) Eckert, N. A.; Vaddadi, S.; Stoian, S.; Lachicotte, R. J.; Cundari, T. R.; Holland, P. L., *Angew. Chem. Int. Ed.* **2006**, *45*, 6868; (b) Cowley, R. E.; DeYonker, N. J.; Eckert, N. A.; Cundari, T. R.; DeBeer, S.; Bill, E.; Ottenwaelder, X.; Flaschenriem, C.; Holland, P. L., *Inorg. Chem.* **2010**, *49*, 6172; (c) Cowley, R. E.; Eckert, N. A.; Elhaïk, J.; Holland, P. L., *Chem. Commun.* **2009**, 1760; (d) Holland, P. L., *Acc. Chem. Res.* **2008**, *41*, 905.

23. (a) Jenkins, D. M.; Di Bilio, A. J.; Allen, M. J.; Betley, T. A.; Peters, J. C., *J. Am. Chem. Soc.* **2002**, *124*, 15336; (b) Jenkins, D. M.; Peters, J. C., *J. Am. Chem. Soc.* **2003**, *125*, 11162; (c) Jenkins, D. M.; Peters, J. C., *J. Am. Chem. Soc.* **2005**, *127*, 7148.

24. (a) Shapiro, I. R.; Jenkins, D. M.; Thomas, J. C.; Day, M. W.; Peters, J. C., *Chem. Commun.* **2001**, 2152; (b) Betley, T. A.; Peters, J. C., *J. Am. Chem. Soc.* **2003**, *125*, 10782.

25. Cotton, F. A.; Wilkinson, G., *Advanced Inorganic Chemistry*. 5th ed.; Wiley: New York, 1988.

26. (a) Garrett, B. B.; Goedken, V. L.; Quaglian, J. V., *J. Am. Chem. Soc.* **1970**, *92*, 489; (b) Gerloch, M.; Hanton, L. R., *Inorg. Chem.* **1980**, *19*, 1692; (c) Gerloch, M.; Manning, M. R., *Inorg. Chem.* **1981**, *20*, 1051; (d) Banci, L.; Benelli, C.; Gatteschi, D.; Mani, F., *Inorg. Chem.* **1982**, *21*, 1133.

27. (a) Gray, H. B., *Chemical Bonds: An Introduction to Atomic and Molecular Structure*. University Science Books: Mill Valley, CA, 1994; (b) Strauss, S. H.; Silver, M. E.; Long, K. M.; Thompson, R. G.; Hudgens, R. A.; Spartalian, K.; Ibers, J. A., *J. Am. Chem. Soc.* **1985**, *107*, 4207; (c) Goedken, V. L.; Pluth, J. J.; Peng, S.-M.; Bursten, B., *J. Am. Chem. Soc.* **1976**, *98*, 8014.

28. Verma, A. K.; Nazif, T. N.; Achim, C.; Lee, S. C., *J. Am. Chem. Soc.* **2000**, *122*, 11013.

29. Mehn, M. P.; Brown, S. D.; Jenkins, D. M.; Peters, J. C.; Que, L., *Inorg. Chem.* **2006**, *45*, 7417.

30. Yap, G. P. A., *CCDC deposition number 253991* **2004**.

31. Shay, D. T.; Yap, G. P. A.; Zakharov, L. N.; Rheingold, A. L.; Theopold, K. H., *Angew. Chem. Int. Ed.* **2005**, *44*, 1508.

32. Wasbotten, I. H.; Ghosh, A., *Inorg. Chem.* **2007**, *46*, 7890.

33. (a) Mankad, N. P.; Müller, P.; Peters, J. C., *J. Am. Chem. Soc.* **2010**, *132*, 4083; (b) Mindiola, D. J.; Hillhouse, G. L., *Chem. Commun.* **2002**, 1840.

34. (a) Shay, D. T.; Yap, G. P. A.; Zakharov, L. N.; Rheingold, A. L.; Theopold, K. H., *Angew. Chem. Int. Ed.* **2006**, *45*, 7870; (b) Thyagarajan, S.; Shay, D. T.; Incarvito, C. D.; Rheingold, A. L.; Theopold, K. H., *J. Am. Chem. Soc.* **2003**, *125*, 4440.

35. Nieto, I.; Cervantes-Lee, F.; Smith, J. M., *Chem. Commun.* **2005**, 3811.

36. (a) Burred, A. K.; Steedman, A. J., *J. Chem. Soc., Chem. Commun.* **1995**, 2109; (b) Danopoulos, A. A.; Wilkinson, G.; Hussain-Bates, B.; Hursthouse, M. B., *Polyhedron* **1992**, *11*, 2961; (c) Bell, B.; Chatt, J.; Dilworth, J. R.; Leigh, G. J., *Inorg. Chim. Acta* **1972**, *6*, 635; (d) Michelman, R. I.; Andersen, R. A.; Bergman, R. G., *J. Am. Chem. Soc.* **1991**, *113*, 5100.

37. Lu, C. C.; Saouma, C. T.; Day, M. W.; Peters, J. C., *J. Am. Chem. Soc.* **2007**, *129*, 4.

38. (a) Kisko, J. L.; Hascall, T.; Parkin, G., *J. Am. Chem. Soc.* **1998**, *120*, 10561; (b) Lappert, M. F.; MacQuitty, J. J.; Pye, P. L., *J. Chem. Soc., Dalton Trans.* **1981**, 1583.

39. (a) Sohn, Y. S.; Hendrickson, D. N.; Gray, H. B., *J. Am. Chem. Soc.* **1970**, *92*, 3233; (b) Sohn, Y. S.; Hendrickson, D. N.; Gray, H. B., *J. Am. Chem. Soc.* **1971**, *93*, 3603.

40. Brown, S. D.; Peters, J. C., *J. Am. Chem. Soc.* **2004**, *126*, 4538.

41. Daida, E. J.; Peters, J. C., *Inorg. Chem.* **2004**, *43*, 7474.

42. Sohn, Y. S.; Hendrickson, D. N.; Hart Smith, J.; Gray, H. B., *Chem. Phys. Lett.* **1970**, *6*, 499.

43. (a) Paine, T. K.; Costas, M.; Kaizer, J.; Que, L., *J. Biol. Inorg. Chem.* **2006**, *11*, 272; (b) Klinker, E. J.; Kaizer, J.; Brennessel, W. W.; Woodrum, N. L.; Cramer, C. J.; Que, L., *Angew. Chem. Int. Ed.* **2005**, *44*, 3690; (c) Rohde, J.-U.; Torelli, S.; Shan, X. P.; Lim, M. H.; Klinker, E. J.; Kaizer, J.; Chen, K.; Nam, W. W.; Que,

L., *J. Am. Chem. Soc.* **2004**, *126*, 16750; (d) Lim, M. H.; Rohde, J.-U.; Stubna, A.; Bukowski, M. R.; Costas, M.; Ho, R. Y. N.; Münck, E.; Nam, W.; Que, L., *Proc. Natl. Acad. Sci. U.S.A.* **2003**, *100*, 3665.

44. Thomas, J. C.; Peters, J. C., *Inorg. Chem.* **2003**, *42*, 5055.

45. (a) Fjare, D. E.; Gladfelter, W. L., *Inorg. Chem.* **1981**, *20*, 3533; (b) Bennett, M. V.; Stoian, S.; Bominaar, E. L.; Münck, E.; Holm, R. H., *J. Am. Chem. Soc.* **2005**, *127*, 12378; (c) Summerville, D. A.; Cohen, I. A., *J. Am. Chem. Soc.* **1976**, *98*, 1747; (d) Li, M.; Shang, M.; Ehlinger, N.; Schulz, C. E.; Scheidt, W. R., *Inorg. Chem.* **2000**, *39*, 580.

46. (a) Wagner, W. D.; Nakamoto, K., *J. Am. Chem. Soc.* **1988**, *110*, 4044; (b) Wagner, W. D.; Nakamoto, K., *J. Am. Chem. Soc.* **1989**, *111*, 1590.

47. (a) Meyer, K.; Bill, E.; Mienert, B.; Weyhermüller, T.; Wieghardt, K., *J. Am. Chem. Soc.* **1999**, *121*, 4859; (b) Aliaga-Alcalde, M.; George, S. D.; Mienert, B.; Bill, E.; Wieghardt, K.; Neese, F., *Angew. Chem. Int. Ed.* **2005**, *44*, 2908.

48. Berry, J. F.; Bill, E.; Bothe, E.; George, S. D.; Mienert, B.; Neese, F.; Wieghardt, K., *Science* **2006**, *312*, 1937.

49. Berry, J. F.; DeBeer George, S.; Neese, F., *PCCP* **2008**, *10*, 4361.

50. (a) Du Bois, J.; Tomooka, C. S.; Hong, J.; Carreira, E. M., *Acc. Chem. Res.* **1997**, *30*, 364; (b) Chang, C. J.; Low, D. W.; Gray, H. B., *Inorg. Chem.* **1997**, *36*, 270.

51. Petrenko, T.; George, S. D.; Aliaga-Alcalde, N.; Bill, E.; Mienert, B.; Xiao, Y.; Guo, Y.; Sturhahn, W.; Cramer, S. P.; Wieghardt, K.; Neese, F., *J. Am. Chem. Soc.* **2007**, *129*, 11053.

52. Mindiola, D. J.; Cummins, C. C., *Angew. Chem. Int. Ed.* **1998**, *37*, 945.

53. (a) Lu, C. C.; Peters, J. C., *Inorg. Chem.* **2006**, *45*, 8597; (b) MacBeth, C. E.; Thomas, J. C.; Betley, T. A.; Peters, J. C., *Inorg. Chem.* **2004**, *43*, 4645.

54. (a) Peters, J. C.; Johnson, A. R.; Odom, A. L.; Wanandi, P. W.; Davis, W. M.; Cummins, C. C., *J. Am. Chem. Soc.* **1996**, *118*, 10175; (b) Laplaza, C. E.; Cummins, C. C., *Science* **1995**, *268*, 861; (c) Yandulov, D. V.; Schrock, R. R., *J. Am. Chem. Soc.* **2002**, *124*, 6252.

55. Nakamoto, K., *Infrared and Raman Spectra of Inorganic and Coordination Compounds Part B: Applications in Coordination, Organometallic, and Bioinorganic Chemistry*. 5 ed.; John Wiley & Sons, Inc: New York, 1997.

56. Hendrich, M. P.; Gunderson, W.; Behan, R. K.; Green, M. T.; Mehn, M. P.; Betley, T. A.; Lu, C. C.; Peters, J. C., *Proc. Natl. Acad. Sci. U.S.A.* **2006**, *103*, 17107.

57. Rohde, J.-U.; Betley, T. A.; Jackson, T. A.; Saouma, C. T.; Peters, J. C.; Que, L., Jr., *Inorg. Chem.* **2007**, *46*, 5720.

58. Scepaniak, J. J.; Vogel, C. A.; Khusniyarov, M. M.; Heinemann, F. W.; Meyer, K.; Smith, J. M., *manuscript submitted for publication* **2010**.

59. Miskowski, V. M.; Gray, H. B.; Hopkins, M. D., *Advances in Transition Metal Coordination Chemistry* **1996**, *1*, 159.

60. (a) Whited, M. T.; Mankad, N. P.; Lee, Y. H.; Oblad, P. F.; Peters, J. C., *Inorg. Chem.* **2009**, *48*, 2507; (b) Mankad, N. P.; Whited, M. T.; Peters, J. C., *Angew. Chem. Int. Ed.* **2007**, *46*, 5768.

61. Lee, Y. H.; Mankad, N. P.; Peters, J. C., *Nature Chemistry* **2010**, *2*, 558.

62. Eckert, N. A.; Vaddadi, S.; Stoian, S.; Lachicotte, R. J.; Cundari, T. R.; Holland, P. L., *Angewandte Chemie-International Edition* **2006**, *45*, 6868.

63. Takaoka, A.; Gerber, L. C. H.; Peters, J. C., *Angew. Chem. Int. Ed.* **2010**, *49*, 4088.

64. Bontemps, S.; Bouhadir, G.; Dyer, P. W.; Miqueu, K.; Bourissou, D., *Inorg. Chem.* **2007**, *46*, 5149.

65. Moret, M.-E.; Peters, J. C., *submitted for publication* **2010**.

66. Lee, Y.; Peters, J. C., *submitted for publication* **2010**.

67. Shan, X.; Que Jr, L., *J. Inorg. Biochem.* **2006**, *100*, 421.

68. Decker, A.; Rohde, J.-U.; Klinker, E. J.; Wong, S. D.; Que, L.; Solomon, E. I., *J. Am. Chem. Soc.* **2007**, *129*, 15983.

69. Nam, W., *Acc. Chem. Res.* **2007**, *40*, 522.

70. England, J.; Martinho, M.; Farquhar, E. R.; Frisch, J. R.; Bominaar, E. L.; Münck, E.; Que, L., *Angew. Chem. Int. Ed.* **2009**, *48*, 3622.

71. England, J.; Guo, Y.; Farquhar, E. R.; Young Jr, V. G.; Münck, E.; Que Jr, L., *J. Am. Chem. Soc.* **2010**, *132*, 8635.

72. Thibon, A.; England, J.; Martinho, M.; Young, V. G.; Frisch, J. R.; Guillot, R.; Girerd, J.-J.; Münck, E.; Que, L.; Banse, F., *Angew. Chem. Int. Ed.* **2008**, *47*, 7064.

73. Borovik, A. S., *Acc. Chem. Res.* **2005**, *38*, 54.

74. MacBeth, C. E.; Golombek, A. P.; Young, V. G.; Yang, C.; Kuczera, K.; Hendrich, M. P.; Borovik, A. S., *Science* **2000**, *289*, 938.

75. Kurtz, D. M., *Chem. Rev.* **1990**, *90*, 585.

76. Hoppe, M. L.; Schlemper, E. O.; Murmann, R. K., *Acta Crystallographica Section B* **1982**, *38*, 2237.

77. Dey, A.; Hocking, R. K.; Larsen, P.; Borovik, A. S.; Hodgson, K. O.; Hedman, B.; Solomon, E. I., *J. Am. Chem. Soc.* **2006**, *128*, 9825.

78. Gupta, R.; Borovik, A. S., *J. Am. Chem. Soc.* **2003**, *125*, 13234.

79. Lacy, D. C.; Gupta, R.; Stone, K. L.; Greaves, J.; Ziller, J. W.; Hendrich, M. P.; Borovik, A. S., *J. Am. Chem. Soc.* **2010**, *132*, 12188.

80. Walstrom, A.; Pink, M.; Yang, X. F.; Tomaszewski, J.; Baik, M. H.; Caulton, K. G., *J. Am. Chem. Soc.* **2005**, *127*, 5330.

81. Laskowski, C. A.; Miller, A. J. M.; Hillhouse, G. L.; Cundari, T. R., *submitted for publication* **2010**.

82. Hoffman, B. M.; Dean, D. R.; Seefeldt, L. C., *Acc. Chem. Res.* **2009**, *42*, 609.

83. Barney, B. M.; Lukoyanov, D.; Igarashi, R. Y.; Laryukhin, M.; Yang, T. C.; Dean, D. R.; Hoffman, B. M.; Seefeldt, L. C., *Biochemistry* **2009**, *48*, 9094.

84. Yandulov, D. V.; Schrock, R. R., *Science* **2003**, *301*, 76.

85. Igarashi, R. Y.; Laryukhin, M.; Dos Santos, P. C.; Lee, H. I.; Dean, D. R.; Seefeldt, L. C.; Hoffman, B. M., *J. Am. Chem. Soc.* **2005**, *127*, 6231.

86. Sellmann, D.; Sutter, J., *Acc. Chem. Res.* **1997**, *30*, 460.

87. (a) Barney, B. M.; McClead, J.; Lukoyanov, D.; Laryukhin, M.; Yang, T. C.; Dean, D. R.; Hoffman, B. M.; Seefeldt, L. C., *Biochemistry* **2007**, *46*, 6784; (b) Barney, B. M.; Lukoyanov, D.; Yang, T. C.; Dean, D. R.; Hoffman, B. M.; Seefeldt, L. C., *Proc. Natl. Acad. Sci. U.S.A.* **2006**, *103*, 17113.

88. (a) Danyal, K.; Inglet, B. S.; Vincent, K. A.; Barney, B. M.; Hoffman, B. M.; Armstrong, F. A.; Dean, D. R.; Seefeldt, L. C., *J. Am. Chem. Soc.* **2010**, *132*, 13197; (b) Barney, B. M.; Laryukhin, M.; Igarashi, R. Y.; Lee, H.-I.; Dos Santos, P. C.; Yang, T.-C.; Hoffman, B. M.; Dean, D. R.; Seefeldt, L. C., *Biochemistry* **2005**, *44*, 8030.

89. (a) Benson, E. E.; Kubiak, C. P.; Sathrum, A. J.; Smieja, J. M., *Chem. Soc. Rev.* **2009**, *38*, 89; (b) Aresta, M.; Dibenedetto, A., *Dalton Trans.* **2007**, 2975; (c) Arakawa, H.; Aresta, M.; Armor, J. N.; Barteau, M. A.; Beckman, E. J.; Bell, A. T.; Bercaw, J. E.; Creutz, C.; Dinjus, E.; Dixon, D. A.; Domen, K.; DuBois, D. L.; Eckert, J.; Fujita, E.; Gibson, D. H.; Goddard, W. A.; Goodman, D. W.; Keller, J.; Kubas, G. J.; Kung, H. H.; Lyons, J. E.; Manzer, L. E.; Marks, T. J.; Morokuma, K.; Nicholas, K. M.; Periana, R.; Que, L.; Rostrup-Nielson, J.; Sachtler, W. M. H.; Schmidt, L. D.; Sen, A.; Somorjai, G. A.; Stair, P. C.; Stults, B. R.; Tumas, W., *Chem. Rev.* **2001**, *101*, 953.

90. (a) Bryan, J. C.; Geib, S. J.; Rheingold, A. L.; Mayer, J. M., *J. Am. Chem. Soc.* **1987**, *109*, 2826; (b) Castro-Rodriguez, I.; Meyer, K., *J. Am. Chem. Soc.* **2005**, *127*, 11242; (c) Fachinetti, G.; Floriani, C.; Chiesivilla, A.; Guastini, C., *J. Am. Chem. Soc.* **1979**, *101*, 1767; (d) Sadique, A. R.; Brennessel, W. W.; Holland, P. L., *Inorg. Chem.* **2008**, *47*, 784.

Chapter 2: Characterization of Structurally Unusual Diiron N_xH_y Complexes

The text in this chapter is reproduced in part with permission from:

Saouma, C. T.; Müller, P.; Peters, J. C. *J. Am. Chem. Soc.* **2009**, *131*, 10358.

Abstract

A series of fascinating diiron complexes featuring bridging N_xH_y ligands stabilized by tris(phosphine)borate ([$PhB(CH_2PR_2)_3$] = [$PhBP^R_3$]) ligands have been characterized. Hydrazine activation by [$PhBP^R_3$]FeMe (R = Ph or CH_2Cy) leads to diiron $Fe_2(\mu\text{-}\eta^1\text{:}\eta^1\text{-}N_2H_4)(\mu\text{-}\eta^2\text{:}\eta^2\text{-}N_2H_2)$ complexes featuring both bridging hydrazine and hydrazido ligands (R= Ph, **2.3**; R = CH_2Cy, **2.4**). Thermolysis of $\{[PhBP^{CH2Cy}_3]Fe\}_2(\mu\text{-}\eta^1\text{:}\eta^1\text{-}N_2H_4)(\mu\text{-}\eta^2\text{:}\eta^2\text{-}N_2H_2)$ at 22 °C leads to a structurally unusual $\{[PhBP^{CH2Cy}]Fe\}_2(\mu\text{-}\eta^1\text{:}\eta^1\text{-}N_2H_2)(\mu\text{-}NH_2)_2$ (**2.5**) complex featuring bridging HN═NH and NH_2^- ligands. This contrasts with $\{[PhBP^{Ph}_3]Fe\}_2(\mu\text{-}\eta^1\text{:}\eta^1\text{-}N_2H_4)(\mu\text{-}\eta^2\text{:}\eta^2\text{-}N_2H_2)$, which can be chemically oxidized to produce either $\{[PhBP^{Ph}_3]Fe\}_2(\mu\text{-}\eta^1\text{:}\eta^1\text{-}N_2H_2)(\mu\text{-}\eta^2\text{:}\eta^2\text{-}N_2H_2)$ (**2.6**) or $\{[PhBP^{Ph}_3]Fe\}_2(\mu\text{-}NH)_2$ (**2.7**), depending on the conditions. The former product is the only known complex to contain bridging N_2H_2 ligands in each of their limiting states of oxidation (HN═NH vs. $HN{-}NH^{2-}$). The latter product constitutes the first example of a diiron $Fe_2(\mu\text{-}NH)_2$ diamond-shaped core.

2.1 Introduction

Mechanistic proposals concerning the pathway of N_2 reduction in biology at the MoFe-cofactor of nitrogenase continue to be advanced.[1] In addition to nitrogen, hydrazine[2] and diazene[1a] are nitrogenase substrates, and recent DFT calculations and spectroscopic studies suggest that whereas initial N_2 binding may occur at one iron center, diiron pathways may be involved at certain N_xH_y intermediate stages *en route* to ammonia formation.[1a,3] In this broad context, recent work has explored the synthesis and spectroscopic characterization of structurally unusual mono- and bimetallic iron complexes featuring nitrogenous ligand functionalities.[4] The demand for such model complexes continues in light of recent ENDOR and ESEEM spectroscopic data that has been obtained under turnover conditions at the cofactor.[1a,2,5] To date there are few synthetic iron systems that feature parent hydrazine (N_2H_4),[6] hydrazido ($N_2H_2^{2-}$), diazene (N_2H_2),[7] amide (NH_2^-),[8] and imide (NH^{2-})[4d] ligands. Herein we describe the synthesis and characterization of a series of structurally distinct diiron complexes that feature each of these ligand types.

2.2 Results and Discussion

Entry into the N_xH_y chemistry of present interest is realized with the iron(II) alkyl precursors [PhBP$^R_3$]FeMe ([PhBP$^R_3$] = PhB(CH_2PR_2)$_3^-$) (R = Ph and CH_2Cy). These high-spin complexes are prepared either by addition of excess Me_2Mg to a benzene solution of [PhBP$^{Ph}_3$]FeCl, or by addition of MeLi to a thawing THF solution of [PhBP$^{CH2Cy}_3$]FeCl. The room temperature addition of one equivalent of hydrazine to

yellow THF solutions of either [PhBP$^{Ph}_3$]FeMe (**2.1**) or [PhBP$^{CH2Cy}_3$]FeMe (**2.2**) results in the immediate release of methane and clean conversion to red and diamagnetic {[PhBP$^{Ph}_3$]Fe}$_2$(μ-η^1:η^1-N_2H_4)(μ-η^2:η^2-N_2H_2), (**2.3**), or purple and diamagnetic {[PhBP$^{CH2Cy}_3$]Fe}$_2$(μ-η^1:η^1-N_2H_4)(μ-η^2:η^2-N_2H_2), (**2.4**), respectively (Scheme 2.1).

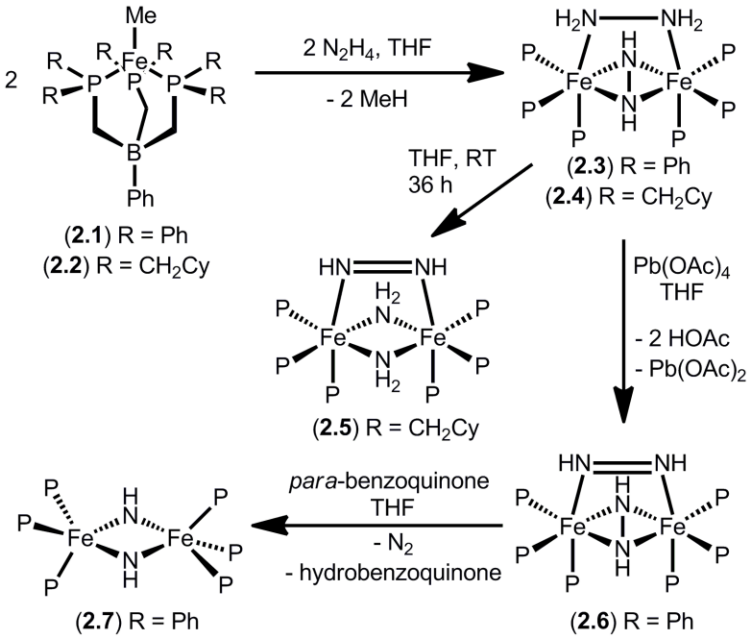

Scheme 2.1.

The solid-state structures of the diiron cores of **2.3** and **2.4** are nearly identical (see Appendix 3). Only that of **2.3** is shown in Figure 2.1. Its two iron centers are bridged by N_2H_4 and $N_2H_2^{2-}$ ligands. We assign the end-on bridging ligand as N_2H_4, and the side-bonded bridging ligand as $N_2H_2^{2-}$.[9] The N3-N4 bond distance of 1.429(3) Å in **2.3** is consistent with an N-N single bond, and hence best assigned as an $N_2H_2^{2-}$ ligand rather than HN=NH. The ^{1}H NMR spectrum (d_8-THF) of **2.3** reveals a solution structure similar to that observed in the solid-state. An N_2H_4 resonance is noted at 2.54 ppm and an $N_2H_2^{2-}$ resonance at 2.59 ppm. Each of these peaks split into an apparent doublet when **2.3** is

prepared using $^{15}N_2H_4$ ($^1J_{NH}$ = 59.5, $N_2H_2^{2-}$; $^1J_{NH}$ = 72.0, N_2H_4). The breadth of the doublets precludes the observation of higher order NH and HH coupling.[10] The corresponding ^{15}N NMR spectrum shows a doublet at -10.0 ppm for $N_2H_2^{2-}$ and a triplet at 58.37 ppm for N_2H_4,[11] both of which collapse into singlets upon ^1H decoupling. Complex **2.4** displays similar ^{15}N NMR characteristics ($N_2H_2^{2-}$: 0.86 ppm, doublet, J = 45.2 Hz; N_2H_4: 50.86 ppm, triplet, J = 68.9 Hz).

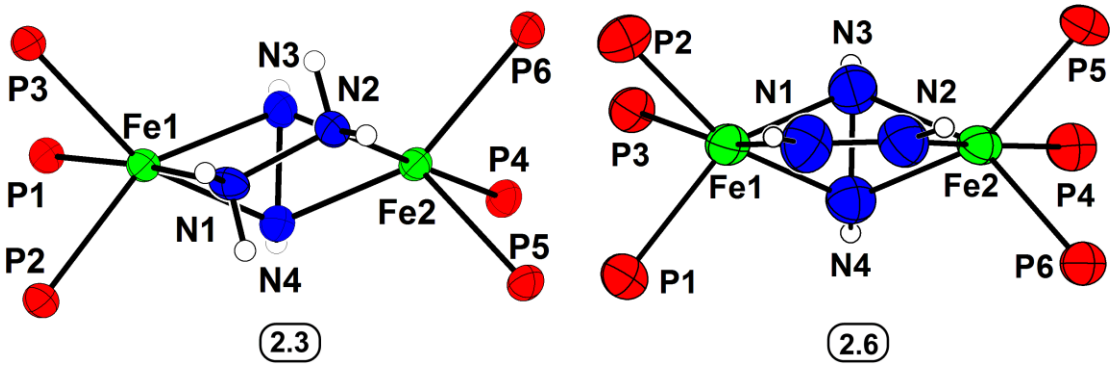

Figure 2.1. 50% thermal ellipsoid representation of the core atoms of {[PhBP$^{Ph}_3$]Fe}$_2$(μ-η^1:η^1-N_2H_4)(μ-η^2:η^2-N_2H_2), (**2.3**) and {[PhBP$^{Ph}_3$]Fe}$_2$(μ-η^1:η^1-N_2H_2)(μ-η^2:η^2-N_2H_2), (**2.6**). Selected bond lengths (Å) for **2.3**: Fe1-N4 1.9789(2), Fe1-N1 2.028(3), Fe1-N3 2.030(2), Fe2-N3 1.999(2), Fe2-N4 2.023(2), Fe2-N2 2.026(3), N1-N2 1.465(3), N3-N4 1.429(3). Selected bond lengths (Å) for **2.6**: Fe1-N1 1.884(4), Fe1-N4 1.972(4), Fe1-N3 1.980(4), Fe2-N2 1.889(4), Fe2-N3 1.975(4), Fe2-N4 1.005(4), N1-N2 1.281(5), N3-N4 1.458(5)

Whereas Sellmann previously reported a few examples of diiron μ-η^1:η^1-HN=NH species,[7] the bimetallic iron cores of **2.3** and **2.4** are unique. Schrock has characterized a ditungsten (μ-η^1:η^1-N_2H_4)(μ-η^2:η^2-N_2H_2) complex whose core is closely related to **2.3** and **2.4**.[12]

Though solutions of **2.3** are stable for days at 60 ^{o}C, purple solutions of **2.4** prove to be thermally unstable even at 22 °C ($t_{1/2}$ = 4 h) and decay quantitatively to the isolable green diamagnetic product {[PhBP$^{CH2Cy}_3$]Fe}(μ-η^1:η^1-N_2H_2)(μ-NH_2)$_2$, (**2.5**). Signature NMR data for **2.5** are as follows. Its ^{1}H NMR spectrum (d_8-THF) features three broad singlets at 16.21, -1.65 and -3.85 ppm, corresponding to bound HN=NH and diastereotopic NH_2^- protons, respectively. Each of these ^{1}H NMR resonances is split into a doublet upon ^{15}N-labeling. Its ^{15}N NMR spectrum gives rise to a doublet at 419.1 ppm ($^1J_{NH}$ = 65.1 Hz) that collapses to a singlet upon decoupling of the proton resonance at 16.21 ppm. The NH_2^- nitrogens are observed as a triplet at -58.1 ppm (J = 59.5 Hz).

The solid-state structure of **2.5** is shown in Figure 2.2. Both the Fe-N1 bond distance of 1.882(8) Å and the N1-N1' bond distance of 1.283(15) Å are similar to those found in Sellmann's Fe_2(μ-η^1:η^1-HN=NH) complex.[7] In addition, the Fe-N bond distance contraction of 0.17 Å that occurs upon oxidation of hydrazine to diazene is also consistent with other structurally characterized diazene complexes,[7,13] and may be due to either the smaller covalent radii of sp^2-hybridized nitrogen compared to sp^3-hybridized nitrogen, or multiple bond character. Notable in the structure of **2.5** is the presence of a *cis*-diazene. Whereas mono-substituted diazenes (HN=NR) are known to bind transition metals in a *cis* conformation,[14] to our knowledge all known complexes of HN=NH show *trans* ligation. Hence **2.5** appears to be structurally distinct in this context.

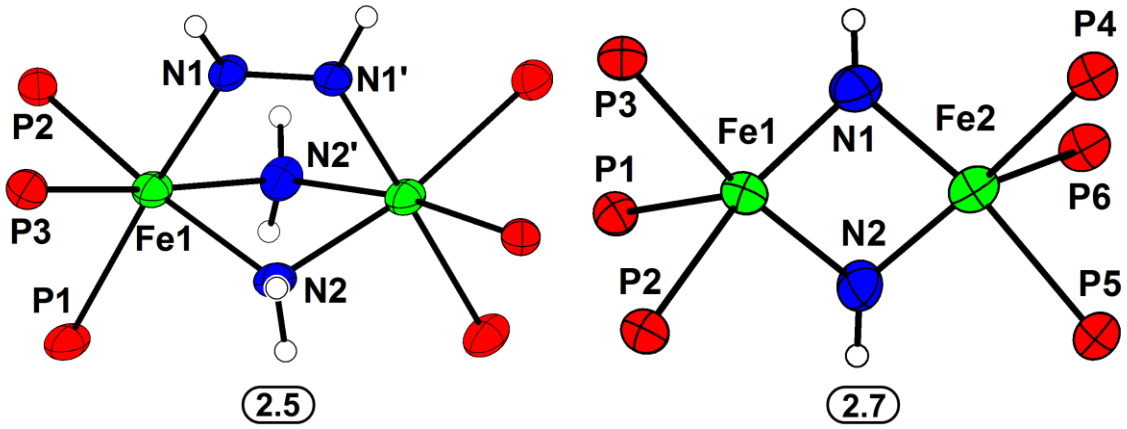

Figure 2.2. 50% thermal ellipsoid representation of the core atoms of $\{[PhBP^{CH2Cy}_3]Fe\}_2(\mu\text{-}\eta^1\text{:}\eta^1\text{-}N_2H_2)(\mu\text{-}NH_2)_2$, (**2.5**) and $\{[PhBP^{Ph}_3]Fe\}_2(\mu\text{-}NH)_2$, (**2.7**). The two imido ligands in **2.7** are disordered over 3 positions, and only the major sites of occupation are shown. Selected bond lengths (Å) for 2.5: Fe1-N1 1.882(8), Fe1-N2 2.049(8), Fe1-N2' 2.034(9), N1-N1' 1.28(2). Selected bond lengths (Å) for 2.7: Fe1-N1 1.794(9), Fe1-N2 1.835(3)

The addition of 2.2 equiv of $Pb(OAc)_4$ to red **2.3** leads to oxidation of the bound N_2H_4[10b] to afford green and diamagnetic $\{[PhBP^{Ph}_3]Fe\}_2(\mu\text{-}\eta^1\text{:}\eta^1\text{-}N_2H_2)(\mu\text{-}\eta^2\text{:}\eta^2\text{-}N_2H_2)$ (**2.6**) as the major product, with concurrent release of acetic acid. The solid-state structure of **2.6** is shown in Figure 2.1. Most striking is the presence of both an $\eta^1\text{:}\eta^1$ bridging *cis*-HN=NH ligand, and a $\mu\text{-}\eta^2\text{:}\eta^2$ HN-NH^{2-} ligand. To our knowledge, **2.6** is the only transition metal complex featuring the N_2H_2 ligand in each of its limiting states of oxidation. The N1-N2 bond distance of 1.281(5) Å for the ligand assigned as HN=NH is similar to that found for the bridging HN=NH ligand of **2.5**. The N3-N4 bond distance of 1.458(5) Å for the ligand assigned as $N_2H_2^{2-}$ is slightly elongated compared with that of the $N_2H_2^{2-}$ ligand of **2.3**. The average Fe-$N_{diazene}$ bond distance of 1.89 Å is appreciably shorter than the average Fe-$N_{hydrazido2-}$ bond distance of 1.99 Å.

As was observed for **2.3** and **2.4**, the structure of **2.6** is preserved in solution. In the ^{1}H NMR spectrum (C_6D_6) of **2.6**, broad singlets at 13.20 and 4.16 ppm are assigned to the HN=NH and the $N_2H_2^{2-}$ protons, respectively; both of these peaks split into broad doublets when samples of **2.6** are prepared using ^{15}N-enriched **2.6**. The ^{15}N NMR spectrum of **2.6** contains a doublet at 58.0 ppm ($^{1}J_{NH}$ = 58.1 Hz) for the $N_2H_2^{2-}$ N-atoms and a doublet of doublets at 407.5 ppm ($^{1}J_{NH}$ = 69.2 Hz, $J \approx 20$ Hz) corresponding to the HN=NH ligand.

Complex **2.6** can further be oxidized with *para*-benzoquinone to cleanly generate a new diamagnetic species, $\{[PhBP^{Ph}_3]Fe\}_2(\mu\text{-}NH)_2$ (**2.7**), with the generation of hydroquinone as a byproduct. In order to ascertain the fate of the bound diazene, the reaction was repeated on a high vacuum manifold, and by Toepler pump analysis we found that one equivalent of N_2 is liberated. This complex can alternatively be prepared by addition of 5 equiv of *para*-benzoquinone to **2.3**. The ^{31}P NMR spectrum of **2.7** displays a single resonance at 32.5 ppm at 22 °C. The ^{1}H NMR spectrum shows a single set of $[PhBP^{Ph}_3]$ resonances, with an additional singlet at 25.3 ppm that integrates to one proton per $[PhBP^{Ph}_3]$. When **2.7** is prepared using isotopically enriched **2.3**, the singlet at 25.3 ppm splits into a doublet ($^{1}J_{NH}$ = 64.0 Hz); the ^{15}N NMR spectrum displays a peak at 563.5 ppm, which is split into a doublet due to proton coupling. Based on these NMR and IR data (see SI), the solution structure of **2.7** is assigned as the diferric $\{[PhBP^{Ph}_3]Fe\}_2(\mu\text{-}NH)_2$. The spectroscopy of the bridging NH ligand in **2.7** is similar to that previously reported for $\{([PhBP^{Ph}_3]Fe)_2(\mu\text{-}NH)(\mu\text{-}H)\}\{Na\}$.[4d]

Crystals of **2.7** can be grown from a THF/cyclopentane solution, and its solid-state structure is shown in Figure 2.2. The bridging imides were disordered over three

positions (see SI), and modeled satisfactorily with a population ratio of 0.93:0.75:0.32. The average Fe-N distance of 1.84 Å is ca. 0.17 Å longer than that found in $\{[PhBP^{Ph}_3]Fe_2(\mu\text{-}NH)(\mu\text{-}H)\}\{Na\}$.[4d] The average Fe-P distance of 2.33 Å is ca. 0.075 Å longer than those found in **2.3** and **2.6**, consistent with its assignment as an anti-ferromagnetically coupled diiron(III) complex.

2.3 Conclusions

In conclusion, we have characterized a series of structurally fascinating diiron N_xH_y species that contain hydrazine, hydrazido, and *cis*-diazene bridges. Thermal and oxidative transformations also lead to unusual examples of diiron species featuring μ-NH_2 and μ-NH ligands. Low temperature experiments reveal the presence of intermediate species in certain instances. Ongoing work concerns detailed vibrational characterization of the species described herein, in addition to mechanistic studies.

2.4 Experimental Section

2.4.1 General Considerations

All manipulations were carried out using standard Schlenk or glove-box techniques under a dinitrogen atmosphere. Unless otherwise noted, solvents were deoxygenated and dried by sparging with Ar followed by passage through an activated alumina column from S.G. Water (Nashua, N.H.). Nonhalogenated solvents were tested with a standard purple solution of benzophenone ketyl in THF to confirm effective oxygen and moisture removal. Deuterated solvents were purchased from Cambridge

Isotopes Laboratories, Inc. and were degassed and stored over activated 3-Å molecular sieves prior to use. Elemental analyses were performed by Columbia Analytics (Tucson, AZ) and Midwest Microlab (Indianapolis, IN).

2.4.2 NMR and IR Spectroscopy

Both Varian 300 MHz and 500 MHz spectrometers were used to record the ^{1}H NMR and ^{31}P NMR spectra at ambient temperature, and a Varian 500 MHz spectrometer was used to record ^{15}N NMR spectra. ^{1}H chemical shifts were referenced to residual solvent, and ^{31}P NMR chemical shifts were referenced to 85% H_3PO_4 at $\delta = 0$ ppm. All ^{15}N NMR spectra are externally referenced to neat $H_3CC^{15}N$ ($\delta = 245$ ppm) in comparison to liquid NH_3 ($\delta = 0$ ppm). The protons that correspond to the N_xH_y ligand all appeared as broad singlets or apparent doublets (^{14}N and ^{15}N respectively) in the ^{1}H NMR spectra, with the half-height peak widths ranging from 13–20 Hz (digital resolution of 0.22 Hz). The half-height peak widths ranged from 14–22 Hz in the ^{15}N NMR (digital resolution of 6.5 Hz). Solution magnetic moments were measured using Evans' method.[15]

IR measurements were obtained with a KBr solution cell or a KBr pellet using a Bio-Rad Excalibur FTS 3000 spectrometer controlled by Varian Resolutions Pro software set at 4 cm^{-1} resolution.

2.4.3 Electrochemistry

Electrochemical measurements were carried out in a glovebox under a dinitrogen atmosphere in a one-compartment cell using a BAS model 100/W electrochemical

analyzer. A glassy carbon electrode and platinum wire were used as the working and auxillary electrodes, respectively. The reference electrode was $Ag/AgNO_3$ in THF. Solutions (THF) of electrolyte (0.4 M tetra-n-butylammonium hexafluorophosphate) and analyte were also prepared in a glovebox.

2.4.4 X-Ray Crystallography Procedures

Low-temperature diffraction data were collected on a Siemens or Bruker Platform three-circle diffractometer coupled to a Bruker-AXS Smart Apex CCD detector with graphite-monochromated Mo or Cu Kα radiation (λ = 0.71073 or 1.54178 Å, respectively), performing φ-and ω-scans. The structures were solved by direct or Patterson methods using SHELXS[16] and refined against F^2 on all data by full-matrix least squares with SHELXL-97.[17] All non-hydrogen atoms were refined anisotropically. All hydrogen atoms (except hydrogen atoms on nitrogen) were included into the model at geometrically calculated positions and refined using a riding model. The isotropic displacement parameters of all hydrogen atoms were fixed to 1.2 times the U value of the atoms they are linked to (1.5 times for methyl groups).

The structures were refined using established methods.[18] Several of the structures reported suffered from disorder in parts of the $[PhBP^R_3]$ ligand and all of the structures showed disorder of solvent molecules (some over more than two independent positions). All disorders were refined with the help of similarity restraints on 1-2 and 1-3 distances and displacement parameters as well as rigid bond restraints for anisotropic displacement parameters. All close contacts, both inter and intramolecular, reported by the Platon

validation software[19] involve at least one partner from a minor component of a disorder. While it is conceivable that more components of the [$PhBP^{R}_{3}$] are disordered and parameterization of these disordered components would remove the close contacts, the data at hand did not allow for further modeling of the disorder. In spite of the relatively poor quality and resolution of the datasets and the severity of the ligand and solvent disorders, the diiron cores of **2.3**, **2.4**, **2.5**, and **2.6** are surprisingly well determined. Even the hydrogen atoms on the iron-bound nitrogen atoms could be located in the difference Fourier synthesis and subsequently those H atoms were refined semi-freely with the help of distance restraints.

The diiron core of **2.7** displays disorder of the two imides over three positions. The occupancies of the three components of this disorder were refined freely, while restraining their sum to be 2.0. The population distribution was found to be 0.93:0.75:0.32 for N1:N2:N3. As NMR spectroscopy confirms the assignment of **2.7** as [$PhBP^{Ph}_{3}Fe$]$Fe_2(\mu\text{-}NH)_2$, we are confident in our procedure for modeling this core disorder. Despite the disorder, we were able to locate the hydrogen atoms on all three imide nitrogen atoms. As N3 is the least highly occupied component of the disorder, when mention is made to the angles or distances to the bridging nitrogen atoms in the main text, those that involve N3 are omitted. The distances between the most highly populated nitrogen (N1) and the two iron centers were found to be identical within experimental error. Therefore, in order to counteract correlation effects, we restrained all six independent Fe-N distances to be equal within a standard uncertainty of 0.02 Å.

2.4.5 Starting Materials and Reagents

$[PhBP^{R}_{3}Fe]Cl$ (R = Ph, CH_2Cy),[20] $^{15}N_2H_4$,[21] and Me_2Mg[22] were prepared according to literature methods. $Pb(OAc)_4$ was purchased from Aldrich (99.999+%), purified as described in the literature,[23] and recrystallized from cold THF to afford a white crystalline solid. All other reagents were purchased from commercial vendors and used without further purification.

2.4.6 Synthesis of Compounds

Synthesis of $[PhBP^{Ph}_{3}]FeMe$, 2.1. Solid Me_2Mg (0.5063 g, 9.310 mmol) was added to a stirring solution of $PhBP_3FeCl$ (1.0886 g, 1.4010 mmol) in 20 mL of benzene. After 2 h, the reaction was filtered through a Celite-lined frit, and the filtrate was lyophilized. The resulting powder was extracted into toluene, filtered through a Celite-lined frit, and the volatiles removed, to give 0.983 mg (93%) of an analytically pure amber solid. ^{1}H NMR (C_6D_6, 300 MHz): δ 47.2, 22.5, 20.7, 2.72, -12.7, -52.8 (bs), -106 (bs). Evans Method (C_6D_6): 5.1 B.M. UV-vis (C_6H_6) λ_{max}, nm (ε, M^{-1} cm^{-1}): 390 (sh, 1500), 345 (sh, 2640). Anal. Calcd. for $C_{46}H_{44}BFeP_3$: C 73.04; H 5.86; N 0. Found: C 72.72; H 5.89; N 0.

Synthesis of $[PhBP^{CH2Cy}_{3}]FeMe$, 2.2. A solution of MeLi in diethyl ether (1 mL, 0.075 mmol) was added dropwise to a thawing solution of $[PhBP^{CH2Cy}_{3}]FeCl$ (67.3 mg, 0.0749 mmol) in 7 mL THF. The reaction was stirred, and allowed to warm to room temperature, during which time it changed color from pale yellow to golden yellow. After 1.5 h, the volatiles were removed, and the solids were extracted into benzene, filtered through

Celite, and lyophilized (56.0 mg, 85.1%). Crystals can be grown out of DME/THF at -35 ^{o}C. ^{1}H NMR (C_6D_6, 300 MHz): δ 82 (bs), 46.0 , 22.1, 20.0, 2.5, 0.8, 0.5, -0.3, -0.5, -1.0, -6.8, -8.0, -17.5, -21 (bs), -23.0, -33 (bs), -39 (bs), -53 (bs), -126 (bs). Evans Method (C_6D_6): 5.6 B.M. UV-vis (THF) λ_{max}, nm (ε, M^{-1} cm^{-1}): 370 (1100), 300 (sh, 1200). Anal. Calcd. for $C_{52}H_{92}BFeP_3$: C 71.23; H 10.58. Found: C 71.44; H 10.62.

Synthesis of {PhBP$^{Ph}_3$Fe}$_2$(μ-η^1:η^1-N$_2$H$_4$)(μ-η^2:η^2-N$_2$H$_2$), 2.3. Complex **2.1** (0.983 mg, 1.30 mmol) was dissolved in 15 mL of THF, and stirred. Anhydrous hydrazine (98%, 46.3 μL, 1.43 mmol) was added neat, which resulted in an immediate color change from amber to dark red with vigorous effervescence. After 5 min., the reaction was capped and allowed to stir for an additional 10 min. The volatiles were removed, to afford analytically pure solids (974.2 mg, 96.9 %). Crystals suitable for X-ray diffraction were grown by layering pentane onto a benzene solution. ^{1}H NMR (C_6D_6, 300 MHz): δ 8.12-8.30 (m, 14H), 7.719 (t, *J* = 7.48 Hz, 8H), 7.46 (t, *J* = 7.12 Hz, 4H), 7.2 (m, 4H), 6.91 (t, *J* = 7.12 Hz, 12H), 6.75 (t, *J* = 7.32 Hz, 4H), 6.66 (t, *J* = 7.12 Hz, 4H), 6.50-6.61 (m, 20H), 2.829 (s, N*H*, 2H), 2.68 (s, NH_2, 4H), 1.95 (d, *J* = 10.5 Hz, 8H), 1.57 (d, *J* = 12.3 Hz, 4H). ^{1}H NMR (d_8-THF, 300 MHz): δ 2.59 (s, N*H*, 2H), 2.54 (s, NH_2, 4H). All other resonances were as reported for C_6D_6. ^{31}P{^{1}H} NMR (C_6D_6, 300 MHz): δ 63.4 (d, $^{2}J_{PP}$ = 53.3 Hz, 4P), 52.5 (t, $^{2}J_{PP}$ = 53.3 Hz, 2P). IR (KBr) (cm^{-1}): 3316, 3299, 3225, 3140. UV-vis (C_6H_6) λ_{max}, nm (ε, M^{-1} cm^{-1}): 355 (19000), 455 (sh, 2900), 566 (1840). Anal. Calcd. for $C_{90}H_{88}B_2FeP_3N_4$: C 69.88; H 5.75; N 3.62. Found: C 69.4; H 5.6; N 3.5.

A sample of 95% ^{15}N-enriched **2.3** was synthesized using an analogous synthetic procedure with $^{15}NH_2{}^{15}NH_2$. ^{1}H NMR (*d*$_8$-THF, 500 MHz): δ 2.59 (d, $^1J_{NH}$ = 59.5 Hz, N*H*, 2H), 2.54 (d, $^1J_{NH}$ = 72.03 Hz, NH_2, 4H). ^{31}P{^{1}H} NMR (C_6D_6, 300 MHz): δ 63.4 (d, $^2J_{PP}$ = 53.3 Hz, 4P), 52.5 (dt, $^2J_{PP}$ = 53.3 Hz, J_{PN} = 10.0 Hz, 2P). ^{15}N NMR (d_8-THF, 500 MHz): δ 58.37 (t, $^1J_{NH}$ = 72.9 Hz, *N*H_2, 2N), -10.02 (d, $^1J_{NH}$ = 64.5 Hz, *N*H, 2N). IR (KBr) (cm^{-1}): 3316, 3283, 3241, 3219, 3139.

Synthesis of {[PhBP$^{CH2Cy}{}_3$]Fe}$_2$(μ-η^1:η^1-N$_2$H$_4$)(μ-η^2:η^2-N$_2$H$_2$)$_2$, 2.4. Neat hydrazine (98%, 2.8 μL, 0.082 mmol) was added to a stirring solution of **2.2** (71.2 mg, 0.081 mmol) in 6 mL of THF. An immediate color change from yellow to dark pink was observed, with evolution of gas bubbles. After 20 min, the volatiles were removed, and the resulting solids were stored at -35 ^{o}C. Crystals suitable for X-ray diffraction were grown from a cold DME solution stored at -35 ^{o}C. ^{1}H NMR (d_8-THF, 500 MHz): δ 7.18 (d, *J* = 7.2 Hz, *o*-C*H*, 4H), 6.93 (t, *J* = 7.0 Hz, *m*-CH, 4H), 6.74 (t, *J* = 7.0 Hz, *p*-CH, 2H), 0.6 – 2.2 (m, 160H), 0.75 (bs, 8H). ^{31}P{^{1}H} NMR (C_6D_6, 300 MHz): δ 64.9 (t, $^2J_{PP}$ = 57.8 Hz), 57.8 (t, J = 57.8 Hz). IR (KBr/THF) (cm^{-1}): 3398, 3327 (br). UV-vis (THF) λ_{max}, nm (ε, M^{-1} cm^{-1}): 420 (1600), 517 (1350).

A sample of 95% ^{15}N-enriched **2.4** was synthesized using an analogous synthetic procedure with $^{15}NH_2{}^{15}NH_2$. No differences were observed in the ^{1}H NMR spectrum. ^{15}N NMR (*d*$_8$-THF, 500 MHz): δ 50.86 (t, $^1J_{NH}$ = 68.9 Hz, *N*H_2, 2N), 0.86 (d, $^1J_{NH}$ = 45.2, *N*H, 2N).

Synthesis of {[PhBP$^{CH2Cy}_3$]Fe}$_2$(μ-η^1:η^1-N_2H_2)(μ-NH_2)$_2$, 2.5. Neat hydrazine (98%, 5.8 μL, 0.179 mmol) was added to a stirring solution of **2.2** (157.2 mg, 0.179 mmol) in 10 mL of DME. An immediate color change from yellow to dark pink was observed, with evolution of gas bubbles. After 5 min, the reaction was capped and allowed to stir for 36 h, during which time a second color change to green was observed. The volatiles were removed to afford a grass-green powder (135.2 mg, 86.7%). Crystals suitable for X-ray diffraction were grown from a cold DME/THF solution stored at -35 ^{o}C. ^{1}H NMR (d_8-THF, 500 MHz): δ 16.209 (s, N*H*, 2H), 7.25 (d, *J* = 6.0 Hz, *o*-C*H*, 4H), 6.95 (t, *J* = 6.5 Hz, *m*-CH, 4H), 6.76 (t, *J* = 6.5 Hz, *p*-CH, 2H), 0.8 – 2.6 (m, 168H), -1.05 (s, NH_2, 2H), -3.85 (s, NH_2, 2H). ^{1}H NMR (C_6D_6, 300 MHz): δ 15.96 (s, N*H*, 2H), -0.65 (s, NH_2, 2H), -3.60 (s, NH_2, 2H). All other resonances were identical to those reported in d_8-THF. ^{31}P{^{1}H} NMR (C_6D_6, 300 MHz): δ 45.6 (d, $^{2}J_{PP}$ = 51.6 Hz, 4P), 40.0 (t, $^{2}J_{PP}$ = 51.6 Hz, 2P). IR (KBr) (cm^{-1}): 3273, 3234. UV-vis (THF) λ_{max}, nm (ε, M^{-1} cm^{-1}): 420 (5800), 699 (9250). Anal. Calcd. For $C_{102}H_{184}B_2P_6Fe_2N_4$: C 68.60; H 10.39; N 314. Found: C 68.15; H 10.24; N 2.94.

A sample of 95% ^{15}N-enriched **2.5** was synthesized using an analogous synthetic procedure with $^{15}NH_2{}^{15}NH_2$. ^{1}H NMR (d_8-THF, 500 MHz): δ 16.21 (d, $^{1}J_{NH}$ = 65.03 Hz, N*H*, 2H), -1.05 (d, *J* = 61.53 Hz, NH_2, 2H), -3.85 (d, *J* = 59.53 Hz, NH_2, 2H). ^{15}N NMR (d_8-THF, 500 MHz): δ 419.1 (d, $^{1}J_{NH}$ = 65.1 Hz, *N*H, 2N), 58.13 (t, *J* = 59.5 Hz, *N*H_2, 2N). IR (KBr) (cm^{-1}): 3316, 3283, 3241, 3219.

Synthesis of {PhBP$^{Ph}_3$Fe}$_2$(μ-η^1:η^1-N_2H_2)(μ-η^2:η^2-N_2H_2), 2.6. To a solution of **2.3** (0.264 mmol) in 40 mL THF prepared *in situ*, a solution of $Pb(OAc)_4$ (0.2570 g, 0.580 mmol) in 10 mL THF was added over 2', in the dark. The solution changed color from red to green, and evolution of gas bubbles was observed. After 3h, an aliquot of the reaction mixture showed ca. 66.6% conversion to the product by ^{31}P NMR spectroscopy. An additional equivalent of solid $Pb(OAc)_4$ (0.1124 g, 0.254 mmol) was added, and the reaction stirred an additional 12 h. The solution was then filtered through Celite, and the volatiles removed. The resulting solids were extracted into toluene, filtered, and the solution layered with pentanes and stored at -35 ^{o}C to afford crystalline solids (45.1 mg, 11%). The mother liquor was pumped down, dissolved in THF, and layered with pentanes to afford a second crop (88.1 mg, 22%). Crystals suitable for X-ray diffraction were grown by layering pentane onto a benzene solution. ^{1}H NMR (C_6D_6, 300 MHz): δ 13.20 (s, *H*N=N*H*, 2H), 8.29 (d, 4H J = 7.5 Hz), 7.75 (t, 2H, J = 7.5 Hz), 7.42-7.61 (m, 12H), 7.06 (bs, 8 H), 6.96 (t, J = 7.5 Hz, 12 H), 6.86 (t, 8H, J = 6.3 Hz), 6.64-6.80 (m, 16H), 6.48 (t, 8H, J = 7.5 Hz), 4.16 (s, *H*N-N*H*, 2H), 2.11 (d, 8H, CH_2, J = 36.0 Hz), 1.84 (d, 4H, CH_2, J = 11.7 Hz). ^{31}P{^{1}H} NMR (C_6D_6, 300 MHz): δ 53.8 (d, $^2J_{PP}$ = 51.9 Hz, 4P), 44.4 (t, $^2J_{PP}$ = 51.9 Hz, 2P). IR (KBr) (cm^{-1}): 3320, 3224, 3210. UV-vis (C_6H_6) λ_{max}, nm (ε, M^{-1} cm^{-1}): 423 (sh 2700), 480 (sh, 1520), 644 (2560). Anal. Calcd. for $C_{90}H_{86}B_2FeP_3N_4$: C 70.06; H 5.62; N 3.63. Found: C 70.10; H 5.72; N 3.21.

A sample of 95% ^{15}N-enriched **2.6** was synthesized using an analogous synthetic procedure with $^{15}NH_2{}^{15}NH_2$. ^{1}H NMR (C_6D_6, 500 MHz): δ 13.20 (d, $^1J_{NH}$ = 66.03 Hz, *H*N=N*H*, 2H), 4.161 ($^1J_{NH}$, *J* = 60.53 Hz, *H*N-N*H*, 2H). ^{15}N NMR (C_6D_6, 500 MHz): δ 407.52 (dd, $^1J_{NH}$ = 69.2 Hz, *J* ≈ 20 Hz, H*N*=*N*H, 2N), 58.04 (d, $^1J_{NH}$ = 58.14 Hz, H*N*-*N*H, 2N). ^{31}P{^{1}H} NMR (C_6D_6, 300 MHz): δ 53.8 (d, $^2J_{PP}$ = 51.9 Hz, 4P), 44.4 (dt, $^2J_{PP}$ = 51.9 Hz, $^2J_{PN}$ = 17.4 Hz, 2P). IR (KBr) (cm^{-1}): 3307, 3217, 3202.

Synthesis of {PhBP$^{Ph}_3$Fe}$_2$(μ-NH)$_2$, 2.7. A solution of *para*-benzoquinone (0.0538 g, 0.488 mmol) in 3 mL THF was added dropwise in the dark to a suspension of **2.6** (0.1510 g, 0.098 mmol) in 15 mL THF. The reaction was stirred for 12 h, and was filtered through a Celite-lined frit, leaving behind purple solids. The volatiles were removed, and the resulting solids were rinsed with diethyl ether. The solids were extracted into THF, and layered with methylcyclohexane, to give amorphous solids (0.0350 g, 23.6%). Crystals suitable for X-ray diffraction can be grown via vapor diffusion of cyclopentane into a THF solution of **7**. ^{1}H NMR (C_6D_6, 300 MHz): δ 25.26 (s, 2H), 8.41 (d, 4H, *J* = 6.0 Hz), 7.79 (t, 4H, *J* = 6.0 Hz), 755 (t, 2H, *J* = 6.0 Hz), 6.85 (d, 24H, *J* = 6.0 Hz), 6.77 (t, 12H, *J* = 6.0 Hz), 6.57 (t, 24H, *J* = 7.5 Hz), 2.37 (bs, 12H). ^{31}P{^{1}H} NMR (C_6D_6, 300 MHz): δ 32.5. IR (KBr) (cm^{-1}): 3308, 3287. UV-vis (THF) λ_{max}, nm (ε, M^{-1} cm^{-1}): 336 (sh, 10890), 448 (9190), 512 (sh, 6380), 602 (4120), 919 (2000). Anal. Calcd. for $C_{90}H_{84}B_2Fe_2N_2$: C 71.42; H 5.60; N 1.85. Found: C 71.08; H 5.88; N 1.42.

A sample of 95% ^{15}N-enriched **2.7** was synthesized using an analogous synthetic procedure with $^{15}NH_2{}^{15}NH_2$. ^{1}H NMR (d_8-THF, 500 MHz): δ 25.04 (d, $|^1J_{NH}|$ = 64.0 Hz, N*H*, 2H). ^{15}N NMR (d_8-THF, 500 MHz) δ 563.5 (d, $^1J_{NH}$ = 64.6 Hz, *N*H, 2N). IR (KBr) (cm^{-1}): 3298, 3272.

2.4.7 Toepler Pump Analysis

Toepler pump analysis of the reaction between 2.3 and excess *para*-benzoquinone. Solid **2.3** (0.3759 g, 0.2430 mmol) and *para*-benzoquinone (0.1367 g, 1.239 mmol) were added to a 100 mL RB flask fitted with a stir bar and a teflon plug. The vessel was cooled in a dry ice/acetone bath and evacuated on a high vacuum manifold (10^{-4} torr), and 50 mL of THF was vac transferred. The flask was allowed to warm to room temperature, and stirred for 18 h in the dark. At this time, the solution as cooled in a dry ice/acetone bath, and the teflon plug opened to the Toepler pump. After 2 h (≈ 40 cycles), 0.276 mmol of gas was transferred over, corresponding to an 88 % release of gas. The volatiles were removed from the reaction vessel, and the proton NMR spectrum of the resulting solids revealed 88% conversion to **2.7**, and 12% conversion to **2.6**. An aliquot of the pumped gas was subjected to a GC analysis (N_2 carrier gas), which did not show a peak that corresponds to H_2. Addition of 0.09 mmol more *para*-benzophenone to the reaction mixture (re-suspended in 50 mL of THF) led to complete conversion to **2.7** after stirring for 18 h. The volatiles were again removed, the solids collected on a frit, and washed profusely with pentanes and diethyl ether, leaving behind a pure powder of **2.7** (0.3518 g, 96%).

Works Cited:

1. (a) Hoffman, B. M.; Dean, D. R.; Seefeldt, L. C., *Acc. Chem. Res.* **2009**, *42*, 609; (b) Peters, J. C.; Mehn, M. P., Bio-organometallic Approaches to Nitrogen Fixation Chemistry In *Activation of Small Molecules*, Tolman, W. B., Ed. Wiley-VCH: 2006; pp 81; (c) Howard, J. B.; Rees, D. C., *Proc. Natl. Acad. Sci. U.S.A.* **2006**, *103*, 17088; (d) Schrock, R. R., *Angew. Chem. Int. Ed.* **2008**, *47*, 5512.

2. Barney, B. M.; Yang, T.-C.; Igarashi, R. Y.; Dos Santos, P. C.; Laryukhin, M.; Lee, H.-I.; Hoffman, B. M.; Dean, D. R.; Seefeldt, L. C., *J. Am. Chem. Soc.* **2005**, *127*, 14960.

3. Kästner, J.; Blöchl, P. E., *J. Am. Chem. Soc.* **2007**, *129*, 2998.

4. (a) Hendrich, M. P.; Gunderson, W.; Behan, R. K.; Green, M. T.; Mehn, M. P.; Betley, T. A.; Lu, C. C.; Peters, J. C., *Proc. Natl. Acad. Sci. U.S.A.* **2006**, *103*, 17107; (b) Smith, J. M.; Lachicotte, R. J.; Pittard, K. A.; Cundari, T. R.; Lukat-Rodgers, G.; Rodgers, K. R.; Holland, P. L., *J. Am. Chem. Soc.* **2001**, *123*, 9222; (c) Betley, T. A.; Peters, J. C., *J. Am. Chem. Soc.* **2003**, *125*, 10782; (d) Brown, S. D.; Mehn, M. P.; Peters, J. C., *J. Am. Chem. Soc.* **2005**, *127*, 13146; (e) Smith, J. M.; Sadique, A. R.; Cundari, T. R.; Rodgers, K. R.; Lukat-Rodgers, G.; Lachicotte, R. J.; Flaschenriem, C. J.; Vela, J.; Holland, P. L., *J. Am. Chem. Soc.* **2006**, *128*, 756; (f) Vogel, C.; Heinemann, F. W.; Sutter, J.; Anthon, C.; Meyer, K., *Angew. Chem. Int. Ed.* **2008**, *47*, 2681; (g) Scepaniak, J. J.; Young, J. A.; Bontchev, R. P.; Smith, J. M., *Angew. Chem. Int. Ed.* **2009**, *48*, 3158.

5. Barney, B. M.; McClead, J.; Lukoyanov, D.; Laryukhin, M.; Yang, T. C.; Dean, D. R.; Hoffman, B. M.; Seefeldt, L. C., *Biochemistry* **2007**, *46*, 6784.

6. (a) Goedken, V. L.; Peng, S.-M.; Molin-Norris, J. A.; Park, Y.-A., *J. Am. Chem. Soc.* **1976**, *98*, 8391; (b) Sellmann, D.; Shaban, S. Y.; Heinemann, F. W., *Eur. J. Inorg. Chem.* **2004**, 4591; (c) Crossland, J. L.; Zakharov, L. N.; Tyler, D. R., *Inorg. Chem.* **2007**, *46*, 10476; (d) Field, L. D.; Li, H. L.; Dalgarno, S. J.; Turner, P., *Chem. Commun.* **2008**, 1680.

7. For a diiron η^1:η^1-NH=NH diazene complex see: Sellmann, D.; Soglowek, W.; Knoch, F.; Moll, M., *Angew. Chem., Int. Ed. Engl.* **1989**, *28*, 1271. For a recent example of a monometallic Fe(h^2:N_2H_2) complex see reference 6d.

8. (a) For a terminal Fe-NH_2 complex see: Fox, D. J.; Bergman, R. G., *Organometallics* **2004**, *23*, 1656; (b) For a bridging $Fe_2(NH_2)$ species see: Dahl, L. F.; Costello, W. R.; King, R. B., *J. Am. Chem. Soc.* **1968**, *90*, 5422.

9. For all structures presented herein, the protons on the NxHy ligands are located in the difference Fourier map and refined semi-freely with the help of distance restraints on the N-H distances and the Fe-N-H angles, while constraining the U_{iso} value of the H-atom to -1.2 times the value of the U_{eq} value of the N-atom that the proton binds to.

10. (a) von Philipsborn, W.; Müller, R., *Angew. Chem., Int. Ed. Engl.* **1986**, *25*, 383; (b) Smith, M. R.; Cheng, T. Y.; Hillhouse, G. L., *J. Am. Chem. Soc.* **1993**, *115*, 8638.

11. All ^{15}N NMR chemical shifts are reported relative to liquid NH_3.

12. Blum, L.; Williams, I. D.; Schrock, R. R., *J. Am. Chem. Soc.* **1984**, *106*, 8316.

13. Cheng, T.-Y.; Ponce, A.; Hillhouse, G. L.; Rheingold, A. L., *Angew. Chem., Int. Ed. Engl.* **1994**, *33*, 657.

14. (a) Albertin, G.; Antoniutti, S.; Lanfranchi, M.; Pelizzi, G.; Bordignon, E., *Inorg. Chem.* **1986**, *25*, 950; (b) Smith, M. R.; Hillhouse, G. L., *J. Am. Chem. Soc.* **1988**, *110*, 4066; (c) Chen, Y.; Zhou, Y.; Chen, P.; Tao, Y.; Li, Y.; Qu, J., *J. Am. Chem. Soc.* **2008**, *130*, 15250.

15. Schubert, E. M., *J. Chem. Educ.* **1992**, *69*, 62.

16. Sheldrick, G. M., *Acta Cryst.* **1990**, *A46*.

17. Sheldrick, G. M., *Acta Cryst.* **2008**, *A64*.

18. Müller, P.; Herbst-Irmer, R.; Spek, A. L.; Schneider, T. R.; Sawaya, M. R., *Crystal Structure Refinement: A Crystallographer's Guide to SHELXL*. Oxford University Press: Oxford, 2006.

19. Spek, A. L., L. PLATON A Multipurpose Crystallographic Tool. Utrecht University: Utrecht, Holland, 2008.

20. (a) Brown, S. D.; Betley, T. A.; Peters, J. C., *J. Am. Chem. Soc.* **2003**, *125*, 322; (b) Lu, C. C.; Saouma, C. T.; Day, M. W.; Peters, J. C., *J. Am. Chem. Soc.* **2007**, *129*, 4.

21. Schrock, R. R.; Liu, A. H.; O'Regan, M. B.; Finch, W. C.; Payack, J. F., *Inorg. Chem.* **1988**, *27*, 3574.

22. Tang, H.; Richey, H. G., *Organometallics* **2001**, *20*, 1569.

23. Armarego, W. L. F.; Chai, C. L. L., *Purification of Laboratory Chemicals*. 5 ed.; Butterworth-Heinmann: London, 2002.

Chapter 3: Transformation of an $[Fe(\eta^2\text{-}N_2H_3)]^{1+}$ Species to π-Delocalized $[Fe_2(\mu\text{-}N_2H_2)]^{2+/1+}$ Complexes

Abstract

A monomeric iron Fe(η^2-N_2H_3) species (**3.1**) has been prepared, and exposure to oxygen yields a diiron complex that features five-coordinate iron centers and an activated bridging diazene ligand (NH=NH). Combined structural, theoretical, and spectroscopic data for the redox pair of complexes $[Fe_2(\mu\text{-}N_2H_2)]^{2+/1+}$ (**3.2**, **3.3**) are consistent with 4-center, 4-electron π-delocalized bonding picture across the Fe-NH-NH-Fe core that finds analogy in butadiene and the butadiene anion.

3.1 Introduction

Several mechanisms have been proposed to describe the reduction of N_2 to NH_3 at the cofactor of MoFe-nitrogenase.[1] Although experimental evidence is consistent with initial coordination of N_2 through a single metal center of the cofactor,[2] recent DFT studies have pointed to plausible diiron intermediates of the type $Fe_2(N_2H_y)$ (y = 1-4) *en route* to NH_3 formation.[3] In this context, it is noteworthy that diazene[4] and hydrazine[5] are readily reduced to NH_3 by nitrogenase under turnover conditions. Diiron model complexes that feature the $Fe_2(N_2H_y)$ core are therefore of timely interest,[6,7,8] especially as a spectral reference point to aid in the interpretation of ENDOR/ESEEM data that is being obtained with the enzymatic system during catalysis.[1d]

Herein we describe the characterization of an $[Fe(\eta^2\text{-}N_2H_3)]^{1+}$ species that gives rise to a binuclear complex with an $[Fe_2(\mu\text{-}N_2H_2)]^{2+}$ core upon exposure to O_2. The latter complex is unique in that combined structural, spectroscopic, and DFT calculations suggest that the bridging 'diazene' is best formulated as $N_2H_2^{2-}$. While this level of diazene activation has been observed in complexes of highly reducing early transition metals,[9] it is not well established for the later transition metals, including iron.[7,10] One-electron reduction of the $[Fe_2(\mu\text{-}N_2H_2)]^{2+}$ complex furnishes the EPR-active mixed-valent $[Fe_2(\mu\text{-}N_2H_2)]^{1+}$ complex, whose electronic structure characterization by combined EPR/ENDOR spectroscopy is described.

3.2 Results and Discussion

Entry to this chemical manifold arises from the addition of N_2H_4 to the iron alkyl precursor [$PhBP_3$]FeMe (**2.1**) ([$PhBP_3$]$^-$ = $PhB(CH_2PPh_2)_3^-$) in the presence of a suitable trap. We have previously reported that the room temperature reaction between **2.1** and N_2H_4 quantitatively forms {[$PhBP_3$]Fe}$_2$(μ-η^1:η^1-N_2H_4)(μ-η^2:η^2-N_2H_2), (**2.3**), with concomitant loss of methane.[7b] A hydrazido complex of the type "[$PhBP_3$]Fe(N_2H_3)" is a plausible thermally unstable intermediate to invoke, and a strong-field trapping ligand was hence pursued. Addition of 1 equiv of N_2H_4 to **2.1** at -78 ^oC, followed by addition of 1 equiv of CO, affords orange [$PhBP_3$]Fe(η^2-N_2H_3)(CO), (**3.1**), in ca. 70% chemical yield (Scheme 3.1). Several side reactions compete with formation of **3.1**, and the crude reaction mixtures invariably contain {[$PhBP_3$]Fe}$_2$(μ-η^1:η^1-N_2H_4)(μ-η^2:η^2-N_2H_2),[7b] [$PhBP_3$]Fe$(CO)_2$H (see Appendix 2), and several other unidentified species. The similar solubilities of [$PhBP_3$]Fe$(CO)_2$H and **3.1** diminish the isolated yield of **3.1** in analytically pure form.

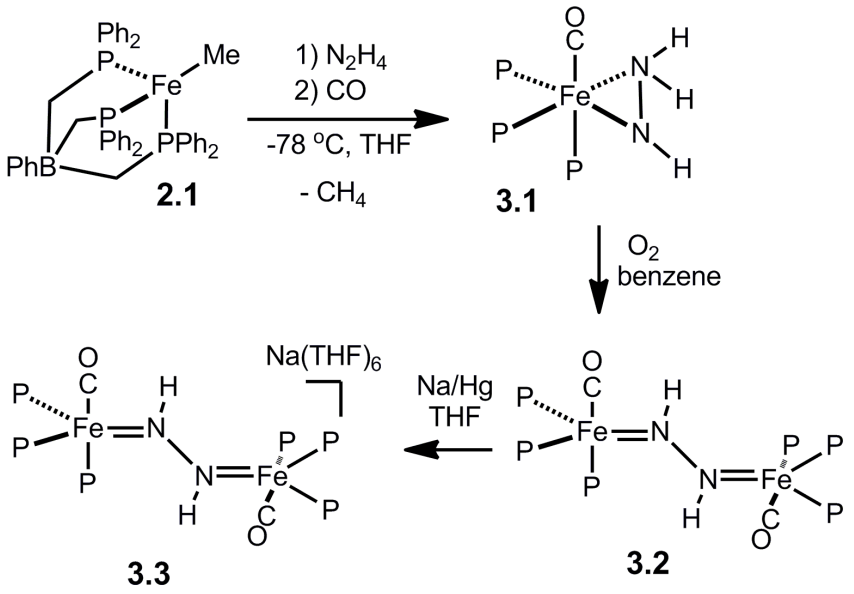

Scheme 3.1.

The solid-state structure of **3.1** was obtained and indicates that the $N_2H_3^-$ ligand coordinates η^2 to the Fe center (Figure 3.1). The Fe-N distances of 1.992(3) and 2.018(3) Å are as expected for coordination of sp^3-hybridized nitrogen to Fe, and are similar to those observed in the related six-coordinate Fe(η^2-N_2H_4) and Fe(η^2-N_2H_2) species.[8a] The N1-N2 bond distance of 1.383(3) Å is shorter than that expected for an N-N single bond, but consistent with that of a related $N_2H_3^-$ complex of tungsten.[11]

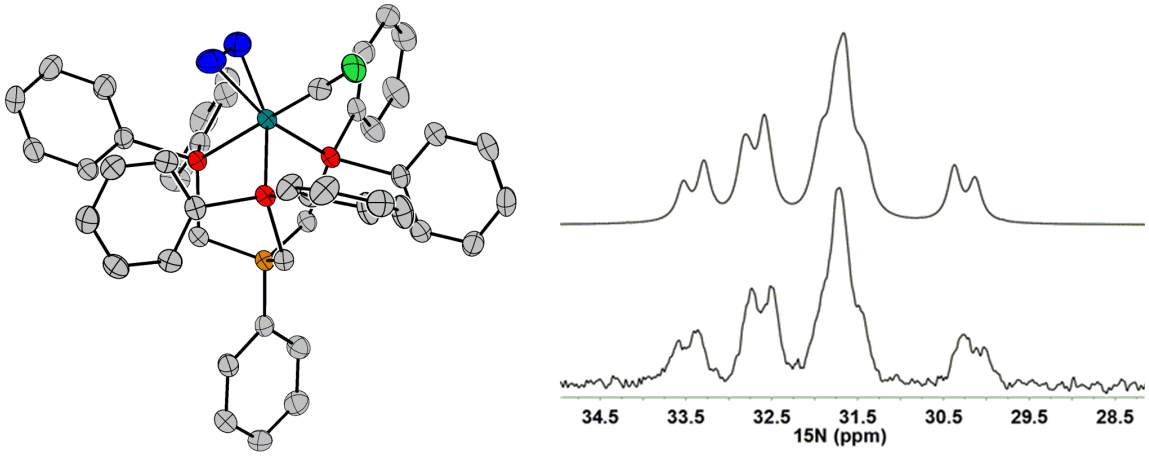

Figure 3.1. (left) Displacement ellipsoid (50%) representation of **3.1**. (right) Simulation (top) of the ^{15}N NMR spectrum of 3.1 (-75 ^{o}C, d_8-THF) and experimental spectrum (bottom). Pertinent fitting parameters: δ 31.8 (NH*N*H$_2$, $^1J_{NH}$ = 86 Hz, $^1J_{NH}$ = 79 Hz, $^1J_{NN}$ = 10 Hz), 32.2 (*N*HNH$_2$, $^1J_{NH}$ = 56 Hz, $^1J_{NN}$ = 10 Hz), linewidth = 7 Hz

The ^{15}N NMR spectrum (-75 ^{o}C, d_8-THF) of **3.1** shows a complicated signal centered around 32 ppm, which was fit to obtain chemical shifts and coupling constants. The NH-*N*H$_2$ and *N*H-NH$_2$ chemical shifts are noted at 31.8 ppm and 32.2 ppm, respectively, with $^1J_{NN}$ = 10 Hz. The ^{1}H NMR spectrum (-75 ^{o}C, d_8-THF) of **3.1** shows three distinct protons for the hydrazido ligand that split into doublets when samples of **3.1** are prepared with ^{15}N$_2$H$_4$. The N*H*-NH$_2$ chemical shift is noted at 2.85 ppm ($^1J_{NH}$ = 56 Hz), and the inequivalent NH-N*H*$_2$ protons appear at 6.55 ($^1J_{NH}$ = 86 Hz) and 1.88 ($^1J_{NH}$ = 79 Hz) ppm. The NMR data collectively indicates that the $N_2H_3^-$ ligand is comprised of two sp^3-hybridized nitrogen atoms.

The orange hydrazido(-) complex **3.1** undergoes decay to the bridged blue diazene complex, {[PhBP$_3$]Fe(CO)}$_2$(μ-η^1:η^1-N$_2$H$_2$), (**3.2**), in the presence of 0.5 equiv oxygen (Scheme 3.1). Other oxidants (e.g., Pb(OAc)$_4$, Cp$_2$Fe$^+$, *p*-quinone), acids (e.g.,

pyridinium, $FeCl_3$, $Sm(OTf)_3$), and bases (e.g., N_2H_4, ^nBuLi, $^tBuN{=}P(\textit{cyclo}\text{-}NC_4H_8)$) were canvassed but do not facilitate this transformation. The reaction is solvent dependent and proceeds in benzene but not in THF, perhaps owing to hydrogen bond stabilization of **3.1** by THF solvent.

The ^{15}N NMR spectrum of **3.2** (prepared from ^{15}N-**3.1**) displays a broad doublet at 292 ppm, indicative of an sp^2-hybridized nitrogen atom. The diazene protons are magnetically inequivalent, and the corresponding $^1H\{^{31}P\}$ NMR spectrum of **3.2** shows a AA'XX' splitting pattern centered at 9.5 ppm. The chemical shifts of both the H and N atoms of the diazene ligand differ from those observed in the related $\{[PhBP_3]Fe\}_2(\mu\text{-}\eta^1{:}\eta^1\text{-}N_2H_2)(\mu\text{-}\eta^2{:}\eta^2\text{-}N_2H_2)$ (^{15}N NMR: 407.5, 58.0; ^1H NMR: 13.20, 4.16),[7b] and suggest that the extent of diazene activation in the two complexes may be different. Simulation of the $^1H\{^{31}P\}$ spectrum of **3.2** gives the following coupling constants: $^1J_{NH}$ = -71.0 Hz, $^2J_{NH}$ = -2.1 Hz, $^3J_{HH}$ = 14.8 Hz, and $^1J_{NN}$ = 9.5 Hz. The magnitude of the three-bond HH coupling is consistent with a *trans* configuration, and can furthermore be used as a probe for the extent of NN activation.[12] For example, $^3J_{HH}$ = 28.0 Hz for $[(CO)_5Cr]_2(\textit{trans}\text{-}\mu\text{-}N_2H_2)$,[13] which has an N-N bond distance of 1.25 Å,[14] while $^3J_{HH}$ = 9.4 Hz for $[(\eta^5\text{-}C_5Me_4H)_2ZrI]_2(\textit{trans}\text{-}\mu\text{-}N_2H_2)$, which has an N-N bond distance of 1.414(3) Å.[9c] Hence, the observed $^3J_{HH}$ coupling in **3.2** is most consistent with a single bond.

The solid-state structure of **3.2** was obtained and its core atoms are shown in Figure 3.2. Both Fe centers have similar metrical parameters, and adopt a distorted trigonal bipyramidal geometry, with the approximate equatorial plane defined by two phosphorous and one nitrogen atom. The two Fe centers are related by a 133° rotation

about the Fe-Fe vector. The *trans* protons on the diazene were located in the difference map, and form a planar diazene. However, the Fe-N-N-Fe linkage departs from planarity and features a 20.3º dihedral angle (Figure 3.2). The average Fe-N bond distance of 1.83 Å in **3.2** indicates the presence of π-bonding, while the elongated N-N bond distance of 1.362(4) Å establishes a significantly activated diazene unit. This distance is closer to that expected for a N(sp^2)-N(sp^2) single bond than that for a double bond (ca. 1.41 Å and 1.24 Å, respectively).[7,15]

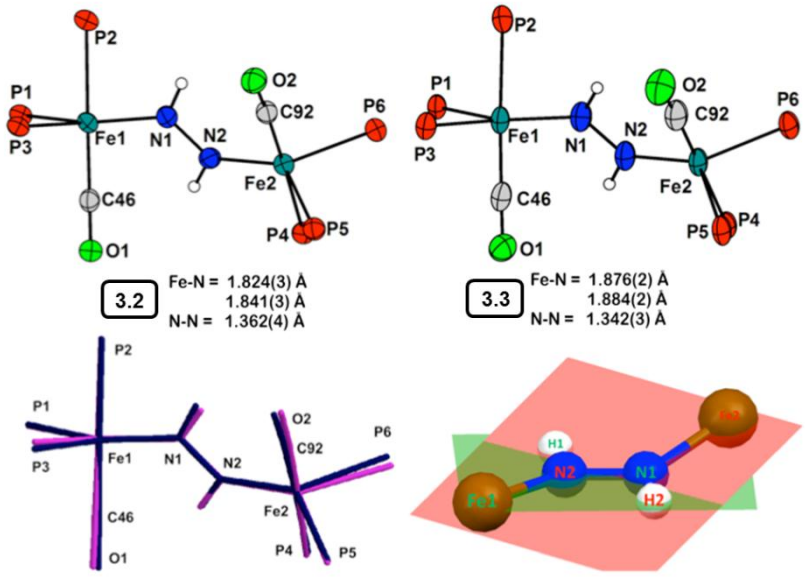

Figure 3.2. Displacement ellipsoid (50%) representations of the core atoms of **3.2** (left, top) and **3.3** (right, top), and an overlay of their core atoms (bottom, left; blue, **3.2**; purple, **3.3**), and a representation showing the twist of the Fe-N-N-Fe linkage of **3.3** (bottom, right)

Complex **3.2** is intensely colored and displays a transition at 716 nm (ε = 8500 M^{-1} cm^{-1}) that is presumably charge transfer in nature by analogy to assignments made for similar bands observed for related dinuclear M(η^1:η^1-N_2H_2)M complexes.[10,16] The rRaman spectrum of **3.2** (633 nm excitation) contains an NN vibration at 1060 cm^{-1},

which shifts to 1032 cm^{-1} in samples of ^{15}N-enriched **3.2** (calculated shift for a diatomic harmonic oscillator: 1023 cm^{-1}). In addition, a second vibration is observed at 665 cm^{-1} (^{15}N: 651 cm^{-1}), which is tentatively assigned as the ν_s(FeN) vibraton that couples with the NN vibration. Both of these vibrations are distinct from those measured by Lehnart and coworkers in an octahedral $Fe_2(\mu\text{-}\eta^1\text{:}\eta^1\text{-}N_2H_2)$ complex (ν(NN) = 1365 cm^{-1}; ν_{as}(FeN) = 496 cm^{-1}),[17] and consistent with appreciably stronger Fe-N and weaker N-N bonds in **3.2**. The combined structural, NMR, and vibrational data suggest that the diazene bridge in **3.2** might better be regarded as a dianionic hydrazido, $N_2H_2^{2-}$, as in the lower left resonance form shown in Figure 3.2.

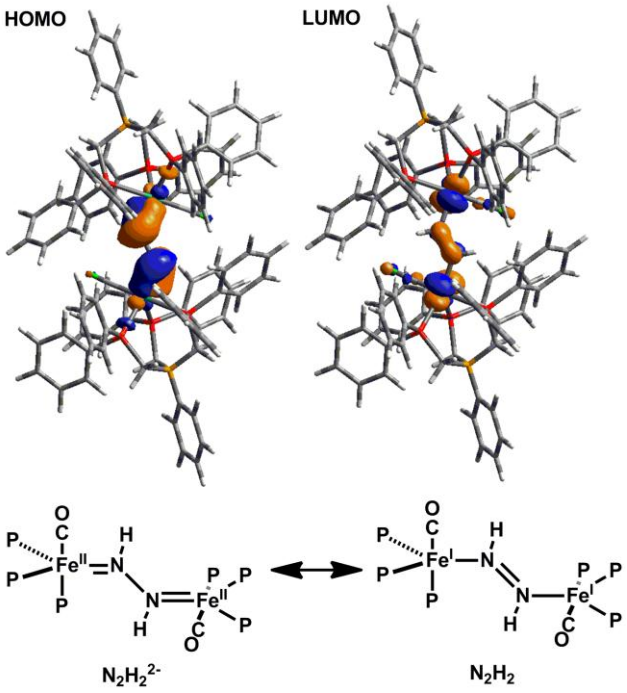

Figure 3.3. (top) HOMO and LUMO of **3.2** (isocontour = 0.04); see SI for computational details. (bottom) Plausible resonance contributors to the electronic structure of **3.2**.

Cyclic voltammetry of **3.2** shows a reversible one-electron reduction to **3.3** at -1.54 V (vs. Fc/Fc^{+}), and chemical treatment of **3.3** with one equiv of Na/Hg in THF cleanly generates the purple mixed-valence $[Fe_2(\mu\text{-}N_2H_2)]^{1+}$ complex, $[\{[PhBP_3]Fe\}_2(\mu\text{-}\eta^1\text{:}\eta^1\text{-}N_2H_2)][Na(THF)_6]$, (**3.3**). Crystals of **3.3** suitable for XRD were grown by vapor diffusion of cyclopentane into a saturated THF solution of **3.3**.

The geometry of the $[Fe_2(\mu\text{-}N_2H_2)]^{1+}$ core of **3.3** is very similar to that of the $[Fe_2(\mu\text{-}N_2H_2)]^{2+}$ core of **3.2**, as shown by an overlay of their core atoms (Figure 3.2). Upon reduction the average Fe-N distance *increases* by ca. 0.03 Å to 1.88 Å. Consistent with this, the ν_s(FeN) stretch decreases from 665 cm^{-1} to 643 cm^{-1} (^{15}N: 624 cm^{-1}) upon reduction.[18] The N-N bond distance in **3.3** is found to exhibit a marginal decrease to 1.342(3) Å upon reduction. These observations are collectively consistent with π-delocalization within the Fe-N-N-Fe core, with the unpaired electron populating an orbital that is predominantly Fe-N antibonding in character.

DFT calculations (see Section 3.4.5 and Appendix 2 for details) were performed to further probe the electronic structures of both **3.2** and **3.3**. The frontier orbitals of **3.2** are isolobal to those of butadiene, and both the HOMO and LUMO are primarily composed of the Fe-N-N-Fe π-system. The HOMO displays Fe-N π-bonding and N-N π^*-bonding character (Figure 3.2, top). The LUMO features N-N π-bonding, and Fe-N π*-bonding character. Population of the LUMO should therefore result in a decrease in the N-N bond distance, and an increase in the Fe-N bond distance. However, the SOMO of **3.3** has only minimal density on the N-N bridge, and so the actual change should be small, as observed. The observation that the reduction of **3.2** to **3.3** yields a shortened N-

N distance in the N_2H_2 ligand in the present case is consistent with the DFT calculations. A similar result has been provided for a series of $[Mo_2(\mu\text{-}N_2)]^{6+/7+/8+}$ species where formal overall oxidation of the complex leads to a more 'activated' bridging N_2 ligand.[19]

To further probe the electronic structure of the $[Fe_2(\mu\text{-}N_2H_2)]^{1+}$ core of **3.3**, we turned to EPR/ENDOR spectroscopy. Complex **3.3** is paramagnetic, with a rhombic S = ½ EPR signal (9:1 THF:Me-THF; g = [2.125, 2.040, 2.020]) that remains essentially invariant from 77 K to 2 K. To test the model of a symmetrical, π-delocalized Fe-N-N-Fe core, 35 GHz ^{15}N electron-nuclear double resonance (ENDOR) measurements were performed at 2 K on ^{15}N-**3.3**.[20] Figure 3.4 displays ^{15}N ENDOR spectra selected from a 2D field-frequency pattern of ENDOR spectra (ν_+ manifold) collected across the EPR envelope of ^{15}N-**3.3** (see Section 3.4.2 and Appendix 2). The 2D pattern can be simulated with a single *type* of ^{15}N, having a nearly axial hyperfine coupling tensor, principal values, $\mathbf{A}(^{15}N)$ = + [6.7, 5.6, 17.8] MHz, isotropic coupling, $a_{iso}(^{15}N)$ = +10 MHz, and anisotropic coupling, $\mathbf{T}(^{15}N)$ = + [-3.3, -4.5, 7.8] MHz (see Section 3.4.2 and Appendix 2). The absence of a Mims ENDOR response associated with a second, more weakly coupled ^{15}N nucleus (not shown),[21] indicates that the two ^{15}N atoms from the bridge are magnetically equivalent and contribute equally to the ENDOR response depicted in Figure 3.4, as expected for a delocalized $[Fe_2(\mu\text{-}N_2H_2)]^{1+}$ ground state.

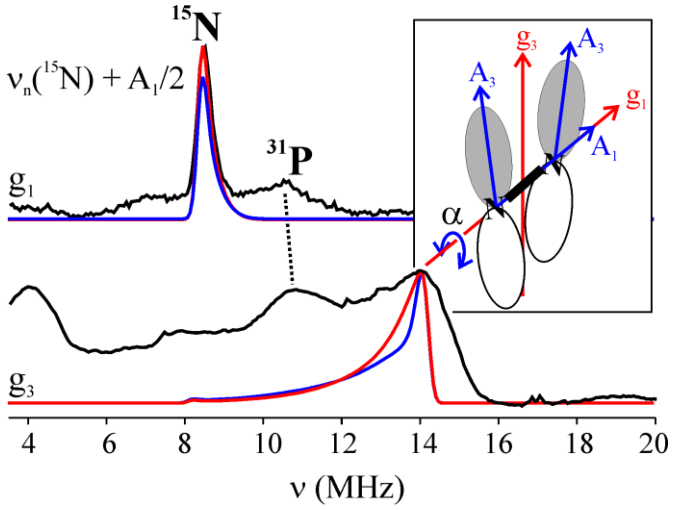

Figure 3.4. 35 GHz Davies ^{15}N pulsed ENDOR spectra (black traces; ν_+ manifold ($\nu_+ = \nu_n + A/2$)) from ^{15}N-**3.3** at the indicated g values. Simulations (red, $\alpha = \pm 7^o$, blue, $\alpha = 0^o$ and 15^o) are described in the text and Section 3.4.2.

The strong anisotropy of **A** requires that the spin density on the two N atoms is of π character (A_3 parallel to the π-orbital for each N).[22] The positive sign of **A** for ^{15}N indicates that the π spin density on the N-N bridge, ρ^{π}(N), is *negative* (see SI), with the anisotropic coupling corresponding to $\rho^{\pi}(N) \sim -0.05$ spins/nitrogen; the majority of the remaining spin density likely resides on Fe. The DFT computations on **3.3** give $\rho^{\pi}(N) \sim -0.36$ spins/nitrogen, which is in satisfactory agreement with experiment given that DFT is well known to overestimate the effects of spin polarization.[23] This finding of rather low spin delocalization onto the bridging nitrogens of **3.3** illustrates why it is instructive to consider **3.2** in terms of the butadiene-like resonance structure shown in Figure 3.4. The butadiene anion is the corresponding analogue to **3.3**, and its SOMO is minimally delocalized onto the central atoms. In **3.3**, delocalization would be decreased further due to the greater electronegativity of N compared to that of Fe.

The orientations of the ^{15}N hyperfine tensors also are informative. The observation of a single, very sharp ^{15}N ENDOR feature at g_1 indicates the g_1 axis is coincident with the N-N vector and normal to the spin-bearing π orbitals on $^{15}N_i$ (i = 1, 2). These are expected to be primarily defined by the Fe_i-H_i-N_j (j = 2, 1) planes (Figure 3.2, bottom right), and thus lie essentially normal to the g_1 axis. Indeed, the 2D ENDOR pattern is satisfactorily simulated by taking the g_3 axis to bisect the angle between the two Fe_i-H_i-N_j planes, $2\alpha \sim 14^o$, and then orienting each $^{15}N_i$ hyperfine tensor along the normal to its plane, which corresponds closely to simply rotating the hyperfine tensors of N1 and N2 around g_1 by equal and opposite angles, $\alpha \sim 7^o$ (see Figure 3.4, blue trace). Unfortunately, the data does not define these rotations with precision; not only is agreement with experiment at g_2 improved with $\alpha = 15^o$ (Figure 3.4), but also, the observation of broad features in the ENDOR spectrum at g_3, in contrast to the narrow peak at g_1, suggests that there may be a distribution of angles in the frozen solution. Overall, the ^{15}N ENDOR results support that **3.3**, *at 2 K*, contains a π-delocalized Fe-N-N-Fe core, as predicted by DFT computations, with the π-orbital 'twist' indicated by the X-ray structure.

3.3 Conclusions

In summary, we have prepared an Fe(η^2-N_2H_3) species, and have shown that the coordinated hydrazido ligand is converted to diazene in the presence of oxygen. The end-on diazene ligands in the $[Fe_2(\mu\text{-}N_2H_2)]^{2+/1+}$ cores of **3.2** and **3.3**, are best regarded as '$N_2H_2^{2-}$,' a bonding formulation previously observed for diazene complexes of highly

reducing early-transition metals. Combined structural, theoretical, and spectroscopic data for the dinuclear complex **3.2** indicate the presence of 4-center, 4-electron π-delocalized bonding across the Fe-N-N-Fe diiron μ-diazene core. This picture is consistent with DFT studies, as well as a combined EPR/ENDOR study of its 1-electron reduced congener **3.4**. This electronic structure, in which the HOMO is N-N π-bonding, provides access to stable diazene complexes in both the $[Fe_2(\mu\text{-}N_2H_2)]^{2+/1+}$ oxidation states. Whether such a fragment arises in the reaction pathway by which nitrogenase reduces N_2 to $2NH_3$ is being explored by detailed comparisons of the results presented here with ENDOR results for nitrogenase intermediates.[24]

3.4 Experimental Section

3.4.1 General Considerations

All manipulations were carried out using standard Schlenk, high-vac, or glove-box techniques under a dinitrogen atmosphere. Unless otherwise noted, solvents were deoxygenated and dried by sparging with Ar followed by passage through an activated alumina column from S.G. Water (Nashua, N.H.). Cyclopentane and 2-methyltetrahydrofuran were stirred over sodium and dried with sodium ketyl radical, and vac-transferred after the solution remained purple for 48 h. Nonhalogenated solvents were tested with a standard purple solution of benzophenone ketyl in THF to confirm effective oxygen and moisture removal. Deuterated solvents were purchased from Cambridge Isotopes Laboratories, Inc. and were degassed and stored over activated 3-Å

molecular sieves prior to use. Elemental analyses were performed Midwest Microlab (Indianapolis, IN).

3.4.2 Spectroscopic Measurements

Varian 300, 400, and 500 MHz spectrometers were used to record the ^{1}H NMR, ^{31}P NMR, and ^{15}N NMR spectra (400 or 500 MHz). ^{1}H chemical shifts were referenced to residual solvent. ^{31}P NMR chemical shifts were referenced to 85% H_3PO_4 at $\delta = 0$ ppm, and ^{15}N NMR chemical shifts were referenced to neat $C_6H_5{}^{15}NO_2$ ($\delta = 370$ ppm) in comparison to liquid ammonia ($\delta = 0$ ppm). MestReNova (6.1.0) was used for NMR data workup, as well as for simulation of spectra.

IR measurements were obtained with a KBr solution cell or a KBr pellet using a Bio-Rad Excalibur FTS 3000 spectrometer controlled by Varian Resolutions Pro software set at 4 cm^{-1} resolution.

The rRaman samples were prepared by loading solutions into capillaries in the glove-box, which were then flame-sealed (for room temperature data collection), or were transferred to a sealable NMR tube which was subsequently flame-sealed (for data collection at 77 K). Excitation was performed at 632.8 nm using a HeNe laser (10 mW) or at 514 nm using an Ar-ion laser. A lens collected the light that scattered at 90^{o} and focused it through a low-pass filter and into the entrance slit of a SPEX 750M monochromator. The dispersed light was detected by a LN/CCD array (5 cm^{-1} resolution), and the spectra recorded using Winspec (Princeton Instrument) software. Conversion from pixels to wavenumber was done by obtaining the spectrum of

cyclohexane, and deriving the linear plot of pixels vs. wavenumber for known vibrations. All spectra were recorded in THF or Me-THF, and in some instances, solvent subtraction or baseline correction was performed.

Optical spectroscopy measurements were taken on a Cary 50 UV-Vis spectrophotometer using a 1 cm two-window quartz cell sealed with standard ground-glass joints or Teflon plugs.

Samples of **3.3** suitable for 35 GHz EPR and ENDOR measurements were prepared in 9:1 THF:2-MeTHF solvent mixtures (3 mM) and transferred into quartz tubes in the glovebox. The samples were frozen in the glovebox, and transferred/stored at 77K. EPR and ENDOR data were collected on a home-built spectrometer, described previously,[25] that was equipped with a liquid helium immersion dewar for measurements at 2 K. Echo-detected EPR spectra of ^{15}N-**3.3** were simulated using the Simfonia program.[26]

Signs of the hyperfine couplings measured from ENDOR spectra (more specifically, the sign of $g_{Nuc}A_{Nuc}$) have been obtained by application of the Pulse-Endor-SaTuration-REcovery (PESTRE) protocol, a pulse sequence comprised of multiple Davies ENDOR sequences, carried out in three distinct experimental phases: (I) an EPR saturation phase (RF off) of 100 Davies sequences whose spin-echo intensities quickly converge to the steady-state 'baseline' (BSL); (II) an ENDOR perturbation phase of 24 sequences, in which each sequence contains a fixed RF set at one or the other of the branches of the ENDOR spectrum ($\nu_{\pm}$); (III) and an EPR recovery phase (RF off) of 132 sequences during which the spin echo corresponds to the spin-echo 'dynamic reference level' (*drl*) associated with ENDOR-induced spin polarization created in the second

phase, with the *drl* relaxing to the BSL during this phase. In the slow-relaxation regime, the sign of A_{Nuc} is unambiguously given by the sign of the difference between the *drl* and BSL echo intensities as observed for *either* ENDOR branch.[27]

Under the typical conditions for a PESTRE experiment t_{mix}, defined as the time between the first and the second of the three microwave pulses within a single Davies sequence, is short relative to the electron spin-lattice relaxation time, T_{1e} ($T_{1e} >> t_{mix} \sim 5$ μs). However, for ^{15}N-**3.3**, in this regime the PESTRE responses, namely the differences between the *drl* and BSL in phase III, are too small to make a reliable hyperfine sign assignment for both the nu+ and nu- manifolds. However, when t_{mix} is long and T_{1e} are of the same order of magnitude the difference between *drl* and BSL becomes readily measured. In this regime, the expected differences between the *drl* and BSL are of opposite sign to the short-t_{mix} experiment: for $\{A_n \times g_n\} > 0$, if ν_+ is being interrogated, the *drl* relaxes to the BSL from *above*; if ν_- is interrogated, the *drl* relaxes to the BSL from *below*; the opposite behavior will be observed for $\{A_n \times g_n\} < 0$.[28]

For ^{15}N-**3.3** in the long-t_{mix} regime, at ν_+ we observe the *drl* relaxing to the BSL from *below*; at ν_-, we observe the *drl* relaxing to the BSL from *above*, which implies that $\{A_n \times g_n\} < 0$. As A_n is proportional to the product of gn and the spin density, the $\{A_n \times g_n\}$ has the sign of the spin density. The experiment thus implies that the spin density on N is negative.

3.4.3 Electrochemistry

Electrochemical measurements were carried out in a glovebox under a dinitrogen atmosphere in a one-compartment cell using a BAS model 100/W electrochemical analyzer. A glassy carbon electrode and platinum wire were used as the working and auxillary electrodes, respectively. The reference electrode was $Ag/AgNO_3$ in THF, and ferrocene was used as an internal standard. Solutions (THF) of electrolyte (0.4 M tetra-n-butylammonium hexafluorophosphate) and analyte were also prepared in a glovebox.

3.4.4 X-Ray Crystallography Procedures

Low-temperature diffraction data were collected on a Siemens or Bruker Platform three-circle diffractometer coupled to a Bruker-AXS Smart Apex CCD detector with graphite-monochromated Mo or Cu Kα radiation (λ = 0.71073 or 1.54178 Å, respectively), performing φ-and ω-scans. The structures were solved by direct or Patterson methods using SHELXS[29] and refined against F^2 on all data by full-matrix least squares with SHELXL-97.[30] All non-hydrogen atoms were refined anisotropically. All hydrogen atoms (except hydrogen atoms on nitrogen) were included into the model at geometrically calculated positions and refined using a riding model. The isotropic displacement parameters of all hydrogen atoms were fixed to 1.2 times the U value of the atoms they are linked to (1.5 times for methyl groups). Hydrogen atoms directly coordinated to nitrogen were located in the Fourier difference map, and refined semi-freely with the aid of distance restraints. If these hydrogen atoms could not be located in the difference map, they were left out of the final refinement model.

The structures were refined using established methods.[31] Several of the structures reported suffered from disorder in parts of the [$PhBP^{R}_{3}$] ligand and all of the structures showed disorder of solvent molecules (some over more than two independent positions). All disorders were refined with the help of similarity restraints on 1-2 and 1-3 distances and displacement parameters as well as rigid bond restraints for anisotropic displacement parameters. All close contacts, both inter and intramolecular, reported by the Platon validation software[32] involve at least one partner from a minor component of a disorder. While it is conceivable that more components of the molecule(s) are disordered and parameterization of these disordered components would remove the close contacts, the data at hand did not allow for further modeling of the disorder.

Crystals of **3.3** proved to be highly sensitive, with noticeable solvent loss/discoloration after ca. 1 minute in paratone oil. Their instability and small size did not allow us to collect a dataset using the above methods, and the dataset was collected at the Stanford Synchatron Radiation Laboratory (SSRL) beam line 12-2 at 17keV using a single phi axis and recorded on a Dectris Pilatus 6M. The ability to rotate just one-axis gave a dataset that was only 88.7% complete. The images were processed using XDS,[33] and XPREP was used to create appropriate files for use with the SHELXL-97 program.

The crystal structures have been deposited in the Cambridge Crystallographic Data Centre and have the following deposition numbers: CCDC 795818–795821.

3.4.5 DFT Calculations

Density functional calculations were carried out using the Gaussian03 suite[34] using the restricted B3LYP functional, unless otherwise noted. The 6-31+G* basis set was used to obtain a minimized structure of **3.2**, and the 6-311++G** basis set was used to do a single-point energy calculation from the optimized coordinates. The 6-31+G* basis set was used to obtain a minimized structure of **3.3** using the unrestricted BPV86 functional, and the 6-311++G** basis set was used to do a single-point energy calculation from the optimized coordinates (B3LYP).

For geometry optimizations, coordinates were taken from the solid-state structures of **3.2** and **3.3**. Truncation of the ligand by replacing the Ph substituents on the phosphines to Me groups gave a minimized structure in which the two carbonyl groups were *trans* to one another, and hence all calculations were done with the full ligand, which preserved the observed coordination at both Fe centers. Molecular orbital plots were generated using GaussView 4.1[35] with isocontor values of 0.04 (MO) and 0.002 (density).

3.4.6 Starting Materials and Reagents

$[PhBP_3]FeMe$ (**2.1**),[7b] $[PhBP_3]Fe(CO)_2Na(THF)_6$,[36] and $^{15}N_2H_4$[11] were prepared according to literature methods. All other reagents were purchased from commercial vendors and used without further purification.

3.4.7 Synthesis of Compounds

Synthesis of [PhBP$_3$]Fe(η^2-N$_2$H$_3$)(CO), 3.1.

1.) In the glovebox, a 20 mM THF solution of **2.1** (856.7 mg, 1.132 mmol) was transferred to a 500 mL round bottom flask, and stirred at -78 ^{o}C. To this, a solution of anhydrous hydrazine (55.0 μL, 1.699 mmol) in 5 mL THF was added dropwise. After stirring for 10 min, a calibrated bulb (56.30 mL) that was fit with Kontes Teflon plugs was attached to the flask, and the reaction taken out of the glovebox and quickly transferred to a dry ice/acetone bath. The bulb was attached to a high vacuum manifold and degassed. CO (1.132 mmol, 37.1 cmHg) was added to the bulb, which was then closed to the manifold, and opened to the reaction flask. The reaction was stirred for 18 h, during which time it gradually warmed to room temperature. The volatiles were removed, and in the glovebox, the solids were rinsed with 20 mL of pentane. The solids were then extracted into minimum THF, filtered, and layered with an equal volume of pentane and stored at -35 ^{o}C. As [PhBP$_3$]Fe(CO)$_2$H readily co-crystallizes with **3.1**, crystals of analytically pure **3.1** are only obtained after several re-crystallizations (yield: 36.1 mg, 4.0%). Synthetically useful samples of **3.1** can be obtained in yields that range between 30–40%. Crystals of **3.1** suitable for diffraction can be grown by slow evaporation of pentane into a saturated benzene solution of **3.1** that contains hydrazine.

2.) A 25 mL schlenk tube fitted with a 8 mm Kontes Teflon plug was charged with a stir bar and a 25 mM solution of **2.1** (31.9 mg, 0.0423 mmol) in THF. The flask was cooled to -78 ^{o}C using a dry ice/acetone bath. To this, a solution of anhydrous hydrazine (2.1 μL, 0.0633 mmol) in 0.4 mL THF was added dropwise, and a color change from amber to strawberry red was noted. The flask was sealed, removed from the glovebox, and immediately placed in a dry ice/acetone bath. The flask was connected to a calibrated bulb (3.24 mL) which was attached to a high vacuum manifold. Once full vacuum was attained (5.1 x 10^{-4} torr), the flask was degassed and closed to the vacuum manifold. CO (0.0423 mmol, 24.0 cmHg) was added to the caliberated bulb, which was then closed to the vacuum manifold and opened to the reaction flask. The reaction was stirred, and allowed to gradually warm to room temperature over the course of 14 h. At this time, the volatiles were removed to yield an orange solid. The solid was taken up in C_6D_6, and ^{31}P NMR data was collected, indicating 68% conversion to **3.1**, with 18% conversion to $\{[PhBP_3]Fe\}_2(\mu\text{-}\eta^2\text{:}\eta^2\text{-}N_2H_2)(\mu\text{-}\eta^1\text{:}\eta^1\text{-}N_2H_4)$ and 10% conversion to $[PhBP_3]Fe(CO)_2H$ (integration against an internal standard of PPh_3).

^{1}H NMR (THF-d_8, 500 MHz, -75 ^{o}C): δ 6.2-8.0 (m, 36H), 2.84 (s, 1H), 1.87 (s, 1H), 1.39 (bs, 4H), 0.95-1.20 (m, 2H). ^{31}P NMR (THF-d_8, 202 MHz, -75 ^{o}C): δ 64.23 (d, J = 82.6 Hz), 58.99 (d, J = 55.5 Hz), 32.59 (dd, J = 82.3, 55.4 Hz). IR (KBr) (cm^{-1}): 3316, 3237, 1917 (CO). UV-vis (THF) λ_{max}, nm (ε, M^{-1} cm^{-1}): 365 (sh, 1580), 492 (sh, 190), 720

(130). Anal. Calcd. for $C_{46}H_{44}BFeP_3N_2O$: C 69.02; H 5.54; N 3.50. Found: C 68.69; H 5.65; N 3.56.

A sample of 95% ^{15}N-enriched **3.1** was synthesized using an analogous synthetic procedure with $^{15}NH_2{}^{15}NH_2$. ^{1}H NMR (THF-d_8, 500 MHz, -75 ^{o}C): δ 6.45 (d, N*H*H, $^1J_{NH}$ = - 86 Hz, 1H), 2.88 (d, NH*H*, $^1J_{NH}$ = - 79 Hz, 1H), 1.88 (d, N*H*, $^1J_{NH}$ = - 56 Hz, 1H). Select ^{1}H{^{31}P} decoupling indicates that the peak at 6.45 ppm is coupled to the ^{31}P NMR resonance at 32.59, suggesting that this proton resonance corresponds to the NHH_{trans} to the phosphine. ^{15}N NMR (THF-d_8, 50 MHz, -75 ^{o}C): δ 32.2 (m, *N*H, $^1J_{NH}$ = - 86 Hz, $^1J_{NN}$ = 10 Hz), 31.8 (m, *N*H$_2$, $^1J_{NH}$ = - 79 Hz, $^1J_{NH}$ = - 86 Hz, $^1J_{NN}$ = 10 Hz). Coupling constants were obtained by simulation of the spectrum. IR (KBr) (cm^{-1}): 3300, 3250, 3226.

Synthesis of {[PhBP$_3$]Fe(CO)}$_2$(μ-η^1:η^1-*trans*-N$_2$H$_2$), 3.2. Complex **3.1** (0.0224 g, 0.0280 mmol) was taken up in 1 mL C_6D_6 and transferred to a J.Young tube. The tube was attached to a calibrated bulb (3.24 mL) on a high vacuum manifold. The solution was frozen and evacuated. Oxygen (0.0140 mmol, 8.0 cmHg) was added to the bulb, which was then closed to the manifold. The oxygen was condensed into the tube (liquid nitrogen), and sealed. The reaction was thawed, and shaken once. After 18 h, the solution had changed color from orange to blue-green. The NMR tube was rotated for an additional 6 h, during which the color changed to blue. In the glovebox, the volatiles were removed, and the solid residue was washed with pentane and diethyl ether, to afford **3.2** as an analytically pure blue solid (yield: 0.0136 g, 61.9%). Crystals suitable for

diffraction could be grown by diffusion of pentane into a benzene solution of **3.2**. $^{1}H\{^{31}P\}$ NMR (400 MHz, THF-d_8) δ 9.5 (bs, 2H, N*H*), 7.72 (d, *J* = 7.4 Hz, 4H), 7.67 (d, *J* = 6.4 Hz, CH_{ortho} 8H), 7.24 (t, *J* = 7.5 Hz, 8H), 6.9-7.15 (m, 50 H), 1.89 (s, CH_2, 4H), 1.53 (d, *J* = 13.4 Hz,C*H*H, 4H), 1.20 (d, *J* = 14.4 Hz, CH*H*, 4H). ^{31}P NMR (162 MHz, THF-d_8) δ 57.04 (d, *J* = 55.3 Hz), 38.95 (t, *J* = 55.6 Hz). IR (THF/KBr) (cm^{-1}): 3270 (NH), 569. IR (KBr) (cm^{-1}): 1931 (CO). rRaman (633 nm) (cm^{-1}): 1060 (NN), 665 (FeN). UV-vis (THF) λ_{max}, nm (ε, M^{-1} cm^{-1}): 527 (sh, 2650), 716 (8470). Anal. Calcd. for $C_{92}H_{84}B_2Fe_2P_6N_2O_2$: C 70.43; H 5.40; N 1.78. Found: C 71.08; H 6.34; N 1.57.

A sample of 95% ^{15}N-enriched **3.2** was synthesized using an analogous synthetic procedure with ^{15}N-enriched **2**. $^{1}H\{^{31}P\}$ NMR (400 MHz, THF-d_8) δ 9.495 (m, $^{1}J_{NH}$ = -71.0 Hz, $^{2}J_{NH}$ = -2.1 Hz, $^{3}J_{HH}$ = 14.8 Hz, $^{1}J_{NN}$ = -9.5 Hz, 2H, N*H*). Coupling constants were obtained by simulation of the spectrum. ^{15}N NMR (THF-d_8, 40 MHz): δ 291.9 (d, *J* ≈ 71 Hz). IR (THF/KBr) (cm^{-1}): 3264 (NH), 565. rRaman (633 nm) (cm^{-1}): 1030 (NN), 651 (FeN).

Synthesis of {[PhBP$_3$]Fe(CO)}$_2$(μ-η^1:η^1-*trans*-N$_2$H$_2$).Na(THF)$_6$, 3.3. A solution of **3.2** (3.7 mg, 0.0024 mmol) in 2 mL THF was added to a stirring 0.32 wt % Na/Hg amalgam (16.9 mg, 0.0024 mmol). After an hour, the reaction solution changed color from blue to purple. The reaction was filtered, and the volatiles were removed to give pure **3.3** (4.4 mg, 92%). Crystals suitable for X-ray diffraction were grown by slow diffusion of cyclopentane into a saturated THF solution of **3.3**. ^{1}H NMR (300 MHz, THF-d_8) δ 8.3 (bs), 7.51, 7.18, 6.86. 4.73, 3.64 (coordinated THF), 1.78 (coordinated THF), 1.23, 0.89.

UV-vis (THF) λ_{max}, nm (ε, M^{-1} cm^{-1}): 532 (5000), 630 (3690). rRaman (514 nm, 77K) (cm^{-1}): 643 (FeN). EPR (35 GHz, 2K, 9:1 THF:2MeTHF): g = [2.125, 2.040, 2.020]. Anal. Calcd. for $C_{116}H_{132}B_2Fe_2P_6N_2O_8Na$: C 68.82; H 6.57; N 1.38. Found: C 62.55; H 5.71; N 2.04.

A sample of 95% ^{15}N-enriched **3.3** was synthesized using an analogous synthetic procedure with ^{15}N-enriched **3.3**. rRaman (514 nm, 77K) (cm^{-1}): 624 (FeN).

Independent Synthesis of $[PhBP_3]Fe(CO)_2H$. A solution of triflic acid (10.8 μL, 0.123 mmol) in 2 mL THF was added dropwise to a stirring solution of $[PhBP_3]Fe(CO)_2Na(THF)_6$ (0.1450 g, 0.1225 mmol) in 10 mL THF. After 10 min, the solution changed color from bright orange to pale yellow, and the volatiles were removed. The resulting solid was rinsed with pentane, extracted into benzene and filtered through celite. Layering the benzene solution with pentane gave crystals suitable for diffraction (0.0779 g, 98%). ^1H NMR (300 MHz, C_6D_6) δ 7.99 (d, J = 7.1 Hz, 2H), 7.54-7.66 (m, 12H), 7.36 (t, J = 7.2 Hz, 1H), 6.66-6.86 (m, 20H), 1.76 (d, 2H, J_{PH} = 13.0 Hz), 1.66 (bs, 4H), -9.42 (td, J = 42.1, 21.2 Hz, 1H). ^{31}P NMR (121 MHz, C_6D_6) δ 47.55 (dd, J = 41.0, 9.8 Hz, 2P), 37.66 (t, J = 41.6 Hz, 1P). IR (KBr) (cm^{-1}): 2004, 1914 (CO). Anal. Calcd. for $C_{47}H_{42}BFeP_3O_2$: C 70.70; H 5.30; N 0. Found: C 70.65; H 5.67; N 0.

Acknowledgements:

The work presented in this chapter was done in collaboration with Prof. Brian M. Hoffman (Northwestern) and Robert Adam Kinney (Northwestern). They are responsible for the EPR and ENDOR spectroscopic studies. Alec Durell and Dr. Jay Winkler are acknowledged for assistance with resonance Raman studies. Dr. Jens Kaiser is acknowledged for assistance with X-ray crystallography.

Works Cited:

1. (a) Howard, J. B.; Rees, D. C., *Proc. Natl. Aca. Sci.* **2006**, *103*, 17088; (b) Peters, J. C.; Mehn, M. P., Bio-organometallic Approaches to Nitrogen Fixation Chemistry In *Activation of Small Molecules*, Tolman, W. B., Ed. Wiley-VCH: 2006; pp 81; (c) Schrock, R. R., *Angew. Chem. Int. Ed.* **2008**, *47*, 5512; (d) Hoffman, B. M.; Dean, D. R.; Seefeldt, L. C., *Acc. Chem. Res.* **2009**, *42*, 609.

2. Barney, B. M.; Lukoyanov, D.; Igarashi, R. Y.; Laryukhin, M.; Yang, T. C.; Dean, D. R.; Hoffman, B. M.; Seefeldt, L. C., *Biochemistry* **2009**, *48*, 9094.

3. (a) Hinnemann, B.; Nørskov, J. K., *J. Am. Chem. Soc.* **2004**, *126*, 3920; (b) Kästner, J.; Blöchl, P. E., *J. Am. Chem. Soc.* **2007**, *129*, 2998; (c) Dance, I., *Dalton Transactions* **2010**, *39*, 2972.

4. Barney, B. M.; McClead, J.; Lukoyanov, D.; Laryukhin, M.; Yang, T. C.; Dean, D. R.; Hoffman, B. M.; Seefeldt, L. C., *Biochemistry* **2007**, *46*, 6784.

5. Barney, B. M.; Yang, T.-C.; Igarashi, R. Y.; Dos Santos, P. C.; Laryukhin, M.; Lee, H.-I.; Hoffman, B. M.; Dean, D. R.; Seefeldt, L. C., *J. Am. Chem. Soc.* **2005**, *127*, 14960.

6. For Fe(N_2H_3) complexes see: (a) Crossland, J. L.; Balesdent, C. G.; Tyler, D. R., *Dalton Transactions* **2009**, 4420; (b) Lee, Y. H.; Mankad, N. P.; Peters, J. C., *Nature Chemistry* **2010**, *2*, 558.

7. For end-on diazene coordination: (a) Sellmann, D.; Sutter, J., *Acc. Chem. Res.* **1997**, *30*, 460; (b) Saouma, C. T.; Müller, P.; Peters, J. C., *J. Am. Chem. Soc.* **2009**, *131*, 10358.

8. For side-on diazene coordination: (a) Field, L. D.; Li, H. L.; Dalgarno, S. J.; Turner, P., *Chem. Commun.* **2008**, 1680; (b) ref. 7b.

9. (a) Churchill, M. R.; Li, Y. J.; Blum, L.; Schrock, R. R., *Organometallics* **1984**, *3*, 109; (b) Blum, L.; Williams, I. D.; Schrock, R. R., *J. Am. Chem. Soc.* **1984**, *106*, 8316; (c) Bernskoetter, W. H.; Pool, J. A.; Lobkovsky, E.; Chirik, P. J., *J. Am. Chem. Soc.* **2005**, *127*, 7901.

10. Fujisawa, K.; Lehnert, N.; Ishikawa, Y.; Okamoto, K.-i., *Angew. Chem. Int. Ed.* **2004**, *43*, 4944.

11. Schrock, R. R.; Liu, A. H.; O'Regan, M. B.; Finch, W. C.; Payack, J. F., *Inorg. Chem.* **1988**, *27*, 3574.

12. Cooper, M. A.; Manatt, S. L., *J. Am. Chem. Soc.* **1969**, *91*, 6325.

13. Smith, M. R.; Cheng, T. Y.; Hillhouse, G. L., *J. Am. Chem. Soc.* **1993**, *115*, 8638.

14. Huttner, G.; Gartzke, W.; Allinger, K., *Angew. Chem., Int. Ed. Engl.* **1974**, *13*, 822.

15. Allman, R., In *The Chemistry of the Hydrazo, Azo, and Azoxy Groups*, Patai, S., Ed. Wiley: New York, 1975; p 28.

16. Lehnert, N.; Wiesler, B. E.; Tuczek, F.; Hennige, A.; Sellmann, D., *J. Am. Chem. Soc.* **1997**, *119*, 8869.

17. Lehnert, N.; Wiesler, B. E.; Tuczek, F.; Hennige, A.; Sellmann, D., *J. Am. Chem. Soc.* **1997**, *119*, 8879.

18. The presence of an additional CT band precluded our ability to obtain strong resonance enhancement, and the NN stretch could hence not be reliably located for **3.3**.

19. Curley, J. J.; Cook, T. R.; Reece, S. Y.; Müller, P.; Cummins, C. C., *J. Am. Chem. Soc.* **2008**, *130*, 9394.

20. The ENDOR response for a ^{15}N nucleus (I = 1/2) in which $A > \nu_n$ is given by the equation $\nu = A/2 \pm \nu_n$. Mims and Davies 35 GHz pulsed ENDOR measurements: Schweiger, A.; Jeschke, G. *Principles of Pulse Electron Paramagnetic Resonance*; Oxford University Press: Oxford, UK, 2001.

21. Tierney, D. L.; Huang, H.; Martásek, P.; Roman, L. J.; Silverman, R. B.; Hoffman, B. M., *J. Am. Chem. Soc.* **2000**, *122*, 7869.

22. Carrington, A.; McLachlan, A. D., . *Introduction to Magnetic Resonance*. Harper & Row: Ney York, 1967.

23. Radoń, M.; Broclawik, E.; Pierloot, K., *The Journal of Physical Chemistry B* **2010**, *114*, 1518.

24. Such comparisons are not straightforward because the Fe ions of nitrogenase presumed to bind substrate-derived species form part of the spin-coupled catalytic [Fe7Mo] molybdenum-iron cofactor.

25. Davoust, C. E.; Doan, P. E.; Hoffman, B. M., *Journal of Magnetic Resonance, Series A* **1996**, *119*, 38.

26. WINEPR SimFonia, version 1.25; Bruker Biospin GmbH: Rheinstetten, Germany, 1996.

27. (a) Kinney, R. A.; Hetterscheid, D. G. H.; Hanna, B. S.; Schrock, R. R.; Hoffman, B. M., *Inorg. Chem.* **2010**, *49*, 704; (b) Doan, P. E., *Journal of Magnetic Resonance In Press, Corrected Proof*.

28. (a) Epel, B.; Pöppl, A.; Manikandan, P.; Vega, S.; Goldfarb, D., *Journal of Magnetic Resonance* **2001**, *148*, 388; (b) Morton, J. J. L.; Lees, N. S.; Hoffman, B. M.; Stoll, S., *Journal of Magnetic Resonance* **2008**, *191*, 315; (c) (c) Doan, P.E., *personal communication*.

29. Sheldrick, G. M., *Acta Cryst.* **1990**, *A46*.

30. Sheldrick, G. M., *Acta Cryst.* **2008**, *A64*.

31. Müller, P.; Herbst-Irmer, R.; Spek, A. L.; Schneider, T. R.; Sawaya, M. R., *Crystal Structure Refinement: A Crystallographer's Guide to SHELXL*. Oxford University Press: Oxford, 2006.

32. Spek, A. L., L. PLATON A Multipurpose Crystallographic Tool. Utrecht University: Utrecht, Holland, 2008.

33. Kabsch, W., *J. Appl. Cryst.* **1993**, *26*, 795.

34. Frisch, M. J.; Trucks, G. W.; Schlegel, H. B.; Scuseria, G. E.; Robb, M. A.; Cheeseman, J. R.; Montgomery, J. A.; Vreven, T.; Kudin, K. N.; Burant, J. C.; Millam, J. M.; Iyengar, S. S.; Tomasi, J.; Barone, V.; Mennucci, B.; Cossi, M.; Scalmani, G.; Rega, N.; Petersson, G. A.; Nakatsuji, H.; Hada, M.; Ehara, M.; Toyota, K.; Fukuda, R.; Hasegawa, J.; Ishida, M.; Nakajima, T.; Honda, Y.; Kitao, O.; Nakai, H.; Klene, M.; Li, X.; Knox, J. E.; Hratchian, H. P.; Cross, J. B.; Bakken, V.; Adamo, C.; Jaramillo, J.; Gomperts, R.; Stratmann, R. E.; Yazyev, O.; Austin, A. J.; Cammi, R.; Pomelli, C.; Ochterski, J. W.; Ayala, P. Y.; Morokuma, K.; Voth, G. A.; Salvador, P.; Dannenberg, J. J.; Zakrzewski, V. G.; Dapprich, S.; Daniels, A. D.; Strain, M. C.; Farkas, O.; Malick, D. K.; Rabuck, A. D.; Raghavachari, K.; Foresman, J. B.; Ortiz, J. V.; Cui, Q.; Baboul, A. G.; Clifford, S.; Cioslowski, J.; Stefanov, B. B.; Liu, G.; Liashenko, A.; Piskorz, P.; Komaromi, I.; Martin, R. L.; Fox, D. J.; Keith, T.; Laham, A.; Peng, C. Y.; Nanayakkara, A.; Challacombe, M.; Gill, P. M. W.; Johnson, B.; Chen, W.; Wong, M. W.; Gonzalez, C.; Pople, J. A., Gaussian 03, Revision C.02. 2003.

35. Dennington, R. I.; Keith, T.; Millam, J., GaussView, Version 4.1. Semichem, Inc.: Shawnee Mission, KS, 2007.

36. Treatment of $[PhBP_3]FeCl$ with two equivalents of Na/Hg under a CO atmosphere generates $[PhBP_3]Fe(CO)_2Na(THF)_6$.

Chapter 4: Multiply Bonded Iron Hydrazido(-) Complexes and Oxidation of Iron Hydrazine/Hydrazido(-) Complexes

Abstract

This chapter describes the synthesis and characterization of several low-spin iron(II) complexes that coordinate hydrazine (N_2H_4), hydrazido($N_2H_3^-$), and ammonia. The sterically encumbered tris(di-*meta*-terphenylphosphino)borate ligand, [$PhBP^{mter}_3$] ([$PhBP^R_3$] = $PhB(CH_2PR_2)_3^-$), is introduced to provide access to species that cannot be stabilized with the [$PhBP^{Ph}_3$] ligand. Treatment of [$PhBP^{mter}_3$]FeMe with hydrazine generates the unusual 5-coordinate hydrazido complex [$PhBP^{mter}_3$]Fe(η^2-N_2H_3) (**4.1**), which features an Fe=N π bond. Coordination of an L-type ligand breaks the π bond and generates [$PhBP^{mter}_3$]Fe(L)(η^2-N_2H_3) (L = N_2H_4 (**4.3**) or NH_3 (**4.4**)). In contrast, treatment of [$PhBP^{Ph}_3$]FeMe with hydrazine forms the adduct [$PhBP^{Ph}_3$]Fe(Me)(η^2-N_2H_4) (**4.5**). Complex **4.5** is thermally unstable to methane loss to generate the intermediate [$PhBP^{Ph}_3$]Fe(η^2-N_2H_3) which undergoes bimolecular coupling to produce {[$PhBP^{Ph}_3$]Fe}$_2$(μ-η^1:η^1-N_2H_2)(μ-η^2:η^2-N_2H_2). The oxidation of these hydrazine and hydrazido species is also presented. For example, oxidation of **4.1** or **4.5** with $Pb(OAc)_4$ results in disproportionation of the N_2H_x ligand (x = 3, 4), and formation of [$PhBP^R_3$]Fe(NH_3)(OAc) (R = Ph (**4.8**) and *m*ter(**4.10**)). This reactivity is discussed in the context of earlier studies on related diiron species. Collectively, these findings underscore the rich redox reactivity of N_2H_x ligands when coordinated to [$PhBP^R_3$]Fe subunits.

4.1 Introduction

An area of ongoing research is geared towards elucidating the mechanism by which N_2 is reduced to NH_3 at the FeMo-cofactor of nitrogenase.[1] Recent spectroscopic studies of the enzyme acquired under turnover conditions suggest that N_2 initially coordinates an iron center.[2] Though the mechanism of subsequent N_2 reduction remains unknown, the ability of the cofactor to reduce both diazene and hydrazine implicates that an alternating reduction scheme may be viable.[3] In this mechanistic scenario, the delivery of protons and electrons alternates between the two nitrogen atoms (i.e., $N{\equiv}N \rightarrow HN{=}NH \rightarrow H_2N\text{-}NH_2 \rightarrow 2NH_3$). To corroborate the feasibility of such a mechanistic scheme, model complexes that coordinate N_2H_x ligands are required, so that the spectroscopic signatures and/or reactivity patterns of these species can be studied.

In addition to their proposed role in N_2 reduction, hydrazine (N_2R_4), hydrazido ($N_2R_3^-$) and hydrazido(2-) ($N_2R_2^{2-}$) species have also been invoked as reactive intermediates in several synthetic transformations, including the hydrohydrazination and diamination of alkynes.[4] In light of this, most studies on M(N_2R_3) species feature substituted hydrazido ligands,[5] and only a few feature the parent hydrazido ($N_2H_3^-$) functionality.[6] This scarcity may also in part be due to the different inherent stabilities of complexes that result from coordination of the parent and substituted hydrazido ligands.[7]

During the course of their studies on protonation of tungsten dinitrogen complexes, both Chatt[6a] and Hidai[6b] reported the isolation of terminal W(η^1-N_2H_3) species. This was followed by a Re(η^1-N_2H_3) species isolated by Dilworth and coworkers,[6c] and more recently, an Fe(η^1-N_2H_3) complex from our own group.[6d] Side-on

hydrazido species, M(η^2-N_2H_3), are also uncommon. Schrock and coworkers have prepared a series of high-valent W(η^2-N_2H_3)[6e-g] and Re(η^2-N_2H_3)[6h] species, and the groups of Huttner[6i] and Tyler[6j] have respectively reported the preparation of Co(η^2-N_2H_3) and Fe(η^2-N_2H_3) species.

As part of our group's ongoing efforts to study the multi-electron reactivity of mono- and diiron complexes that feature nitrogenous ligands,[6d,8] we recently turned to hydrazine and hydrazido ligated species of iron. Using the tris(phosphino)borate ligand scaffold (abbreviated as [PhBP$^R_3$], [PhBP$^R_3$] = [PhB(CH_2PR_2)$_3$]$^-$; R = Ph, CH_2Cy), low-spin mono- and diiron complexes were explored. We found that the bridging hydrazine in {[PhBP$^{Ph}_3$]Fe}$_2$(μ-η^1:η^1-N_2H_4)(μ-η^2:η^2-N_2H_2) (**2.3**) undergoes clean oxidation to diazene, generating {[PhBP$^{Ph}_3$]Fe}$_2$(μ-η^1:η^1-N_2H_2)(μ-η^2:η^2-N_2H_2) (**2.6**).[9] In a related system, we found that O_2 effects the transformation of [PhBP$^{Ph}_3$]Fe(CO)(η^2-N_2H_3) (**3.1**) to {[PhBP$^{Ph}_3$]Fe(CO)}$_2$(μ-N_2H_2) (**3.2**).[10] These transformations suggest that the reverse reaction, the reduction of diazene to hydrazine, might be realized at a diiron(II/II) scaffold. Motivated by these results, we wanted to determine if similar transformations could be achieved at a single iron center to form monomeric Fe-(η^1-N_2H_2) or Fe-(η^2-N_2H_2)[6j,11] species. As added impetus to target these complexes, the group of Tyler recently published a computational study that suggested that N_2 reduction to NH_3 at a 6-coordinate iron center likely proceeds via monomeric diazene and hydrazine intermediates.[12]

In this study, we report hydrazine and hydrazido complexes of iron(II). In order to preclude formation of diiron species, a new tris(phosphino)borate ligand scaffold was

developed. The added steric protection of this ligand allowed us to isolate species that are distinct from those obtained using less sterically encumbering ligands, and the characterization of these species is described. The oxidation of these hydrazine and hydrazido species of iron was also canvassed. In contrast to the above-mentioned examples, treatment with oxidizing reagents results in disproportionation of the N_2H_x ligand to afford $Fe(NH_3)$ species.

4.2 Results and Discussion

4.2.1 Synthesis and Characterization of [PhBP$^{mter}_3$]Fe-X Species (X = Cl, Me)

In order to prevent formation of diiron species that feature bridging N_2H_x ligands as discussed above,[9-10] a new, more sterically encumbering [PhBP$^{R}_3$] ligand variant was sought.[8a,8d,13] To achieve vertical bulk above the metal center while keeping the steric congestion about the metal similar to that of the related [PhBP$^{Ph}_3$] ligand, the [PhBP$^{m\text{ter}}_3$] variant was targeted (*m*ter = *meta*-terphenyl). The incorporation of a bulky terphenyl substituent into a ligand scaffold has successfully been used by others to prepare and stabilize monomeric and/or coordinatively unsaturated metal complexes.[13]

The synthesis of the ligand [PhBP$^{m\text{ter}}_3$]Tl is readily achieved following a similar synthetic protocol to that employed for [PhBP$^{Ph}_3$]Tl (Scheme 4.1).[14] The precursor phosphine (*m*-terphenyl)$_2$PMe is prepared in 84 % yield by lithium-halogen exchange of *m*-terphenyl bromide with ^{n}BuLi at -78 ^{o}C, followed by quenching with half an equivalent of $MePCl_2$. Subsequent deprotonation with ^{s}BuLi at – 78 ^{o}C in the presence of TMEDA affords the phosphine carbanion, (*m*-terphenyl)$_2$P(CH_2)Li(TMEDA) in 61 %

yield. Addition of three equivalents of the carbanion to $PhBCl_2$, followed by addition of [Tl][PF_6] gives the desired ligand, [$PhBP^{mter}_3$]Tl, which is isolated as a white powder in 62 % yield (32 % over three steps).[15]

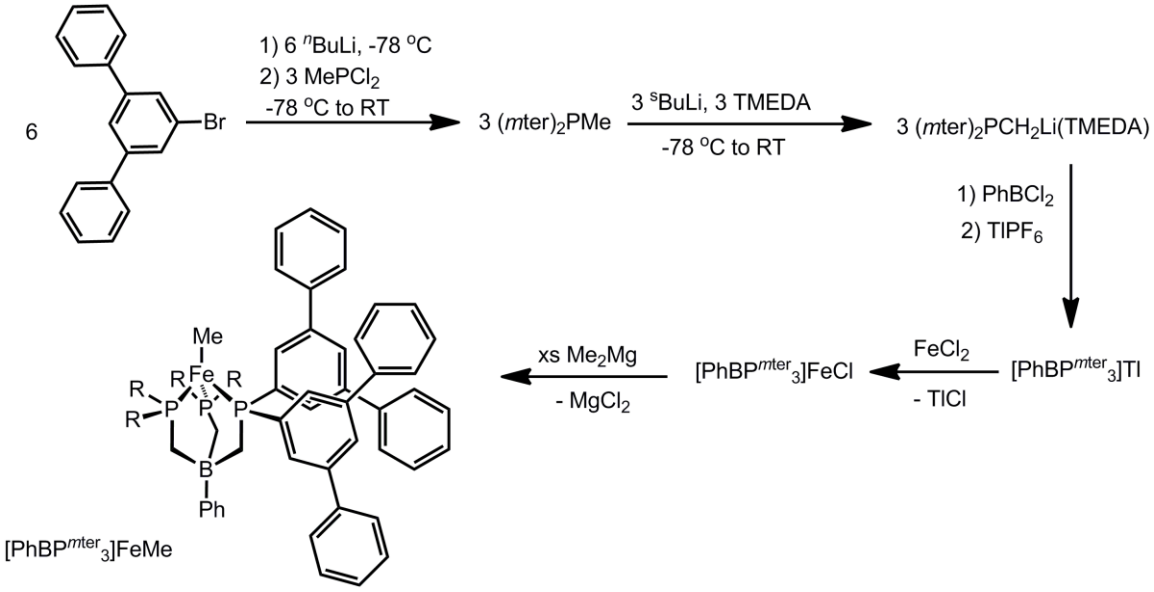

Scheme 4.1.

Likewise, the syntheses of the Fe(II) complexes, [$PhBP^{mter}_3$]FeCl and [$PhBP^{mter}_3$]FeMe, are achieved using similar protocols to those used for the syntheses of [$PhBP^{Ph}_3$]FeCl[8b] and [$PhBP^{Ph}_3$]FeMe[9] (Scheme 4.1). Thus, mixing of [$PhBP^{mter}_3$]Tl with $FeCl_2$ affords yellow and high-spin [$PhBP^{mter}_3$]FeCl, and treatment of [$PhBP^{mter}_3$]FeCl with excess Me_2Mg in benzene results in formation of amber and high-spin [$PhBP^{mter}_3$]FeMe.

The steric and electronic parameters of the [$PhBP^{mter}_3$] ligand were investigated by comparison of the [$PhBP^{R}_3$]FeCl species (R = *m*ter, Ph). The solid-state structure of [$PhBP^{mter}_3$]FeCl was obtained and reveals Fe-P and Fe-Cl bond distances and angles similar to those of [$PhBP^{Ph}_3$]FeCl.[8b] Space-filling representations of the structures of both

[PhBP$^{mter}_3$]FeCl and [PhBP$^{Ph}_3$]FeCl are shown in Figure 4.1. The *m*-terphenyl substituents clearly add vertical protection, as the chlorine atom no longer extends beyond the pocket of the aryl substituents. As the *m*-terphenyl substituents are not locked in a rigid position, the congestion about the iron center is similar in both species. The cyclic voltammogram (CV) of [PhBP$^{mter}_3$]FeCl was also obtained, and features an irreversible reduction at -1.52 V vs. Fc/Fc$^+$ that is very close to the analogous reduction observed in the CV of [PhBP$^{Ph}_3$]FeCl. For comparison, these reductions are ca. 0.4-0.5 V more positive than those for the alkyl substituted complexes, [PhBP$^R_3$]FeCl (R = ^{i}Pr, CH_2Cy).[16] Combined, these studies suggest that the two ligand scaffolds have similar electron-donating capabilities, yet different steric properties. It is anticipated that these differences might result in different reaction pathways or stabilities of iron species.

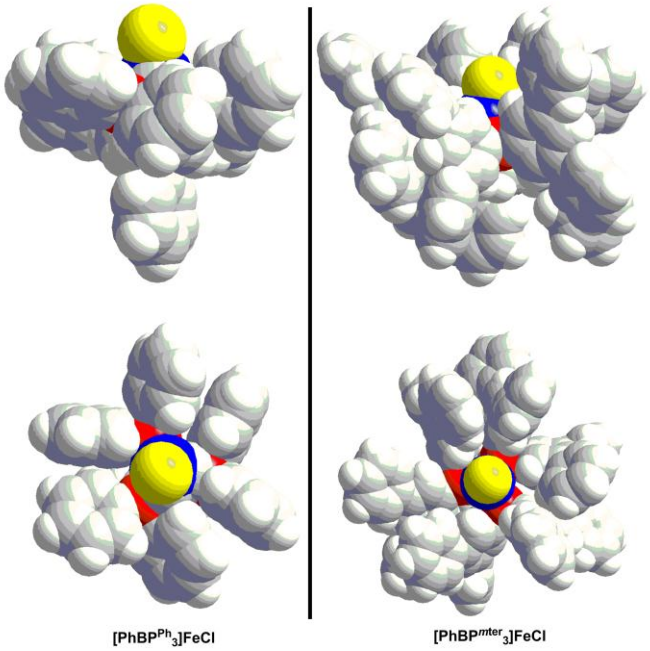

Figure 4.1. Space-filling models of [PhBP$^{Ph}_3$]FeCl (left) and [PhBP$^{mter}_3$]FeCl (right). The representation perpendicular to the B-Fe-Cl vector (top) highlights the added vertical steric

protection that the bulkier [PhBP$^{m\text{ter}}_3$]$^-$ provides, and the representation parallel to the B-Fe-Cl vector (bottom) indicates that the two ligand scaffolds give a similar level of steric congestion about the Fe. Cl atoms are shown in yellow, Fe in blue, P in red, C in grey, H in white, and B in orange.

4.2.2 Synthesis and Characterization of 5-Coordinate and π-Bonded [PhBP$^R_3$]Fe(η^2-$N_2R'_3$) Species

The room temperature addition of one equiv of hydrazine to [PhBP$^{m\text{ter}}_3$]FeMe results in the formation of green and diamagnetic [PhBP$^{m\text{ter}}_3$]Fe-(η^2-N_2H_3), (**4.1**), with concomitant release of methane (Scheme 4.2). When the addition is carried out at -78 ^{o}C, a short-lived red intermediate is observed (*vide infra*). The room temperature NMR spectra of **4.1** display broad peaks that sharpen up upon cooling to -25 ^{o}C, in accordance with it being diamagnetic.

The ^{31}P NMR spectrum of **4.1** (-25 ^{o}C, THF-d_8) features a single resonance at 89.1 ppm. The equivalence of the three phosphines suggests that the iron center in **4.1** is either 4-coordinate and pseudotetrahedral, or 5-coordinate and fluxional. As 4-coordinate [PhBP$^R_3$]Fe^{II}-X species display high-spin S = 2 electronic configurations in the absence of an Fe≡X triple bond linkage,[8b,17] **4.1** is most likely 5-coordinate in solution.

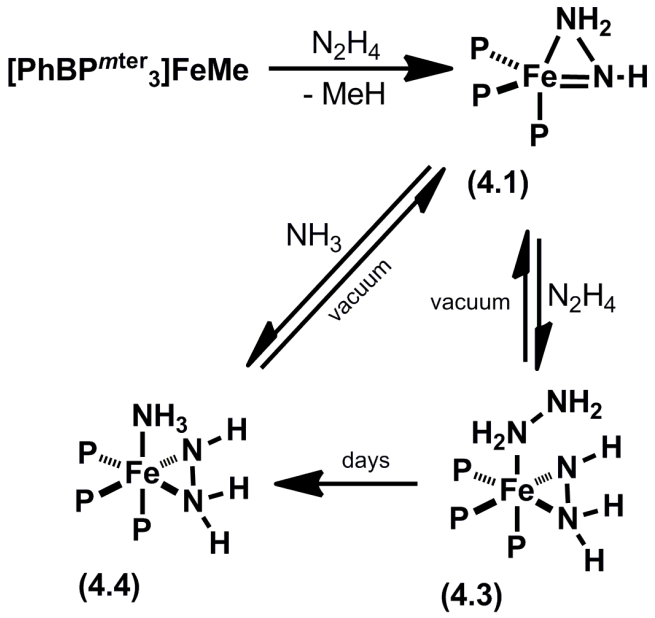

Scheme 4.2.

The ^{1}H NMR spectrum (-25 ^{o}C, THF-d_8) of ^{15}N-**4.1** features broad doublets centered at 6.43 and 3.81 ppm. These peaks integrate to one and two protons (relative to ligand), consistent with the presence of a hydrazido ligand. In the corresponding ^{15}N NMR spectrum (-25 ^{o}C, THF-d_8) of ^{15}N-**4.1**, the *N*H$_2$ nitrogen resonates at -14.5 ppm (dt, $^{1}J_{NH} \approx 83$ Hz, $^{1}J_{NN} \approx 11.3$ Hz), while the *N*H nitrogen resonates at 139.0 ppm (dd, $^{1}J_{NH} \approx 79$ Hz, $^{1}J_{NN} \approx 11.3$ Hz). The $^{3}J_{HH}$ and the $^{2}J_{NH}$ coupling could not be resolved in either the ^{1}H or ^{15}N NMR spectra.

The ^{15}N NMR chemical shifts for Fe(η^2-N$_2$H$_x$) species (x = 2, 3, 4) are summarized in Table 4.1. Most of these species have ^{15}N NMR chemical shifts that are in the range for free hydrazines and amines, and are consistent with sp^3-hybridized nitrogen atoms (Table 4.1).[18] For reference, free hydrazine resonates around 50 ppm, and ammonia resonates at 0 ppm. In the case of hydrazido species, similar chemical shifts are observed for both

types of nitrogen atoms (i.e. *N*H and *N*H_2). These complexes are all 6-coordinate and iron(II), and hence similar coordination shifts associated with each ligand type are anticipated.[18] Thus, the low-field chemical shift for the hydrazido *N*H nitrogen atom of **4.1** is unusual, and suggests a different bonding scenario, in which π bonding between an sp^2-hybridized nitrogen atom and the iron is present. A similar discrepancy between the hydrazido *N*H and *N*H_2 chemical shifts was noted by Schrock and coworkers for $WCp^*Me_3(\eta^2\text{-}N_2H_3)^+$ (*N*H: 241.26 ppm, *N*H_2: 30.97 ppm).[6e] The presence of a π bond in this latter species was further validated by its solid-state structure, which features a *W*-*N*H bond distance of 1.86(1) Å and a *W*-*N*H_2 bond distance of 2.15(1) Å.

Table 4.1. NMR and structural parameters for Fe(η^2-N_2H_x) species (x = 2, 3, 4)

Compound	^{15}N NMR chemical shift (δ)[a]	^{1}H NMR chemical shift (δ)	Fe-N bond distance (Å)	Ref
{*cis*-[Fe(N_2H_4)(dmpe)$_2$]}{BPh_4}$_2$[d]	-11.9	5.39, 4.69	1.981(2), 2.003(2)	[11]
{*cis*-[Fe(N_2H_4)(DMeOPrPE)$_2$]}{BPh_4}$_2$[e]	-19.9[b]	4.8, 3.8	1.993(2), 2.006(2)	[19,6j]
[PhBP$^{Ph}_3$]Fe(Me)(N_2H_4)[f]	17.1	4.33, 3.13	--	this work
{[PhBP$^{Ph}_3$]Fe(NH_3)(N_2H_4)}{PF_6}	--	--	2.006(2), 2.025(3)	this work
{[PhBP$^{Ph}_3$]Fe(CO)(N_2H_4)}{PF_6}	--	5.48, 2.90	1.984(4), 2.005(3)	this work
{*cis*-[Fe(N_2H_3)(DMeOPrPE)$_2$]}{BPh_4}[g]	8.4/6.1 (*N*H)[b,c] -1.4 (*N*H$_2$)[b]	1.05/0.65 (N*H*)[c] 4.23/4.14 (N*H*H)[c] 3.66/3.44 (NH*H*)[c]	--	[6j]
[PhBP$^{mter}_3$]Fe(N_2H_3)[h]	139.0 (*N*H) -14.5 (*N*H$_2$)	6.43 (N*H*) 3.81 (N*H*$_2$)	--	this work
[PhBP$^{mter}_3$]Fe(N_2H_3)(N_2H_4)[i]	40.6 (*N*H) ~ 23 (*N*H$_2$, *N*$_□$H$_2$) 47,4 (*N*$_□$H$_2$)	3.18 (N*H*) 2.52 – 4.66 (NH$_2$)	--	this work
[PhBP$^{mter}_3$]Fe(N_2H_3)(NH_3)[j]	31.8 (*N*H) 26.0 (*N*H$_2$) -18.9 (*N*H$_3$)	1.83 (N*H*) 5.32 (N*H*H) 3.58 (NH*H*) 0.41 (NH$_3$)	2.003(2) (Fe-NH) 2.076(2) (Fe-NH$_2$)	this work
[PhBP$^{Ph}_3$]Fe(CO)($NHNH_2$)[k]	32.2 (*N*H) 31.8 (NH$_2$)	2.85 (N*H*) 1.88 (N*H*H) 6.55 (NH*H*)[l]	1.992(3), 2.018(3)	[10]
[PhBP$^{Ph}_3$]Fe(NHNMe$_2$)	--	4.00	1.788(2) (Fe-NH) 2.058(2) (Fe-NMe$_2$)	this work
cis-[Fe(N_2H_2)(dmpe)$_2$][d]	65.3[b]	2.04	2.016(5), 2.032(7)	[11]
cis-[Fe(N_2H_2)(DMeOPrPE)$_2$][e]	60.8[b]	2.1	--	[6j]

[a]Chemical shifts are referenced to liquid ammonia at 0 ppm. [b]Converted from the nitromethane referencing scale. The chemical shift of nitromethane was taken as 376 ppm relative to liquid ammonia. [c]The two chemical shifts correspond to different isomers. [d]dmpe = 1,2-bis-(dimethylphosphino)ethane. [e]DMeOPrPE = 1,2-bis[(methoxypropyl)phosphino]ethane. [f]NMR collected at -50 ^{o}C. [g]NMR collected at -85 ^{o}C. [h]NMR collected at -25 ^{o}C. [i]NMR collected at -40 ^{o}C. [j]NMR collected at -45 ^{o}C. [k]NMR collected at -75 ^{o}C. [l]Due to H-bonding, the chemical shift of this proton is highly dependent on solvent, concentration, and temperature.

To further address the hybridization of the hydrazido *N*H in **4.1**, the related complex [PhBP$^{Ph}_3$]Fe(η^2-NHNMe$_2$) (**4.2**) was prepared. The synthesis of **4.2** is readily achieved by addition of NH_2NMe_2 to a benzene solution of [PhBP$^{Ph}_3$]FeMe (Scheme 4.3). On the basis of the similarities between the UV-vis spectra and ^{31}P NMR chemical shifts for **4.1** and **4.2**, the coordination mode of the hydrazido ligand is inferred to be the same in both complexes.

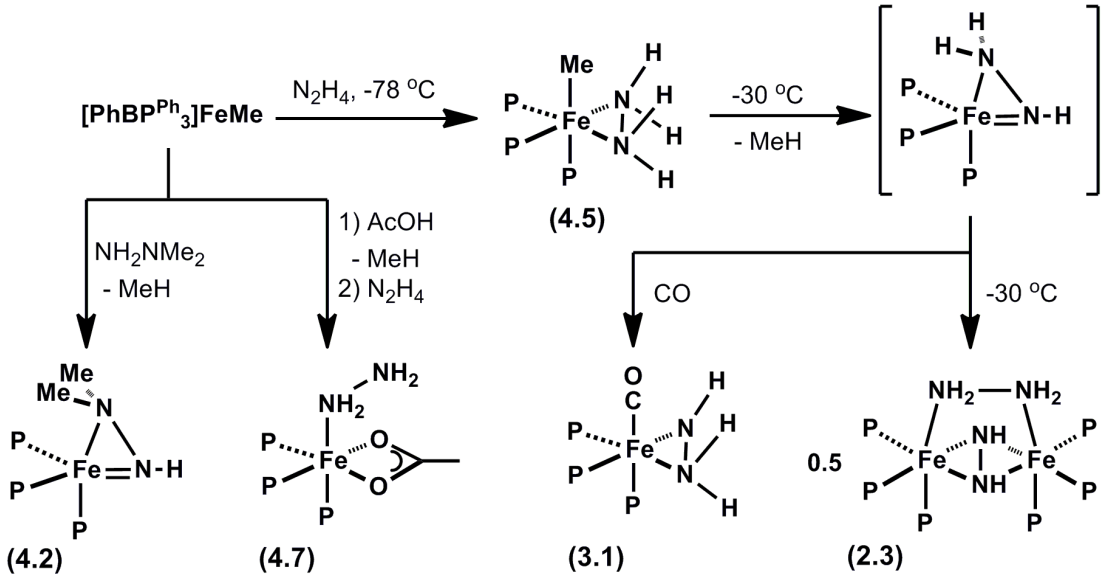

Scheme 4.3.

The solid-state structure of **4.2** was obtained, and is shown in Figure 4.2. The geometry about the Fe center is best described as distorted trigonal bipyramidal, with P1, P3, and N1 comprising the equatorial plane. The sum of the angles about N1 is 352^o, indicating a nearly planar sp^2-hybridized nitrogen atom. The *Fe-N*Me$_2$ distance of 2.058(2) Å is similar to the Fe-N(sp^3) bond distances observed in other hydrazido and hydrazine species of iron (Table 4.1). The *Fe-N*H bond distance of 1.788(2) Å is

significantly shorter, and indicates the presence of a single π bond. For comparison, the bond distance in the low-spin imido species, [PhBP$^{Ph}_3$]Fe(NAr)$^-$, which features a *bona fide* Fe≡N triple bond, is 1.6578(2) Å,[8b] and the bond distance in the high-spin amido species [PhBP$^{Ph}_3$]Fe(NHAr) (Ar = *p*-tolyl) is 1.913(2) Å,[8c] though caution must be taken in comparing the Fe-N bond distances in these species to **4.2**, as the η^2-coorination affects the Fe-N distance relative to η^1-coordination.

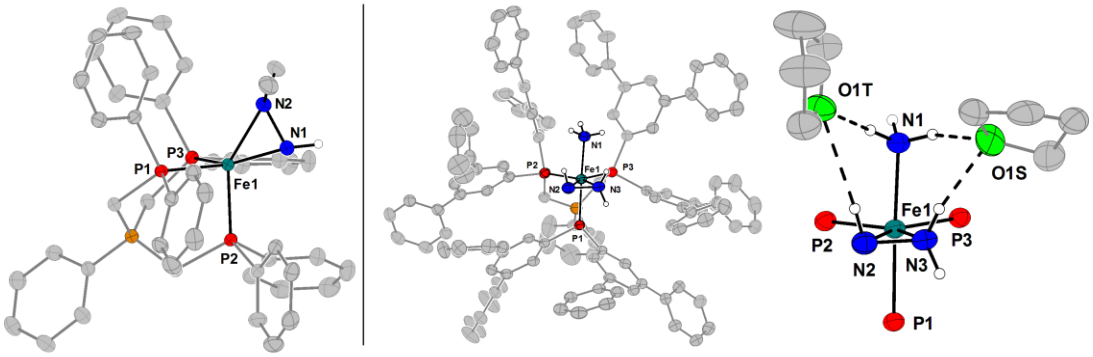

Figure 4.2. Solid-state structure (50% displacement ellipsoids) of **4.2** (left) and **4.4** (right). Most hydrogen atoms, solvent molecules, and minor components of disorder have been removed for clarity. The protons directly coordinated to nitrogen were located in the difference map and are shown. The core atoms of **4.4** are also shown with H-bonded THF molecules. Select bond distances (Å) and angles (deg) for **4.2**: Fe1-N1 1.788(2), Fe1-N2 2.058(2), Fe1-P1 2.2054(6), Fe1-P2 2.1775(6), Fe1-P3 2.1777(6), N1-N2 1.423(2), N1-Fe1-N2 42.72(6), P1-Fe1-P2 90.52(3), P1-Fe1-P3 91.23(2), P2-Fe1-P3 90.09(3), N1-Fe1-P1 139.71(5), N1-Fe1-P2 147.07(4), N1-Fe1-P3 110.92(5), N2-Fe1-P1 113.16(5), N2-Fe1-P2 147.07(4), N2-Fe1-P3 110.92(5). Select bond distances (Å) and angles (deg) for **4.4**: Fe1-N1 2.076(2), Fe1-N2 2.003(2), Fe1-N3 1.968(2), Fe1-P1 2.2188(7), Fe1-P2 2.1964(7), Fe1-P3 2.2173(7), N2-N3 1.418(3), N2-Fe1-N3 67.8(1). Donor acceptor distances (Å) and angles (deg) for hydrogen-bonds: N1-O1T 3.087(3), N1-O1S 3.11(2), N2-O1T 3.471(3), N3-O1S 2.94(2), N1-H1N-O1T 169(2), N1-H2N-O1S 144(2), N2-H4N-O1T 169(3), N3-H6N-O1S 159(3)

Though formation of a π bond in M(η^2-NRNR$_2$) species is typical for early-to-mid transition metal complexes of this type,[4a,5a-c,5e,6e,20] the high d-electron counts for later transition metals usually precludes this coordination mode. As a result, most M(η^2-NRNR$_2$)[6j] and M(η^1-NRNR$_2$)[4d,6d,21] species of the later transition metals feature an sp^3-hybridized hydrazido *N*R atom (*vide infra*). An exception is Huttner's d^7 L$_3$Co(η^2-N$_2$H$_3$)$^+$ species,[6i] which adopts a distorted trigonal bipyramidal geometry akin to that of **4.2** (L$_3$ = MeC(CH$_2$PPh$_2$)$_3$). Like **4.2**, the *Co*-*N*H and *Co*-*N*H$_2$ bond distances are distinct (1.898(11) Å and 1.950(9) Å respectively), albeit the discrepancy is less than in **4.2**. Also, the short M-N bond is in the pseudo-trigonal plane.

4.2.3 Synthesis and Characterization of 6-Coordinate [PhBP$^{mter}_3$]Fe(η^2-N$_2$H$_3$) Species

The open coordination site in **4.1** readily binds L-type ligands. For example, addition of one equivalent of hydrazine produces orange [PhBP$^{mter}_3$]Fe(η^2-N$_2$H$_3$)(η^1-N$_2$H$_4$), (**4.3**) (Scheme 4.2). The hydrazine is labile, and exposure to vacuum or dilution regenerates **1**. The coupled ^{1}H NMR spectrum of ^{15}N-**4.3** (-50 ^{o}C, THF-d_8) displays six distinct NH doublets, ranging from 2.52 to 4.66 ppm, indicating that all but two of the NH$_x$ protons are unique (see Appendix 3). The ^{15}N NMR spectrum of ^{15}N-**4.3** (-50 ^{o}C, THF-d_8) features four resonances between 23 and 48 ppm that are associated with four chemically inequivalent sp^3-hybridized nitrogen atoms. The chemical shift of the hydrazido *N*H is readily assigned by its splitting into a doublet (d, $^1J_{NH} \approx 58$ Hz), and is observed at 40.6 ppm. The assignments of the hydrazido NH$_2$ and hydrazine N$_\alpha$H$_2$ and N$_\beta$H$_2$ nitrogen atoms are less obvious, as three triplets are observed in the ^{15}N NMR

spectrum of ^{15}N-3: one at 47.4 ppm (t, $^{1}J_{NH} \approx 68$ Hz), and two at ca. 23 ppm (overlapping). Select $^{1}H\{^{15}N\}$ decoupling of the resonances at 23 ppm results in collapse of four NH doublets. As the inequivalence of the (η^2-N_2H_3) nitrogen atoms renders the hydrazine $N_\alpha H_2$ protons inequivalent, the resonances at 23 ppm are assigned to the hydrazido NH_2 and the hydrazine $N_\alpha H_2$. In contrast, $^{1}H\{^{15}N\}$ decoupling of the resonance at 47.4 ppm results in collapse of a single NH doublet at 4.66 ppm in the ^{1}H NMR spectrum, indicating identical N*H*H and NH*H* protons. Thus, the peak at 47.4 ppm is assigned to the hydrazine $N_\beta H_2$.

Our attempts to grow crystals of **4.3** resulted in isolation of a related adduct species [PhBP$^{m\text{ter}}_3$]Fe(η^2-N_2H_3)(NH_3) (**4.4**), presumably through disproportionation of the coordinated hydrazine.[22] This species can alternatively be prepared by addition of one atmosphere of ammonia to 1. The ^{15}N NMR spectrum of ^{15}N-**4.4** (-45 ^{o}C, THF-d_8) displays chemical shifts distinct from those of **4.3**, with resonances at 31.8, 26.0, and -18.9 ppm which are assigned to the hydrazido *N*H, the hydrazido NH_2, and the NH_3 nitrogen atoms, respectively.

The solid-state structure of **4.4** is shown in Figure 4.2. Though **4.4** does not pack well, resulting in large solvent channels that affect the overall quality of the dataset, all of the protons directly coordinated to nitrogen atoms were located in the difference map and were refined semi-freely with the aid of distance restraints.[23] The structure clearly establishes the presence of η^2-N_2H_3 and NH_3 ligands coordinating the iron center, with several of the protons engaging in hydrogen bonds to THF solvent molecules that co-crystallize with **4.4**. The *Fe-N*H_3 distance of 2.076(2) Å is consistent with that of other

low-spin Fe-NH_3 complexes.[24] The similar *Fe-N*H and *Fe-N*H_2 distances of 2.003(2) Å and 1.968(2) Å, respectively, are close to those observed in [$PhBP^{Ph}_3$]Fe(CO)(η^2-N_2H_3),[10] and is in contrast to the disparity in bond distances observed in **4.2**. Thus, upon coordination of a ligand, the change in geometry from trigonal bipyramidal to octahedral disrupts the Fe=N π bond in **4.1**.

4.2.4 Synthesis and Characterization of [$PhBP^{Ph}_3$]Fe(η^2-N_2H_4) and [$PhBP^{Ph}_3$]Fe(η^1-N_2H_4) Species

In contrast to the reaction between [$PhBP^{mter}$]FeMe and hydrazine, the room temperature addition of one equivalent of hydrazine to [$PhBP^{Ph}$]FeMe results in quantitative formation of the diiron species {[$PhBP^{Ph}_3$]Fe}$_2$(μ-η^1:η^1-N_2H_4)(μ-η^2:η^2-N_2H_2) (Scheme 4.3).[9] To establish whether this reaction proceeds through an intermediate hydrazido species akin to **4.1**, the reaction between [$PhBP^{Ph}$]FeMe and hydrazine was repeated at -78 ^{o}C. VT NMR studies (see Appendix 3) on this reaction manifold established that at -78 ^{o}C, an initial hydrazine adduct [$PhBP^{Ph}$]Fe(Me)(η^2-N_2H_4) (**4.5**) forms. The ^{1}H NMR spectrum of **4.5** (-50 ^{o}C, THF-d_8) shows a broad singlet at -0.2 ppm corresponding to the Me protons. In addition, two broad singlets at 4.33 and 3.13 ppm are observed that correspond to the hydrazine protons that are cis and trans to the Me group, respectively, as ascertained by a NOESY experiment. These resonances split into broad doublets when **4.5** is prepared with $^{15}N_2H_4$ ($^1J_{NH} \approx$ 77, 75 Hz, respectively). The corresponding ^{15}N NMR spectrum displays a triplet at 17.3 ppm ($^1J_{NH} \approx$ 76 Hz), similar to that of other Fe(η^2-N_2H_4) species (Table 4.1). Consistent with the assignment of **4.5** as

[PhBP^{Ph}]Fe(Me)(η^2-N_2H_4), the ^{31}P NMR spectrum (-50 ^{o}C) of **4.5** shows a triplet (52.5 ppm) that corresponds to the unique phosphine trans to the Me ligand and a broad doublet centered at 79.2 ppm for the phosphines trans to the hydrazine ligand.

The VT NMR profile of **4.5** establishes that this species is stable in solution below -30 ^{o}C. At this temperature, resonances ascribed to methane and {[PhBP$^{Ph}_3$]Fe}$_2$(μ-η^1:η^1-N_2H_4)(μ-η^2:η^2-N_2H_2) begin to grow in. Additionally, the hydrazido species "[PhBP$^{Ph}_3$]Fe(N_2H_3)" appears to be detectable by a single sharp resonance at 84.0 ppm in the ^{31}P NMR spectrum, similar to that of **4.1** and **4.2**. Though this species does not appreciably build up in solution, trapping with CO generates the 6-coordinate species, [PhBP$^{Ph}_3$]Fe(CO)(η^2-N_2H_3) (**3.1**).[10]

The synthesis of thermally stable hydrazine complexes was also sought. Following a similar protocol to that employed by both Tyler[19] and Field,[11] one equivalent of hydrazine was added to a THF solution of [PhBP$^{Ph}_3$]FeCl in the presence of [Tl][PF_6] to generate {[PhBP$^{Ph}_3$]Fe(η^2-N_2H_4)}{X}, (**4.6**) (X = Cl, PF_6) (Scheme 4.4). This reaction is hampered by an equilibrium between [PhBP^{Ph}]FeCl and {[PhBP$^{Ph}_3$]Fe(η^2-N_2H_4)}{Cl}. Addition of excess hydrazine to the equilibrium mixture results in precipitation of an unidentified but presumably iron containing species, and formation of free Ph_2PMe, a byproduct of ligand degradation.[25] Likewise, the addition of excess [Tl][PF_6] results in precipitation of an unidentified but presumably iron containing species, and formation of [PhBP$^{Ph}_3$][Tl]. Similar results were obtained when [Na][BPh_4] was used as the halide abstractor. The hydrazine species 6 could hence not be obtained in analytically pure form, as the chloride and hexafluorophosphate salt co-crystallize. Nonetheless, a structure of

4.6 was obtained (see Appendix 3 for structure). The disorder present was satisfactorily modeled and the structure established connectivity and a 5-coordinate square pyramidal geometry.

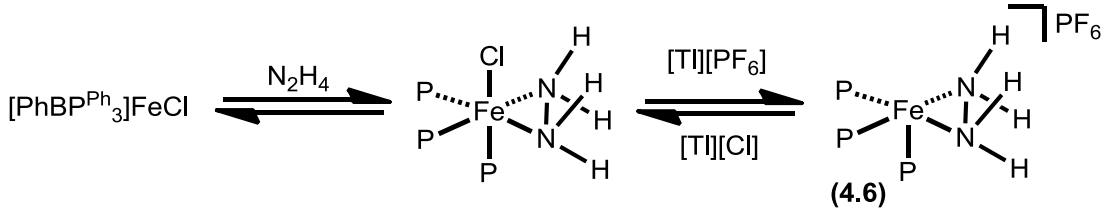

Scheme 4.4.

An end-on coordinated hydrazine species of iron was also targeted. Treatment of [PhBP$^{Ph}_3$]FeMe with one equiv of AcOH, followed by addition of one equiv of hydrazine results in clean formation of [PhBP$^{Ph}_3$]Fe(OAc)(η^1-N_2H_4), (**4.7**). Now, the acetate enforces an end-on coordination of the hydrazine, as shown in the solid-state structure of **4.7** (Figure 4.3). This coordination mode is preserved in solution, and two chemical shifts for the hydrazine $N_\alpha H_2$ and $N_\beta H_2$ nitrogen atoms are respectively noted at 56.2 and 33.3 ppm in the ^{15}N NMR spectrum of ^{15}N-**4.7**.[26] In the corresponding ^{1}H NMR spectrum (-50 ^{o}C, THF-d_8), the $N_\alpha H_2$ protons resonate at 4.61 ppm and the $N_\beta H_2$ protons resonate at 3.94 ppm. As **4.7** has approximate C_s symmetry, the two protons attached to each nitrogen atom are equivalent.

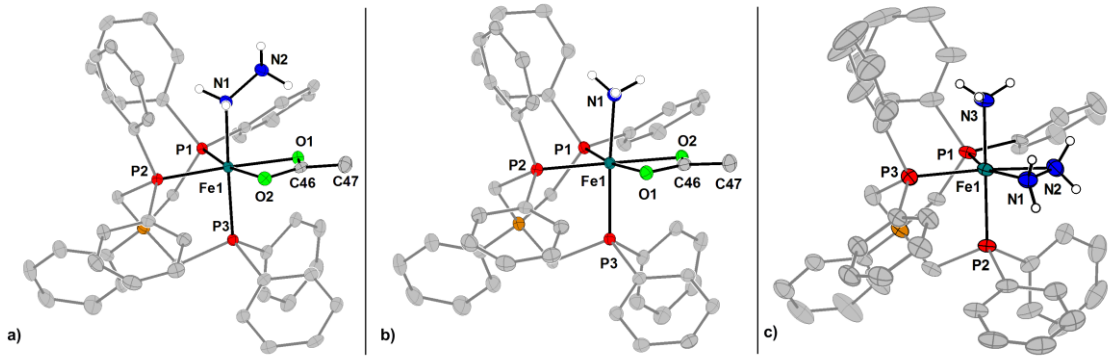

Figure 4.3. Solid-state structure (50% displacement ellipsoids) of **4.7** (a), **4.8** (b), and **4.9** (c). Hydrogen atoms, solvent molecules, minor components of disorder have been removed for clarity, as well as the {PF_6} counteranion of **4.9**. The protons directly coordinated to nitrogen were located in the difference map and are shown. Select bond distances (Å) and angles (deg) for **4.7**: Fe1-N1 2.071(2), N1-N2 1.450(3). Select bond distances (Å) for **4.8**: Fe1-N1 2.064(1). Select bond distances (Å) and angles (deg) for **4.9**: Fe1-N1 2.006(2), Fe1-N2 2.025(3), Fe1-N3 2.076(2), N1-N2 1.451(3), N1-Fe1-N2 42.20(9), N1-Fe1-N3 85.14(9), N2-Fe1-N3 86.3(1)

4.2.5 Exploring the Oxidation of Hydrazine and Hydrazido(-) Species

The instability of free diazene precludes its use as a reagent for the synthesis of M(N_2H_2) species.[27] The oxidation of hydrazine complexes has thus proven to be a valuable route for the generation of 6-coordinate $M_2(\mu\text{-}\eta^1\text{:}\eta^1\text{-}N_2H_2)$ species (M = Fe,[9,28] Ru,[29] Cr,[30] Mn,[31] Cu[32]) and M(η^1-N_2H_2) species (M = W,[33] Re,[34] Ru,[35] Os[35]). The hydrazine species described above may therefore be reasonably expected to serve as precursors to Fe(η^1-N_2H_2) species. However, the present system gives an alternative reaction, in which hydrazine disproportionation ensues and Fe(NH_3) species are instead isolated.

Treatment of the hydrazine adduct **4.5** with $Pb(OAc)_4$ at -78 ^oC (Scheme 4.5) results in a color change from red to purple and formation of $[PhBP^{Ph}_3]Fe(OAc)(NH_3)$, (**4.8**). The identity of **4.8** was readily deduced by NMR spectroscopy (^{15}N: -13.8 ppm, Fe-*N*H_3; ^1H: 2.36 ppm, Fe-N*H*$_3$). Additionally, its solid-state structure was obtained and is depicted in Figure 4.3. Addition of $Pb(OAc)_4$ to either side-on or end-on hydrazine adducts **4.6** or **4.7** likewise generates **4.8**. Thus, oxidation results in disproportionation of the coordinated hydrazine ligand in both η^1-N_2H_4 and η^2-N_2H_4 coordination modes, with loss of an oxidized N_2H_x fragment, presumably N_2 or N_2H_2. When **4.5** is treated with quinone oxidants, for example *para*-benzoquinone or 3,5-di-^{t}Bu-*ortho*-quinone, no nitrogen-containing iron species could be isolated (see Appendix 3).

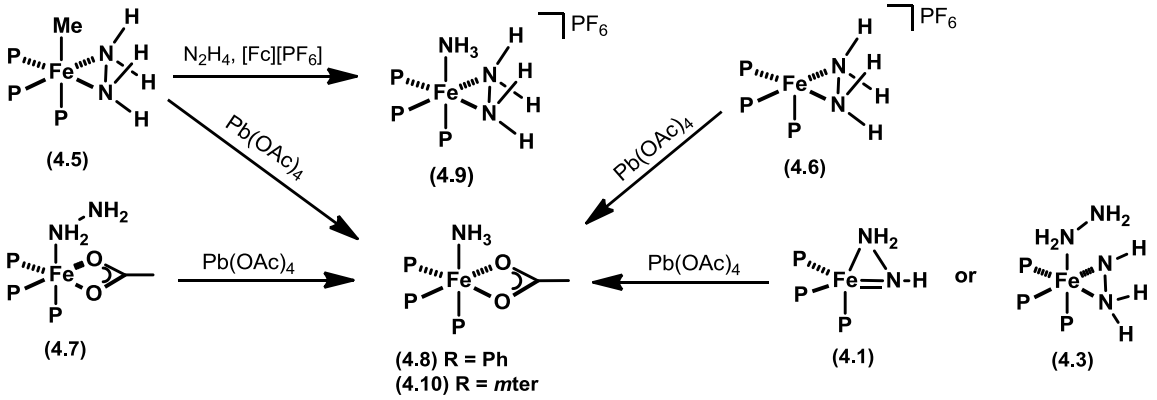

Scheme 4.5.

To establish whether the hydrazine disproportionation in **4.5** results from formal loss of an electron or loss of an H-atom, **4.5** was treated with $[Fc][PF_6]$. Now, addition of $[Fc][PF_6]$ to a THF solution of **4.5** at -78 ^oC gives an ill-defined reaction mixture, though in the presence of an additional equiv of hydrazine, the 6-coordinate ammonia complex $\{[PhBP^{Ph}_3]Fe(NH_3)(\eta^2\text{-}N_2H_4)\}\{(PF_6)\}$ (**4.9**) is cleanly generated (Figure 4.3). These

results suggest that the disproportionation of the bound hydrazine in **4.5** results from oxidation via electron loss, not H-atom loss.

This reactivity pathway contrasts that of {[PhBP$^{Ph}_3$]Fe}$_2$(μ-η^1:η^1-N_2H_4)(μ-η^2:η^2-N_2H_2) (**2.3**), which when treated with $Pb(OAc)_4$ results in oxidation of hydrazine to diazene, and generation of {[PhBP$^{Ph}_3$]Fe}$_2$(μ-η^1:η^1-N_2H_2)(μ-η^2:η^2-N_2H_2) (**2.6**). In this reaction, the oxidation ensues by loss of two H-atoms. When **2.3** is treated with [Fc][PF_6], no net reaction ensues, despite it exhibiting a quasi-reversible oxidation at -0.38 V vs. Fc/Fc^+.[9] As hydrazine disproportionation to generate N_2 (or N_2H_2) and NH_3 likely proceeds through a bimolecular mechanism, the stability of **2.3** towards disproportionation may be attributed to the steric protection afforded by the diiron complex; it is unlikely that two dimers can come together to facilitate this disproportionation reaction.

Examples of parent diazenido species are rare in the literature, and are formed by protonation of a dinitrogen complex.[36] Akin to hydrazine oxidation to diazene, oxidation of hydrazido species could, in principle, give diazenido species. However, treatment of hydrazido **4.1** or **4.3** with one equivalent of $Pb(OAc)_4$ results in a color change to purple and formation of the ammonia complex [PhBP$^{mter}_3$]Fe(OAc)(NH_3), (**4.10**). This species displays similar spectroscopic and structural parameters as that of **4.8** (see Appendix 3). Again, treatment with $Pb(OAc)_4$ results in disproportionation of the N_2H_x ligand. When *para*-benzoquinone is instead used as a potential H-atom abstractor, no nitrogen containing iron species could be isolated (see Appendix 3).

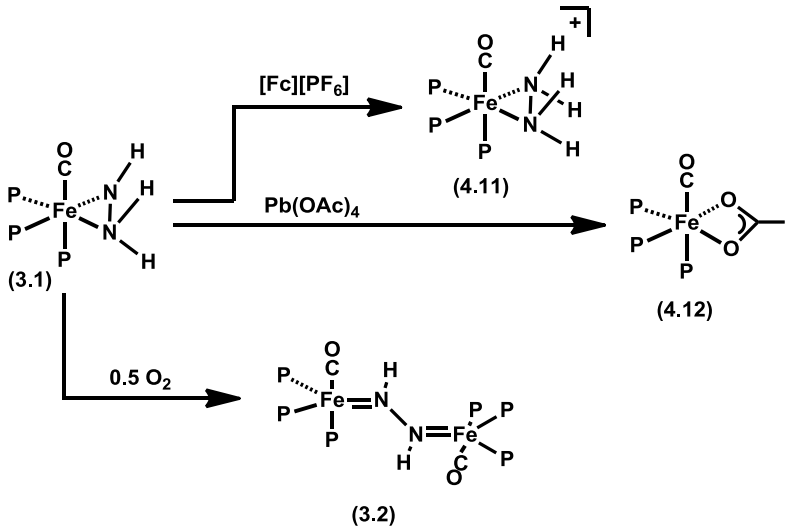

Scheme 4.6.

Finally, the oxidation of [PhBP$^{Ph}_3$]Fe(CO)(η^2-N_2H_3) (**3.1**) was further explored. We recently reported that exposure of **3.1** to 0.5 equiv O_2 forms the diiron species, {[PhBP$^{Ph}_3$]Fe(CO)}$_2$(μ-η^1:η^1-N_2H_2) (**3.2**).[10] The use of O_2 as an oxidant was previously used by Sellman for oxidation of Fe_2(μ-η^1:η^1-N_2H_4) species to Fe_2(μ-η^1:η^1-N_2H_2).[28] Treatment of **3.1** with [Fc][PF_6] gives the hydrazine complex {[PhBP$^{Ph}_3$]Fe(CO)(η^2-N_2H_4)}{PF_6}, (**4.11**). This transformation likely proceeds via an intermediate [PhBP$^{Ph}_3$]Fe(CO)(η^2-N_2H_3)$^{\bullet+}$ species that abstracts an H-atom from solvent. In contrast, the reaction between **3.1** and $Pb(OAc)_4$ results in formation of [PhBP$^{Ph}_3$]Fe(CO)(OAc), (**4.12**). This reactivity contrasts that observed between hydrazido species **4.1** or **4.3** and $Pb(OAc)_4$, and may be due to the presence of the carbonyl, which might affect the stability of intermediate species.

4.3 Concluding Remarks

With this report, we have extended our study of the chemistry of hydrazine and hydrazido coordinated iron(II) complexes to include low-spin monomeric species. The coordination chemistry of $N_2H_3^-$ remains relatively scarce, with most examples involving high-valent early metals for both parent and substituted hydrazido ligands. Here we showed that in a 6-coordinate metal environment, the hydrazido ligand acts as an L_2-type ligand, with the lone-pair of the sp^3-hybridized NH nitrogen atom not engaging in π bonding interactions with the metal. In contrast, in a 5-coordinate environment the iron adopts a trigonal bipyramidal geometry that allows for formation of a π bond between the Fe center and an sp^2-hybridized NH nitrogen atom. This latter coordination mode of $N_2R_3^-$ was previously not known for iron and is rare for late transition metals. In the absence of structural data, the coordination mode is readily discernable by ^{15}N NMR spectroscopy; a downfield shift is observed for the sp^2-hybridized nitrogen relative to the NH_2 nitrogen atom, whereas similar chemical shifts are observed when both nitrogen atoms are sp^3-hybridized.

Oxidation of the monomeric hydrazine complexes invariably results in disproportionation, and we isolate ammonia complexes of iron. These results contrast the reactivity that we previously described for a diiron species, whereby oxidation occurs via formal loss of two H-atoms to generate a diazene species. Similarly, the oxidation of the hydrazido species **4.1** or **4.3** also resulted in isolation of an ammonia species. Finally, the oxidation of **3.1** by O_2 generates a diiron diazene species, whilst the oxidation of **3.1** by

[Fc][PF_6] gave the cationic hydrazine species **3.11**. Collectively, these oxidation reactions highlight the diverse redox reactions of N_2H_x ligands.

4.4 Experimental Section

4.4.1 General Considerations

All manipulations were carried out using standard Schlenk or glove-box techniques under a dinitrogen atmosphere. Unless otherwise noted, solvents were deoxygenated and dried by sparging with Ar followed by passage through an activated alumina column from S.G. Water (Nashua, N.H.). Non-halogenated solvents were tested with a standard purple solution of benzophenone ketyl in THF to confirm effective oxygen and moisture removal. Deuterated solvents were purchased from Cambridge Isotopes Laboratories, Inc. and were degassed and stored over activated 3-Å molecular sieves prior to use. Elemental analyses were performed by Midwest Microlab, Indianapolis, IN. In certain instances, the coordinated N_xH_y ligand proved too labile to obtain satisfactory EA analysis.

4.4.2 NMR and IR Spectroscopy

Both Varian 300 MHz and 500 MHz spectrometers were used to record the ^{1}H NMR and ^{31}P NMR spectra at ambient temperature, and either a Varian 400 MHz or 500 MHz spectrometer was used to record ^{15}N NMR spectra and all VT- NMR spectra. ^{1}H NMR chemical shifts were referenced to residual solvent, and ^{31}P NMR chemical shifts were referenced to 85% H_3PO_4 at δ 0 ppm. All ^{15}N NMR spectra were externally

referenced to neat $H_3CC^{15}N$ (δ = 245 ppm) in comparison to liquid NH_3 (δ = 0 ppm). Select decoupling experiments were used to correlate ^1H and ^{15}N NMR chemical shifts. IR measurements were obtained with a KBr solution cell or a KBr pellet using a Bio-Rad Excalibur FTS 3000 spectrometer controlled by Varian Resolutions Pro software set at 4 cm^{-1} resolution. Solution magnetic moments were measured using Evans method.[37]

4.4.3 X-Ray Crystallography Procedures

X-ray quality crystals were grown as indicated in the experimental procedures per individual complex. The crystals were mounted on a glass fiber with paratone N oil, and data were collected on a Siemens or Bruker Platform three-circle diffractometer coupled to a Bruker-AXS Smart Apex CCD detector with graphite-monochromated Mo or Cu Kα radiation (λ = 0.71073 or 1.54178 Å, respectively), performing φ-and ω-scans. The structures were solved by direct or Patterson methods using SHELXS[38] and refined against F^2 on all data by full-matrix least squares with SHELXL-97.[39] All non-hydrogen atoms were refined anisotropically. All hydrogen atoms (except hydrogen atoms on nitrogen) were included into the model at geometrically calculated positions and refined using a riding model. The isotropic displacement parameters of all hydrogen atoms were fixed to 1.2 times the U value of the atoms they are linked to (1.5 times for methyl groups). Hydrogen atoms directly coordinated to nitrogen were located in the Fourier difference map, and refined semi-freely with the aid of distance restraints. If these hydrogen atoms could not be located in the difference map, they were left out of the final refinement model.

Some of the structures reported suffered from disorder in parts of the [$PhBP^{R}_{3}$] ligand, and the disorder was modeled over two positions. Similarity restraints on 1,2 and 1-3 distances were applied where possible. Similar ADP and rigid bond restraints were applied to all atoms. In addition, several of the structures had solvent disorder, which was modeled as 2 or more component disorder. In some instances, discrete solvent molecules were disordered over several positions, and were modeled using the SUMP command. In other instances, several molecules of solvent were disordered over several positions. In order to determine the total number of solvent molecules, different free variables were assigned to each partially occupied solvent molecule, and the structure refined. The sum of the free variables was then restrained using the SUMP command to whatever value was obtained without the restraint. Some of the crystals were comprised of two or three different species that co-crystallized. {[$PhBP^{Ph}_{3}$]Fe(N_2H_4)}{PF_6} (**4.6**), co-crystallized with {[$PhBP^{Ph}_{3}$]Fe(N_2H_4)(Cl) and [$PhBP^{Ph}_{3}$]FeCl. With the aid of free variables, it was determined that there was a 3% impurity of [$PhBP^{Ph}_{3}$]FeCl and 20% {[$PhBP^{Ph}_{3}$]Fe(N_2H_4)(Cl). [$PhBP^{mter}_{3}$]FeCl co-crystallized with [$PhBP^{mter}_{3}$]Tl (3%). This was modeled with the aid of a free variable (part 1: Fe, Cl, part 2: Tl). All close contacts, both inter and intramolecular, involve at least one partner from a minor component of a disorder. Specific details concerning the refinement of each structure is included in the .cif file.

4.4.4 Starting Materials and Reagents

[PhBP$^{Ph}_3$Fe]Me (**2.1**),[16] **3.1**,[17] $^{15}NH_2{}^{15}NH_2$,[11a] *meta*-terphenyl,[47] and Me_2Mg[48] were prepared according to literature methods. $Pb(OAc)_4$ was purchased from Aldrich (99.999+%), purified as described in the literature,[49] and recrystallized from cold THF to afford a white crystalline solid. Acetic acid was dried according to literature methods.[49] All other reagents were purchased from commercial vendors and used without further purification.

4.4.5 Synthesis of Complexes

Synthesis of MeP(*m*-terphenyl)$_2$. Terphenyl bromide (8.909 g, 28.81 mmol) was dissolved in 75 mL THF and chilled at -78 °C. ^{n}BuLi (1.6 M in hexanes, 28.8 mmol) was added dropwise over 15 min, and the reaction was stirred cold for 1 h. In the meantime, $MePCl_2$ (1.736 g, 14.4 mmol) was diluted in 15 mL toluene and chilled at -78 °C. After 1 h, the phosphine was added dropwise over 10 min to the reaction, which was then stirred for 15 h, slowly warming to RT. The reaction solution was concentrated *in vacuo*. The resulting residue was washed profusely with petroleum ether, giving cream-colored solids, which were extracted into benzene, filtered through a Celite-lined frit, and lyophilized to afford the desired phosphine (5.765 g, 84% yield). ^{1}H NMR (C_6D_6, 300 MHz): δ 7.92 (d, J = 6.9 Hz, 4H), 7.73 (s, 2H), 7.46 (d, J = 6.9 Hz, 8H), 7.18 – 7.11 (m, 12H), 1.56 (d, $^2J_{H\text{-}P}$ = 3.6 Hz, 3H, CH_3P). ^{31}P NMR (C_6D_6, 121 MHz): δ -24.2 ppm.

Synthesis of (*m*-terphenyl)$_2$PCH$_2$Li(TMEDA). In a 125 mL Erlenmeyer flask with a stir bar, MeP(*m*-terphenyl)$_2$ (3.7379 g, 7.405 mmol) and TMEDA (1.05 mL, 7.41 mmol) was dissolved in 30 ml of a 2:1 mixture of THF:Et$_2$O and chilled to -78 °C. ^{s}BuLi (1.4 M in cyclohexane, 8.15 mmol) was added dropwise to the reaction over 10 minutes. The reaction was stirred for 12 h during which it warmed to room temperature. The resulting red/brown solution was concentrated *in vacuo* and the resulting solids were triturated with Et$_2$O to afford yellow solids which were collected on a frit, and rinsed with Et$_2$O and pentane. (2.7826 g, 61% yield). ^{1}H NMR (THF-d_8, 300 MHz): δ 7.92 (d, J = 6.9 Hz, 4H), 7.63 (d, J = 6.9 Hz, 8H), 7.50 (s, 2H), 7.35 (t, J = 6.9 Hz, 8H), 7.23 (t, J = 6.9 Hz, 4H), 2.30 (4H), 2.15 (12H), -0.14 (d, $^2J_{H\text{-}P}$ = 3.3 Hz, 2H). ^{31}P NMR (THF, 121 MHz): δ -4.08 ppm.

Synthesis of [PhBP$^{m\text{ter}}_3$]Tl. In a vial, (*m*-terphenyl)$_2$PCH$_2$Li(TMEDA) (365.0 mg, 608.6 μmol) was dissolved in 10 mL Et$_2$O and then chilled to -90 °C**.** PhBCl$_2$ (33.2 mg, 202.8 μmol) was diluted in 3 mL toluene and added drop wise to the solution. The reaction was stirred for 18 h, slowly warming to RT to give [PhBP$^{ter}_3$]Li(tmeda) (^{31}P NMR: -10.4 ppm). The reaction was concentrated under reduced pressure to dryness and then suspended in 10 mL EtOH. TlPF$_6$ (61.1 mg, 202.8 mmol) was added, and the reaction was stirred for 12 h. The white solids in the reaction were collected on a frit and washed with EtOH and petroleum ether (237.1 mg, 62% yield). ^{1}H NMR (C$_6$D$_6$, 500 MHz): δ 8.65 (br d, J = 6.0 Hz, 2H), 7.88 – 7.85 (m, 13H), 7.68 (t, J = 6.0 Hz, 2H), 7.16 – 7.13 (overlaps with solvent peak, ~18H), 7.00 – 6.99 (overlapping s, 48H), 2.77 (br, 6H). ^{31}P

NMR (C_6D_6, 121 MHz): δ 21.7 ppm (d, $^1J_{TlP}$ = 4870 Hz). Anal. Calcd. for $C_{117}H_{89}BP_3Tl$: C 77.93; H 4.98; N 0. Found: C ; H ; N .

Synthesis of [PhBP$^{m\text{ter}}_3$]FeCl. [PhBP$^{m\text{ter}}_3$]Tl (0.473 g, 0.262 mmol) and $FeCl_2$ (0.034 g, 0.262 mmol) were stirred in 8 mL THF for 12 h. The reaction was filtered through Celite and concentrated under reduced pressure to dryness. The yellow residue was mashed to a fine powder and washed with petroleum ether and Et_2O (0.369 g, 83%). Single crystals suitable for X-ray diffraction were grown from vapor diffusion of petroleum ether into a benzene solution. ^{1}H NMR (C_6D_6, 300 MHz): δ 206.1 (s), 40.9 (s), 19.8 (s), 18.4 (s), 7.1 (s), 6.9 (s), 3.6 (s), -14.3 (s), -37.3 (s)**.** Evans Method (C_6D_6): 5.32 B.M. Anal. Calcd. for $C_{117}H_{89}BClFeP_3$: C 83.15; H 5.31; N 0. Found: C 83.09; H 5.41; N none found.

Synthesis of [PhBP$^{m\text{ter}}_3$]FeMe. A solution of [PhBP$^{m\text{ter}}_3$]FeCl (0.2096 g, 0.141 mmol) in 15 mL benzene was added to a stirring slurry of Me_2Mg (0.0186g, 0.342 mmol) in 2 mL benzene. After stirring for an hour, the reaction was filtered through a Celite-lined frit, and the solution was lyophilized to dryness. The residue was extracted into 20 mL benzene, filtered through a Celite-lined frit, and again lyophilized to yield analytically pure [PhBP$^{m\text{ter}}_3$]FeMe (0.1629 g, 78.8 %). ^{1}H NMR (C_6D_6, 300 MHz): δ 46.1 (s), 22.0 (s), 20.3 (s), 6.8 (s), 6.6 (s), 1.7 (s), -13.5 (s), -49.8 (s). Evans Method (C_6D_6): 4.9 B.M. UV-vis (C_6H_6) λ_{max}, nm (ε, M^{-1} cm^{-1}): 405 (1750), 370 (2300). Anal. Calcd. for $C_{118}H_{92}BFeP_3$: C 84.88; H 5.55. Found: C 84.67; H 5.62.

Synthesis of [PhBP$^{Ph}_3$]Fe(OAc). Neat acetic acid (29.5 μL, 0.515 mmol) was added to a solution of [PhBP$^{Ph}_3$]FeMe (**2.1**) (0.3892 g, 0.515 mmol) in 18 mL THF. After stirring for 24 h, the volatiles were removed to afford analytically pure material. Crystals suitable for XRD were grown from benzene/pentane. ^{1}H NMR (C_6D_6, 300 MHz): δ 171 (bs), 130.0 (s), 30.1 (s), 16.0 (s), 14.8 (s), -7.1 (s), -26.4 (s). Evans Method (C_6D_6): 4.6 B.M. Anal. Calcd. for $C_{47}H_{44}BFeO_2P_3$: C 70.52; H 5.74; N 0. Found: C 71.85; H 5.74; N 0.

Synthesis of [PhBP$^{mter}_3$]Fe(η^2-N$_2$H$_3$), 4.1. [PhBP$^{mter}_3$]FeMe (0.0318 g, 0.0217 mmol) was dissolved in 2 mL of THF, and a solution of hydrazine (0.77 μL, 0.0217 mmol) in 1 mL THF was added dropwise. The stirring reaction immediately changed color from yellow to green, and **1** was quantitatively formed. Micro-crystals of **4.1** were grown by slow evaporation of pentane into a THF solution (16.1 mg, 50.0 %). Complex **4.1** displays broad NMR spectra at all temperatures, -25 ^{o}C was found to give the sharpest spectra. ^{1}H NMR (THF-d_8, 500 MHz, -25 ^{o}C): δ 6.75−8.20 (bm, 83H), 6.43 (s, 1H, NH), 3.81 (s, 2H, NH_2). 1.79 (m, 6H, CH_2, overlapping with THF). ^{31}P NMR (THF-d_8, 202.3 MHz, -25 ^{o}C): δ 89.1. IR (KBr) (cm^{-1}): 3301, 3174. UV-vis (THF) λ_{max}, nm (ε, M^{-1} cm^{-1}): 348 (sh, 4900), 420 (sh, 1600), 605 (625), 708 (500). Anal. Calcd. for $C_{117}H_{92}BFeN_2P_3$: C 83.36; H 5.50; N 1.66. Found: C 82.97; H 5.76; N 1.55.

A sample of 95% ^{15}N-enriched **4.1** was synthesized using an analogous synthetic procedure with $^{15}NH_2{}^{15}NH_2$. ^{1}H NMR (THF-d_8, 500 MHz, -25 ^{o}C): δ 6.43 (d, $^1J_{NH} \approx$ 78

Hz, 1H, NH), 3.81 (d, $^1J_{NH} \approx 83$ Hz, 2H, NH_2). ^{15}N NMR (THF-d_8, 50.7 MHz, -25 ^{o}C): δ 139.0 (dd, $^1J_{NH} \approx 78.6$ Hz, $^1J_{NN} \approx 11.3$ Hz), -14.5 (dt, $^1J_{NH} \approx 83$ Hz, $^1J_{NN} \approx 11.3$ Hz).

Synthesis of [PhBP$^{Ph}_3$]Fe(η^2-NHNMe$_2$), 4.2. Neat NH_2NMe_2 (28.2 μL, 0.363 mmol) was added to a stirring solution of [PhBP$^{Ph}_3$]FeMe (0.2495 g, 0.3299 mmol) in 10 mL benzene. The reaction was heated to 50 ^{o}C for 48 h, during which time the color changed from yellow to green. The volatiles were removed to afford a green solid (0.2356 g, 89.5 %). Crystals suitable for XRD were grown from the slow evaporation of pentane into a saturated benzene solution of **4.2**. ^{1}H NMR (C_6D_6, 300 MHz): δ 8.13 (d, 2H, *J* = 6 Hz), 7.64 (t, 2H, *J* = 6 Hz), 7.40 (t, 1H, *J* = 6 Hz), 7.31 (bs, 12H), 6.88 (t, 6H, *J* = 7 Hz), 6.76 (t, 12H, *J* = 7 Hz), 4.00 (s, 1H, NH), 2.16 (s, 6H, NMe_2), 1.63 (bs, 6H, CH_2). ^{31}P NMR (C_6D_6, 121.4 MHz): δ 79.9. IR (KBr) (cm^{-1}): 3234. UV-vis (THF) λ_{max}, nm (ε, M^{-1} cm^{-1}): 300 (sh, 8450), 340 (sh, 4400), 440 (700), 600 (466), 742 (320). Anal. Calcd. for $C_{47}H_{48}BFeN_2P_3$: C 70.52; H 6.04; N 3.50. Found: C 69.97; H 6.14; N 3.18.

Synthesis of [PhBP$^{mter}_3$]Fe(η^2-N$_2$H$_3$)(η^1-N$_2$H$_4$), 4.3. [PhBP$^{mter}_3$]FeMe (0.0269 g, 0.0184 mmol) was dissolved in 2 mL of THF, and a solution of hydrazine (3.00 μL, 0.0918 mmol) in 1 mL THF was added dropwise. The stirring reaction immediately changed color from yellow to green to red, and **4.3** was formed. Micro-crystals of **4.3** can be grown by evaporation of pentane into a THF solution containing **4.3** and excess hydrazine (11.4 mg, 36.2 %). The coordinated hydrazine is labile, and exposure of **4.3** to vacuum results in formation of **4.3**. ^{1}H NMR (THF-d_8, 500 MHz, -40 ^{o}C): δ 9.90 (s, 1H),

8.38 (m, 6H), 6.7-8.1 (m, 76H), 4.92 (s, 1H, NH_2 or $N_\alpha H_2$), 4.66 (s, 2H, $N_\beta H_2$), 3.18 (s, 1H, NH_2 or $N_\alpha H_2$), 2.91 (s, 1H, NH_2 or $N_\alpha H_2$), 2.72 (s, 1H, NH), 2.52 (s, 1H, NH_2 or $N_\alpha H_2$), 2.18 (m, 2H, CH_2), 1.20 (m, 4H, CH_2). ^{31}P NMR (THF-d_8, 202.3 MHz, -40 ^{o}C): δ 76.45 (d, 1P, J = 39.7 Hz), 73.25 (bs, 1P), 59.58 (d, 1P, J = 66.2 Hz). The ^{31}P coupling was ill-defined at all temperatures scanned. IR (KBr) (cm^{-1}): 3305, 3170. UV-vis (THF, with 20 equiv N_2H_4) λ_{max}, nm (ε, M^{-1} cm^{-1}): 383 (2600, sh), 512 (1280). EA was performed on crystals of **3** (grown from THF/pentane) that were dried under an N_2 atmosphere for 20 min prior to sealing in an ampule, and it thus is likely that THF or pentane is still present in the crystals. Anal. Calcd. for $C_{117}H_{96}BFeN_4P_3$: C 81.77; H 5.63; N 3.26. Anal. Calcd. for [PhBP$^{m\text{ter}}_3$]Fe(η^2-N_2H_3)(η^1-N_2H_4).5THF, $C_{137}H_{136}BFeN_4P_3O_5$: C 79.18; H 6.60; N 2.70 Found: C 78.95; H 6.16; N 3.09.

A sample of 95% ^{15}N-enriched **4.3** was synthesized using an analogous synthetic procedure with $^{15}NH_2{}^{15}NH_2$. ^{1}H NMR (THF-d_8, 500 MHz, -40 ^{o}C): δ 4.92 (d, $^1J_{NH}$ ≈ 80 Hz 1H, NH_2 or $N_\alpha H_2$), 4.66 (d, $^1J_{NH}$ ≈ 65 Hz, 2H, $N_\beta H_2$), 3.18 (d, $^1J_{NH}$ ≈ 75 Hz 1H, NH_2 or $N_\alpha H_2$), 2.91 (d, $^1J_{NH}$ ≈ 75 Hz, 1H, NH_2 or $N_\alpha H_2$), 2.72 (d, $^1J_{NH}$ ≈ 60 Hz, 1H, NH), 2.52 (d, $^1J_{NH}$ ≈ 80 Hz, 1H, NH_2 or $N_\alpha H_2$). ^{15}N NMR (THF-d_8, 50.7 MHz, -40 ^{o}C): δ 47.4 (t, $N_\beta H_2$, $^1J_{NH}$ ≈ 68 Hz), 40.6 (d, NH, $^1J_{NH}$ ≈ 58 Hz), 23.5 (t, NH_2 or $N_\alpha H_2$, $^1J_{NH}$ ≈ 75 Hz), 22.7 (t, NH_2 or $N_\alpha H_2$, $^1J_{NH}$ ≈ 70 Hz). Select ^{1}H{^{15}N} decoupling was employed to confirm the HN connectivity.

Synthesis of [PhBP$^{mter}_3$]Fe(η^2-N_2H_3)(NH_3), 4.4. A solution of **4.1** (0.0150 g, 0.00890 mmol) in 1 mL THF was transferred to a 15 mL Shlenk tube, and evacuated. One atm of NH_3 was added, and the solution immediately turned red. Slow evaporation of pentane into a THF solution of **4.4** afforded crystalline material (0.0122 g, 80.5 %). Exposure of either solutions of **4.4** or crystals of **4.4** to vacuum resulted in formation of **4.1**. Upon removal of solvent, crystals of **4.4** rapidly changed color to green. ^{1}H NMR (THF- d_8, 400 MHz, -45 ^{o}C): δ 10.3 (s, 1H), 8.66 (s, 1H), 8.53 (s, 1H), 8.22 (s, 2H), 8.08 (s, 2H), 6.5-8.1 (m, 76H), 5.32 (s, 1H), 3.58 (s, 1H, overlapping with THF), 2.6 (s, 2H), 2.2 (s, 2H), 1.83 (s, 1H, overlapping with solvent), 1.5 (s, 2H), 0.41 (s, 3H, overlapping with residual NH_3). ^{31}P NMR (THF-d_8, 162 MHz, -45 ^{o}C): δ 81.1 (d, 1P, J = 47.7 Hz), 66.2 (d, 1P, J = 66.7 Hz), 52.3 (m, 1P). The ^{31}P coupling was ill-defined at all temperatures scanned (20 ^{o}C to -70 ^{o}C). IR (KBr) (cm^{-1}): 3245, 3198. UV-vis (THF, under 1 atm NH_3) λ_{max}, nm (ε, M^{-1} cm^{-1}): 400 (2900, sh), 516 (1460).

A sample of 95% ^{15}N-enriched **4.4** was synthesized using an analogous synthetic procedure with $^{15}NH_2{}^{15}NH_2$. ^{1}H NMR THF-d_8, 400 MHz, -45 ^{o}C): δ 5.32 (d, $^1J_{NH} \approx 82$ Hz, 1H, N*H*H), 3.58 (d, 1H, NH*H*), 1.83 (1H, N*H*), 0.41 (d, $^1J_{NH} \approx 60$ Hz, 3H, NH_3). gHMQC ^{15}N{^{1}H} NMR (THF-d_8, 40.5 MHz, -45 ^{o}C): δ 31.8 (*N*H), 26.0 (*N*H_2), -18.9 (*N*H_3). Select ^{1}H{^{15}N} decoupling was employed to confirm the HN connectivity.

Synthesis of [PhBP$^{Ph}_3$]Fe(Me)(η^2-N_2H_4), 4.5. [PhBPPh3]FeMe (0.0343 g, 0.0391 mmol) was dissolved in 500 μL THF, and stirred at -78 ^{o}C. To this, a solution of

hydrazine (1.27 μL, 0.0391 mmol) dissolved in 280 μL of THF was added dropwise, resulting in a color change from yellow to strawberry red and conversion to **4.5**. ^{1}H NMR (THF-d_8, 500 MHz, -50 ^{o}C): δ 7.56 (bs, 7H), 7.27 (m, 2H), 7.19 (m, 4H), 7.12 (m, 2H), 6.97 (m, 4H), 6.89 (bs, 8H), 6.74 (m, 8H), 4.33 (s, 2H, NH_{cis}H), 3.13 (s, 2H, NHH_{trans}), 1.30 (m, 6H, CH_2), -0.2 (s, 3H, Me). NOESY was employed to assign the hydrazine protons that are *cis* and *trans* to the methyl ligand. ^{31}P NMR (THF- d_8, 202.3 MHz, -50 ^{o}C): δ 79.18 (d, 2P, J = 28.4 Hz), 52.50 (t, 1P, J = 32.1 Hz). The doublet is broad and not well-resolved. UV-vis (THF, -78 ^{o}C) λ_{max}, nm (ε, M^{-1} cm^{-1}): 524 (940). IR (THF/KBr, -78 ^{o}C) (cm^{-1}): 3302, 3246, 3161.

A sample of 95% ^{15}N-enriched **4.5** was synthesized using an analogous synthetic procedure with $^{15}NH_2{}^{15}NH_2$. ^{1}H NMR (THF-d_8, 500 MHz, -50 ^{o}C): δ 4.31 (d, $^{1}J_{NH}$ ≈ 77 Hz, 1.5H, NH_{cis}H), 3.12 (d, $^{1}J_{NH}$ ≈ 75 Hz, 1.5H, NHH_{trans}). ^{15}N NMR (THF-d_8, 50.7 MHz, -50 ^{o}C): δ 17.1 (t, $^{1}J_{NH}$ ≈ 71 Hz, 2N). IR (THF/KBr, -78 ^{o}C) (cm^{-1}): 3312, 3251, 3223.

Synthesis of {[PhBP$^{Ph}_3$]Fe(η^2-N_2H_4)}{PF_6}, 4.6. To a solution of PhBP$^{Ph}_3$FeCl (0.6023 g, 0.775 mmol) in 20 mL THF was added neat hydrazine (37.7 μL, 1.16 mmol) and solid $TlPF_6$ (0.2764 g, 0.775 mmol). After stirring for 24 h, hydrazine was again added (12.2 μL, 0.39 mmol), and the reaction stirred an additional 24 h. The solution was filtered through Celite, and the volatiles removed. The solid was extracted into DME, filtered through a Celite-lined frit, and the volatiles removed to give 0.6739 g of a pink solid (95

%). Crystals suitable for X-ray diffraction were grown from a THF/pentane solution. ^{1}H NMR (THF-d_8, 500 MHz, -20 ^{o}C): δ 7.8 (m, 3H), 7.58 (d, J = 7.50 Hz, 2H), 7.44 (m, 3H), 7.38 (m, 3H), 7.19 (m, 5H), 7.12 (t, J = 7.54 Hz, 4H), 7.08 (t, J = 6.70, 2H), 7.00 (m, 5H), 6.83 (t, J = 7.54 Hz, 4H), 6.78 (J = 7.54 Hz, 4H), 4.78 (bs, NH_2, 2H), 4.31 (bs, NH_2, 2H), 1.30 (d, CH_2, $^{1}J_{CP}$ = 15.0 Hz, 6H). ^{31}P NMR (THF-d_8, 202.3 MHz, -20 ^{o}C): δ 66.0 (d, J = 59.3 Hz, 2P), 58.9 (t, J = 59.3 Hz, 1P), -138.6 (m, 1P). IR (KBr) (cm^{-1}): 3335, 3281, 3143. UV-vis (THF) λ_{max}, nm (ε, M^{-1} cm^{-1}): 420 (250), 525 (675). Crystals of **6** invariable contained both {[PhBP$^{Ph}_3$]Fe(η^2-N_2H_4)}{PF_6} and {[PhBP$^{Ph}_3$]Fe(η^2-N_2H_4)}{Cl}, precluding our ability to obtain analytically pure material.

Synthesis of [PhBP$^{Ph}_3$]Fe(η^1-N_2H_4)(OAc), 4.7. Neat anhydrous hydrazine (10.2 μL, 0.3159 mmol) was added to a 2 mL THF solution of [PhBP$^{Ph}_3$]Fe(OAc) (0.2529 g, 0.3159 mmol). An immediate color change from pale yellow to purple was noted. After stirring for 24 h, the reaction was filtered and solid **4.7** was rinsed with THF and pentane to afford analytically pure material (0.1920 g, 73 %). Crystals suitable for diffraction were grown by layering a saturated benzene solution of **4.7** with pentane. ^{1}H NMR (THF-d_8, 500 MHz, -50 ^{o}C): δ 6.5-8.0 (m, 35H), 4.61 (bs, NH_2, 2H), 3.94 (bs, NH_2, 2H), 1.5-1.8 (m, 3H, overlapping with THF), 1.5-1.8 (m, 6H) ^{31}P NMR (THF-d_8, 202.3 MHz, -50 ^{o}C): δ 59.1 (bs, 2P), 50.5 (t, J = 57.0 Hz, 1P). IR (KBr) (cm^{-1}): 3378, 3313, 1464. Anal. Calcd. for $C_{47}H_{48}BFeP_3N_2O_2$: C 67.81; H 5.81; N 3.36. Found: C 67.43; H 5.62; N 3.06.

A sample of 95% ^{15}N-enriched **4.7** was synthesized using an analogous synthetic procedure with $^{15}NH_2{}^{15}NH_2$. ^{1}H NMR (THF-d_8, 500 MHz, -50 ^{o}C): δ 4.61 (d, $^1J_{NH}$ = 70 Hz, 2H, $N_\alpha H_2$), 3.94 (d, $^1J_{NH}$ = 67 Hz, 2H, $N_\beta H_2$). ^{15}N NMR (THF-d_8, 50.7 MHz, -50 ^{o}C): δ 56.2 (t, $^1J_{NH}$ = 67 Hz, 1N, $N_\beta H_2$), 33.3 (t, $^1J_{NH}$ = 68 Hz, 1N, $N_\alpha H_2$). ^{1}H{^{15}N} experiments with selective decoupling were used to correlate the ^{1}H and ^{15}N NMR chemical shifts. IR (KBr) (cm^{-1}): 3367, 3300, 3274.

Synthesis of [PhBP$^{Ph}_3$]Fe(NH$_3$)(OAc), 4.8. A suspension of Pb(OAc)$_4$ (0.0161 g, 0.0360 mmol) in 1 mL THF was added dropwise to a stirring solution of **4.6** (36.0 mg, 0.036 mmol) in 2 mL THF. The reaction gradually changed color from pink to purple, as Pb(OAc)$_2$ precipitated out. The volatiles were removed, and the solid residue was extracted into benzene, and filtered through a Celite-lined frit. The solution was lyophilized, extracted into benzene, and again filtered through a Celite-lined frit. Crystals were grown by layering pentane over the benzene solution (10.3 mg, 35.5 %). Complex **4.8** is sparingly soluble and crystals of **4.8** are invariably covered with a white film, presumably Pb(OAc)$_2$.

Complex **4.8** can alternatively be prepared by addition of 1 atmosphere of NH$_3$ to a solution of [PhBP$^{Ph}_3$]Fe(OAc) (0.0284 g, 0.0355 mmol) in 4 mL of benzene (in an evacuated 50 mL Schlenk-tube). After stirring for 5 minutes, the solution was degassed, filtered through Celite, and layered with pentane to afford crystalline material (0.0211 g, 72.7 %).

^{1}H NMR (THF-d_8, 500 MHz, -40 ^{o}C): δ 7.75 (bs, 5H), 7.51 (d, J = 6.9 Hz, 4H), 7.38 (m, 5H), 7.24 (m, 3H), 6.9-7.2 (m, 15H), 6.83 (m, 3H), 2.36 (s, 3H, NH_3), 0.95-1.40 (m, 9H, CH_2/OAc). ^{31}P NMR (d_8-THF, 202.3 MHz, -40 ^{o}C) δ 61.5 (bs, 2P), 46.9 (t, J = 58.6 Hz, 1P). IR (KBr) (cm^{-1}): 3362, 3334, 1466. UV-vis (THF) λ_{max}, nm (ε, M^{-1} cm^{-1}): 580 (855). Crystals of **8** were exposed to minimal vacuum prior to sealing in an ampule/combustion analysis. Anal. Calcd. for $C_{47}H_{47}BFeP_3NO_2$: C 69.05; H 5.80; N 1.71. Anal. Calcd. for [PhBP$^{Ph}_3$]Fe(NH_3)(OAc).C_6H_6, $C_{53}H_{53}BFeP_3NO_2$: C 71.10; H 5.96; N 1.56. Found: C 70.70; H 6.06; N 1.50.

A sample of 95% ^{15}N-enriched **4.8** was synthesized following the alternative procedure, using $^{15}NH_3$. ^{1}H NMR (THF-d_8, 400 MHz, -30 ^{o}C): δ 2.36 (d, $^{1}J_{NH}$ = 67 Hz, 3H, NH_3). HSQC ^{15}N{^{1}H} NMR (THF-d_8, 40.5 MHz, -30 ^{o}C): δ -13.8. ^{31}P NMR (THF-d_8, 161.8 MHz, -40 ^{o}C): δ 61.5 (bs, 2P), 46.9 (dt, $^{1}J_{PP}$ ≈ 58.6 Hz, $^{1}J_{NP}$ ≈ 10 Hz, 1P). IR (KBr) (cm^{-1}): 3354, 3327, 1466.

Synthesis of {[PhBP$^{Ph}_3$]Fe(η^2-N_2H_4)(NH_3)}{PF_6}, 4.9. A solution of [PhBP$^{Ph}_3$]FeMe (0.2181 g, 0.2883 mmol) in 15 mL THF was cooled to -41 ^{o}C and set stirring. To this, a solution of hydrazine (18.7 μL, 0.5767 mmol) in 1 mL THF was added dropwise over the course of 5 min. A suspension of $FcPF_6$ (0.0954 g, 0.2883 mmol) in 4 mL THF was added dropwise, and the reaction was stirred for 1 h at -41 ^{o}C, and was then warmed to RT and stirred an additional 12 h. Volatiles were removed from the reaction mixture, and the pink residue was rinsed with 15 mL of pentane, followed by 10 mL of diethyl ether.

Extraction of the remaining solid into THF, followed by layering with pentane, afforded crystals of **4.9** (0.1887 g, 70.0 %). ^{1}H NMR (THF-d_8, 300 MHz): δ 6.5-8.5 (m, 35H), 5.5 (bs, NH_2, 2H), 4.2 (bs, NH_2, 2H), 2.7 (bs, NH_3, 3H), 1.37 (m, CH_2, 6H) ^{31}P NMR (THF-d_8, 300 MHz): δ 60.8 (bs, 2P), 53.5 (bs, 1P), -143.3 (m, 1P). IR (KBr) (cm^{-1}): 3334, 3260. UV-vis (THF) λ_{max}, nm (ε, M^{-1} cm^{-1}): 537 (750). Anal. Calcd. for $C_{45}H_{48}BFeN_3P_4F_6$: C 57.78; H 5.17; N 4.49. Found: C 57.85; H 5.25; N 4.29.

Synthesis of [PhBP$^{m\text{ter}}_3$]Fe(NH$_3$)(OAc), 4.10. Hydrazine (6.4 μL, 0.020 mmol) was added to a stirring solution of [PhBP$^{m\text{ter}}_3$]FeMe (0.1439 g, 0.0982mmol) in 5 mL THF. After stirring for 10 min, a suspension of $Pb(OAc)_4$ (0.0871 g, 0.0196 mmol) in 5 mL THF was added dropwise, and the solution stirred for 12 h. The volatiles were removed, and the resulting residue was rinsed with pentane and extracted into DME. The resulting solution was layered with pentane to yield crystalline **4.10** (0.0803 g, 53.6 %). The bulk crystals contained a white precipitate, presumably $Pb(OAc)_2$.

Complex **4.10** can alternatively be prepared from [PhBP$^{m\text{ter}}_3$]FeMe. One equivalent of AcOH (2.4 μL, 0.041 mmol) was added to a solution of [PhBP$^{m\text{ter}}_3$]FeMe (0.0686 g, 0.0411 mmol) in 2 mL benzene. After stirring for 10 min, the reaction was transferred to a 5 mL Schlenk tube which was evacuated. One atmosphere of NH_3 was added to the Schlenk tube, and after stirring for 1 h, the reaction was degassed, the solution filtered through Celite, and layered with pentane to afford crystalline material (0.0444 g, 62.4 %).

^{1}H NMR (THF-d_8, 400 MHz, -30 ^{o}C): δ 8.7 (bs, 6H), 7.6-8.4 (m, 7H), 6.8-8.4(m, 70H), 3.05 (bs, NH_3, 3H), 1.5-2.0 (m, 6H, overlap with THF), 1.29 (s, 3H, OAc). ^{31}P NMR (THF-d_8, 161.8 MHz, -30^{o}C): δ 60.7 (bs, 2P), 50.1 (t, J = 59.4 Hz, 1P), -143.3 (m, 1P). IR (KBr) (cm^{-1}): 3365, 1450. UV-vis (THF) λ_{max}, nm (ε, M^{-1} cm^{-1}): 557 (580). Anal. Calcd. for $C_{123}H_{95}BFeNO_2P_3$: C 85.36; H 5.53; N 0.81. Found: C 81.20; H 6.02; N 0.87.

A sample of 95% ^{15}N-enriched **4.10** was synthesized using the alternative synthesis using $^{15}NH_3$. ^{1}H NMR (THF-d_8, 400 MHz, -30 ^{o}C): δ 3.05 (d, $^{1}J_{NH}$ = 67 Hz, 3H, NH_3). HSQC ^{15}N{^{1}H} NMR (THF-d_8, 40.5 MHz, -30 ^{o}C): δ -12.7. IR (KBr) (cm^{-1}): 3308, 3302.

Synthesis of {[PhBP$^{Ph}_3$]Fe(η^2-N$_2$H$_4$)(CO)}{PF$_6$}, 3.11. A suspension of FcPF$_6$ (15.0 mg, 0.0455 mmol) in 1 mL benzene was added dropwise to a stirring solution of **3.1** (36.4 mg, 0.0455 mmol) in 2 mL benzene. The reaction stirred for 24 h, during which a color change from orange to red ensued. The reaction mixture was lyophilized, and the resulting solids were rinsed with pentane and diethyl ether. The remaining solids were extracted into THF, filtered, and layered with pentane, yielding analytically pure crystals suitable for XRD (18.2 mg, 42.3 %). ^{1}H NMR (C_6D_6, 300 MHz): δ 8.03 (bs, 2H), 7.66 (bs, 5H), 7.41 (bs, 5H), 7.03 (bs, 8H), 6.5-6.8 (m, 15H). ^{31}P NMR (C_6D_6, 300 MHz) δ 50.22 (d, $^{1}J_{PP}$ = 63.6 Hz, 2P), 36.00 (t, $^{1}J_{PP}$ = 63.6 Hz, 1P), -142.7 (m, 1P). IR (KBr) (cm^{-1}): 3332, 3276, 3253, 1986. Anal. Calcd. for $C_{46}H_{45}BFeN_2OP_4F_6$: C 58.35; H 4.79; N 2.96. Found: C 58.56; H 5.02; N 2.60.

Synthesis of [PhBP$^{Ph}_3$]Fe(OAc)(CO), 4.12. A suspension of $Pb(OAc)_4$ in 1 mL THF (13.5 mg, 0.0305 mmol) was added dropwise to a stirring solution of **3.1** (24.4 mg, 0.0305 mmol) in 2 mL THF. An immediate color change from orange to green was noted, and after stirring for an additional 12 h, the volatiles were removed to yield a green residue. The solids were rinsed with pentane, extracted into benzene, filtered, and lyophilized. The green powder was then taken up in THF and layered with pentane to yield crystalline material suitable for XRD (12.0 mg, 47.5 %). ^{1}H NMR (C_6D_6, 300 MHz): δ 8.13 (d, *J* = 6.8 Hz, 2H), 7.77 (bs, 4 H), 7.69 (t, *J* = 7.3 Hz, 2H), 7.42 (bs, 6H), 7.31 (t, *J* = 8.4 Hz, 4H), 6.99 (bs, 6H), 6.90 (bs, 4H), 6.82 (bs, 4H), 6.73 (t, *J* = 7.0 Hz, 3H), 2.1 – 2.3 (m, 4H), 1.76 (bs, 2H), 1.47 (s, 3H). ^{31}P NMR (121 MHz, C_6D_6) δ 48.58 (d, *J* = 66.3 Hz, 2P), 29.81 (t, *J* = 66.4 Hz, 1P). IR (KBr) (cm^{-1}): 1976, 1469.

Acknowledgements:

Dr. Connie C. Lu is acknowledged for preliminary results (complete synthesis and characterization of [PhBP$^{m\text{ter}}_3$][Tl] and all of the precursors), and Dr. David VanderVelde, and Dr. Jeff Simpson are acknowledged for insightful discussions regarding the NMR spectroscopy of the compounds.

Works Cited:

1. (a) Hoffman, B. M.; Dean, D. R.; Seefeldt, L. C., *Acc. Chem. Res.* **2009**, *42*, 609; (b) Howard, J. B.; Rees, D. C., *Proc. Natl. Acad. Sci. U.S.A.* **2006**, *103*, 17088; (c) Dance, I., *Dalton Trans.* **2010**, *39*, 2972; (d) Kästner, J.; Blöchl, P. E., *J. Am. Chem. Soc.* **2007**, *129*, 2998; (e) Hinnemann, B.; Nørskov, J. K., *J. Am. Chem. Soc.* **2004**, *126*, 3920; (f) Crossland, J. L.; Tyler, D. R., *Coord. Chem. Rev.* **2010**, *254*, 1883.

2. (a) Barney, B. M.; Lukoyanov, D.; Igarashi, R. Y.; Laryukhin, M.; Yang, T. C.; Dean, D. R.; Hoffman, B. M.; Seefeldt, L. C., *Biochemistry* **2009**, *48*, 9094; (b) Barney, B. M.; Yang, T.-C.; Igarashi, R. Y.; Dos Santos, P. C.; Laryukhin, M.; Lee, H.-I.; Hoffman, B. M.; Dean, D. R.; Seefeldt, L. C., *J. Am. Chem. Soc.* **2005**, *127*, 14960; (c) Barney, B. M.; Laryukhin, M.; Igarashi, R. Y.; Lee, H.-I.; Dos Santos, P. C.; Yang, T.-C.; Hoffman, B. M.; Dean, D. R.; Seefeldt, L. C., *Biochemistry* **2005**, *44*, 8030.

3. (a) Barney, B. M.; McClead, J.; Lukoyanov, D.; Laryukhin, M.; Yang, T. C.; Dean, D. R.; Hoffman, B. M.; Seefeldt, L. C., *Biochemistry* **2007**, *46*, 6784; (b) Barney, B. M.; Lukoyanov, D.; Yang, T. C.; Dean, D. R.; Hoffman, B. M.; Seefeldt, L. C., *Proc. Natl. Acad. Sci. U.S.A.* **2006**, *103*, 17113; (c) Danyal, K.; Inglet, B. S.; Vincent, K. A.; Barney, B. M.; Hoffman, B. M.; Armstrong, F. A.; Dean, D. R.; Seefeldt, L. C., *J. Am. Chem. Soc.* **2010**, *132*, 13197.

4. (a) Li, Y.; Shi, Y.; Odom, A. L., *J. Am. Chem. Soc.* **2004**, *126*, 1794; (b) Hoover, J. M.; DiPasquale, A.; Mayer, J. M.; Michael, F. E., *J. Am. Chem. Soc.* **2010**, *132*, 5043; (c) Herrmann, H.; Lloret Fillol, J.; Wadepohl, H.; Gade, L. H., *Angew. Chem. Int. Ed.* **2007**, *46*, 8426; (d) Huang, Z.; Zhou, J.; Hartwig, J. F., *J. Am. Chem. Soc.* **2010**, *132*, 11458.

5. (a) Herrmann, H.; Wadepohl, H.; Gade, L. H., *Dalton Trans.* **2008**, 2111; (b) Cowie, M.; Gauthier, M. D., *Inorg. Chem.* **1980**, *19*, 3142; (c) Latham, I. A.; Leigh, G. J.; Huttner, G.; Jibril, I., *J. Chem. Soc., Dalton Trans.* **1986**, 385; (d) Carroll, J. A.; Sutton, D., *Inorg. Chem.* **1980**, *19*, 3137; (e) Dilworth, J. R.; Henderson, R. A.; Dahlstrom, P.; Nicholson, T.; Zubieta, J. A., *J. Chem. Soc., Dalton Trans.* **1987**, 529.

6. (a) Vale, M. G.; Schrock, R. R., *Inorg. Chem.* **1993**, *32*, 2767; (b) Shaver, M. P.; Fryzuk, M. D., *J. Am. Chem. Soc.* **2005**, *127*, 500.

7. Chatt, J.; Pearman, A. J.; Richards, R. L., *J. Chem. Soc., Dalton Trans.* **1977**, 2139.

8. Takahashi, T.; Mizobe, Y.; Sato, M.; Uchida, Y.; Hidai, M., *J. Am. Chem. Soc.* **1979**, *101*, 3405.

9. Dilworth, J. R.; Lewis, J. S.; Miller, J. R.; Zheng, Y., *J. Chem. Soc., Dalton Trans.* **1995**, 1357.

10. Lee, Y. H.; Mankad, N. P.; Peters, J. C., *Nature Chemistry* **2010**, *2*, 558.

11. (a) Schrock, R. R.; Liu, A. H.; O'Regan, M. B.; Finch, W. C.; Payack, J. F., *Inorg. Chem.* **1988**, *27*, 3574; (b) Cai, S.; Schrock, R. R., *Inorg. Chem.* **1991**, *30*, 4105; (c) Schrock, R. R.; Glassman, T. E.; Vale, M. G.; Kol, M., *J. Am. Chem. Soc.* **1993**, *115*, 1760.

12. Vale, M. G.; Schrock, R. R., *Organometallics* **1991**, *10*, 1661.

13. Vogel, S.; Barth, A.; Huttner, G.; Klein, T.; Zsolnai, L.; Kremer, R., *Angew. Chem., Int. Ed. Engl.* **1991**, *30*, 303.

14. Crossland, J. L.; Balesdent, C. G.; Tyler, D. R., *Dalton Trans.* **2009**, 4420.

15. (a) Betley, T. A.; Peters, J. C., *J. Am. Chem. Soc.* **2004**, *126*, 6252; (b) Brown, S. D.; Betley, T. A.; Peters, J. C., *J. Am. Chem. Soc.* **2003**, *125*, 322; (c) Brown, S. D.; Mehn, M. P.; Peters, J. C., *J. Am. Chem. Soc.* **2005**, *127*, 13146; (d) Brown, S. D.; Peters, J. C., *J. Am. Chem. Soc.* **2005**, *127*, 1913; (e) Mankad, N. P.; Whited, M. T.; Peters, J. C., *Angew. Chem. Int. Ed.* **2007**, *46*, 5768; (f) Mehn, M. P.; Peters, J. C., *J. Inorg. Biochem.* **2006**, *100*, 634; (g) Betley, T. A.; Peters, J. C., *J. Am. Chem. Soc.* **2003**, *125*, 10782.

16. Saouma, C. T.; Müller, P.; Peters, J. C., *J. Am. Chem. Soc.* **2009**, *131*, 10358.

17. Saouma, C. T.; Kinney, R. A.; Hoffman, B. M.; Peters, J. C., *manuscript submitted* **2010**.

18. Field, L. D.; Li, H. L.; Dalgarno, S. J.; Turner, P., *Chem. Commun.* **2008**, 1680.

19. Yelle, R. B.; Crossland, J. L.; Szymczak, N. K.; Tyler, D. R., *Inorg. Chem.* **2009**, *48*, 861.

20. Lu, C. C.; Saouma, C. T.; Day, M. W.; Peters, J. C., *J. Am. Chem. Soc.* **2007**, *129*, 4.

21. (a) Peters, J. C.; Feldman, J. D.; Tilley, T. D., *J. Am. Chem. Soc.* **1999**, *121*, 9871; (b) Shapiro, I. R.; Jenkins, D. M.; Thomas, J. C.; Day, M. W.; Peters, J. C., *Chem. Commun.* **2001**, 2152.

22. Lu, C. C. The Chemistry of Tris(phosphino)borate Manganese and Iron Platforms. Caltech, Pasadena, 2006.

23. Betley, T. A.; Peters, J. C., *Inorg. Chem.* **2003**, *42*, 5074.

24. Mason, J., *Chem. Rev.* **1981**, *81*, 205.

25. Crossland, J. L.; Zakharov, L. N.; Tyler, D. R., *Inorg. Chem.* **2007**, *46*, 10476.

26. Sellmann, D.; Kern, W.; Pöhlmann, G.; Knoch, F.; Moll, M., *Inorg. Chim. Acta* **1991**, *185*, 155.

27. Smith, J. M.; Lachicotte, R. J.; Holland, P. L., *J. Am. Chem. Soc.* **2003**, *125*, 15752.

28. B. Hitchcock, P.; L. Hughes, D.; J. Maguire, M.; Marjani, K.; L. Richards, R., *J. Chem. Soc., Dalton Trans.* **1997**, 4747.

29. Müller, P.; Herbst-Irmer, R.; Spek, A. L.; Schneider, T. R.; Sawaya, M. R., *Crystal Structure Refinement: A Crystallographer's Guide to SHELXL*. Oxford University Press: Oxford, 2006.

30. Fox, D. J.; Bergman, R. G., *Organometallics* **2004**, *23*, 1656.

31. (a) Daida, E. J.; Peters, J. C., *Inorg. Chem.* **2004**, *43*, 7474; (b) Lu, C. C.; Peters, J. C., *Inorg. Chem.* **2006**, *45*, 8597.

32. As free hydrazine has a chemical shift of ca. 45 ppm (-80^{o}C, d_8-THF), it is anticipated that a downfield coordination shift will be observed for the nitrogen atom that coordinats the iron.

33. Foner, S. N.; Hudson, R. L., *The Journal of Chemical Physics* **1978**, *68*, 3162.

34. Sellmann, D.; Soglowek, W.; Knoch, F.; Moll, M., *Angew. Chem., Int. Ed. Engl.* **1989**, *28*, 1271.

35. (a) Sellmann, D.; Böhlen, E.; Waeber, M.; Huttner, G.; Zsolnai, L., *Angew. Chem., Int. Ed. Engl.* **1985**, *24*, 981; (b) Collman, J. P.; Hutchison, J. E.; Lopez, M. A.; Guilard, R.; Reed, R. A., *J. Am. Chem. Soc.* **1991**, *113*, 2794.

36. Huttner, G.; Gartzke, W.; Allinger, K., *Angew. Chem., Int. Ed. Engl.* **1974**, *13*, 822.

37. Sellmann, D., *J. Organomet. Chem.* **1972**, *44*, C46.

38. Fujisawa, K.; Lehnert, N.; Ishikawa, Y.; Okamoto, K.-i., *Angew. Chem. Int. Ed.* **2004**, *43*, 4944.

39. Smith, M. R.; Cheng, T. Y.; Hillhouse, G. L., *J. Am. Chem. Soc.* **1993**, *115*, 8638.

40. (a) Cheng, T. Y.; Peters, J. C.; Hillhouse, G. L., *J. Am. Chem. Soc.* **1994**, *116*, 204; (b) Albertin, G.; Antoniutti, S.; Giorgi, Maria T., *Eur. J. Inorg. Chem.* **2003**, *2003*, 2855.

41. Cheng, T.-Y.; Ponce, A.; Hillhouse, G. L.; Rheingold, A. L., *Angew. Chem., Int. Ed. Engl.* **1994**, *33*, 657.

42. We have not been able to stabilize a 4-coordinate ammonia complex. This reaction yielded a major paramagnetic product, which has identical chemical shifts to that obtained when [$PhBPPh_3$]FeMe is treated with [NH_4][PF_6].

43. Yandulov, D. V.; Schrock, R. R., *Can. J. Chem.* **2005**, *83*, 341.

44. Warren, J. J.; Tronic, T. A.; Mayer, J. M., *Chem. Rev.* **2010**, null.

45. Schubert, E. M., *J. Chem. Educ.* **1992**, *69*, 62.

46. (a) Sheldrick, G. M., *Acta Cryst.* **2008**, *A64*; (b) Sheldrick, G. M., *Acta Cryst.* **1990**, *A46*.

47. Du, C. J. F.; Hart, H.; Ng, K. K. D., *The Journal of Organic Chemistry* **1986**, *51*, 3162.

48. Tang, H.; Richey, H. G., *Organometallics* **2001**, *20*, 1569.

49. Armarego, W. L. F.; Chai, C. L. L., *Purification of Laboratory Chemicals*. 5 ed.; Butterworth-Heinmann: London, 2002.

Chapter 5: A Diiron Site Can Support Bridging N_2, N_2H_2, and N_2H_4 Ligands

Abstract

A family of complexes that feature the same auxiliary ligands (i.e., [$PhBP^{CH2Cy}{}_3$]Fe(OAc)), that are all iron(II), and that only differ in the oxidation state of the nitrogenous ligand are presented ([$PhBP^{CH2Cy}{}_3$] = $PhB(CH_2P(CH_2Cy)_2)_3^-$). Thus, {[$PhBP^{CH2Cy}{}_3$]Fe(OAc)}$_2$(μ-N_2), (**5.2**), {[$PhBP^{CH2Cy}{}_3$]Fe(OAc)}$_2$(μ-N_2H_2), (**5.4**), [$PhBP^{CH2Cy}{}_3$] {[$PhBP^{CH2Cy}{}_3$]Fe(OAc)}$_2$(μ-N_2H_4), (**5.3**), and {[$PhBP^{CH2Cy}{}_3$]Fe(OAc)(NH_3), (**5.5**), have all been prepared. These complexes have been thoroughly characterized, and preliminary disproportionation and reduction reactions are described.

5.1 Introduction

Due to its biological and industrial relevance, establishing mechanisms for the reduction of N_2 to NH_3 is a longstanding goal of chemists.[1] Chatt proposed a distal reduction scheme, in which the addition of protons and electrons to a M-N_2 species first reduces the distal nitrogen atom, resulting in ammonia release and generation of a metal nitride species, which is subsequently reduced to ammonia (i.e., M^n-N≡N → M^{n+3}≡N + NH_3 → M^n + NH_3).[2] This mechanism was proposed for group six metals, and has since been corroborated by Schrock and coworkers, who have shown that a single molybdenum center can catalytically reduce N_2 to NH_3.[3] That the reduction occurs by such a mechanism is supported by their isolation and characterization of several of the intermediates in this cycle. A similar reduction scheme has since been proposed for iron-mediated reduction of N_2 to NH_3.[4]

A second reduction scheme, termed alternating, has also been proposed,[5] and Sellmann was an early proponent for such a scheme.[6] In this mechanism, the protons and electrons are delivered in an alternating manner to both of the nitrogen atoms of a M-N_2 or M_2(μ-N_2) species (i.e., M^n-N≡N → M^n-HN=NH → M^n-H_2N-NH_2 → M^n + 2 NH_3). Though this mechanism has not been validated by a well-defined catalyst, support for such a mechanism comes from the observation that diazene (N_2H_2)[7] and hydrazine (N_2H_4)[8] are both substrates for nitrogenase. Additionally, computational studies on both the enzyme active-site[9] and a model iron complex[10] have favored this mechanism.

Driven by these findings, as well as recent studies on the FeMo cofactor that suggest that N_2 reduction occurs at iron,[11] there has been much interest in the preparation and isolation of mono- and diiron species that coordinate N_2H_x (x = 2, 3, 4) ligands,[6b,12]

though species of this type remain relatively rare. Herein we report a family of dimeric iron(II) complexes that coordinate N_2, N_2H_2, and N_2H_4 in a bridging fashion, as well as a monomeric iron species that coordinates NH_3. A key feature within this series of complexes is the invariance of the ancillary ligands, which allows for direct comparisons of members of this family to be made. In addition, this family represents the first iron system that can coordinate N_2, N_2H_2, and N_2H_4.[13,14] The synthesis and spectroscopy of these complexes are discussed, as well as preliminary disproportionation (of the N_2H_x ligand) and redox reactivity.

5.2 Results and Discussion

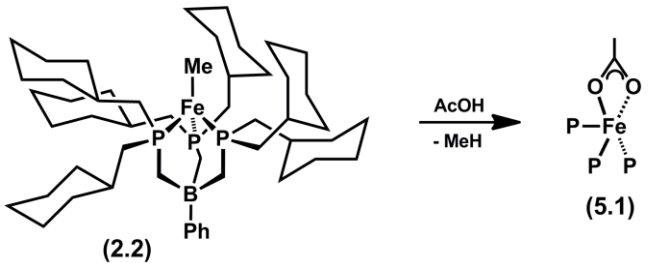

Scheme 5.1.

Access to the N_2H_x chemistry of present interest is realized using a tris(phosphino)borate ligand scaffold, ([PhBP$^{CH2Cy}_3$] = [PhB($CH_2P(CH_2Cy)_2)_3$]$^-$) to support iron(II). Treatment of [PhBP$^{CH2Cy}_3$]FeMe (**2.2**) with one equiv of AcOH cleanly generates the 5-coordinate complex, [PhBP$^{CH2Cy}_3$]Fe(OAc), (**5.1**) (Scheme 5.1). Unlike the 4-coordinate species of the type [PhBP$^{R}_3$]Fe-X, which are high-spin at all temperatures,[15] **5.1** exhibits temperature dependent two-phase spin cross-over behavior.[16,17] Thus, cooling solid samples of **5.1** results in a spin-transition from $S = 2$ to

an intermediate spin system at 120 K, and from this state to S = 1 at 30 K (Figure 5.1). Such behavior has been observed in six-coordinate iron(II) systems,[18] though the spin transition is typically S = 2 to S = 0. This behavior is described by magnetic coupling between iron centers in the crystalline lattice, which together form discrete clusters of two or three iron ions. Thus, it seems likely that the intermediate state observed between 30 and 120 K for **5.1** represents coupling between an S = 1 and S = 2 iron center within the crystalline lattice.

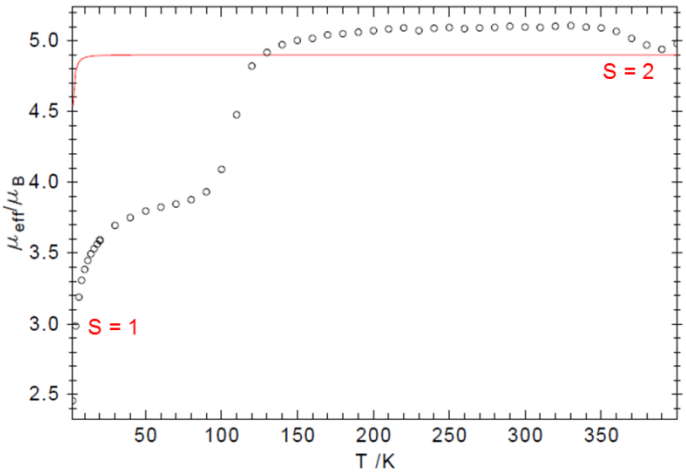

Figure 5.1. Solid-state magnetic susceptibility of **5.1**, plotted as μ_{eff} (μ_B) vs. T (K). The data was collected by warming a zero-field cooled solid-sample of **5.1** in a 1 T field in a SQUID magnetometer. The red line represents the spin-only magnetic moment for an isolated S = 2 center.

Despite the spin transitions, **5.1** readily binds L-type ligands to generate low-spin 6-coordinate mono- and diiron species (Scheme 5.2). Cooling solutions of **5.1** under an N_2 atmosphere results in reversible binding of 0.5 equiv of N_2, generating pink and diamagnetic $\{[PhBP^{CH2Cy}_3]Fe(OAc)\}_2(\mu\text{-}N_2)$, (**5.2**). The coordinated N_2 ligand in **5.2** is labile; THF solutions of **5.2** that are kept at -78 ^oC fully dissociate N_2 under a static

vacuum, as determined by N_2 quantification with a Toepler pump. Thus, all analysis of **5.2** must be done at reduced temperatures.

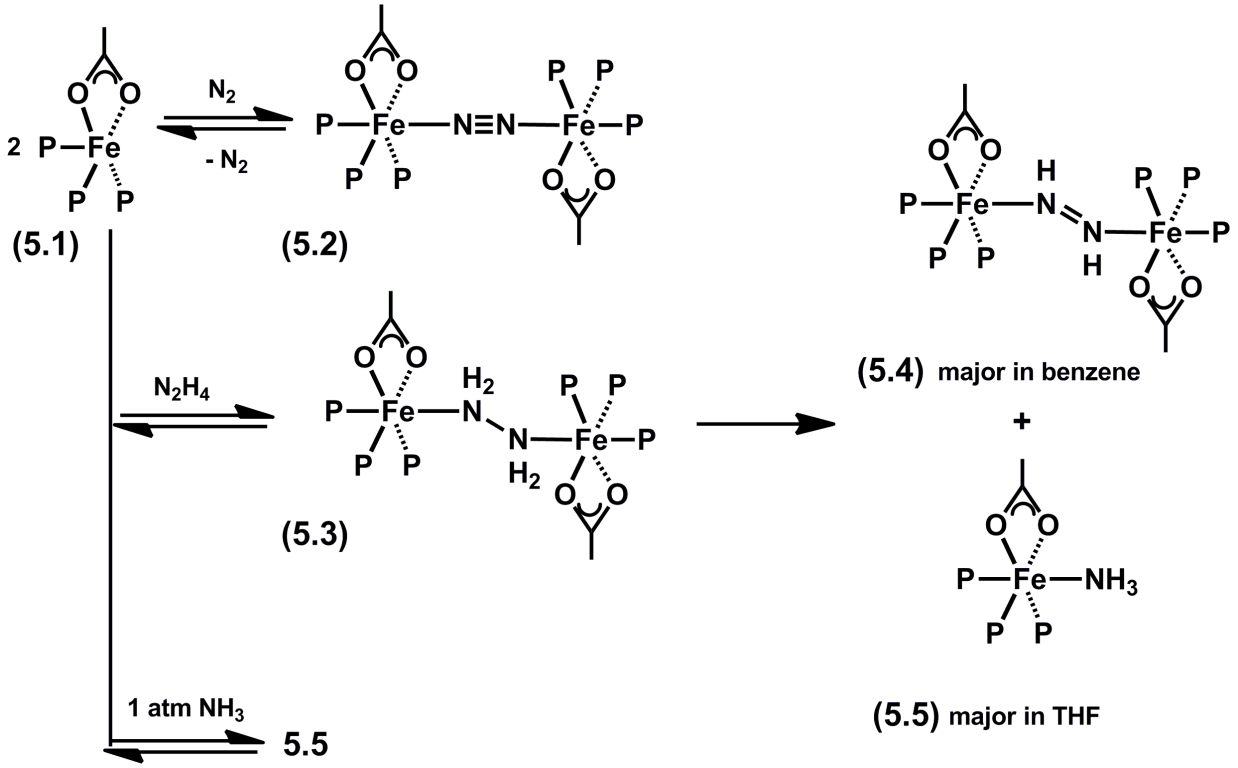

Scheme 5.2.

Crystals of **5.2** suitable for diffraction can be grown from saturated diethyl ether solutions of **5.2** stored at -35 ^{o}C in the glove-box, and the solid-state structure has been obtained. The core atoms are shown in Figure 5.2. The Fe-N and N-N distances of 1.874(3) and 1.120(5) Å, respectively, indicate a small degree of N_2 activation, and are similar to those observed in $[((PP_3)FeH)_2(\mu\text{-}N_2)]^{2+}$ (PP_3=$P(CH_2CH_2PMe_2)_3$).[19] Consistent with the small degree of N_2 activation, the rRaman spectrum of **5.2** (514 nm excitation, MeTHF glass, 77K) exhibits the ν(NN) stretch at 2083 cm^{-1}, which shifts to 2010 cm^{-1} upon ^{15}N-isotopic labeling. This is in excellent agreement with the shift predicted assuming a diatomic harmonic oscillator (2012 cm^{-1}), indicating minimal vibrational

coupling between ν(NN) and other vibrational modes about the iron centers. In solution, as in the solid-state, **5.2** exists as a diiron species; the ^{15}N NMR spectrum of ^{15}N-**5.2** (THF-d_8, -75 ^{o}C) shows a single resonance at 328.6 ppm, which is split into a doublet by the *trans* phosphine phosphorous atom ($^{2}J_{PN} \approx 15$ Hz).

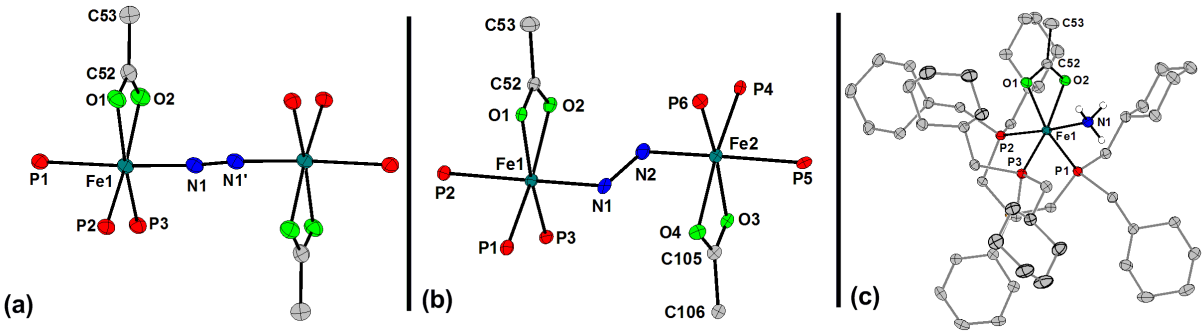

Figure 5.2. Displacement ellipsoid (50%) representation of (a) the core atoms of **5.2**, (b) the core atoms of **5.4** (major component only), and (c) **5.5**. Protons that were not located in the difference map have been removed for clarity. Select bond distances (Å) and angles (^{o}) for **5.2**: Fe1-P1 2.285(1); Fe1-P2 2.2319(9); Fe1-P3 2.2361(9); Fe1-O1 2.076(2); Fe1-O2 2.083(2); Fe1-N1 1.874(3); N1-N1' 1.120(5); Fe1-N1-N1' 174.9(3). Select bond distances (Å) and angles (^{o}) for **5.3**: Fe1-P1 2.219(3); Fe1-P2 2.311(4); Fe1-P3 2.240(4); Fe1-O1 2.082(8); Fe1-O2 2.100(7); Fe1-N1 1.912(8); Fe2-N2 1.898(8); N1-N1' 1.31(1); Fe1-N1-N2 128.1(7); Fe2-N2-N1 129.0(7). Select bond distances (Å) for **5.5**: Fe1-P1 2.2333(5); Fe1-P2 2.2422(5); Fe1-P3 2.2159(5); Fe1-O1 2.216(1); Fe1-O2 2.085(1); Fe1-N1 2.061(2)

Treatment of **5.1** with 0.5 equiv N_2H_4 generates the purple diiron species, {[PhBP$^{CH2Cy}{}_3$]Fe(OAc)}$_2$(μ-η^1:η^1-N_2H_4), (**5.3**). As for **5.2**, the hydrazine ligand is labile; at -30 ^{o}C resonance ascribed to **5.1** and **5.3** are observed by ^{1}H NMR spectroscopy. The presence of a single ^{15}N NMR (THF-d_8, -75 ^{o}C) chemical shift for ^{15}N-**5.3** (103 ppm), coupled with a single NH_2 resonance in the ^{1}H NMR spectrum (2.51 ppm), indicates a bridging coordination mode of the hydrazine.[12f,20] The presence of a terminally coordinated hydrazine ligand would give rise to two distinct resonances in both the ^{15}N

and ^{1}H NMR spectra, which correspond to the α-NH_2 and β-NH_2 nitrogen and hydrogen atoms, respectively. Indeed, this is observed in the previously described [PhB^{Ph}_3]Fe(OAc)(η^1-N_2H_4) species (**4.7**).

The hydrazine species **5.3** is not thermally stable, and further reacts to generate the blue diazene species, {[$PhBP^{CH2Cy}_3$]Fe(OAc)}$_2$(*trans*-μ-η^1:η^1-N_2H_2), (**5.4**), as well as the purple ammonia complex, [$PhBP^{CH2Cy}_3$]Fe(OAc)(NH_3), (**5.5**) (Scheme 5.2). The diethyl ether insolubility of **5.4** allows for facile separation and isolation of both **5.4** and **5.5**. The relative amounts of the disproportionation products **5.4** and **5.5** vary according to solvent and equivalents of hydrazine added to **5.1**. For example, the room temperature addition of 0.5 equiv of N_2H_4 to a benzene solution of **5.1** results in isolated yields of 75% and 15% for **5.4** and **5.5**, respectively (after stirring for 24 h). Under identical reaction conditions in THF, isolated yields of 25% and 66% for **5.4** and **5.5** are, respectively, achieved. When the reaction is monitored by VT-NMR spectroscopy (THF-d_8), both **5.4** and **5.5** are observed as products of the initial reaction. Subsequent addition of hydrazine to the reaction mixture results in complete conversion of **5.4** to **5.5**. Thus, when 2.5 equiv of N_2H_4 are added to THF solutions of **5.1** and allowed to stir for 48 h, only **5.5** is isolated. Similar disproportionation reactions have been observed at diiron[12f,21] and diruthenium systems,[13b,22] though in those systems, the stoichiometry is better defined.

The presence of a bridging diazene ligand in **5.4** is readily discerned by NMR spectroscopy. The ^{1}H{^{31}P} NMR spectrum of ^{15}N-**5.4** features an AA'XX' multiplet centered at 17.72 ppm, consistent with the presence of a diazene ligand (Figure 5.3).[12a,12f,13b,23] The splitting pattern was simulated, which allowed for coupling constants

to be obtained. The $^{3}J_{HH}$ can be used to infer *cis* or *trans* ligation, as well as to infer the extent of diazene activation.[24] For example, in the related species, {[PhB$^{Ph}_{3}$]Fe}$_2$(*cis*-μ-η^1:η^1-N_2H_2)(*cis*-μ-η^2:η^2-N_2H_2), **2.6**, $^{3}J_{HH}$ values of 13.0 and 9.0 Hz are obtained, which correspond to the *cis*-η^1:η^1-N_2H_2 (N-N bond distance: 1.281(5) Å) and the *cis*-η^2:η^2-N_2H_2 (N-N bond distance: 1.458(5) Å) ligands, respectively.[12f] The large $^{3}J_{HH}$ = 21.0 Hz of **5.4** suggests *trans* ligation, with a moderately activated diazene ligand. The extent of diazene activation in **5.4** is between that of [(CO)$_5$Cr]$_2$(*trans*-μ-N_2H_2), which has a $^{3}J_{HH}$ = 28.0 Hz[23] and an N-N bond distance of 1.25 Å,[25] and that of [(η^5-C_5Me_4H)$_2$ZrI]$_2$(*trans*-μ-N_2H_2), which has $^{3}J_{HH}$ = 9.4 Hz and an N-N bond distance of 1.414(3) Å.[26] In accordance with the observed NMR parameters, the rRaman spectrum of **5.4** (633 nm, THF) reveals the ν(NN) stretch at 1299 cm^{-1}, which shifts to 1263 cm^{-1} upon ^{15}N-labelling (1254 cm^{-1} predicted assuming a diatomic harmonic oscillator). Several additional vibrations that are sensitive to ^{15}N labeling are also observed in the Raman and IR spectra, and are likely coupled to one another. Sellmann has observed similar stretching frequencies in related 6-coordinate diiron(II) species that have similar structural parameters (*vide infra*).[27]

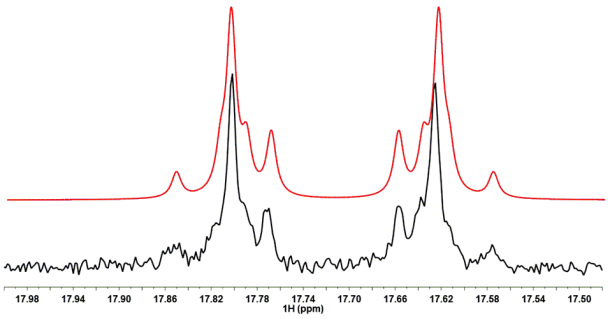

Figure 5.3. Diazene resonance of the $^{1}H\{^{31}P\}$ NMR spectrum (C_6D_6, 25 °C) of **5.4** indicating the AA'XX' splitting pattern (experimental, black; fit, red). The data was fit using the following parameters: $^{1}J_{NH}$ = -71.0 Hz, $^{2}J_{NH}$ = -1.1 Hz, $^{3}J_{HH}$ = 21.0 Hz, $^{1}J_{NN}$ = 12.0, linewidth = 3.5 Hz.

To confirm the *trans* ligation of the diazene, the solid-state structure of **5.4** was obtained (Figure 5.2). Crystals of **5.4** suitable for diffraction can be grown from the slow diffusion of pentane into either THF or benzene solutions of **5.4**, though they invariably suffer from total molecule disorder. Nonetheless, a complete dataset for crystals of **5.4** was collected, and the disorder was modeled, with 12% of the molecules being slightly translocated along the b-axis of the unit cell (monoclinic; P2(1)/c). Though the diazene protons could not be located in the difference map, the structure confirms the *trans* diazene ligation. The average Fe-N-N angle of 128.5^{o} is consistent with sp^{2}-hybridized nitrogen atoms, and the N-N distance of 1.31(1) Å and Fe-N distance of 1.89(8) Å are the same (within error) to those of other 6-coordinate diiron(II) bridging diazene complexes.[6b,12f]

Finally, the ammonia complex, [PhBP$^{CH2Cy}{}_3$]Fe(OAc)(NH$_3$), **5.5**, has also been structurally characterized (Figure 5.2). This species can alternatively be prepared by the addition excess ammonia to a THF solution of **5.1** (Scheme 5.2). The NMR parameters for **5.5** are similar to those of other low-spin iron(II) ammonia complexes.[20,28] For example, the ^{15}N NMR chemical shift for ^{15}N-**5.5** is noted at -21.1 ppm, with the ammonia protons resonating at 2.49 ppm in the corresponding ^{1}H NMR spectrum.

With this series of complexes in hand, it is of interest to establish whether the nitrogenous ligands can be interconverted via oxidation or reduction (Scheme 5.3). The present system is attractive for such studies, as the addition or removal of H-atom equivalents should not result in major structural or coordination changes to the "[PhBP$^{CH2Cy}{}_3$]Fe(OAc)" fragment. Though the stoichiometric and catalytic reductions of hydrazine by mono-[29] and bimetallic[21-22] systems are known, there are no well-defined

examples of the reduction of diazene to hydrazine (or ammonia). Such a transformation is inferred in the catalytic reduction of hydrazine by a related diiron species, "{Cp*Fe(μ-$SR)_2$}",[21] though the transformation was not explicitly observed. Likewise, there are no well-defined examples of complexes that can reduce N_2 to diazene (or to hydrazine or ammonia via diazene).

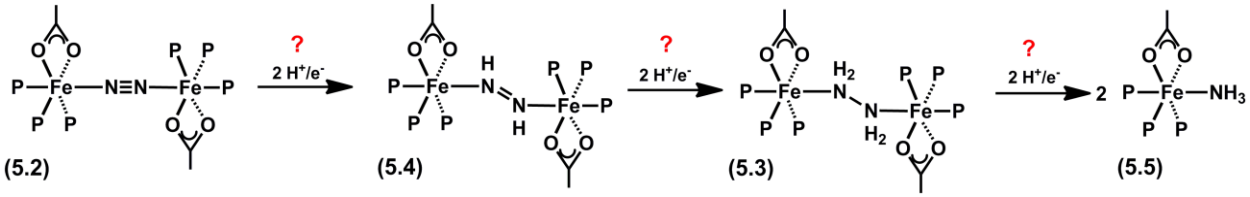

Scheme 5.3.

Initial oxidation studies suggest that the diazene species **5.4** can be oxidized to **5.2** by addition of either $Pb(OAc)_4$ or TEMPO. This reactivity suggests that the reverse, reduction of N_2 to diazene, may be feasible. Initial attempts to reduce **5.2** to **5.4** focused on using well-defined H-atom transfer agents (i.e., catechol, hydroquinone, Bu_3SnH, or cyclohexadiene), none of which reacted in the desired fashion. Likewise, the addition of reductants (i.e., Cp^*_2Fe, Cp^*_2Co, Cp_2Co) and acids (i.e., HOAc, HOTf, [lutH][BPh_4]) did not yield the desired transformation, and in most instances, **5.2** is isolated as the only iron-containing species. Cyclic voltammetry on **5.2** (at -35 ^oC) establish a quasi-reversible reduction at -2.3 V vs. Fc/Fc^+, suggesting that stronger reductants may be required to facilitate the reduction (the reduction event is absent in the cyclic voltammogram of **5.1**).[30]

Initial attempts to reduce the diazene species **5.4** with 4 equiv of Cp^*_2Fe and [lutH][BPh_4] (THF, -78 ^oC and 22 ^oC) did not yield hydrazine or ammonia. Treatment of **5.3** with 2 equiv of Cp^*_2Fe and [lutH][BPh_4] did yield 40 % NH_3,[31] though caution must

be taken in interpreting this preliminary result, as ammonia is also formed in the disproportionation reaction of **5.3**. Under the reaction conditions described for the reduction of **5.3** or **5.4**, protonation of the [$PhBP^{CH2Cy}_3$] ligand to release free $(CH_2Cy)_2PMe$ is observed, along with competitive formation of [$PhBP^{CH2Cy}_3$]Fe(η^6-$C_6H_5BPh_3$). This latter product is also observed in initial attempts to reduce **5.2** when [lutH][BPh_4] is used as the acid source. These findings suggest that AcOH may be a suitable acid for these studies. Its higher pK_a relative to [lutH][BPh_4] should result in less ligand degradation,[32] and will also allow for its use in combination with stronger reductants.[33] Additionally, as the series of iron(II) complexes already feature an acetate ligand, counter-anion exchange with acetate is degenerate, and thus formation of different and inactive iron(II) species is avoided.

5.3 Summary

In summary, a series of iron(II) complexes that can coordinate N_2, N_2H_2, N_2H_4, and NH_3 have been prepared and characterized. This family of complexes only differ in the oxidation state of the coordinating N_2H_x ligand, and represent the first such series for iron. Reduction studies aimed at interconverting these species are ongoing, with the hopes of achieving the stoichiometric reduction of N_2 to N_2H_2, or N_2H_2 to N_2H_4 (or NH_3).

5.4 Experimental Section

5.4.1 General Considerations

All manipulations were carried out using standard Schlenk or glove-box techniques under a dinitrogen atmosphere. Unless otherwise noted, solvents were deoxygenated and dried by sparging with Ar followed by passage through an activated alumina column from S.G. Water (Nashua, N.H.). Nonhalogenated solvents were tested with a standard purple solution of benzophenone ketyl in THF to confirm effective oxygen and moisture removal. Deuterated solvents were purchased from Cambridge Isotopes Laboratories, Inc. and were degassed and stored over activated 3-Å molecular sieves prior to use. Elemental analyses were performed by Midwest Microlab (Indianapolis, IN).

3.4.2 Spectroscopic Measurements

Varian 300, 400, and 500 MHz spectrometers were used to record the ^{1}H NMR, ^{31}P NMR, and ^{15}N NMR spectra (400 or 500 MHz). ^{1}H chemical shifts were referenced to residual solvent. ^{31}P NMR chemical shifts were referenced to 85% H_3PO_4 at δ = 0 ppm, and ^{15}N NMR chemical shifts were referenced to neat $C_6H_5{}^{15}NO_2$ (δ = 370 ppm) in comparison to liquid ammonia (δ = 0 ppm). MestReNova (6.1.0) was used for NMR data workup, as well as for simulation of spectra.

IR measurements were obtained with a KBr solution cell or a KBr pellet using a Bio-Rad Excalibur FTS 3000 spectrometer controlled by Varian Resolutions Pro software set at 4 cm^{-1} resolution.

The rRaman samples were prepared by loading solutions into capillaries in the glove-box, which were then flame-sealed (for room temperature data collection), or were transferred to a sealable NMR tube which was subsequently flame-sealed (for data collection at 77 K). Excitation was performed at 632.8 nm using a HeNe laser (10 mW) or at 514 nm using an Ar-ion laser. A lens collected the light that scattered at 90^{o} and focused it through a low-pass filter and into the entrance slit of a SPEX 750M monochromator. The dispersed light was detected by a LN/CCD array (5 cm^{-1} resolution), and the spectra recorded using Winspec (Princeton Instrument) software. Conversion from pixels to wavenumber was done by obtaining the spectrum of cyclohexane, and deriving the linear plot of pixels vs. wavenumber for known vibrations. All spectra were recorded in THF or Me-THF, and in some instances, solvent subtraction or baseline correction was performed.

Optical spectroscopy measurements were taken on a Cary 50 UV-Vis spectrophotometer using a 1 cm two-window quartz cell sealed with standard ground-glass joints or Teflon plugs.

5.4.3 Electrochemistry

Electrochemical measurements were carried out in a glovebox under a dinitrogen atmosphere in a one-compartment cell using a BAS model 100/W electrochemical analyzer. A glassy carbon electrode and platinum wire were used as the working and auxillary electrodes, respectively. The reference electrode was $Ag/AgNO_3$ in THF. Solutions (THF) of electrolyte (0.4 M tetra-n-butylammonium hexafluorophosphate) and

analyte were also prepared in a glovebox. All experiments were conducted in a drop freezer maintained at -35 ^{o}C.

5.4.4 SQUID Magnetometry

Solid-state magnetic susceptibility data was collected on a Quantum Design SQUID magnetometer at a field strength set at 1 T. Data were collected between 4K and 400K. Samples were prepared by loading a fine powder of the compound of interest into a polycarbonate capsule which was sealed with Teflon tape, poked with a hole, and loaded into a plastic straw. Diamagnetic corrections were made using the corrections of Pascal's constants. The molar magnetic susceptibility was calculated by converting the calculated magnetic susceptibility obtained from the magnetometer to a molar susceptibility (using the multiplication factor {(molecular weight)/[sample weight)*(field strength)]}). Effective magnetic moments were calculated from the molar susceptibility (μ_{eff} = sqrt(7.997χ_mT). The data was analyzed using julX.[34]

5.4.5 X-Ray Crystallography Procedures

Low-temperature diffraction data were collected on a Siemens or Bruker Platform three-circle diffractometer coupled to a Bruker-AXS Smart Apex CCD detector with graphite-monochromated Mo or Cu Kα radiation (λ = 0.71073 or 1.54178 Å, respectively), performing φ-and ω-scans. The structures were solved by direct or Patterson methods using SHELXS[35] and refined against F^2 on all data by full-matrix least squares with SHELXL-97.[36] All non-hydrogen atoms were refined anisotropically. All hydrogen atoms (except hydrogen atoms on nitrogen) were included into the model at

geometrically calculated positions and refined using a riding model. The isotropic displacement parameters of all hydrogen atoms were fixed to 1.2 times the U value of the atoms they are linked to (1.5 times for methyl groups).

The structures were refined using established methods.[37] Several of the structures reported suffered from disorder in parts of the [$PhBP^{CH2Cy}_3$] ligand and/or solvent molecules (some over more than two independent positions). All disorders were refined with the help of similarity restraints on 1-2 and 1-3 distances and displacement parameters as well as rigid bond restraints for anisotropic displacement parameters. All close contacts, both inter and intramolecular, reported by the Platon validation software[38] involve at least one partner from a minor component of a disorder. While it is conceivable that more components of the [$PhBP^{R}_3$] are disordered and parameterization of these disordered components would remove the close contacts, the data at hand did not allow for further modeling of the disorder. The protons attached to the iron-bound nitrogen atoms of **5.5** could be located in the difference Fourier synthesis and subsequently those H atoms were refined semi-freely with the help of distance restraints.

The structure of **5.4** suffers from total molecule disorder, with 12% of the molecules translocated along the b-axis of the unit cell. The data was modeled assuming this disorder to obtain a satisfactory solution.

5.4.6 Starting Materials and Reagents

[$PhBP^{CH2Cy}_3$Fe]Cl (**2.2**),[12f] $^{15}N_2H_4$,[39] and Me_2Mg[40] were prepared according to literature methods. $Pb(OAc)_4$ was purchased from Aldrich (99.999+%), purified as described in the literature,[41] and recrystallized from cold THF to afford a white

crystalline solid. Acetic acid was dried according to literature methods.[41] All other reagents were purchased from commercial vendors and used without further purification.

2.4.7 Synthesis of Compounds

Synthesis of [PhBP$^{CH2Cy}_3$]Fe(OAc), 5.1. To a stirring solution of [PhBP$^{CH2Cy}_3$]FeMe (**2.2**) (0.2732 g, 0.3116 mmol) in 16 mL DME, neat anhydrous acetic acid (17.9 μL, 0.312 mmol) was added. The solution immediately changed color from yellow to pale grey/purple. After stirring for 24 h, the volatiles were removed, and triturated with pentane. The suspension was filtered through a frit, and analytically pure solid was obtained. ^{1}H NMR (THF-d_8, 400 MHz, 25 ^{o}C) δ 98.1, 65 (bs), 25.2, 13.9, 12.8, 1.9, 1.2, 0.6, 0.1, -2.6, -7.3, -8.2, -9.0, -9.7, -16.5, -23.2. Evans Method (C_6D_6): 4.5 B.M. Anal. Calcd. for $C_{53}H_{92}BFeO_2P_3$: C 69.12; H 10.07; N 0. Found: C 68.77; H 9.93; N 0.

Synthesis of {[PhBP$^{CH2Cy}_3$]Fe(OAc)}$_2$(μ-N$_2$), 5.2. Upon cooling, 5.**1** reversibly binds 0.5 equiv of N_2 to generate **1-N$_2$**. The bound N_2 in **2** is labile; by Toepler analysis, qualitative release of N_2 is observed when THF solutions of **2** are maintained at -78 ^{o}C. Pink crystals **5.2** suitable for diffraction were grown by chilling a saturated diethyl ether solution of **5.1** to -35 ^{o}C in a nitrogen-filled glovebox. In the solid-state, the bound N_2 is also labile, as pink crystals of **5.2** change color to grey/purple upon exposure to vacuum. rRaman (514 nm, Me-THF, 77 K) (cm^{-1}): 2083 (NN).

Samples of ^{15}N-**5.2** were prepared by freeze pump thawing solutions of **5.1**/**5.2** and subsequently exposing **5.1** to a ^{15}N atmosphere prior to cooling of the solution. ^{1}H NMR

(THF-d_8, 400 MHz, -75 ^{o}C) δ 7.1 (4H), 6.9 (4H), 6.9 (2H), 0 – 2.7 (m, overlap with solvent, 174H). ^{31}P NMR (THF-d_8, 162 MHz, -75 ^{o}C) δ 53.7 (bs, 2P), 44.54 (dt, $^{2}J_{PP}$ = 71.1 Hz, $^{2}J_{PN}$ ≈ 15 Hz). ^{15}N NMR (THF-d_8, 40 MHz, -75 ^{o}C) δ 328.6 (d, $^{2}J_{PN}$ ≈ 15 Hz). rRaman (514 nm, Me-THF, 77 K) (cm^{-1}): 2010 (NN).

Synthesis of {[PhBP$^{CH2Cy}_3$]Fe(OAc)}$_2$(μ-N_2H_4), 5.3. A solution of **5.1** (0.0356 g, 0.0393 mmol) in 1 mL THF was cooled to – 78 ^{o}C. To this, a solution of anhydrous hydrazine in 1 mL THF (0.68 μL, 0.02 mmol) was added dropwise. The solution changed color from pink to purple, as **3** quantitatively formed. The bound hydrazine in **5.3** is labile, and at -30 ^{o}C, resonances for **5.1** are observed by ^{1}H NMR. At this temperature **5.3** is also unstable, and resonances ascribed to **5.4** are also observed by ^{1}H NMR spectroscopy.

Samples of ^{15}N-**5.3** were prepared following an analogous synthetic procedure using $^{15}N_2H_4$. ^{1}H NMR (THF-d_8, 400 MHz, -75 ^{o}C) δ 7.1 (bs, 4H), 6.88 (t, J = 6.4 Hz, 4H), 6.71 (t, J = 6.1 Hz, 2H), 2.51 (d, $^{1}J_{NH}$ = 66.0 Hz, NH_2, 4H), 0.75 – 2.2 (m, overlap with solvent, 167H), 0.19 (bs, 4H), -0.15 (bs, 3H). ^{31}P NMR (THF-d_8, 162 MHz, -75 ^{o}C) δ 66.17 (δ, $^{2}J_{PP}$ = 60.3 Hz), 54.51 (dt, $^{2}J_{PP}$ = 55.9 Hz, $^{2}J_{PN}$ = 8.2 Hz). ^{15}N NMR (THF-d_8, 40 MHz, gHSQCAD, -75 ^{o}C) δ 103.

Synthesis of {[PhBP$^{CH2Cy}_3$]Fe(OAc)}$_2$(μ-N_2H_2), 5.4. Neat anhydrous hydrazine (0.54 μL, 0.017 mmol) was added to a stirring solution of **5.1** (0.0300 g, 0.0335 mmol) in 1 mL benzene. The solution immediately changed color from pale grey to dark blue. After stirring for 24 h, the volatiles were removed. The solids were rinsed with diethyl ether,

and a midnight blue analytically pure powder of **5.4** was isolated (0.0236 g, 75.3%). Crystals suitable for diffraction were grown by the vapor diffusion of pentane into a dilute solution of **5.4** in benzene or THF. ^{1}H NMR (C_6D_6, 400 MHz, 25 ^{o}C) δ 17.72 (bs, 2H, N*H*), 7.98 (d, *J* = 7.2 Hz, 4H), 7.51 (t, *J* = 7.3 Hz, 4H), 7.25 (t, overlap with solvent, *J* = 6.9 Hz, 2H), 0.5 – 2.5 (m, 174H). ^{31}P NMR (C_6D_6, 162 MHz, 25 ^{o}C) δ 52.7 (d, $^{2}J_{PP}$ = 60.8 Hz), 34.9 (t, $^{2}J_{PP}$ = 60.8 Hz). UV-vis (THF) λ_{max}, nm (ε, M^{-1} cm^{-1}): 726 (17,700). IR (KBr) (cm^{-1}): 3244, 748, 446. rRaman (633 nm, THF) (cm^{-1}): 1299, 1232, 608.

Samples of ^{15}N-**5.4** were prepared following an analogous synthetic procedure using $^{15}N_2H_4$. ^{1}H{^{31}P} NMR (C_6D_6, 400 MHz, 25 ^{o}C) δ 17.72 (m, $^{1}J_{NH}$ = -71.0 Hz, $^{2}J_{NH}$ = -1.1 Hz, $^{3}J_{HH}$ = 21.0 Hz, $^{1}J_{NN}$ = 12.0 Hz, 2H, N*H*). Coupling constants were obtained by simulation of the spectrum. ^{31}P NMR (C_6D_6, 162 MHz, 25 ^{o}C) δ 52.7 (d, $^{2}J_{PP}$ = 60.8 Hz), 34.9 (dt, $^{2}J_{PP}$ = 60.8 Hz, $^{2}J_{PN} \approx$ 13 Hz). ^{15}N NMR (C_6D_6, 40 MHz, gHSQCAD, 25 ^{o}C) δ 434. IR (KBr) (cm^{-1}): 3242, 745, 438. rRaman (633 nm, THF) (cm^{-1}): 1263, 1223, 603.

Synthesis of [PhBP$^{CH2Cy}_3$]Fe(OAc)(NH$_3$), 5.5. Neat anhydrous hydrazine (0.40 μL, 0.012 mmol) was added to a stirring solution of **5.1** (0.0213 g, 0.0231 mmol) in 1 mL THF. The solution immediately changed color from pale grey to dark blue. After stirring for 24 h, the solution was purple, and the volatiles were removed. The solids were extracted into diethyl ether, the solution was pumped down, and the resulting purple solids were rinsed with pentane (0.0144 g, 66%) Crystals suitable for diffraction were grown by the vapor diffusion of pentane into a benzene solution of **5.5**.

Samples of ^{15}N-**5.5** were prepared following an analogous synthetic procedure using $^{15}N_2H_4$, or by addition of 1 atm of $^{15}NH_3$ to a THF solution of **5.1**. ^{1}H NMR (THF-d_8, 500 MHz, -40 ^{o}C) δ 7.12 (bs, 2H), 6.92 (bs, 2H), 6.76 (bs, 1H), 2.49 (d, $^1J_{NH}$ = 68.0 Hz, NH_3, 3H), 0.10 – 2.27 (m, 171H, overlap with solvent/$^{15}NH_3$), -0.09 (bs, 3H). ^{31}P NMR (THF-d_8, 202 MHz, -40 ^{o}C) δ 61.89 (d, J = 56 Hz), 51.09 (t, J = 56 Hz). ^{15}N NMR (THF-d_8, 50 MHz, -40 ^{o}C) δ -21.1 (q, $^1J_{NH}$ = 68.0 Hz).

2.4.8 Reduction Studies

Reduction Studies of 5.4. In a typical experiment, **5.4** was massed out in the glovebox (ca. 10–20 mg) and transferred to a 25 mL round bottom flask fitted with a stir bar. Solid oxidant and acid were added (4 equiv each), and a 180^o ground glass adaptor with a Teflon plug was attached to the flask. On a high-vac line, the flask was evacuated and THF was vac-transferred into the flask. The reaction was stirred at either -78 ^{o}C or 25 ^{o}C for 24 h. At this time, the volatiles were vac transferred onto a frozen ethereal solution of HCl (1.0 M; 6 mL), and the residual solids were analyzed by ^{31}P and ^{1}H NMR spectroscopy. The acidic solution was stirred for 45 min at room temperature, and the volatiles were removed. The remaining solids were analyzed by ^{1}H NMR spectroscopy (d_6-DMSO), and ammonium was quantified[31] by integration against a mesitylene standard (5.0 mM).

Reduction Studies of 5.3. A similar protocol was employed as that described for the reduction of 5.**4**. Briefly, **5.3** was generated *in situ* (-78 ^{o}C) in a 25 mL round bottom flask that is attached to a 180^o ground glass adaptor with a Teflon plug. The reaction

vessel was evacuated, and a THF solution containing the reductant and acid (2 equiv) was added to the top of the adaptor. The plug was briefly opened to allow transfer of the solution into the flask and immediately closed. The reaction was stirred, and warmet to 22 ^{o}C over 24 h. The subsequent work up was as described for **5.4**, with the exception that the reaction mixture was freeze-pump-thawed (3x) prior to vac-transferring of the volatiles onto the frozen ethereal HCl solution.

Reduction Studies of 5.2. A similar protocol was employed as that described for the reduction of **5.3**, with slight modifications. In the glove-box, THF solutions of **5.1** were chilled to -78 ^{o}C in a 2-neck round bottom flask. After 30 min, a 180^{o} ground glass adaptor with a Teflon plug was attached, as was a rubber septum. The reductant and acid (6 equiv) were added via syringe as either a single or separate THF solutions. The workup of the reaction is as described for the reduction studies of **5.3**.

Acknowledgements:

Curtis Moore (UCSD) is thanked for mounting and collecting the dataset for **5.4**.

Works Cited:

1. (a) MacKay, B. A.; Fryzuk, M. D., *Chem. Rev.* **2004**, *104*, 385; (b) Crossland, J. L.; Tyler, D. R., *Coord. Chem. Rev.* **2010**, *254*, 1883; (c) Hoffman, B. M.; Dean, D. R.; Seefeldt, L. C., *Acc. Chem. Res.* **2009**, *42*, 609; (d) Howard, J. B.; Rees, D. C., *Proc. Natl. Acad. Sci. U.S.A.* **2006**, *103*, 17088.

2. Chatt, J.; Pearman, A. J.; Richards, R. L., *J. Chem. Soc.;Dalton Trans.* **1977**, 1852.

3. (a) Schrock, R. R., *Angew. Chem. Int. Ed.* **2008**, *47*, 5512; (b) Yandulov, D. V.; Schrock, R. R., *Inorg. Chem.* **2005**, *44*, 1103; (c) Yandulov, D. V.; Schrock, R. R., *Science* **2003**, *301*, 76.

4. Hendrich, M. P.; Gunderson, W.; Behan, R. K.; Green, M. T.; Mehn, M. P.; Betley, T. A.; Lu, C. C.; Peters, J. C., *Proc. Natl. Acad. Sci. U.S.A.* **2006**, *103*, 17107.

5. Dilworth, M. J.; Thorneley, R. N., *Biochem. J.* **1981**, *193*, 971.

6. (a) Sellmann, D.; Sutter, J., *J. Biol. Inorg. Chem.* **1996**, *1*, 587; (b) Sellmann, D.; Soglowek, W.; Knoch, F.; Moll, M., *Angew. Chem., Int. Ed. Engl.* **1989**, *28*, 1271.

7. (a) Barney, B. M.; McClead, J.; Lukoyanov, D.; Laryukhin, M.; Yang, T. C.; Dean, D. R.; Hoffman, B. M.; Seefeldt, L. C., *Biochemistry* **2007**, *46*, 6784; (b) Barney, B. M.; Lukoyanov, D.; Yang, T. C.; Dean, D. R.; Hoffman, B. M.; Seefeldt, L. C., *Proc. Natl. Acad. Sci. U.S.A.* **2006**, *103*, 17113.

8. (a) Danyal, K.; Inglet, B. S.; Vincent, K. A.; Barney, B. M.; Hoffman, B. M.; Armstrong, F. A.; Dean, D. R.; Seefeldt, L. C., *J. Am. Chem. Soc.* **2010**, *132*, 13197; (b) Barney, B. M.; Laryukhin, M.; Igarashi, R. Y.; Lee, H.-I.; Dos Santos, P. C.; Yang, T.-C.; Hoffman, B. M.; Dean, D. R.; Seefeldt, L. C., *Biochemistry* **2005**, *44*, 8030.

9. (a) Kästner, J.; Blöchl, P. E., *J. Am. Chem. Soc.* **2007**, *129*, 2998; (b) Dance, I., *Dalton Trans.* **2010**, *39*, 2972.

10. Yelle, R. B.; Crossland, J. L.; Szymczak, N. K.; Tyler, D. R., *Inorg. Chem.* **2009**, *48*, 861.

11. Barney, B. M.; Lukoyanov, D.; Igarashi, R. Y.; Laryukhin, M.; Yang, T. C.; Dean, D. R.; Hoffman, B. M.; Seefeldt, L. C., *Biochemistry* **2009**, *48*, 9094.

12. (a) Sellmann, D.; Sutter, J., *Acc. Chem. Res.* **1997**, *30*, 460; (b) Crossland, J. L.; Zakharov, L. N.; Tyler, D. R., *Inorg. Chem.* **2007**, *46*, 10476; (c) Crossland, J. L.; Balesdent, C. G.; Tyler, D. R., *Dalton Trans.* **2009**, 4420; (d) Field, L. D.; Li, H.

L.; Dalgarno, S. J.; Turner, P., *Chem. Commun.* **2008**, 1680; (e) Vela, J.; Stoian, S.; Flaschenriem, C. J.; Münck, E.; Holland, P. L., *J. Am. Chem. Soc.* **2004**, *126*, 4522; (f) Saouma, C. T.; Müller, P.; Peters, J. C., *J. Am. Chem. Soc.* **2009**, *131*, 10358; (g) Lee, Y. H.; Mankad, N. P.; Peters, J. C., *Nature Chemistry* **2010**, *2*, 558.

13. For diruthenium systems, see: (a) Collman, J. P.; Hutchison, J. E.; Lopez, M. A.; Guilard, R.; Reed, R. A., *J. Am. Chem. Soc.* **1991**, *113*, 2794; (b) Sellmann, D.; Hille, A.; Rösler, A.; Heinemann, F. W.; Moll, M.; Brehm, G.; Schneider, S.; Reiher, M.; Hess, B. A.; Bauer, W., *Chemistry – A European Journal* **2004**, *10*, 819.

14. For a manganese system, see: (a) Sellmann, D., *J. Organomet. Chem.* **1972**, *44*, C46; (b) Sellmann, D., *Z. Natureforsch* **1970**, *25 b*; (c) Sellmann, D., *Angew. Chem., Int. Ed. Engl.* **1971**, *10*, 919.

15. (a) Brown, S. D.; Betley, T. A.; Peters, J. C., *J. Am. Chem. Soc.* **2003**, *125*, 322; (b) Betley, T. A.; Peters, J. C., *Inorg. Chem.* **2003**, *42*, 5074.

16. Spiering, H.; Kohlhaas, T.; Romstedt, H.; Hauser, A.; Bruns-Yilmaz, C.; Kusz, J.; Gütlich, P., *Coord. Chem. Rev.* **1999**, *190-192*, 629.

17. Spin-crossover is observed at related $[PhBP^{R}_{3}]Co^{II}$-X species: (a) Jenkins, D. M.; Peters, J. C., *J. Am. Chem. Soc.* **2003**, *125*, 11162; (b) Jenkins, D. M.; Peters, J. C., *J. Am. Chem. Soc.* **2005**, *127*, 7148.

18. (a) Bonnet, S.; Siegler, M. A.; Costa, J. S.; Molnar, G.; Bousseksou, A.; Spek, A. L.; Gamez, P.; Reedijk, J., *Chem. Commun.* **2008**, 5619; (b) Zhang, L.; Xu, G.-C.; Xu, H.-B.; Zhang, T.; Wang, Z.-M.; Yuan, M.; Gao, S., *Chem. Commun.* **2010**, *46*, 2554; (c) Klingele, J.; Kaase, D.; Klingele, M. H.; Lach, J.; Demeshko, S., *Dalton Trans.* **2010**, *39*, 1689; (d) Sato, T.; Nishi, K.; Iijima, S.; Kojima, M.; Matsumoto, N., *Inorg. Chem.* **2009**, *48*, 7211.

19. Field, L. D.; Guest, R. W.; Turner, P., *Inorg. Chem.* **2010**, *49*, 9086.

20. Saouma, C. T.; Peters, J. C., *manucript in preparation* **2010**.

21. Chen, Y.; Zhou, Y.; Chen, P.; Tao, Y.; Li, Y.; Qu, J., *J. Am. Chem. Soc.* **2008**, *130*, 15250.

22. Kuwata, S.; Mizobe, Y.; Hidai, M., *Inorg. Chem.* **1994**, *33*, 3619.

23. Smith, M. R.; Cheng, T. Y.; Hillhouse, G. L., *J. Am. Chem. Soc.* **1993**, *115*, 8638.

24. Cooper, M. A.; Manatt, S. L., *J. Am. Chem. Soc.* **1969**, *91*, 6325.

25. Huttner, G.; Gartzke, W.; Allinger, K., *Angew. Chem., Int. Ed. Engl.* **1974**, *13*, 822.

26. Bernskoetter, W. H.; Pool, J. A.; Lobkovsky, E.; Chirik, P. J., *J. Am. Chem. Soc.* **2005**, *127*, 7901.

27. Lehnert, N.; Wiesler, B. E.; Tuczek, F.; Hennige, A.; Sellmann, D., *J. Am. Chem. Soc.* **1997**, *119*, 8879.

28. Fox, D. J.; Bergman, R. G., *Organometallics* **2004**, *23*, 1656.

29. (a) Schrock, R. R.; Glassman, T. E.; Vale, M. G., *J. Am. Chem. Soc.* **1991**, *113*, 725; (b) Schrock, R. R.; Glassman, T. E.; Vale, M. G.; Kol, M., *J. Am. Chem. Soc.* **1993**, *115*, 1760.

30. Connelly, N. G.; Geiger, W. E., *Chem. Rev.* **1996**, *96*, 877.

31. Mankad, N. P.; Whited, M. T.; Peters, J. C., *Angew. Chem. Int. Ed.* **2007**, *46*, 5768.

32. Eckert, F.; Leito, I.; Kaljurand, I.; Kütt, A.; Klamt, A.; Diedenhofen, M., *J. Comput. Chem.* **2009**, *30*, 799.

33. Warren, J. J.; Tronic, T. A.; Mayer, J. M., *Chem. Rev.* **2010**, null.

34. The program julX was written by E. Bill, and is available at: http://ewww.mpi-muelheim.mpg.de/bac/logins/bill/julX_en.php

35. Sheldrick, G. M., *Acta Cryst.* **1990**, *A46*.

36. Sheldrick, G. M., *Acta Cryst.* **2008**, *A64*.

37. Müller, P.; Herbst-Irmer, R.; Spek, A. L.; Schneider, T. R.; Sawaya, M. R., *Crystal Structure Refinement: A Crystallographer's Guide to SHELXL*. Oxford University Press: Oxford, 2006.

38. Spek, A. L., L. PLATON A Multipurpose Crystallographic Tool. Utrecht University: Utrecht, Holland, 2008.

39. Schrock, R. R.; Liu, A. H.; O'Regan, M. B.; Finch, W. C.; Payack, J. F., *Inorg. Chem.* **1988**, *27*, 3574.

40. Tang, H.; Richey, H. G., *Organometallics* **2001**, *20*, 1569.

41. Armarego, W. L. F.; Chai, C. L. L., *Purification of Laboratory Chemicals*. 5 ed.; Butterworth-Heinmann: London, 2002.

Chapter 6: Solvent Coordination Induces the Reductive Coupling of Carbon Dioxide at Iron(I)

Abstract

This chapter presents the reaction between several tris(phosphino)borate supported iron(I) complexes and carbon dioxide ([PhBP$^{R}_{3}$] = [PhB($CH_2P(R)_2)_3$]$^-$; R = CH_2Cy, Ph, ^{i}Pr, *m*ter). Exposure of MeCy solutions of [PhBP$^{CH2Cy}_{3}$]Fe(PR_3) (R = Ph (**6.7**), Cy (**6.8**)) to CO_2 yields the partial decarbonylation product {[PhBP$^{CH2Cy}_{3}$]Fe}$_2$(μ–O)(μ–CO) (**6.2**). When the reaction is carried out in benzene or THF, reductive coupling of CO_2 instead occurs to give the oxalate species {[PhBP$^{CH2Cy}_{3}$]Fe}$_2$(μ –η^2:η^2–oxalato) (**6.3**). Thus whether CO_2 is reduced by one or two electrons is solvent dependent. Reaction studies aimed at understanding this solvent effect are presented, and they suggest that the reaction profile is ultimately determined by the ability of the solvent to coordinate the iron center. When more sterically encumbering auxiliary ligands are employed to support the iron(I) center (i.e., [PhBP$^{Ph}_{3}$] and [PhBP$^{iPr}_{3}$]), only decarbonylation is observed, and {[PhBP$^{R}_{3}$]Fe}$_2$(μ-O) is isolated (R = ^{i}Pr (**6.10**), Ph (**6.12**)). A mechanistic scheme that is consistent with combined experimental and computational results is presented, and suggests that reductive coupling of CO_2 occurs from an electronically saturated 19-electron iron(I) species.

6.1 Introduction

Due to its vast supply and proposed role in global warming, CO_2 is poised as a C1 source for both fine chemicals and fuels.[1] Several multi-electron transformations of CO_2 that either reduce CO_2 to other C1 sources or create C-C bonds are feasible. For example, the coupled two electron/two proton reduction of CO_2 to CO can serve as a chemical feedstock for CO, which can then be converted to liquid fuels via Fisher-Tröpsch chemistry.[2] Examples of coupling reactions that involve CO_2 include cross-coupling with epoxides to generate polycarbonates or cyclic carbonates,[3] and coupling with organozinc or other carbanion equivalents to generate carboxylic acids.[4,5]

The aforementioned examples proceed via multi-electron transformations, but the direct one-electron reduction of CO_2 to give $CO_2^{\bullet-}$ can also facilitate a multitude of transformations. Once formed, the CO_2 radical anion can disproportionate to CO and CO_3^{2-},[6] in the presence of water it can generate formate,[7] it can cross-couple to other radicals,[8] or it can undergo C-C coupling to give oxalate.[9,10,11,12,13] The selective reduction of CO_2 to oxalate is a potentially desirable transformation, as oxalate can be hydrogenated to give ethylene glycol,[14] itself a useful fuel feedstock and gasoline additive. While trace oxalate formation has been observed in several electrocatalytic reduction systems,[15] well-defined homogeneous metal complexes that mediate reductive CO_2 coupling to oxalate remain rare. Evans and coworkers first reported that $Cp^*_2Sm(THF)_2$ reacts with CO_2 to produce the bridging oxalate species $\{Cp^*_2Sm\}_2(\mu\text{-}\eta^2\text{:}\eta^2\text{-oxalato})$.[9a] Subsequently, there have been a few reports of similar transformations at lanthanides,[9b,c] copper,[10] nickel,[11] titanium,[13] and iron,[12] though oxalate formation in these systems is sometimes ill-defined. Very recently, a dimeric Cu(I) complex was

found to mediate the selective reduction of CO_2 to oxalate, both stoichiometrically and electrocatalytically.[10b] In this system, the reduction occurs at ca. 2 V more positive than the direct one electron reduction of CO_2, and excellent Faradaic yields are obtained for the electrocatalytic reaction. These results underscore the importance of establishing systems that can selectively reduce CO_2, as well as understanding factors that facilitate such transformations.

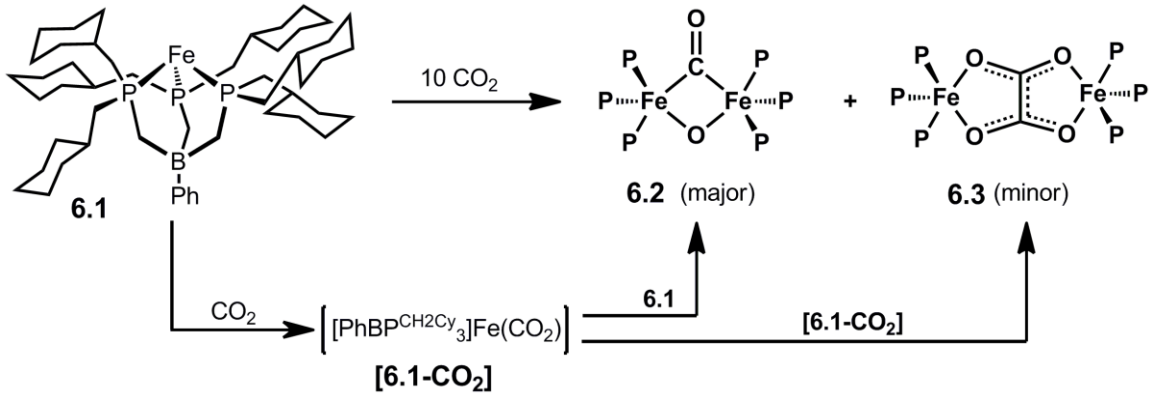

Scheme 6.1.

Our group has previously described an iron(I) mediated reduction of CO_2 in which an oxalate species was formed as a minor product (Scheme 6.1).[12] The iron(I) synthon [PhBP$^{CH2Cy}_3$]Fe (**6.1**) ([PhBP$^{CH2Cy}_3$] = PhB($CH_2P(CH_2Cy)_2)_3^-$) reacts with CO_2 to generate green and diamagnetic {[PhBP$^{CH2Cy}_3$]Fe}$_2$(μ–O)(μ–CO) (**6.2**) as a major product, and red and paramagnetic {[PhBP$^{CH2Cy}_3$]Fe}$_2$(μ–η^2:η^2–oxalato) (**6.3**) as a minor product (ca. 3:1). These products are the result of the two and one electron reductions of CO_2, respectively. As to our knowledge there are no other systems displaying such dual reactivity, that is, competitive one and two electron reduction of CO_2, we sought to establish the dominant factors that dictate the selectivity.

Initial attempts to alter the reaction profile between **6.1** and CO_2 focused on systematically varying the CO_2 equivalents (and CO_2 pressure) and the reaction temperature. When a sample of **6.1** in THF (11 mM) was highly diluted in pentane to 0.03 mM, and subsequently exposed to an atmosphere of CO_2 (ca. 300 equiv), the selectivity changed. Under these conditions, the product profile was inverted, with the formation of the oxalate product **6.3** favored over the decarbonylation product **6.2**. However, the reactive nature of **6.1**, combined with the dilute reaction conditions employed, no longer afforded a clean reaction, precluding further studies. These combined results did however suggest a mechanistic scenario (Scheme 6.1) to account for the product profile. If enough CO_2 is present to tie up all of **6.1** in the form of an intermediate CO_2 adduct species, $[PhBP^{CH2Cy}_3]Fe(CO_2)$ (**6.1**-CO_2), then bimolecular C-C coupling to give μ-oxalate **6.3** would ensue. Otherwise, **6.1** is available to intercept $[PhBP^{CH2Cy}_3]Fe(CO_2)$ to generate μ-O/μ-CO **6.2**.

Herein we present studies that provide insights into the iron-mediated reductive coupling of CO_2 described above. To achieve selectivity for either formation of **6.2** or **6.3**, two strategies were implemented. First, various four-coordinate iron(I) phosphine adducts of the type $[PhBP^{CH2Cy}_3]Fe(PR_3)$ were prepared and reacted with CO_2. Because it was anticipated that phosphine dissociation would precede iron interactions with CO_2, this approach would allow the concentration of the active iron(I) species in solution to be kept low relative to that of CO_2, without requiring high dilution. Second, we explored the *in situ* generation of iron(I) in the presence of an atmosphere of CO_2. Both of these approaches proved useful for controlling the relative concentrations of the active iron(I) species relative to CO_2 in solution. This allowed for the determination of the role that the

ancillary ligand (i.e., [PhBP$^{R}_{3}$] R = Ph, ^{i}Pr, CH_2Cy, *m*ter) and the reaction solvent has on the reaction profile. We found that reductive coupling to oxalate only occurs with the "[PhBP$^{CH2Cy}_{3}$]Fe" platform and, moreover, that this coupling is preferred in a solvent that can coordinate the iron center. Thus, in THF CO_2 coupling to μ-oxalate **6.3** is favored, and in MeCy decarbonylation to generate μ-O/μ-CO **6.2** occurs exclusively. Combined experimental and DFT studies allow us to propose a plausible mechanistic scheme to account for the dual CO_2 reactivity and its tunability.

6.2 Results

6.2.1 Synthesis and Characterization of Iron(I) Precursors

In our initial report, it was noted that the sodium amalgam reduction of [PhBP$^{CH2Cy}_{3}$]FeCl (Scheme 6.2) in THF produces a lime-green species whose empirical formula, in the solid-state, is "[PhBP$^{CH2Cy}_{3}$]Fe".[12] To simplify its characterization, spectroscopic data for **6.1** have now been collected in MeCy, whose non-coordinating nature should lead to a structure analogous to that in the solid-state. Our data are consistent with its formulation as the cyclometalated iron(III) hydride complex depicted in Scheme 6.2, though the exact position of metalation on the ring is unclear. Relevant data are as follows: Powders, as well as MeCy solutions of **6.1** are yellow in color, whereas they are lime-green in a donor solvent such as THF. Also, a low intensity but reliably discernable ν(Fe-H) vibration is present in MeCy (2056 cm^{-1}) and in the solid-state (2058 cm^{-1}; KBr), but absent in THF solutions. Both the EPR spectrum of **6.1** in MeCy at 4 K (see Appendix 5), as well as the room temperature d_{14}-MeCy solution

magnetic moment of 2.3 μ_B, are consistent with an S = ½ spin system, as would be expected for a cyclometalated iron(III) isomer of **6.1**, as depicted in Scheme 6.2. Finally, the addition of phosphines to **6.1** in MeCy leads to formation of the corresponding d^7 S = 3/2 [PhBP$^{CH2Cy}_3$]Fe(PR$_3$) complexes (*vide infra*), consistent with a reversible metalation process. As communicated previously,[12] green THF solutions of **6.1** are more complex than those in MeCy. They contain a mixture of species (e.g., [PhBP$^{CH2Cy}_3$]Fe(THF)$_x$). As a temperature dependent ^{31}P NMR signal is observed for **6.1** in d_8-THF, one of these species is presumed to be {κ^2-[PhBP$^{CH2Cy}_3$]}Fe(THF)$_x$, in which one of the phosphine arms has dissociated. Despite this equilibrium mixture of species, **6.1** behaves as an iron(I) synthon in THF, for example, reacting cleanly in the presence of phosphines to provide [PhBP$^{CH2Cy}_3$]Fe(PR$_3$).

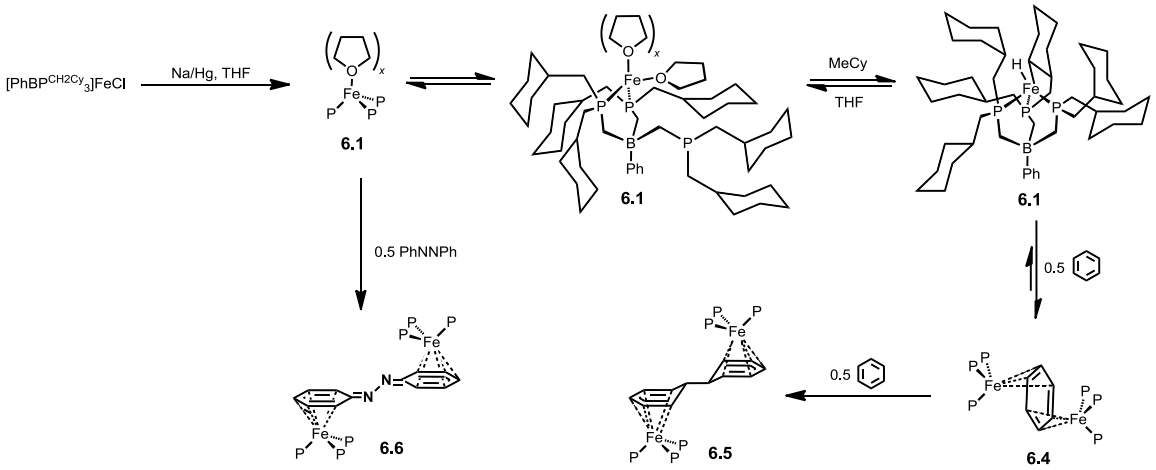

Scheme 6.2.

Though we have been unable to obtain crystals of **6.1** suitable for X-ray diffraction studies from MeCy or THF, the structure of **6.1** in benzene has been determined and is shown in Figure 6.1.[12] The quantitative coordination of benzene occurs

upon addition of one equivalent of benzene to THF solutions of **6.1** (Scheme 6.2). Two iron centers coordinate benzene to generate {[PhBP$^{CH2Cy}_3$]Fe}$_2$(μ–η^3:η^3-C_6H_6) (**6.4**). The solid-state structure of **6.4** reveals an average C-C bond distance for the bound benzene ring of 1.40 Å, as well as a relatively small bend angle (ca. 12^o) that distorts the bound benzene into a pseudo-chair conformation. These data are consistent with a resonance structure in which a diiron(I) species forms an aromatic μ-adduct of benzene.[16] The alternative diiron(II) bis-allyl resonance structure, in which the bound benzene is reduced by two electrons, is not consistent with the observed metrical parameters of the benzene ring. The diamagnetic nature of **6.4** indicates that the two d^7 iron centers are strongly antiferromagnetically coupled via the benzene ring. In the presence of excess benzene, **6.4** is thermally unstable and decomposes at 25 ^{o}C to give the 18-electron species, {[PhBP$^{CH2Cy}_3$]Fe}$_2$(μ–η^5:η^5-6,6'-bicyclohexadienyl) (**6.5**) (Figure 6.1). The transformation from **6.4** to **6.5** presumably results from the dimerization of a 19-electron intermediate species "[PhBP$^{CH2Cy}_3$]Fe(η^6-C_6H_6)", which undergoes radical C-C coupling between the two ativated benzene ligands.[17] Though the coordination of benzene in **6.4** is reversible (*vide infra*), this subsequent reaction makes **6.4** unsuitable as an iron(I) synthon.

In a conceptually related reaction, **6.1** reacts with 0.5 equivalents of azobenzene to generate {[PhBP$^{CH2Cy}_3$]Fe}$_2$(μ–η^5:η^5-azobenzene) (**6.6**), whose solid-state structure shows an unprecedented binding mode for aryl-substituted diazenes (Figure 6.1). Instead of coordinating the nitrogen atom(s),[18,19] the iron centers are bound by the aryl rings in an η^5- fashion as seen in **6.5**. Interestingly, the N-N bond distance is 1.340(9) Å, which is

significantly reduced compared to free azobenzene, wherein the N=N bond distance is 1.23 Å.[20] This suggests that the N=N bond of azobenzene in **6.6** is reduced by two electrons, which is capped by two 18-electron iron(II) centers.

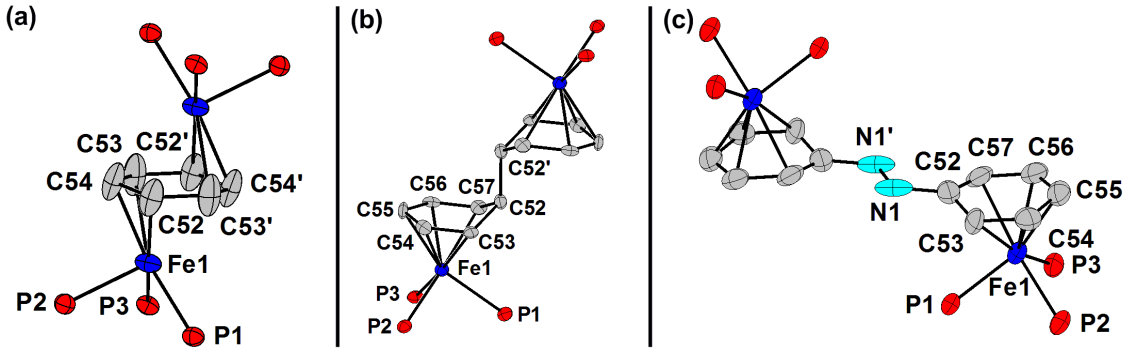

Figure 6.1. 50% thermal ellipsoid representation of the core atoms of: (a) {[PhBP$^{CH2Cy}{}_3$]Fe}$_2$(μ–η^3:η^3-C_6H_6), (**6.4**), and (b) {[PhBP$^{CH2Cy}{}_3$]Fe}$_2$(μ-η^5:η^5-6,6'-bicyclohexadienyl), (**6.5**). Selected bond distances (Å) and angles (deg.) for **6.4**: Fe-P1 2.234(2), Fe-P2 2.231(2), Fe-P3 2.268(2) Fe-C52 2.219(5), Fe-C53 2.234(5), Fe-C54 2.169(5), C53-C54 1.385(5), C54-C52 1.420(5), C52-C53' 1.384(5), C53-C53'-C54'-C52' dihedral 12.84(1). Selected bond distances (Å) and angles (deg.) for **6.5**: Fe–P1 2.262(2), Fe–P2 2.235(2), Fe–P3 2.250(2), Fe–C53 2.174(5), Fe–C54 2.100(5), Fe–C55 2.112(5), Fe–C56 2.103(5), Fe–C57 2.188(5), C52–C52´ 1.56(1), P1–Fe–P2 91.31(6), P2–Fe–P3 88.70(6), P1–Fe–P3 89.74(6), C54-C53-C52-C57 dihedral 50.25(1). Select bond distances (Å) **6.6**: Fe1–P1 2.250(2), Fe1–P2 2.230(2), Fe1–P3 2.246(2), Fe1–C53 2.238(6), Fe1–C54 2.094(6), Fe1–C55 2.089(6), Fe1–C56 2.110(6), Fe1–C57 2.212(6), N1–C52 1.429(8), N1–N1´ 1.340(9)

Access to well-defined and less reactive iron(I) complexes is achieved by the preparation of four-coordinate species of the type [PhBP$^{CH2Cy}{}_3$]Fe(PR$_3$). These complexes are readily prepared by the addition of a suitable phosphine to THF or MeCy solutions of **6.1**. For example, the addition of PPh$_3$ to a THF solution of **6.1** results in a rapid color change from lime-green to sanguine-orange, and quantitative formation of four-

coordinate [PhBP$^{CH2Cy}_3$]Fe(PPh$_3$) (**6.7**). The solution magnetic moment of 4.2 μ_B measured in C_6D_6 is consistent with the formulation of **6.7** as a high-spin, S = 3/2 Fe(I) center, akin to related 4-coordinate [PhBP$^R_3$]Fe(PR'$_3$) species.[12,21,22]

In contrast, the addition of one equivalent of bulkier PCy$_3$ to a solution of **6.1** results in an equilibrium between **6.1** and [PhBP$^{CH2Cy}_3$]Fe(PCy$_3$) (**6.8**), as determined by UV-vis absorption spectroscopy. The addition of one equivalent of PCy$_3$ to **6.1** gives an equilibrium mixture at room temperature in which ca. 70 % of the PCy$_3$ is tied up to give **6.8** in THF, versus ca. 94 % in MeCy. The addition of 10 equiv of PCy$_3$ to solutions of **6.1** in either solvent ensures that **6.8** is the only detectable species. The lability of PCy$_3$ manifests itself in the intolerance of **6.8** towards arene solvents. For instance, whereas benzene solutions of PPh$_3$-capped **6.7** are stable over a period of weeks, a C_6D_6 solution of **6.8**, generated by the addition of one equiv PCy$_3$ to **6.1**, shows full conversion to **6.4**-d_6 after a period of hours. Additionally, cooling THF or MeCy solutions of **6.8** results in a color change to lime-green or yellow (respectively), as PCy$_3$ precipitates out and **6.1** is left in solution.

6.2.2a Reaction of [PhBP$^{CH2Cy}_3$]Fe(I) Complexes Towards CO_2

When solutions of **6.1** in either THF or MeCy are exposed to 10 equivalents of CO_2, the decarbonylation pathway to generate μ-O/μ-CO **6.2** predominates over the coupling pathway to generate μ-oxalate **6.3**, with a ca. 3:1 distribution of **6.2** to **6.3** as previously reported (Scheme 6.1).[12] To decrease the concentration of reactive **6.1** in

solution relative to CO_2, the four-coordinate phosphine complexes were instead exposed to CO_2.

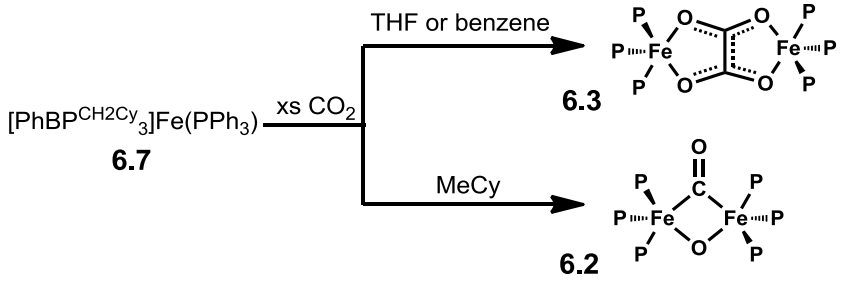

Scheme 6.3.

Exposure of a benzene solution of PPh_3-adduct **6.7** to CO_2 (1 atm) results in a change in color from sanguine-orange to dark red, and both NMR and IR analysis show a clean, albeit incomplete, conversion to oxalate **6.3** over a period of 26 h (Scheme 6.3). When the reaction is monitored by ^{31}P NMR spectroscopy, the dinuclear benzene adduct **6.4** is observed at intermediate reaction times, though subsequent formation of **6.5** via benzene coupling does not ensue. A typical experiment (15 mM in **6.7**, 10 equiv CO_2, 26 h) gives rise to ca. 70% **6.3**, with ca. 30% of the starting material remaining. Exposure of such solutions to additional CO_2 with prolonged stirring does not completely convert **6.7** to **3**, suggesting that the gradual release of PPh_3 has an inhibitory effect on the reaction. Indeed, when excess PPh_3 (10-fold) is added to solutions of **6.7** prior to CO_2 exposure, the reaction is completely shut down at room temperature. In THF a similar selectivity is observed, though after 26 h only 30 % conversion to **3** is observed. In contrast, when the reaction between **6.7** and CO_2 is carried out in MeCy, a sharp attenuation in rate and *complete inversion* of selectivity is observed. The partial decarbonylation product **6.2** is

now produced exclusively, albeit in low yield (ca. 10%), with the remaining iron present as starting material after stirring for 26 h at 50 ^{o}C. The varying inhibition effect that PPh_3 has on the reaction in the various solvents may be due to different equilibria between **6.1** and **6.7** in the various solvents. The reaction between the dinuclear benzene adduct **6.4** and CO_2 displays the same solvent-dependence, though the competitive conversion of **6.4** to **6.5** precludes a thorough study using this iron(I) synthon.

To further probe the role that solvent plays on the reaction profile, the reaction between PCy_3-adduct **6.8** and CO_2 was investigated, as the reaction with CO_2 under similar conditions is complete after 24 h. For these studies, solutions of **6.8** were prepared by the addition of one equiv of PCy_3 to **6.1** (20 mM) followed by exposure to 10 equiv of CO_2 for 24 h (Scheme 6.4). We sought a means to readily discern the ratio between μ-O/μ-CO **6.2** and μ-oxalate **6.3**, which is non-trivial by NMR spectroscopy owing to the paramagnetism of **6.3**. As a viable protocol, after the reaction with CO_2 was complete, the reaction headspace was evacuated, and an atmosphere of CO was introduced. The addition of CO serves to quantitatively convert all μ-oxalate **6.3** to its diamagnetic carbonyl adduct **6.9**, $\{[PhBP^{CH2Cy}{}_3]Fe(CO)\}_2(\mu\text{–}\eta^2\text{:}\eta^2\text{–oxalato})$, while not affecting **6.2**. This approach allowed for the quantification of **6.2** and **6.9** by ^{31}P NMR spectroscopy, permitting the relative rates of the one and two electron reductions of CO_2 to be obtained.

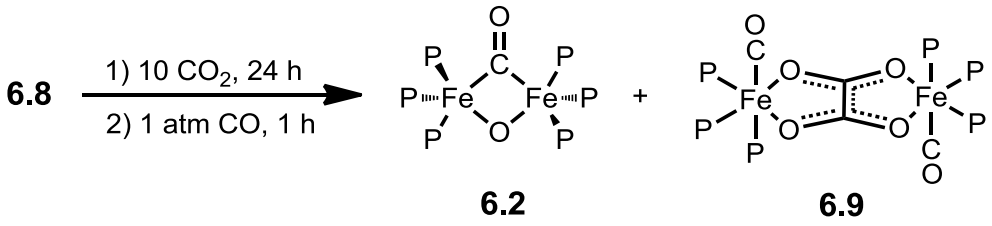

Scheme 6.4.

Under such conditions, the only observable product in MeCy is that of partial decarbonylation, **6.2** (Table 6.1). This is also true if less CO_2 is administered (2 equiv), or if 5 equiv of PCy_3 is added to the reaction, though in these cases incomplete conversion to **6.2** is observed after 24 h. If THF is employed rather than MeCy, **6.8** reacts under analogous conditions to instead favor μ-oxalate **6.3**. In fact, if the CO_2 content is reduced to 2 equiv, a ratio of 13:1 in favor of **6.3** (versus **6.2**) is observed. The addition of excess PCy_3 also heightens the selectivity for **6.3**.

Table 6.1. Reactivity of **6.8** towards CO_2

Entry[a]	Solvent	Conc. / mM	CO_2 Equiv.	Additives	6.2 : 6.9[b]
1	MeCy	20	10	--	1 : 0
2	MeCy	20	10	5 PCy_3	1 : 0
3	MeCy	20	2	--	1 : 0
4	THF	20	10	--	1 : 4.3
5	THF	20	10	5 PCy_3	1 : 9
6	THF	20	2	--	1 : 13
7	THF	60	10	--	1: 1.6
8	2-MeTHF	20	2	--	1 : 7
9	2,5-diMeTHF	20	2	--	4 : 1

[a]Reactions were run in 15 mL schlenk tubes fitted with a Teflon stopcock and a stir bar and stirred for 24 h. The ration **6.2** : **6.9** was determined by ^{31}P NMR integration against an internal standard of $^{t}Bu_3P$ (see experimental section for details).

To determine whether solvent coordination or solvent polarity play an important role in determining the observed reaction profile, the reaction between PCy_3-adduct **6.8** and CO_2 was also examined in 2-Me-THF and 2,5-dimethyl-THF.[23] These two solvents have dielectric constants very similar to THF,[24] yet the added steric bulk renders them less coordinating than THF, 2,5-dimethyl-THF being the most distinct in this regard. In 2-Me-THF, as for THF, the major product remains μ-oxalate **6.3**, though the amount of

μ-O/μ-CO **6.2** increases relative to when the reaction is run in THF. When one adds an additional methyl group to the solvent, as for 2,5-dimethyl-THF, the selectivity *inverts* (4:1 in favor of **6.2**), and better mimics that observed in MeCy (Table 6.1 and Figure 6.2). The implication is clear: a more coordinating solvent favors C-C coupling.

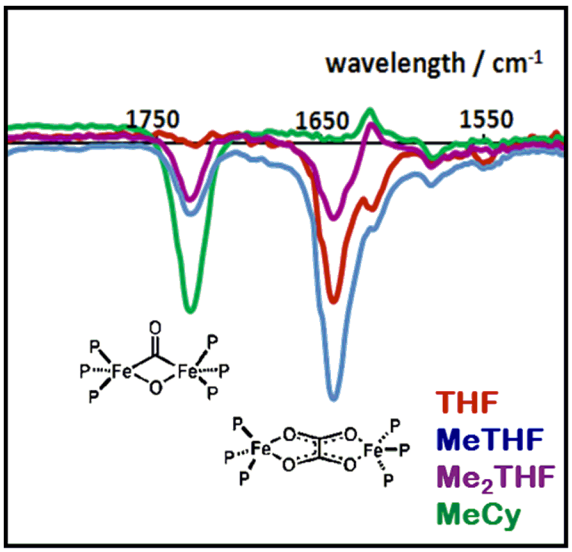

Figure 6.2. Stacked IR spectra of the crude reaction solutions for the reaction between **6.7** and 10 equivalents of CO_2 in various solvents. As the ability of the solvent to coordinate iron decreases, more decarbonylation product **6.2** relative to coupled product **6.3** is observed. ν(CO) for **6.2**: 1730 cm^{-1}; ν(CO) for **6.3**: 1647 cm^{-1}

6.2.2b Reaction Between In Situ Generated Iron(I) and CO_2

In addition to exploring the reactivity of well-defined Fe(I) complexes, the *in situ* Na/Hg reductions of [$PhBP^R_3$]FeCl under a CO_2 atmosphere (R = CH_2Cy, ^iPr, Ph, *m*ter) were studied. In a typical experiment, an atmosphere of CO_2 was introduced to an evacuated reaction vessel containing 2.5 equiv of Na/Hg and a THF solution of

[PhBP$^{R}_{3}$]FeCl at 0 ^{o}C. The solution was slowly stirred to ensure an excess of CO_2 in solution relative to Fe(I) (Scheme 6.5).

When [PhBP$^{CH2Cy}_{3}$]FeCl is employed as the Fe source, **6.3** is isolated as the major species (51 %), with no observable formation of **6.2** (as deduced by NMR and IR spectroscopy). The remainder of the iron is converted to unidentifiable products. As reducing amalgams can themselves reductively couple CO_2 to give oxalate salts,[25] it is conceivable that **6.3** forms from the reaction between sodium oxalate and [PhBP$^{CH2Cy}_{3}$]FeCl. In a control experiment no reaction between [PhBP$^{CH2Cy}_{3}$]FeCl and sodium oxalate under similar conditions (i.e., 0 ^{o}C, THF) is observed. This is true when either crystalline sodium oxalate or *in situ* generated sodium oxalate (prepared by stirring a sodium amalgam suspended in THF under a blanket of CO_2) is employed. Thus, **3** must form from the reaction between **6.1** and CO_2.

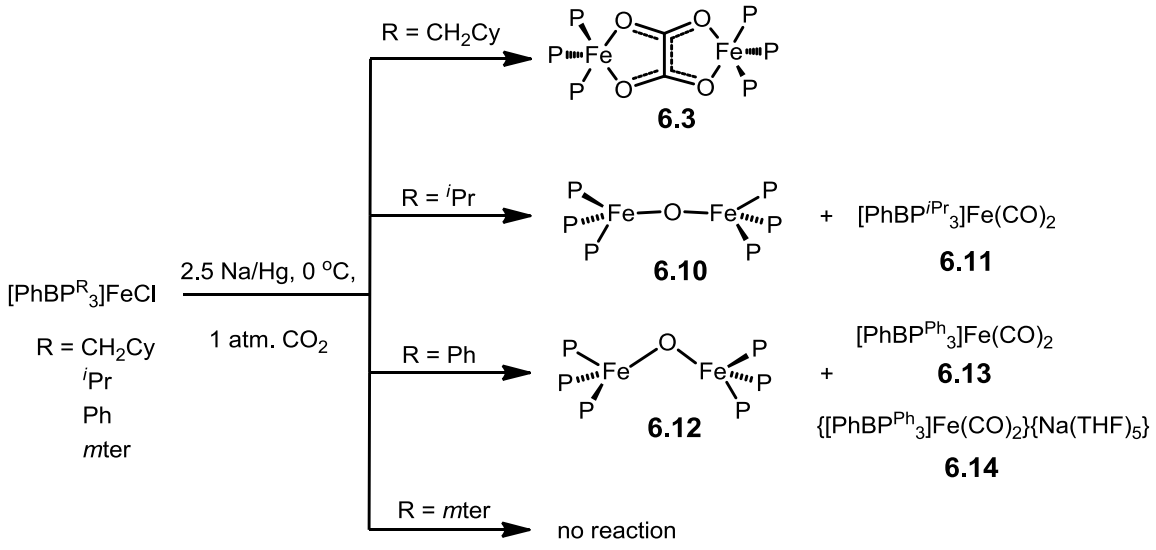

Scheme 6.5.

In contrast, the reduction of [PhBP$^{iPr}_3$]FeCl[26] under an atmosphere of CO_2 leads to complete decarbonylation (Scheme 6.5), and mixtures of {[PhBP$^{iPr}_3$]Fe}$_2$(μ–O) (**6.10**), and [PhBP$^{iPr}_3$]Fe(CO)$_2$ (**6.11**) are observed, amongst other unidentified products. Though these reactions are reproducible in that **6.10** and **6.11** are always observed, the product distributions were found to vary between independent runs. Similar disparities in the product profile were also observed in the reaction between the well-defined iron(I) source, {[PhBP$^{iPr}_3$]Fe}$_2$(μ-N_2), and CO_2. Subsequent exposure of μ-O **6.10** to one equiv of either CO or CO_2 at -78 ^{o}C gives rise to incomplete conversion to several products, many of which correlate to the spectroscopically observed but unidentified products in the above reaction. Thus, the reactivity of **6.10** towards CO and CO_2 contributes to the variability in the product distribution from the reaction between "[PhBP$^{iPr}_3$]Fe" and CO_2.

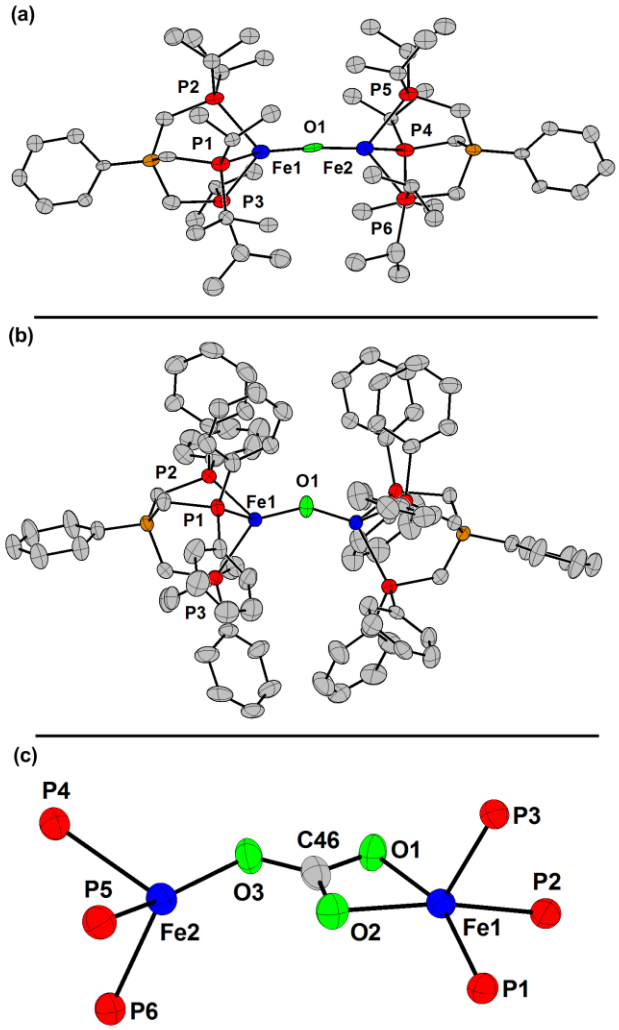

Figure 6.3. 50% thermal ellipsoid representation of (a) {[PhBP$^{iPr}_3$]Fe}$_2$(μ–O) (**6.10**), (b) {[PhBP$^{Ph}_3$]Fe}$_2$(μ–O) (**6.12**), and (c) the core atoms of {[PhBP$^{Ph}_3$]Fe}$_2$(μ-η^2:η^1-CO_3), (**6.15**). Hydrogen atoms, solvent molecules, and minor components of disorder are omitted for clarity. Select bond distances (Å) and angles (deg.) for **6.10**: Fe1–P1 2.523(5), Fe1–P2 2.441(6), Fe1–P3 2.464(5), Fe1-O1 1.786(16), Fe2-O1 1.794(16), P1–Fe–P2 88.82(18), P2–Fe–P3 92.10(18), P1–Fe–P3 86.98(3), P1-Fe-O1 135.2(4), P2-Fe1-O1 120.5(4), P3-Fe1-O1 117.2(4), B1-Fe1-O1 170.07(2), Fe1-O-Fe1 174.67(2). The bond distances and angles about Fe2 are similar to those of Fe1. Select bond distances (Å) and angles (deg.) for **6.12**: Fe1–P1 2.3953(11), Fe1–P2 2.3969(10), Fe1–P3 2.4096(10), Fe1-O1 1.7525(15), P1–Fe1–P2 88.96(4), P2–Fe1–P3 90.99(3), P1–Fe1–P3 92.94(4), P1-Fe1-O1 120.54(9), P2-Fe1-O1 116.08(11), P3-Fe1-O1

135.38(16), B1-Fe1-O1 167.9, Fe1-O-Fe1 147.7(3). Select bond distances (Å) for **6.15**: Fe1-P1 2.209(2), Fe1-P2 2.198(2), Fe1-P3 2.157(2), Fe2-P4 2.428(2), Fe2-P5 2.469(2), Fe2-P6 2.413(2), Fe1-O1 1.984(3), Fe1-O2 2.012(3), Fe2-O3 1.907(3), O1-C46 1.288(6), O2-C46 1.305(6), O3-C46 1.279(6)

Likewise, the *in situ* reduction of $[PhBP^{Ph}_3]FeCl$[21] under an atmosphere of CO_2 also results in complete decarbonylation, generating $\{[PhBP^{Ph}_3]Fe\}_2(\mu\text{–O})$ (**6.12**), $[PhBP^{Ph}_3]Fe(CO)_2$ (**6.13**),[21] and $\{[PhBP^{Ph}_3]Fe(CO)_2\}\{Na(THF)_5\}$ (**6.14**). This reaction is much cleaner and the product profile is more reproducible. Now, exposure of μ-O **6.12** to CO cleanly affords **6.13**, presumably with concomitant loss of CO_2. Also, CO_2 can reversibly insert into an Fe-O bond of **6.12** to generate the paramagnetic bridging carbonate $\{[PhBP^{Ph}_3]Fe\}_2(\mu\text{-}\eta^2\text{:}\eta^1\text{-}CO_3)$ (**6.15**). This reaction requires prolonged stirring at room temperature (days) or heating to 60 ^oC for 1 hour. Upon removal of the CO_2 atmosphere, **6.15** reverts back to **6.12**. Despite this equilibrium, crystals of **6.15** could be grown, and the solid-state structure of **6.15** clearly establishes the presence of a bridging carbonate (Figure 6.3).

The μ-O species **6.10** and **6.12** are unusual in that they are rare examples of diferrous bridging oxo species, $Fe_2(\mu\text{-O})$, the only other example being Holland's $\{L^{tBu}Fe\}_2(\mu\text{-O})$ (L^{tBu} = ArNC(^{t}Bu)CHC(^{t}Bu)Ar$^-$, Ar = 2,6-diisopropylphenyl).[27] The metrical parameters about each iron center in both **6.10** and **6.12** are highly similar (Figure 6.3), with the exceptions being that the phosphines are eclipsed in **6.12** and staggered in **6.10**, and that each iron center in **6.10** has one long and two short Fe-P bonds, whereas all three Fe-P bond distances are similar in **6.12**. Additionally, the bridging oxo is nearly linear in **6.10** (174.67(2)^o), whereas it is bent in **6.12** (147.7(3)^o),

the latter of which is reminiscent of the related nitride species, {[PhBP$^{Ph}_3$]Fe}$_2$(μ–N)$^-$ (Fe-N-Fe: 135.9(3)^o).[28] Despite these differences, both **6.10** and **6.12** have a similar room temperature solution magnetic susceptibility (ca. 2.8 μ_B). The low magnetic susceptibility, combined with the long Fe-P bond distances,[12,21,26] suggest that there is moderately strong antiferromagnetic coupling between two high-spin iron centers in both **6.10** and **6.12**.

Finally, the *in situ* reduction of the highly sterically encumbered precursor [PhBP$^{mter}_3$]FeCl[29] under a CO_2 atmosphere yields no net reaction, and [PhBP$^{mter}_3$]FeCl is the only iron containing species observed by NMR and IR spectroscopy. Additionally, in the *in situ* reductions of [PhBP$^{Ph}_3$]FeCl, [PhBP$^{iPr}_3$]FeCl and PhBP$^{mter}_3$]FeCl with CO_2, no stretches that would correspond to an oxalate are observed by IR spectroscopy.[30] Thus, reductive coupling of CO_2 to oxalate at tris(phosphino)borate supported iron(I) only occurs when the iron is supported by the [PhBP$^{CH2Cy}_3$] ligand scaffold. Moreover, this ligand scaffold gives rise to the exceptional diiron μ-O/μ-CO structure type, which to our knowledge, is the only species to exhibit the M_2(μ-O)(μ-CO) core.

*6.2.3 DFT Models of **6.1**-CO_2*

During the course of these studies, no mononuclear intermediates of the type "[PhBP$^{CH2Cy}_3$]Fe(CO_2)" (**6.1**-CO_2) could be observed by either VT NMR or VT react-IR spectroscopy. To try to gain insight into the mode of CO_2 coordination, the spin-state, and the ability of solvent to also coordinate such a species, DFT studies were performed.

Though initial calculations used the full [PhBP$^{CH2Cy}_3$] ligand, we found that DFT could not reproduce the floppiness of the ligand, whereby the cyclohexylmethyl substituents can point up towards a coordinated ligand (i.e., PR_3 or CO_2) or down towards the [PhBP$^{CH2Cy}_3$] ligand backbone. As we have obtained crystal structures in which all of the cyclohexylmethyl substituents point down (i.e., the structure of μ-O/μ-CO **6.3**), thereby rendering the iron center more sterically accessible, we opted to use the truncated [PhBP$^{Me}_3$] ligand, in which the cyclohexylmethyl substituents have been replaced by methyl groups. Though this truncated ligand does not take into account energies that are affected by steric interactions, the calculations are pedagogical in that the spin distribution should not be affected by this substitution. Geometry optimizations were carried out on CO_2 adducts of **6.1** that coordinate zero, one, or two THF molecules, in both S = ½ and S = 3/2 spin states. To confirm that the minimized structures corresponded to an intermediate and not a transition state, a frequency analysis was also performed. A total of ten structures were targeted (Figure 6.4), of which only six could be satisfactorily minimized. Nonetheless, these results are instructive.

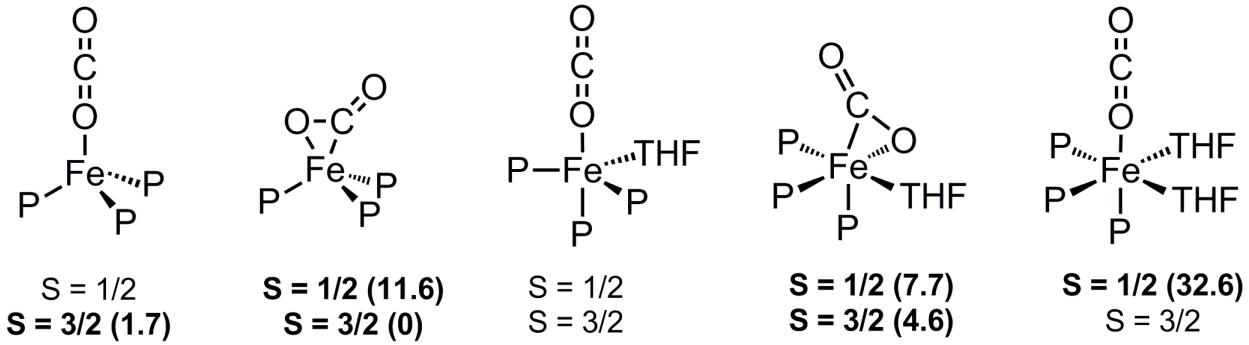

Figure 6.4. [PhBP$^{Me}_3$]Fe(CO_2)(THF)$_x$ structures and spin-states that were investigated by DFT methods. The structures/spin-states that could satisfactorily be minimized are bolded, with their relative energy (kcal mol^{-1}) in parenthesis. The energies were normalized by adding the energy of

either one or two THF molecules (calculated using the same basis set/level of theory). Geometry optimizations on η^2-*OC*O and η^1-*C*O_2 species both minimized to the η^2-*OC*O bonding mode. See the experimental section for more details on the calculations.

In the absence of THF, minimized structures can be obtained for the side-on coordinated species [PhBP$^{Me}_3$]Fe(η^2-*OC*O) (*S* = ½ and 3/2), as well as for the end-on coordinate species [PhBP$^{Me}_3$]Fe(η^1-*O*CO) (*S* = 3/2) (Figure 6.4). The optimized structure for the intermediate-spin [PhBP$^{Me}_3$]Fe(η^2-*OC*O) is shown in Figure 6.5. This species is 11.6 kcal/mol lower in energy than its low-spin congener, and 1.7 kcal/mol lower in energy than the end-on isomer [PhBP$^{Me}_3$]Fe(η^1-*O*CO). A minimized structure for [PhBP$^{Me}_3$]Fe(η^2-*OC*O)(THF), in which the CO_2 coordinates side-on and a single THF molecule also coordinates the iron, was also obtained. Now the *S* = 3/2 state is only 3.1 kcal/mol lower in energy than the *S* = ½ state. In these five minimized structures, the spin density almost exclusively resides on the iron center, with less than 1 % residing on the O and C atoms of the coordinated CO_2 ligand.

A minimized structure for low-spin [PhBP$^{Me}_3$]Fe(η^1-*O*CO)$(THF)_2$ could also be obtained (Figure 6.5). This structure shows appreciable activation of the CO_2 ligand, which is no longer linear; the O-C-O angle is 136^o. Both of the C-O distances are elongated relative to that of free CO_2, with the Fe-(O*C*-*O*) distance being 1.22 Å, and the Fe-(*O*-*C*O) distance being 1.26 Å (free CO_2: 1.16 Å).[31] The Fe-O distance of 2.04 Å suggests little or no π-bonding between the Fe and CO_2. Now, 77 % of the spin density resides on the CO_2 carbon atom, with the remaining density being located primarily on the Fe and O's of the CO_2. The combined metrical parameters and spin-density suggest

an iron(II) resonance structure with a carbon-based radical, Fe^{II}-O-$C^{\bullet -}$=O, as opposed to a CO_2 adduct of iron(I), Fe^{I}-O=C=O. This electronic structure is consistent with the observation that reductive coupling of CO_2 ensues in coordinating solvents.

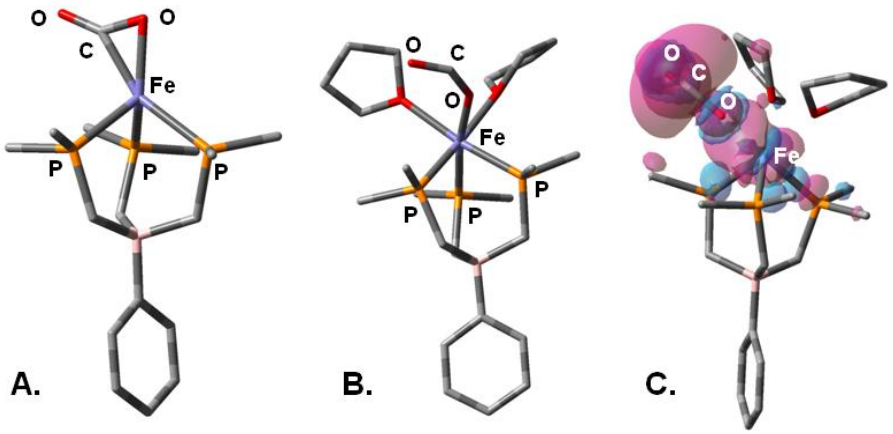

Figure 6.5. Theoretically predicted geometry for Fe(η^2-*OC*O) quartet (A), and Fe(η^1-*O*CO)$(THF)_2$ doublet (B), and the calculated spin-density of Fe(η^1-*O*CO)$(THF)_2$ (C) (DFT, B3LYP/6-311++G**). Select bond distances (Å) and angles for Fe(η^2-*OC*O) quartet: Fe-O, 2.02; Fe-C, 2.00; C-O (bound), 1.25; C-O (distal), 1.20, O-C-O, 143.5°. Select bond distances (Å) and angles for Fe(η^1-*O*CO)$(THF)_2$ doublet: Fe-O, 2.04; Fe-THF_{ave}, 2.25; O-C (bound), 1.26; O-C (distal), 1.22; O-C-O, 136.0°

6.3 Discussion

6.3.1 The Role of the Auxiliary [$PhBP^R_3$] Ligand

The role that the auxiliary [$PhBP^R_3$] ligand plays on the outcome of the reaction between iron(I) and CO_2 was established by comparing the product profiles of the *in situ* reductions of [$PhBP^R_3$]FeCl in the presence of CO_2. Whereas phosphine adducts

$[PhBP^{CH2Cy}{}_3]Fe(PR_3)$ react with CO_2, the corresponding adduct species $[PhBP^{iPr}{}_3]Fe(PMe_3)$[22] and $[PhBP^{Ph}{}_3]Fe(PPh_3)$,[21] do not yield a reaction with CO_2 (1 atm, RT), precluding their use to establish the role of the auxiliary ligand.

The similar reduction potentials for $[PhBP^{CH2Cy}{}_3]FeCl$ and $[PhBP^{iPr}{}_3]FeCl$ (respective quasi-reversible reductions at -1.94 and -2.03 V vs. Fc/Fc^+),[12,26] combined with the similar ν(CO) for $[PhBP^{CH2Cy}{}_3]Fe(CO)_2$ and $[PhBP^{iPr}{}_3]Fe(CO)_2$ (1959/1894 cm^{-1} and 1955/1888 cm^{-1}, respectively) indicate that the two ligands have similar electron-releasing properties. However these ligands lend a different degree of steric protection, which is best exemplified in the ease of preparing stable 4-coordinate iron(I) phosphine adducts of the type $[PhBP^{R}{}_3]Fe(PR'_3)$ (R' = Me, Ph, Cy). Whereas the $[PhBP^{CH2Cy}{}_3]$ ligand platform can be used to prepare PMe_3-, PPh_3- and PCy_3-capped iron(I) adducts,[12] only the PMe_3-capped iron(I) species can be prepared using the $[PhBP^{iPr}{}_3]$ ligand scaffold[22] (respective cone angles of PCy_3, PPh_3 and PMe_3 are ca. 170°, 145° and 118°).[32] Thus, the observation that no oxalate forms when $[PhBP^{iPr}{}_3]FeCl$ is reduced in the presence of CO_2 suggests that the steric protection offered from the auxiliary ligand precludes this reaction pathway and complete decarbonylation is instead observed. Whereas the partial decarbonylation product **6.2** is formed with the $[PhBP^{CH2Cy}{}_3]$ ligand scaffold, only products associated with complete decarbonylation (**6.10** and **6.11**) are observed with the $[PhBP^{iPr}{}_3]$ ligand scaffold; the partial decarbonylation μ-O/μ-CO product is likely not stable for steric reasons.

The *in situ* reduction of $[PhBP^{Ph}{}_3]FeCl$ with CO_2 also results in complete decarbonylation. The aryl substituted ligand is less electron-donating than the alkyl counterparts (the quasi-reversible reduction potential of $[PhBP^{Ph}{}_3]FeCl$ is -1.61 V vs.

Fc/Fc^{+}),[21] and is somewhat between [$PhBP^{iPr}_3$] and [$PhBP^{CH2Cy}_3$] in the steric protection it affords, as [$PhBP^{Ph}_3$]Fe(PPh_3) can be generated,[21] but not [$PhBP^{Ph}_3$]Fe(PCy_3). Thus, a direct comparison between [$PhBP^{Ph}_3$] and [$PhBP^{CH2Cy}_3$] is more difficult as they differ in both their steric and electronic properties. We simply note that here too, no reductive coupling of CO_2 is observed.

Finally, the *in situ* reduction of [$PhBP^{mter}_3$]FeCl yielded no net reaction with CO_2. This ligand offers similar electronic-donating properties as [$PhBP^{Ph}_3$] ligand (the quasi-reversible reduction potential of [$PhBP^{mter}_3$]FeCl is at -1.52 V vs. Fc/Fc^{+}), but the *m*-terphenyl substituents afford a much deeper binding pocket, making bimolecular reactions less feasible. CO_2 presumably binds to some extent, but cannot readily go on to product.

Combined, these results suggest that a sterically accessible iron(I) center is required to facilitate the reductive coupling pathway. When this requirement is not met, decarbonylation to generate bridging oxo species (**6.2**, **6.10**, **6.12**) instead occurs. Such decarbonylation reactions are well precedented for early transition metals,[33] but there are fewer examples of such transformations at mid-to-late transition metals.[34] That no decarbonylation is observed in the reaction between *in situ* generated [$PhBP^{mter}_3$]Fe(I) and CO_2 suggests that the irreversible C-O bond cleavage step likely involves two iron centers.

6.3.2 The Role of Solvent in CO_2 Reductive Coupling

The ability of [$PhBP^{CH2Cy}_3$]Fe(PR_3) to reduce CO_2 by one electron to give oxalate **6.3** or to reduce CO_2 by two electrons to give the partial decarbonylation product **6.2** is solvent dependent. Thus, in both benzene and THF, reductive coupling to give oxalate occurs preferentially over reductive cleavage (Table 6.1). This contrasts with the reactivity in MeCy, in which reductive cleavage is exclusively observed. The solvent dependence of the reaction could be attributed to: (i) the different solubility of CO_2 in the solvents employed, (ii) the different polarities of the solvents, or (iii) the ability of the solvent to coordinate the iron center.

If the concentration of CO_2 affects the outcome of the reaction (i), then the product distribution of the reaction between PPh_3-capped **6.7** and CO_2 in various solvents should mirror the solubility of CO_2 in the solvents. Assuming that the Henry's law constant for CO_2 in ^{n}heptane is similar to that of MeCy, and that the value for toluene is similar to that of benzene, then the solubility of CO_2 should increase in the order: THF < MeCy < benzene (Henry's law constants at 25 ^{o}C for THF, ^{n}heptane, and toluene are 44.9, 84, and 98.1 atm^{-1}, respectively).[35] If solubility was limiting the reaction outcome for the reaction between **6.7** and CO_2, then a distinct outcome should be observed in THF relative to that in benzene and MeCy. This is not the case, as the reaction in MeCy is distinct from that in either benzene or THF. Thus the solubility of CO_2 (and hence the relative concentrations of iron(I) and CO_2) does not control the outcome of the reaction.

To determine whether solvent polarity (ii) or solvent coordination (iii) controls which reduction pathway ensues, the reaction between **6.8** and CO_2 was carried out in THF, 2-Me-THF and 2,5-diMe-THF, and the product profile of these reactions were

compared with that of the reaction run in MeCy. That the relative amounts of **6.2** and **6.3** formed in the reaction between **6.8** and CO_2 gradually changes as the ability of the solvent to coordinate decreases clearly implicates that solvent coordination (scenario iii) and not solvent polarity (scenario ii) is responsible for the reaction outcome (Figure 6.2).

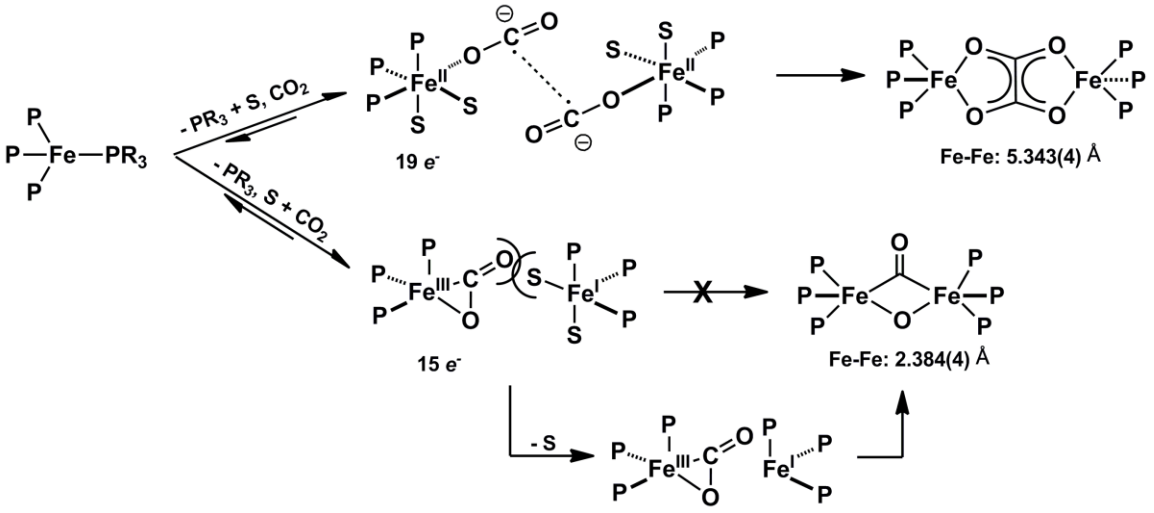

Scheme 6.6.

To account for the facilitation of CO_2 reductive coupling by solvent-coordinated iron(I) species, an electronic argument is proposed, which is complimented by steric arguments (Scheme 6.6). In this mechanistic scenario, the radical coupling reaction to give μ-oxalate **6.3** ensues from a 19-electron Fe(I) complex, whereas the reaction to give μ-O/μ-CO **6.2** occurs from a non-electronically saturated iron center. Coordination of two solvent molecules and CO_2 to an Fe(I) center gives a formally 19-electron complex, $[PhBP^{CH2Cy}{}_3]Fe(\eta^1\text{-}OCO)(THF)_2$ (Scheme 6.6), in which the unpaired electron could be pushed out from the iron onto the coordinated CO_2 ligand. Subsequent C-C coupling would then generate **6.3** (with loss of the coordinating solvent). This idea draws parallels

to the related reductive coupling of benzene that is mediated by 19-electron metal species.[17a] Consistent with this notion, the DFT minimized structure of the 19-electron species [PhBP$^{Me}_3$]Fe(η^1-*O*CO)(THF)$_2$ features 77 % of the spin-density on the CO_2 carbon atom, whereas the spin-density on the electronically unsaturated 4- and 5-coordinate species is iron centered (*vide supra*). Note that for this electronic argument, the steric effects of the auxiliary ligand and coordinated solvent molecules also play a role. In order to achieve a 19-electron configuration, the iron must be able to coordinate two solvent molecules as well as CO_2 (*vide supra*); the inability to do so leads to decarbonylation reactions. Hence, reductive coupling of CO_2 is only observed for the least sterically encumbering ancillary ligand. Additionally, solvent coordination should add steric bulk about each iron center, disfavoring the formation of dimeric intermediate and product species. Though both **6.2** and **6.3** are dimeric species, the steric impact of solvent coordination should be more marked for formation of **6.2** (Scheme 6.6). The coupling reaction to generate **6.3** occurs between two ligand radicals, and hence the reaction is removed from the iron centers, which are 5.343(4) Å apart in the resulting μ-oxalate **6.3**. In contrast, the reaction to generate μ-O/μ-CO **6.2** likely occurs between the iron center of **6.1** and the coordinated CO_2 of **6.1**-CO_2. Hence, the added bulk induced by solvent coordination would have a more pronounced effect on the rate of the reaction, as the Fe-Fe distance in **6.2** is a mere 2.384(4) Å.

6.3.3 Overall Mechanistic Summary

The scarcity of both M(η^1-*O*CO) species and well-defined systems that couple CO_2 to oxalate renders it difficult to draw solid conclusions. There is only one example of an isolated M(η^1-*O*CO) species.[36] Meyer and co-workers have synthesized and studied ((AdArO)$_3$tacn)U^{IV}(η^1-*O*CO) (((AdArOH)$_3$tacn) = 1,4,7-tris(3-adamantyl-5-tert-butyl-2-hydroxybenzyl)1,4,7-triazacyclononane), which features a linear $CO_2^{\bullet-}$ ligand. The linearity in this system is likely manifested by the extreme bulk of the ligand. In this system, subsequent C-C coupling to oxalate does not ensue.

Reductive coupling of CO_2 to oxalate has been observed at the lanthanides[9] and at iron,[12] nickel,[11] titanium,[13] and copper.[10] In the copper mediated reduction that generates {(LCu)$_2$(μ-oxalate)}{BPh_4}$_2$ (L = N,N',N"-triallyl-1,4,7-triazacyclanonane),[10a] a carbonate radical is invoked as an intermediate because the oxalate product can be generated in the reaction of copper(I) with either CO_2 or $CsHCO_3$. In other systems,[9a,10b] $CO_2^{\bullet-}$ has been invoked as an intermediate. In no instance has the radical intermediate been observed. Though the putative [PhBP$^{CH2Cy}_3$]Fe(η^1-*O*CO)(THF)$_2$ radical species could not be observed, the combined data is consistent with its formation.

A mechanistic scheme that is consistent with the experimental and computational data is shown in Scheme 6.7. In the reaction between phosphine-capped iron(I) and CO_2, phosphine dissociation first occurs to give **6.1**, either as a solvated or cyclometallated species. That the reaction between **6.7** and CO_2 is inhibited by PPh_3, and that the benzene adduct **6.4** is observed at intermediate reaction times (when the reaction is carried out in benzene), is consistent with this first step. Subsequent coordination of CO_2 forms a

reactive adduct species that is solvent dependent. In coordinating solvents, a 19-electron species of the type [PhBP$^{CH2Cy}_3$]Fe(η^1-*O*CO)(THF)$_2$ or [PhBP$^{CH2Cy}_3$]Fe(η^1-*O*CO)(η^4–C_6H_6) is proposed as an unstable intermediate. Subsequent C-C coupling generates μ-oxalate **6.3**. Such a species is invoked based on the results of the DFT calculations (which show significant spin density on the CO_2 carbon atom of [PhBP$^{Me}_3$]Fe(η^1-*O*CO)(THF)$_2$), and the parallel benzene coupling reaction (i.e., converting **6.4** to **6.5**) and the reaction between **6.1** and azobenzene to generate μ-azobenzene **6.6** (which features a significantly elongated N-N bond). In the absence of coordinating solvents (or in the presence of a single THF molecule), 15- or 17-electron CO_2 adduct intermediates are proposed. Though these species are drawn as η^2-*OC*O adducts of iron in Scheme 6.7, the DFT calculations suggest that both η^1-*O*CO and η^2-*OC*O species may be viable intermediates. These species interact with a second equivalent of iron(I) to give the decarbonylation product **6.2**. The notion that different M-CO_2 adduct isomers gives rise to different reaction profiles has also been proposed for a related nickel system.[11] Though solvent coordination facilitates the reductive coupling pathway, it is possible that oxalate **6.3** can also form via a solvent-free iron(I) CO_2 adduct (Scheme 6.7, dotted line), as **6.3** forms as a minor product in the reaction between **6.1** and CO_2 in MeCy. Likewise, **6.2** might also be accessible from solvated iron(I) CO_2 adducts.

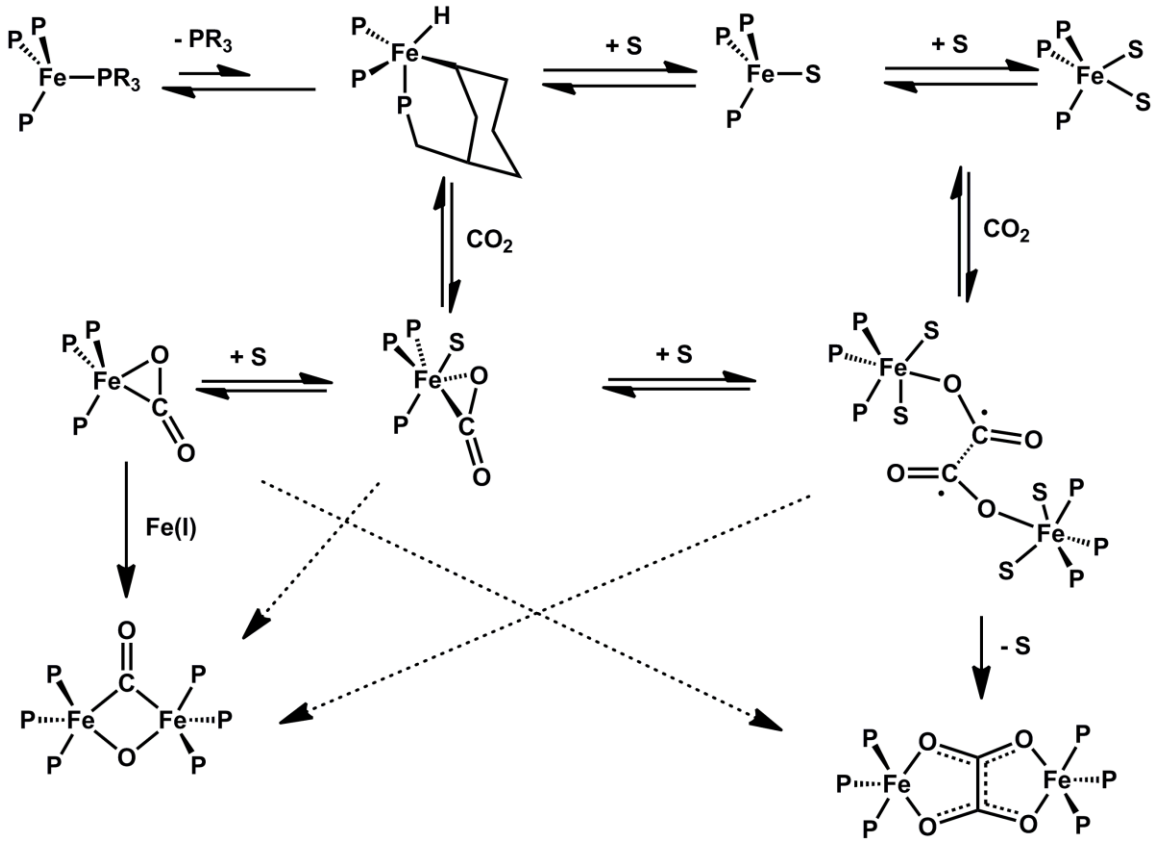

Scheme 6.7.

Overall, we have shown that once the reactivity of the iron(I) synthon is subdued such that selectivity can be achieved, the reaction between iron(I) and CO_2 becomes selective for either CO_2 reductive coupling to yield μ-oxalate **6.3**, or CO_2 decarbonylation to give μ-O/μ-CO **6.2**. The selectivity is imparted by coordination of the solvent to the iron center, with reductive coupling being favored in coordinating solvents. We propose that this solvent coordination results in a 19-electron intermediate species $[PhBP^{CH2Cy}{}_3]Fe(\eta^1\text{-}OCO)(THF)_2$, which undergoes radical coupling. The combined results emphasize the importance that both the electronic structure and solvent

coordinating a metal center can have on a reaction outcome, and suggests that the one-electron reduction of CO_2 might be more accessible from electronically saturated and sterically unsaturated metal complexes.

6.4 Experimental Section

6.4.1 General Considerations

All manipulations were carried out using standard Schlenk or glove-box techniques under a dinitrogen atmosphere. Unless otherwise noted, solvents were deoxygenated and dried by sparging with N_2 followed by passage through an activated alumina column. Non-halogenated solvents were tested with a standard purple solution of benzophenone ketyl in THF to confirm effective oxygen and moisture removal. Deuterated solvents were purchased from Cambridge Isotopes Laboratories, Inc. and were degassed and stored over activated 3-Å molecular sieves prior to use. Elemental analyses were performed by Desert Analytics, Tucson, AZ.

6.4.2 Spectroscopic Methods

NMR data was collected at the MIT department of chemistry instrumentation facility or at the Caltech High-resolution NMR facility. Both Varian 300 MHz and 500 MHz spectrometers were used to record the ^{1}H NMR and ^{31}P NMR spectra at ambient temperature. ^{1}H chemical shifts were referenced to residual solvent, while ^{31}P NMR chemical shifts were referenced to 85% H_3PO_4 at δ 0 ppm. EPR data was collected at the MIT department of chemistry instrumentation facility and were carried out on a Bruker

EMX spectrometer outfitted with 13" magnets, an ER 4102ST cavity and a newly upgraded Gunn diode microwave source producing X-band (8-10 GHz) radiation outfitted with a cryo-cooled cavity. Spectra were recorded in a methylcyclohexane glass at 4K, and the data were fit using winEPR.[37] IR measurements were obtained with a KBr solution cell or a KBr pellet using a Bio-Rad Excalibur FTS 3000 spectrometer controlled by Varian Resolutions Pro software set at 4 cm^{-1} resolution. Solution magnetic moments were measured using Evans method.[38] Optical spectroscopy measurements were taken on a Cary 50 UV-Vis spectrophotometer using a 1 cm two-window quartz cell sealed with standard ground-glass joints or Teflon plugs. The equilibrium between **1** and **7** was determined as described elsewhere.[39]

6.4.3 X-Ray Crystallography Procedures

Data were collected at the X-ray crystallography facility at Caltech or at the MIT department of chemistry X-ray diffraction facility. Low-temperature diffraction data were collected on a Siemens or Bruker Platform three-circle diffractometer coupled to a Bruker-AXS Smart Apex CCD detector with graphite-monochromated Mo or Cu Kα radiation (λ = 0.71073 or 1.54178 Å, respectively), performing φ-and ω-scans. The structures were solved by direct or Patterson methods using SHELXS[40] and refined against F^2 on all data by full-matrix least squares with SHELXL-97.[41] All non-hydrogen atoms were refined anisotropically. All hydrogen atoms were included into the model at geometrically calculated positions and refined using a riding model. The isotropic

displacement parameters of all hydrogen atoms were fixed to 1.2 times the U value of the atoms they are linked to (1.5 times for methyl groups).

The structures were refined using established methods.[42] Several of the structures reported suffered from disorder in parts of the [$PhBP^{R}_{3}$] ligand and/or disorder of solvent molecules (some over more than two independent positions). All disorders were refined with the help of similarity restraints on 1-2 and 1-3 distances and displacement parameters as well as rigid bond restraints for anisotropic displacement parameters. All close contacts, both inter and intramolecular, reported by the Platon validation software[43] involve at least one partner from a minor component of a disorder. While it is conceivable that more components of the molecule(s) are disordered and parameterization of these disordered components would remove the close contacts, the data at hand did not allow for further modeling of the disorder. Specific refinement details for each structure are included in the .cif file.

6.4.4 DFT Methods

Density functional calculations were carried out using the Gaussian03 suite[44] using the unrestricted B3LYP functional. In most instances, the 6-31++g(d,p) basis set was used for geometry optimizations, the 6-311g++(d,p) basis set was used for single point energy and frequency calculations. For geometry optimizations, coordinates were taken from the solid-state structures of [$PhBP^{CH2Cy}_{3}$]Fe(PMe_3). For structures that could be minimized, the total energies were compared by adding the energy of THF, calculated

at the same level of theory/basis set. Molecular orbital plots were generated using GaussView 4.1[45] with isocontor values of 0.002 (density).

Geometry optimizations were carried out on [PhBP$^{Me}_3$]Fe(CO_2)(THF)$_x$, where x = 0, 1, or 2, in both the doublet and quartet states, with the CO_2 bound either (η^2-*OC*O) or (η^1-*O*CO), for a total of 10 structures (Figure 6.4). The *S* = ½ Fe(η^1-*O*CO)(THF) species could be minimized, but the resulting structure had a linear CO_2 molecule ca. 5 Å away from the Fe center. As it had two imaginary vibrations associated with the CO_2, it was not considered a viable intermediate. The minimized structure of *S* = 3/2 Fe(η^1-*O*CO)(THF) was similar to that of the S = ½ congener, and hence no subsequent single point calculations were pursued. Both *S* = 1/2 Fe(η^1-*O*CO) and *S* = 3/2 Fe(η^1-*O*CO)$(THF)_2$ suffered from spin contamination,[46] and their geometries could not be minimized despite trying several basis sets/levels of theory. The remaining structures converged.

6.4.5 Starting Materials and Reagents

Compounds **6.1**, **6.4**, **6.12** {[PhBP$^{iPr}_3$]Fe}$_2$(μ-N_2), and [PhBP$^{R}_3$]FeCl (R = Ph, ^{i}Pr, CH_2Cy, *m*ter), were prepared according to literature procedures.[9e,12a,15a,19-20] All other reagents were purchased from commercial vendors and used without further purification.

6.4.6 Synthesis and Characterization of Complexes

Further characterization of 6.1. UV-vis (methylcyclohexane) λmax, nm (ε, M-1 cm-1): 340 (sh, 2200), 390 (sh, 1500), 690 (220), 920 (sh, 290). Evans Method (d14-methylcyclohexane): 2.3 μB.

Synthesis of {[PhBP$^{CH2Cy}_3$]Fe}$_2$(μ-oxalate), 6.3.

1) Sodium amalgam (0.48 wt %, 1.12 mmol) and a magnetic stir bar were added to a frozen solution of [PhBP$^{CH2Cy}_3$]FeCl (0.4013 g, 0.447 mmol) in 20 mL THF in a 100 mL Schlenk tube fitted with a Teflon valve. The vessel was evacuated, and allowed to warm to 0 ^{o}C in an acetone bath followed by an ice bath. One atmosphere of CO_2 was added, and the reaction was slowly stirred. The color changed from yellow to red/brown over 2.5 h, at which point the vessel was degassed. The solution was filtered through a thick Celite plug, and the remaining solids generously washed with benzene. The resulting solution was concentrated to a solid under partial vacuum. The resulting solids were extracted into 50 mL of benzene, filtered through Celite, and again concentrated to a solid under partial vacuum. The solid was washed with petroleum ether, extracted into benzene, and filtered through Celite. The resulting solution was lyophilized to give a red/brown solid (0.202 g, 50.1 %). Crystals suitable for X-ray diffraction can be grown from a THF/petroleum ether solution at -35 ^{o}C.
2) A solution of [PhBP$^{CH2Cy}_3$]FeCl (0.5647 g, 0.6293 mmol) and PCy_3 (0.2001 g, 0.0.6922 mmol) in 20 mL THF was added to an Na/Hg amalgam (39.4 wt %, 0.7449 mmol), and subsequently stirred for 2 h. The reaction was filtered through a Celite-lined frit, diluted to 30 mL (ca. 20 mM), and transferred to a 100 mL Schlenk tube fitted with a stir bar and Teflon plug. The vessel was attached to a calibrated bulb (56.30 mL), and the solution frozen with liquid N_2. After evacuating the headspace, CO_2 was added to the bulb and condensed (2 x 51.3 cm

Hg, 3.15 mmol) into the reaction vessel. The reaction was warmed to room temperature and stirred for 24 h, during which the solution changed color from yellow to red-brown. The volatiles were removed and the resulting solids were triterated with pentane and collected on a frit. The pentane was concentrated, and the remaining solids were extracted into minimal THF. Both fractions were cooled to -35^{o}C, allowing for **3** to crystallize out (pentane: 0.1504 g, 26.5 %; THF: 0.2182 g, 38.5 %).

^{1}H NMR (C_6D_6, 300 MHz) δ 25.3, 14.9, 13.5, -0.5, -0.7, -1.29, -1.5, -2.7, -3.3, -3. 7, -4.4, -6.2 (bs), -17.7 (bs). IR (KBr): 1644 cm^{-1}. UV-vis (C_6H_6) λ_{max}, nm (ε, M^{-1} cm^{-1}): 775 (1000), 480 (sh, 760), 400 (sh, 1600), 330 (2600). Evans Method (C_6D_6): 4.3 μ_B. Anal. Calcd. For $C_{104}H_{178}B_2Fe_2O_4P_6$: C 68.95; H 9.90; N 0. Found: C 68.42; H 9.31; N <0.05.

Synthesis of {[PhBP$^{CH_2Cy}{}_3$]Fe}$_2$(μ-η^5:η^5-1,1'-bicyclohexadienyl), 6.5. A 5 mL benzene solution of **6.4** (0.050 g, 27.75 μmol) was heated at 60 °C for 20 h. The solution changed from dark green to yellow with precipitation of orange microcrystals. Solids were collected and washed with petroleum ether, benzene, and THF (0.048 g, 92% yield). Single crystals suitable for X-ray diffraction can be grown from vapor diffusion of petroleum ether into a dichloromethane solution. ^{1}H NMR ($CDCl_3$, 500 MHz) δ 7.33 (m, 4H, H_o of Ph), 7.20 (t, 4H, J = 7.5 Hz, H_m of Ph), 7.02 (t, 2H, J = 7.0 Hz, H_p of Ph), 5.48 (br s, 2H), 4.15 (br s, 4H), 2.12 (br s, 4H), 1.99 (m, 12H), 1.75 – 1.66 (84H), 1.32 – 0.97

(62 H), 0.38 (br s, 12H). ^{31}P NMR (121 MHz, CD_2Cl_2): δ 44.5 (br) ppm. Anal. Calcd. for $C_{114}H_{190}B_2Fe_2P_6$: C 72.84; H 10.19; N 0. Found: C 72.65; H 9.77; N <0.05.

Synthesis of {[PhBP$^{CH_2Cy}{}_3$]Fe}$_2$(μ-η^5:η^5-azobenzene), 6.6: To a 10 mL THF solution of **6.1** (0.1178 mmol), azobenzene (10.7 mg, 58.72 μmol) was added, and the reaction was stirred for 2 h. The dark-red solution was concentrated under reduced pressure to dryness. The residue was washed with petroleum ether and ether until the washings were nearly colorless. The residue was then extracted with dichloromethane and concentrated under reduced pressure to a red powder (0.075 g, 38% yield). Single crystals suitable for X-ray diffraction can be grown from vapor diffusion of diethyl ether into a dichloromethane solution. ^{1}H NMR (300 MHz, $CDCl_3$): δ 7.31 (d, *J* = 7.5 Hz, 2H), 7.20 (t, *J* = 7.5 Hz, 2H), 7.04 (t, *J* = 7.5 Hz, 1H), 5.07 (m, 2H), 4.91 (m, 1H), 4.45 (m, 1H), 3.81 (m, 1H), 1.97 (m, 6H), 1.73 - 1.67 (m, 42H), 1.26 – 0.99 (m, 30H), 0.44 (br s, 6H). ^{13}C NMR (126 MHz, CD_2Cl_2): δ 166.2 (br), 146.4, 131.8, 127.3, 123.5, 96.0, 95.0, 69.6, 68.1, 62.2, 43.1 (br), 40.9 (br), 37.6, 37.2, 37.1, 36.0, 35.8, 27.4, 27.1, 26.8, 14.3 (br m). ^{31}P NMR (121 MHz, CD_2Cl_2): δ 47.4 ppm. UV-vis (C_6H_6) λ_{max}, nm (ε, M^{-1} cm^{-1}): 465 (19,700), 324 (35,500). Anal. Calcd. for $C_{114}H_{188}B_2Fe_2N_2P_6$: C 71.84; H 9.94; N 1.47. Found: C 72.13; H 9.64; N 1.57.

Synthesis of [PhBP$^{CH2Cy}{}_3$]FePPh$_3$, 6.7. Triphenylphosphine (0.0963 g, 0.367 mmol) was added as a solid to a stirring solution of **6.1** (0.3295 g, 0.367 mmol) in 20 mL of THF. The reaction mixture was stirred for 20', during which the color changed from lime green

to sanguine orange. The solution was concentrated under reduced pressure to dryness, extracted with benzene, and filtered through a glass wool pipette. The solution was concentrated under reduced pressure to give analytically pure solids (0.3369 g, 82%). Single crystals suitable for X-ray diffraction can be grown from a benzene/petroleum ether mixture at -35 ^{o}C. ^{1}H NMR (d_8-THF, 300 MHz) δ 54 (bs), 13.31, 9.73, 8.57, 7.92, 7.30, 7.04, 4.67, 3.52, 3.40, 2.57, 2.31, 1.95, 1.88, 1.67, 1.55, 1.11, -8 (bs). UV-vis (THF) λ_{max}, nm (ε, M^{-1} cm^{-1}): 470 (sh, 780), 365 (2900), 260 (sh, 12800). Evans Method (C_6D_6): 4.2 μ_B. Anal. Calcd. For $C_{69}H_{104}BFeP_4$: C 73.72; H 9.33; N 0. Found: C 73.56; H 9.14; N 0.

Synthesis of [PhBP$^{CH2Cy}_3$]FePCy$_3$, 6.8. A solution of [PhBP$^{CH2Cy}_3$]FeCl (0.1070 g, 0.119 mmol) in 10 mL of THF was added to Na/Hg (0.39 wt %, 0.183 mmol). The reaction stirred for 1.5 h, during which the color changed from yellow to pale green. The solution was decanted off the amalgam, and the volatiles removed under reduced pressure. The residue was triturated with pentane, and the solids extracted into MeCy. The solution was filtered through a Celite-lined frit, and the volatiles were removed under reduced pressure (0.1300g, 96%). ^{1}H NMR (d_8-THF, 300 MHz) δ 50 (bs), 9.7, 8.2, 7.9, 7.3, 7.1, 6.14, 3.2, 2.9, 2.6, 1.0, -1.7, -9.4 (bs). UV-vis (THF) λ_{max}, nm (ε, M^{-1} cm^{-1}): 325 (sh, 2500), 996 (sh 330). UV-vis (methylcyclohexane) λ_{max}, nm (ε, M^{-1} cm^{-1}): 320 (sh, 5280), 978 (sh, 760). Evans Method (*d_8*-THF): 3.9 μ_B. Anal. Calcd. For $C_{69}H_{122}BFeP_4$: C 72.55; H 10.76; N 0. Found: C 72.39; H 10.59; N 0.

Synthesis of {[PhBP$^{CH2Cy}_3$]Fe(CO)}$_2$(μ-oxalate), 6.9. {[PhBP$^{CH2Cy}_3$]Fe}$_2$(μ-oxalate) (0.0612 g, 0.074 mmol) was dissolved in 15 mL of THF and transferred to a 25 mL Schlenk tube fitted with a stir bar. The tube was fitted with a calibrated bulb (3.89 cm^{-1}). The vessel was placed in a dry ice/acetone bath, and CO was added to the bulb (35 cm Hg, 0.074 mmol). The gas was introduced to the stirring solution, and the color changed from brown to rose-red over 2 h. Volatiles were removed under reduced pressure. The resulting solids were extracted into benzene, filtered through Celite, and lyophilized to give a brown solid (0.0527 g, 82.4%). Crystals suitable for X-ray diffraction can be grown from toluene at -35 ^{o}C. ^{1}H NMR (C_6D_6, 300 MHz) δ 7.91 (d, J = 7.5 Hz), 7.51 (t, J = 7.5 Hz), 7.24 (t), 1.0-2.5 (m). ^{31}P NMR (C_6D_6, 121.4 MHz): 50.81 (d, J = 67.7 Hz, 4P), 25.09 (t, J = 67.7 Hz, 2P). IR (KBr): 1945, 1634 cm^{-1}. UV-vis (THF) λ_{max}, nm (ε, M^{-1} cm^{-1}): 548 (270), 398 (sh, 2200), 293 (7900), 245 (19,800). Anal. Calcd. For $C_{106}H_{178}B_2Fe_2O_6P_6$: C 68.17; H 9.61; N 0. Found: C 67.48; H 9.35; N < 0.05.

Synthesis of {[PhBP$^{iPr}_3$]Fe}$_2$(μ-O), 6.10. Solid [PhBP$^{iPr}_3$]FeCl (0.2553 g, 0.446 mmol) and sodium amalgam (0.48 wt %, 1.17 mmol), and a stir bar were transferred to a 25 mL Schlenk tube fitted with a Teflon valve. THF (13 mL) was vac-transferred onto the solids, and the yellow solution was warmed to 0^{o}C in an acetone bath followed by an ice bath. An atmosphere of CO_2 was added to the vessel, and the reaction was stirred slowly for 2 h to give a red solution. The ice bath was removed, and the reaction was vigorously stirred for an additional 2 h before being degassed. The solution was filtered through Celite, and the volatiles removed. IR (KBr): 1984, 1956, 1892 cm^{-1}. The remaining solids were extracted into benzene, filtered, and lyophilized. The solids were washed with

petroleum ether, and the remaining solids crystallized from THF in a vapor diffusion chamber containing MeCy (0.0368 g, 15.2%). Crystals suitable for diffraction can be grown via vapor diffusion of petroleum ether into a benzene solution. ^{1}H NMR (C_6D_6, 300 MHz) δ 27.3, 15.6, 10.8, 10.0 (t, J = 6 Hz), -0.26, -5.1. UV-vis (THF) λ_{max}, nm (ε, M^{-1} cm^{-1}): 948 (180), 624 (sh, 120), 535 (sh, 390), 470 (sh, 910). Evans Method (C_6D_6): 2.8 μ_B. Anal. Calcd. For $C_{54}H_{106}B_2Fe_2OP_6$: C 59.46; H 9.80; N 0. Found: C 59.37; H 9.61; N < 0.05.

Synthesis of [PhBP$^{iPr}_3$]Fe(CO)$_2$, 6.11. {[PhBP$^{iPr}_3$]Fe}$_2$(μ-N_2) (0.0775 mmol, 0.070 mmol) was dissolved in 5 mL benzene, and transferred to a 25 mL Schlenk tube fitted with a Teflon valve. The vessel was evacuated, and an atmosphere of CO was introduced to the brown solution. After 20 min, the light brown solution was degassed and lyophilized. The resulting solids were crystallized in minimal toluene stored at -35 ^{o}C (0.0673 mg, 72.9%). ^{1}H NMR (C_6D_6, 300 MHz) δ 8.4, 7.8, 7.6, 5.3 (bs), 1.2, -1.3 (bs). IR (KBr): 1955, 1888 cm^{-1} UV-vis (THF) λ_{max}, nm (ε, M^{-1} cm^{-1}): 460 (sh, 854), 400 (sh, 1800), 311 (15000). Evans Method (C_6D_6): 1.73 μ_B. Anal. Calcd. For $C_{29}H_{53}BFeO_2P_3$: C 58.71; H 9.00; N 0. Found: C 58.40; H 8.96; N < 0.05.

Synthesis of {[PhBP$^{Ph}_3$]Fe}$_2$(μ-O), 6.12 and [PhBP$^{Ph}_3$]Fe(CO)$_2$Na(THF)$_5$, 6.14. Solid [PhBP$^{Ph}_3$]FeCl (0.1712 g, 0.22 mmol) and sodium amalgam (0.46 wt %, 0.587 mmol) was transferred to a 25 mL Schlenk tube fitted with a Teflon valve. THF (13 mL) was vac-transferred onto the solids, and the solution was warmed to 0 ^{o}C in an acetone bath followed by an ice bath, at which time 1 atmosphere of CO_2 was introduced to the vessel.

The reaction was stirred slowly for 1 h, then vigorously for 3 h. The orange/brown solution was degassed, filtered through Celite, and the volatiles were removed under partial pressure. The solids were extracted into benzene and filtered through celite. The remaining benzene-insoluble orange solids were extracted into THF, and volatiles were removed from both solutions.

The benzene extract (**6.12**) was re-extracted into benzene, filtered, and lyophilized. The solids were washed with methylcyclohexane, and triply crystallized via a benzene/petroleum ether layer to afford $\{[PhBP^{Ph}_3]Fe\}_2(\mu\text{-}O)$ (**6.12**) (0.0731 g, 22.3%). ^{1}H NMR (C_6D_6, 300 MHz) δ 25.6 (s), 14.6 (d, J = 6 Hz), 10.41 (t, J = 6 Hz), 9.73 (t, J = 7.5 Hz), 5.17 (s), 4.22 (t, J = 6 Hz), 2.87 (s). UV-vis (THF) λ_{max}, nm (ε, M^{-1} cm^{-1}): 896 (240), 653 (sh, 250), 555 (sh, 520), 491 (sh, 1270). Evans Method (C_6D_6): 2.8 μ_B. Anal. Calcd. For $C_{90}H_{82}B_2Fe_2OP_6$: C 72.12; H 5.51; N 0. Found: C 71.70; H 5.96; N < 0.05.

The benzene-insoluble solids (**6.14**) were re-extracted into THF, filtered through celite, and layered with petroleum ether at -35 ^{o}C to give $[PhBP^{Ph}_3]Fe(CO)_2Na(THF)_5$ (**6.13**) (17.0 mg, 6.4%). ^{1}H NMR (*d*$_8$-THF, 300 MHz) δ 7.53 (s), 7.37 (s), 7.06 (t, J = 6.1 Hz), 6.83 (s), 3.61, 1.77, 1.26 (bs). ^{31}P NMR (*d*$_8$-THF, 121.4 MHz) δ 57.0. IR (KBr): 1870, 1781 cm^{-1}. UV-vis (THF) λ_{max}, nm (ε, M^{-1} cm^{-1}): 335 (5600). Anal. Calcd. For $C_{67}H_{81}BFeNaO_7P_3$: C 68.14; H 6.91; N 0. Found: C 56.59; H 5.27; N < 0.05.

Alternative Synthesis of $[PhBP^{Ph}_3]Fe(CO)_2Na(THF)_5$, 6.14: To a stirring solution of **6.13** (0.4363 g, 0.547 mmol) in 20 mL THF, sodium amalgam (0.40 wt %, 0.602 mmol). After 2 h, the solution was filtered through a Celite-lined frit, and volatiles were removed. The resulting solids were washed with petroleum ether, extracted into benzene,

and filtered through Celite. The benzene solution was then lyophilized to give an orange/red powder (0.3405 g, 0.288 mmol, 53%).

Synthesis of {[PhBP$^{Ph}_3$]Fe}(μ-η^1:η^2-carbonate), 6.15: A solution of **6.12** (7.5 mg, 0.005 mmol) in 1 mL of C_6D_6 was transferred to a resealable j.young NMR tube. On a Schlenk-line, the solution was frozen with liquid nitrogen and the headspace was evacuated. The vessel was warmed to room temperature and an atmosphere of CO_2 was added to the tube. The reaction stirred for 1 h at 60 ^oC, during which time clean and quantitative conversion to **6.15** occurs, as noted by a single set of paramagnetically shifted resonances in the ^1H NMR spectrum. Upon exposure to an N_2 atmosphere or vacuum, solutions of **6.15** revert to **6.12**, precluding our ability to obtain analytically pure material in the solid-state. Crystals of **6.15** suitable for diffraction were obtained by layering a THF solution of **6.15** with pentane at -35 ^oC. ^1H NMR (C_6D_6, 300 MHz) δ 120 (bs), 28.6, 15.7, 14.6, 6.2, -4.2, -13 (bs). IR (C_6D_6/KBr): 1470 cm^{-1}. Evans Method (C_6D_6): 5.8 μ_B.

Synthesis of [PhBP$^{CH2Cy}_3$]Fe(CO)$_2$. A solution of **6.1** (0.147 mmol, 0.015 M) was transferred to a 50 mL Schlenk tube fitted with a Teflon plug, and cooled to -78 ^oC. The tube was attached to a calibrated bulb that contained two equivalents of CO (56.4 mL, 9.6 cm Hg), and the tube opened to the bulb. The reaction stirred for 18 h during which it warmed to room temperature and changed color from lime green to dark orange. Volatiles were removed under partial pressure, and the solids were extracted into benzene and filtered through Celite. The resulting solution was concentrated under reduced

pressure, and extracted into petroleum ether (64.7 mg, 47.6%). ^{1}H NMR (C_6D_6, 300 MHz) δ 8.1 (bs), 7.8, 7.4, 7.05, 2.0 (bs), 1.2 (bs). IR (KBr): 1959, 1894 cm^{-1}. UV-vis (THF) λ_{max}, nm (ε, M^{-1} cm^{-1}): 410 (2130), 355 (sh, 1600), 295 (sh, 4540), 253 (sh, 8300). Evans Method (C_6D_6): 1.73 μ_B. Anal. Calcd. For $C_{53}H_{89}BFeO_2P_3$: C 69.35; H 9.77; N 0. Found: C 66.52; H 9.59; N < 0.05.

6.4.7 Reaction Studies Between [PhBP$^{CH2Cy}{}_3$]Fe(PR$_3$) and CO$_2$

In a typical reaction, a 20 mM solution of [PhBP$^{CH2Cy}{}_3$]Fe(PR$_3$) (0.02 mmol) was transferred to a 15 mL Schlenk tube fitted with a Teflon plug and a stir bar. On a Schlenk-line, the vessel was attached to a calibrated bulb. The line was flushed 3 times with CO_2, and the tip of the vessel was cooled with liquid nitrogen. The vessel was then evacuated, and ten equivalents of CO_2 were loaded into the calibrated bulb and condensed into the vessel with liquid nitrogen. The reaction was allowed to stir for 24 h prior to removal of the volatiles. The solids were dissolved in 700 μL of a standard C_6D_6 solution containing 10 mM P^{t}Bu$_3$ and transferred to a j.young resealable NMR tube, saving an aliquot for IR analysis. Both ^{1}H and ^{31}P NMR were collected, and peaks corresponding to **6.2**, PtBu$_3$, and PR$_3$ were integrated. The samples were then attached to a Shlenk line, frozen, and evacuated, and filled with an atmosphere of CO. The NMR tubes were sealed and allowed to stir for an hour prior to repeating the NMR analysis. Now, in the ^{31}P NMR spectra peaks corresponding to **6.2**, **6.9**, P^{t}Bu$_3$, and PR$_3$ were integrated. This method allowed us to determine the percent conversion, as well as the relative ratio of CO bond cleavage to C-C coupling.

Acknowledgements:

Connie C. Lu is acknowledged for preliminary studies, and full characterization of **6.5** and **6.6**.

Works Cited:

1. (a) Sakakura, T.; Choi, J.-C.; Yasuda, H., *Chem. Rev.* **2007**, *107*, 2365; (b) Braunstein, P.; Matt, D.; Nobel, D., *Chem. Rev.* **1988**, *88*, 747; (c) Aresta, M.; Dibenedetto, A., *Dalton Trans.* **2007**, 2975; (d) Arakawa, H.; Aresta, M.; Armor, J. N.; Barteau, M. A.; Beckman, E. J.; Bell, A. T.; Bercaw, J. E.; Creutz, C.; Dinjus, E.; Dixon, D. A.; Domen, K.; DuBois, D. L.; Eckert, J.; Fujita, E.; Gibson, D. H.; Goddard, W. A.; Goodman, D. W.; Keller, J.; Kubas, G. J.; Kung, H. H.; Lyons, J. E.; Manzer, L. E.; Marks, T. J.; Morokuma, K.; Nicholas, K. M.; Periana, R.; Que, L.; Rostrup-Nielson, J.; Sachtler, W. M. H.; Schmidt, L. D.; Sen, A.; Somorjai, G. A.; Stair, P. C.; Stults, B. R.; Tumas, W., *Chem. Rev.* **2001**, *101*, 953; (e) Benson, E. E.; Kubiak, C. P.; Sathrum, A. J.; Smieja, J. M., *Chem. Soc. Rev.* **2009**, *38*, 89.

2. West, N. M.; Miller, A. J. M.; Labinger, J. A.; Bercaw, J. E., *Coord. Chem. Rev. In Press, Corrected Proof*.

3. (a) Darensbourg, D. J., *Chem. Rev.* **2007**, *107*, 2388; (b) Cheng, M.; Lobkovsky, E. B.; Coates, G. W., *J. Am. Chem. Soc.* **1998**, *120*, 11018.

4. Yeung, C. S.; Dong, V. M., *J. Am. Chem. Soc.* **2008**, *130*, 7826.

5. (a) Vechorkin, O.; Hirt, N.; Hu, X., *Org. Lett.* **2010**, *12*, 3567; (b) Boogaerts, I. I. F.; Nolan, S. P., *J. Am. Chem. Soc.* **2010**, *132*, 8858.

6. Amatore, C.; Saveant, J. M., *J. Am. Chem. Soc.* **1981**, *103*, 5021.

7. Savéant, J.-M., *Chem. Rev.* **2008**, *108*, 2348.

8. Mendiratta, A.; Cummins, C. C., *Inorg. Chem.* **2005**, *44*, 7319.

9. (a) Evans, W. J.; Seibel, C. A.; Ziller, J. W., *Inorg. Chem.* **1998**, *37*, 770; (b) Angamuthu, R.; Byers, P.; Lutz, M.; Spek, A. L.; Bouwman, E., *Science* **2010**, *327*, 313; (c) Farrugia, L. J.; Lopinski, S.; Lovatt, P. A.; Peacock, R. D., *Inorg. Chem.* **2000**, *40*, 558; (d) Evans, W. J.; Lorenz, S. E.; Ziller, J. W., *Inorg. Chem.* **2009**, *48*, 2001; (e) Lu, C. C.; Saouma, C. T.; Day, M. W.; Peters, J. C., *J. Am. Chem. Soc.* **2007**, *129*, 4; (f) Aresta, M.; Gobetto, R.; Quaranta, E.; Tommasi, I., *Inorg. Chem.* **1992**, *31*, 4286.

10. Gaffney, A. M.; Leonard, J. J.; Sofranko, J. A.; Sun, H. N., *J. Catal.* **1984**, *90*, 261.

11. (a) Bhugun, I.; Lexa, D.; Saveant, J. M., *J. Am. Chem. Soc.* **1996**, *118*, 1769; (b) Fisher, B.; Eisenberg, R., *J. Am. Chem. Soc.* **1980**, *102*, 7361; (c) Collin, J. P.; Jouaiti, A.; Sauvage, J. P., *Inorg. Chem.* **1988**, *27*, 1986.

12. (a) Brown, S. D.; Betley, T. A.; Peters, J. C., *J. Am. Chem. Soc.* **2003**, *125*, 322; (b) Jenkins, D. M.; Peters, J. C., *J. Am. Chem. Soc.* **2005**, *127*, 7148.

13. (a) Orpen, A. G.; Brammer, L.; Allen, F. H.; Kennard, O.; Watson, D. G.; Taylor, R., *J. Chem. Soc., Dalton Trans.* **1989**, S1; (b) Konze, W. V.; Scott, B. L.; Kubas, G. J., *J. Am. Chem. Soc.* **2002**, *124*, 12550; (c) Thomas, J. C.; Peters, J. C., *J. Am. Chem. Soc.* **2003**, *125*, 8870.

14. (a) Astruc, D., *Chem. Rev.* **1988**, *88*, 1189; (b) Hamon, J. R.; Astruc, D.; Michaud, P., *J. Am. Chem. Soc.* **1981**, *103*, 758.

15. (a) Betley, T. A.; Peters, J. C., *J. Am. Chem. Soc.* **2003**, *125*, 10782; (b) Mehn, M. P.; Peters, J. C., *J. Inorg. Biochem.* **2006**, *100*, 634.

16. Wax, M. J.; Bergman, R. G., *J. Am. Chem. Soc.* **1981**, *103*, 7028.

17. Aycock, D. F., *Organic Process Research & Development* **2006**, *11*, 156.

18. Schwabe, K.; Gebhardt, G., *Z. Anorg. Allg. Chem.* **1954**, *277*, 329.

19. Betley, T. A.; Peters, J. C., *Inorg. Chem.* **2003**, *42*, 5074.

20. Saouma, C. T.; Peters, J. C., *manucript in preparation* **2010**.

21. Nakamoto, K., *Infrared and Raman Spectra of Inorganic and Coordination Compounds Part B: Applications in Coordination, Organometallic, and Bioinorganic Chemistry*. 5 ed.; John Wiley & Sons, Inc: New York, 1997.

22. Aresta, M.; Nobile, C. F.; Albano, V. G.; Forni, E.; Manassero, M., *J. Chem. Soc., Chem. Commun.* **1975**, 636.

23. Daida, E. J.; Peters, J. C., *Inorg. Chem.* **2004**, *43*, 7474.

24. Tolman, C. A., *Chem. Rev.* **1977**, *77*, 313.

25. (a) Fachinetti, G.; Floriani, C.; Chiesivilla, A.; Guastini, C., *J. Am. Chem. Soc.* **1979**, *101*, 1767; (b) Bianchini, C.; Meli, A., *J. Am. Chem. Soc.* **1984**, *106*, 2698; (c) Bryan, J. C.; Geib, S. J.; Rheingold, A. L.; Mayer, J. M., *J. Am. Chem. Soc.* **1987**, *109*, 2826.

26. (a) Laitar, D. S.; Müller, P.; Sadighi, J. P., *J. Am. Chem. Soc.* **2005**, *127*, 17196; (b) Raebiger, J. W.; Turner, J. W.; Noll, B. C.; Curtis, C. J.; Miedaner, A.; Cox, B.; DuBois, D. L., *Organometallics* **2006**, *25*, 3345; (c) Rakowski Dubois, M.;

Dubois, D. L., *Acc. Chem. Res.* **2009**, *42*, 1974; (d) Sadique, A. R.; Brennessel, W. W.; Holland, P. L., *Inorg. Chem.* **2008**, *47*, 784.

27. Gennaro, A.; Isse, A. A.; Vianello, E., *J. Electroanal. Chem.* **1990**, *289*, 203.

28. Castro-Rodriguez, I.; Nakai, H.; Zakharov, L. N.; Rheingold, A. L.; Meyer, K., *Science* **2004**, *305*, 1757.

29. Schubert, E. M., *J. Chem. Educ.* **1992**, *69*, 62.

30. Neese, F., *QCPE Bull.* **1995**, *15*, 5.

31. Sheldrick, G. M., *Acta Cryst.* **1990**, *A46*.

32. Sheldrick, G. M., *Acta Cryst.* **2008**, *A64*.

33. Müller, P.; Herbst-Irmer, R.; Spek, A. L.; Schneider, T. R.; Sawaya, M. R., *Crystal Structure Refinement: A Crystallographer's Guide to SHELXL*. Oxford University Press: Oxford, 2006.

34. Spek, A. L., L. PLATON A Multipurpose Crystallographic Tool. Utrecht University: Utrecht, Holland, 2008.

35. Frisch, M. J.; Trucks, G. W.; Schlegel, H. B.; Scuseria, G. E.; Robb, M. A.; Cheeseman, J. R.; Montgomery, J. A.; Vreven, T.; Kudin, K. N.; Burant, J. C.; Millam, J. M.; Iyengar, S. S.; Tomasi, J.; Barone, V.; Mennucci, B.; Cossi, M.; Scalmani, G.; Rega, N.; Petersson, G. A.; Nakatsuji, H.; Hada, M.; Ehara, M.; Toyota, K.; Fukuda, R.; Hasegawa, J.; Ishida, M.; Nakajima, T.; Honda, Y.; Kitao, O.; Nakai, H.; Klene, M.; Li, X.; Knox, J. E.; Hratchian, H. P.; Cross, J. B.; Bakken, V.; Adamo, C.; Jaramillo, J.; Gomperts, R.; Stratmann, R. E.; Yazyev, O.; Austin, A. J.; Cammi, R.; Pomelli, C.; Ochterski, J. W.; Ayala, P. Y.; Morokuma, K.; Voth, G. A.; Salvador, P.; Dannenberg, J. J.; Zakrzewski, V. G.; Dapprich, S.; Daniels, A. D.; Strain, M. C.; Farkas, O.; Malick, D. K.; Rabuck, A. D.; Raghavachari, K.; Foresman, J. B.; Ortiz, J. V.; Cui, Q.; Baboul, A. G.; Clifford, S.; Cioslowski, J.; Stefanov, B. B.; Liu, G.; Liashenko, A.; Piskorz, P.; Komaromi, I.; Martin, R. L.; Fox, D. J.; Keith, T.; Laham, A.; Peng, C. Y.; Nanayakkara, A.; Challacombe, M.; Gill, P. M. W.; Johnson, B.; Chen, W.; Wong, M. W.; Gonzalez, C.; Pople, J. A., Gaussian 03, Revision C.02. 2003.

36. Dennington, R. I.; Keith, T.; Millam, J., GaussView, Version 4.1. Semichem, Inc.: Shawnee Mission, KS, 2007.

37. Young, D. C., *Spin Contamination*. John Wiley & Sons, Inc.: 2002; p 227.

Appendix 1: Supplementary Data for Chapter 2

Table A1.1. Cyclic voltammetry data for complexes **2.3**–**2.6**[a]

Compound	**$E_{1/2}$ (vs. Fc/Fc$^+$) / V**	**Event**
2.3	-0.38	Quasi-reversible oxidation
	0.27	Irreversible oxidation
2.4	-0.94	Quasi-reversible oxidation
	-0.22	Irreversible oxidation
	0.21	Quasi-reversible oxidation
2.5	-0.92	Quasi-reversible oxidation
	-0.10	Quasi-reversible oxidation
2.6	-0.38	Reversible oxidation
	-2.43	Reversible reduction

[a]Experimental parameters: 0.4 M [^{n}Bu$_4$N][PF$_6$], 0.5 mM analyte. Reversible peaks revealed no scan-rate dependence.

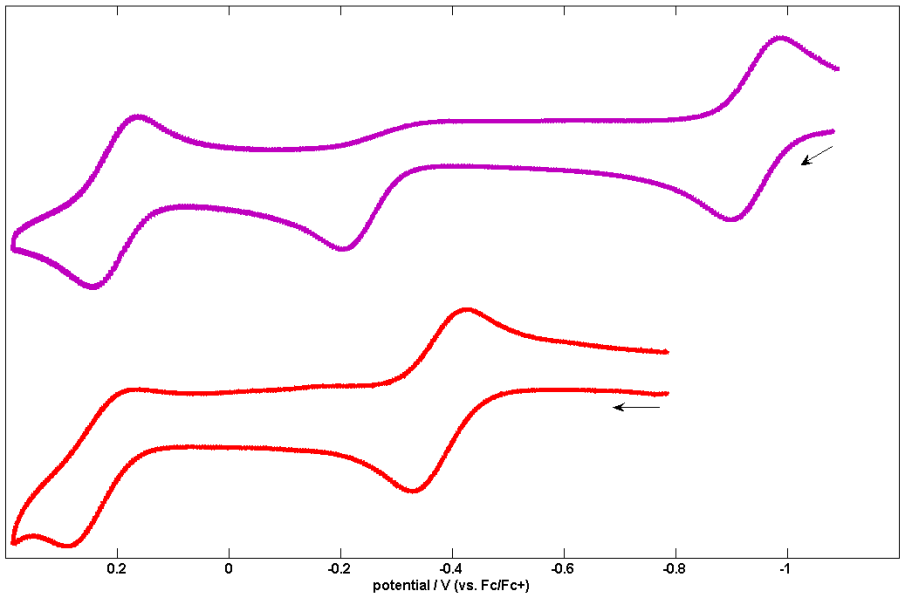

Figure A1.1. Cyclic voltammograms of **2.3** (bottom) and **2.4** (top)

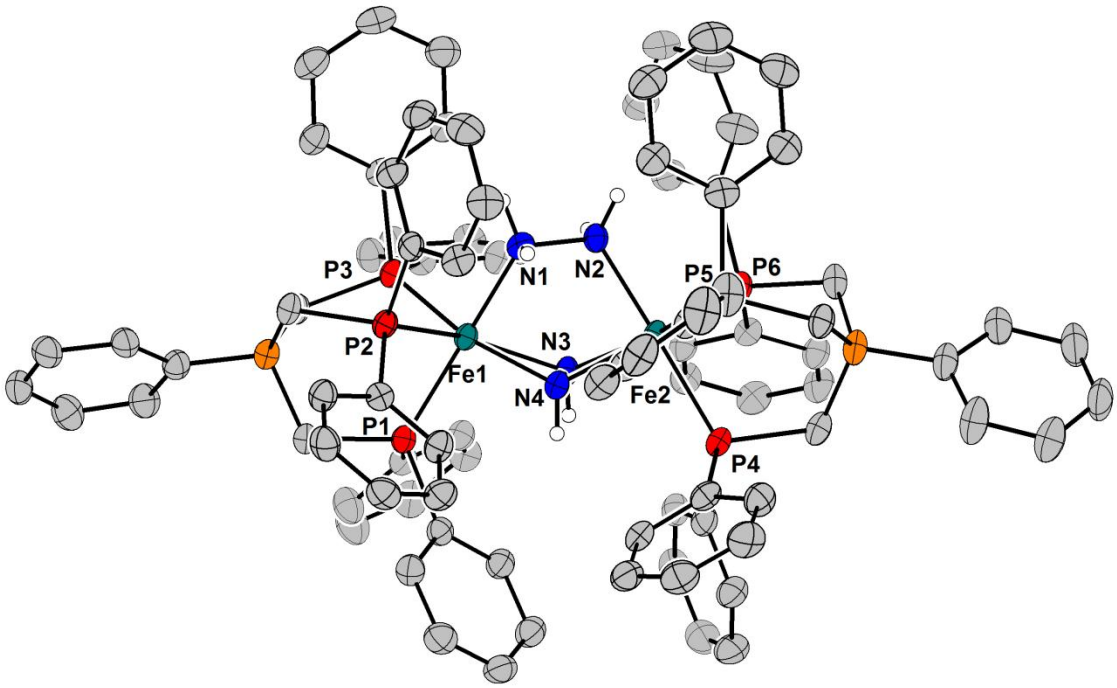

Figure A1.2. Displacement ellipsoid (50%) representation of **2.3**. Hydrogen atoms, solvent molecules, and the minor components of the disorder were removed for clarity.

Table A1.2. Select bond lengths [Å] and angles [°] for **2.3**

Fe(1)-N(4)	1.978(2)	N(2)-N(1)-H(2N)	105(2)
Fe(1)-N(1)	2.028(3)	Fe(1)-N(1)-H(2N)	106(2)
Fe(1)-N(3)	2.030(2)	H(1N)-N(1)-H(2N)	100(3)
Fe(1)-P(2)	2.2202(8)	N(1)-N(2)-Fe(2)	111.89(17)
Fe(1)-P(1)	2.2477(9)	N(1)-N(2)-H(3N)	111(2)
Fe(1)-P(3)	2.2610(8)	Fe(2)-N(2)-H(3N)	118(2)
Fe(2)-N(3)	1.999(2)	N(1)-N(2)-H(4N)	103(2)
Fe(2)-N(4)	2.023(2)	Fe(2)-N(2)-H(4N)	108(2)
Fe(2)-N(2)	2.026(3)	H(3N)-N(2)-H(4N)	104(3)
Fe(2)-P(6)	2.2369(9)	N(4)-N(3)-Fe(2)	70.10(14)
Fe(2)-P(4)	2.2472(8)	N(4)-N(3)-Fe(1)	67.15(13)
Fe(2)-P(5)	2.2695(8)	Fe(2)-N(3)-Fe(1)	115.53(12)
N(1)-N(2)	1.465(3)	N(4)-N(3)-H(5N)	109(2)
N(1)-H(1N)	0.870(17)	Fe(2)-N(3)-H(5N)	120(2)
N(1)-H(2N)	0.861(17)	Fe(1)-N(3)-H(5N)	119(2)
N(2)-H(3N)	0.899(17)	N(3)-N(4)-Fe(1)	71.11(14)
N(2)-H(4N)	0.875(17)	N(3)-N(4)-Fe(2)	68.29(14)
N(3)-N(4)	1.429(3)	Fe(1)-N(4)-Fe(2)	116.84(12)
N(3)-H(5N)	0.892(17)	N(3)-N(4)-H(6N)	103(2)
N(4)-H(6N)	0.875(17)	Fe(1)-N(4)-H(6N)	118(2)
N(4)-Fe(1)-N(1)	80.10(10)	Fe(2)-N(4)-H(6N)	117(2)
N(4)-Fe(1)-N(3)	41.74(10)		
N(1)-Fe(1)-N(3)	86.30(10)		
N(4)-Fe(1)-P(2)	108.66(8)		
N(1)-Fe(1)-P(2)	88.40(7)		
N(3)-Fe(1)-P(2)	150.39(7)		
N(4)-Fe(1)-P(1)	98.98(8)		
N(1)-Fe(1)-P(1)	176.49(7)		
N(3)-Fe(1)-P(1)	95.27(8)		
P(2)-Fe(1)-P(1)	88.69(3)		
N(4)-Fe(1)-P(3)	158.62(8)		
N(1)-Fe(1)-P(3)	95.77(8)		
N(3)-Fe(1)-P(3)	117.42(7)		
P(2)-Fe(1)-P(3)	92.08(3)		
P(1)-Fe(1)-P(3)	86.30(3)		
N(3)-Fe(2)-N(4)	41.62(10)		
N(3)-Fe(2)-N(2)	80.30(10)		
N(4)-Fe(2)-N(2)	86.76(10)		
N(3)-Fe(2)-P(6)	111.12(8)		
N(4)-Fe(2)-P(6)	152.71(8)		
N(2)-Fe(2)-P(6)	89.19(7)		
N(3)-Fe(2)-P(4)	97.84(8)		
N(4)-Fe(2)-P(4)	92.42(7)		
N(2)-Fe(2)-P(4)	177.94(8)		
P(6)-Fe(2)-P(4)	90.69(3)		
N(3)-Fe(2)-P(5)	157.18(8)		
N(4)-Fe(2)-P(5)	116.34(8)		
N(2)-Fe(2)-P(5)	94.47(8)		
P(6)-Fe(2)-P(5)	90.87(3)		
P(4)-Fe(2)-P(5)	87.58(3)		
N(2)-N(1)-Fe(1)	113.21(17)		
N(2)-N(1)-H(1N)	105(2)		
Fe(1)-N(1)-H(1N)	125(2)		

Table A1.3. Crystal data and structure refinement for **2.3**

Identification code	d8_08057	
Empirical formula	C114 H112 B2 Fe2 N4 P6	
Formula weight	742.89	
Temperature	100(2) K	
Wavelength	1.54178 Å	
Crystal system	triclinic	
Space group	P-1	
Unit cell dimensions	a = 13.8645(3) Å	α= 97.9010(10)°.
	b = 16.9859(3) Å	β= 99.3150(10)°.
	c = 20.7527(4) Å	γ = 92.5280(10)°.
Volume	4766.03(16) Å^3	
Z	2	
Density (calculated)	1.294 Mg/m^3	
Absorption coefficient	3.793 mm^{-1}	
F(000)	1952	
Crystal size	0.20 x 0.15 x 0.10 mm^3	
Theta range for data collection	2.18 to 68.98°.	
Index ranges	-16<=h<=16, -20<=k<=20, -25<=l<=23	
Reflections collected	92552	
Independent reflections	16868 [R(int) = 0.0380]	
Completeness to theta = 68.98°	95.2 %	
Absorption correction	Semi-empirical from equivalents	
Max. and min. transmission	0.7029 and 0.5176	
Refinement method	Full-matrix least-squares on F^2	
Data / restraints / parameters	16868 / 3643 / 1277	
Goodness-of-fit on F^2	1.059	
Final R indices [I>2sigma(I)]	R1 = 0.0558, wR2 = 0.1503	
R indices (all data)	R1 = 0.0626, wR2 = 0.1557	
Largest diff. peak and hole	1.454 and -0.601 e.Å^{-3}	

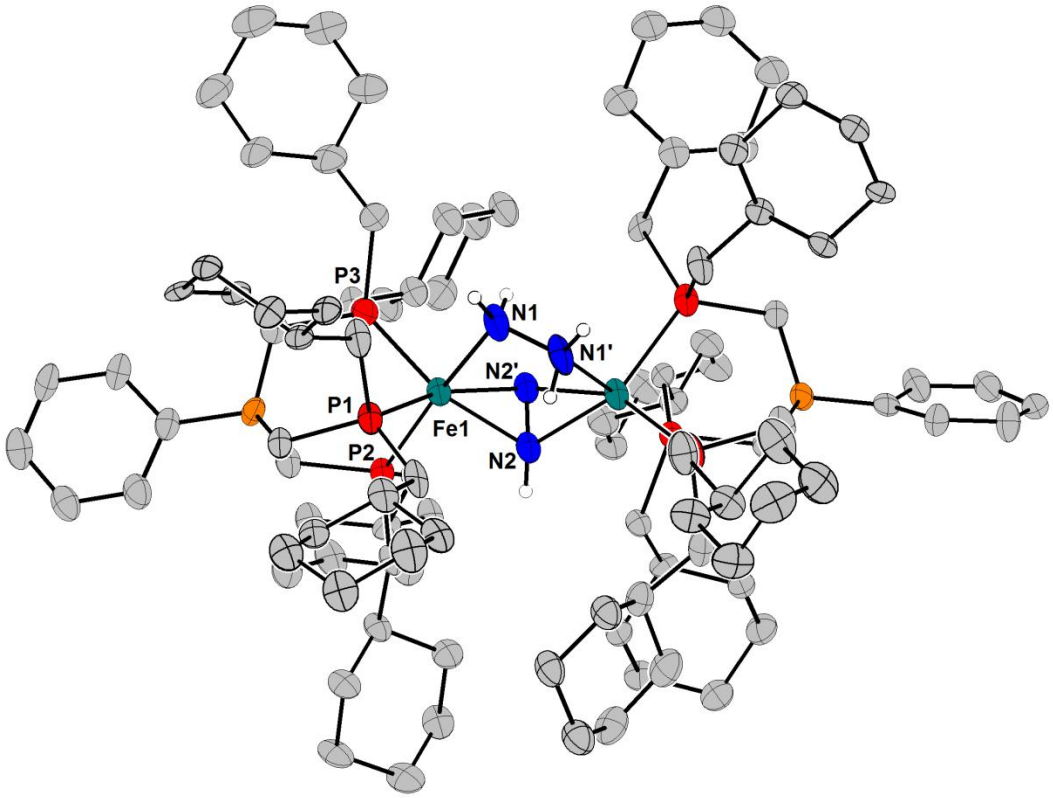

Figure A1.3. Displacement ellipsoid (50%) representation of **2.4**. Hydrogen atoms, solvent molecules, and the minor components of the disorder were removed for clarity.

Table A1.4. Select bond lengths [Å] and angles [°] for **2.4**

N(1)-N(1)#1	1.446(10)	Fe(1)-N(2)-H(2B)	94(4)
N(1)-Fe(1)#1	1.980(5)	N(2)#1-N(2)-H(2C)	114(4)
N(1)-Fe(1)	2.026(5)	Fe(1)-N(2)-H(2C)	118(4)
N(1)-H(1)	0.901(18)	H(2B)-N(2)-H(2C)	110(6)
N(2)-N(2)#1	1.456(11)	N(1)#1-Fe(1)-N(1)	42.3(3)
N(2)-Fe(1)	2.047(5)	N(1)#1-Fe(1)-N(2)	79.07(19)
N(2)-H(2B)	0.897(18)	N(1)-Fe(1)-N(2)	86.1(2)
N(2)-H(2C)	0.883(18)	N(1)#1-Fe(1)-P(3)	110.04(16)
Fe(1)-N(1)#1	1.980(5)	N(1)-Fe(1)-P(3)	151.78(15)
Fe(1)-P(3)	2.206(2)	N(2)-Fe(1)-P(3)	94.40(18)
Fe(1)-P(2)	2.2278(16)	N(1)#1-Fe(1)-P(2)	98.77(14)
Fe(1)-P(1)	2.2398(18)	N(1)-Fe(1)-P(2)	90.15(14)
N(1)#1-N(1)-Fe(1)#1	70.5(3)	N(2)-Fe(1)-P(2)	176.15(17)
N(1)#1-N(1)-Fe(1)	67.2(3)	P(3)-Fe(1)-P(2)	89.33(7)
Fe(1)#1-N(1)-Fe(1)	116.3(2)	N(1)#1-Fe(1)-P(1)	156.73(16)
N(1)#1-N(1)-H(1)	121(4)	N(1)-Fe(1)-P(1)	116.23(15)
Fe(1)#1-N(1)-H(1)	124(4)	N(2)-Fe(1)-P(1)	92.17(16)
Fe(1)-N(1)-H(1)	118(4)	P(3)-Fe(1)-P(1)	91.97(7)
N(2)#1-N(2)-Fe(1)	110.8(3)	P(2)-Fe(1)-P(1)	88.64(6)
N(2)#1-N(2)-H(2B)	108(4)		

Table A1.5. Crystal data and structure refinement for **2.4**

Identification code	08362	
Empirical formula	C55 H102 B1 Fe1 N2 P3 O1	
Formula weight	1965.91	
Temperature	100(2) K	
Wavelength	0.71073 Å	
Crystal system	monoclinic	
Space group	c2/c	
Unit cell dimensions	a = 16.4698(22) Å	α= 90°.
	b = 27.3840(37) Å	β= 93.697(2) °.
	c = 25.1537(46) Å	γ = 90°.
Volume	11321(3)Å^3	
Z	16	
Density (calculated)	1.153 Mg/m^3	
Absorption coefficient	0.391 mm^{-1}	
F(000)	4304	
Crystal size	0.35 x 0.35 x 0.10 mm^3	
Theta range for data collection	1.44 to 23.26°.	
Index ranges	-18<=h<=18, -30<=k<=30, -27<=l<=27	
Reflections collected	72933	
Independent reflections	8144 [R(int) = 0.1036]	
Completeness to theta = 23.26°	100 %	
Absorption correction	Semi-empirical from equivalents	
Max. and min. transmission	0.9620 and 0.8754	
Refinement method	Full-matrix least-squares on F^2	
Data / restraints / parameters	8144 / 3201 / 1013	
Goodness-of-fit on F^2	1.203	
Final R indices [I>2sigma(I)]	R1 = 0.0717, wR2 = 0.1520	
R indices (all data)	R1 = 0.1417, wR2 = 0.2045	
Largest diff. peak and hole	0.803 and -0.546 e.Å^{-3}	

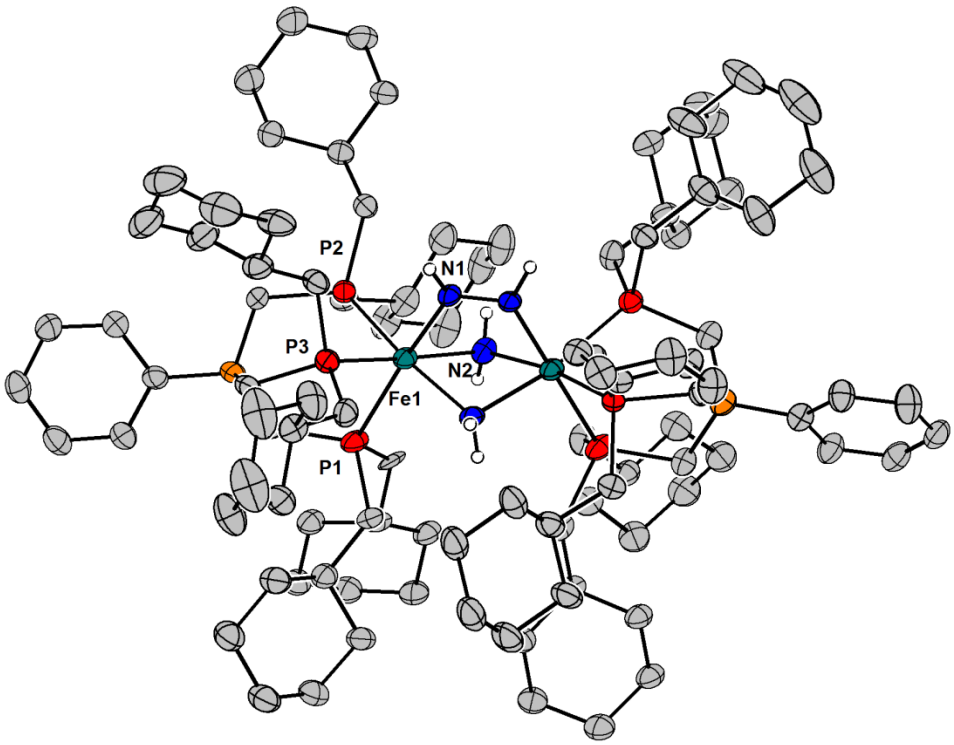

Figure A1.4. Displacement ellipsoid (50%) representation of **2.5**. Hydrogen atoms, solvent molecules, and the minor components of the disorder were removed for clarity.

Table A1.6. Select bond lengths [Å] and angles [°] for **2.5**

Fe(1)-N(1)	1.882(8)	N(2)#1-Fe(1)-P(3)	170.6(2)
Fe(1)-N(2)#1	2.034(9)	N(2)-Fe(1)-P(3)	100.4(3)
Fe(1)-N(2)	2.049(8)	P(2)-Fe(1)-P(3)	89.61(10)
Fe(1)-P(2)	2.252(3)	N(1)-Fe(1)-P(1)	174.5(3)
Fe(1)-P(3)	2.273(3)	N(2)#1-Fe(1)-P(1)	99.7(2)
Fe(1)-P(1)	2.291(3)	N(2)-Fe(1)-P(1)	92.9(2)
N(1)-N(1)#1	1.283(15)	P(2)-Fe(1)-P(1)	87.87(10)
N(1)-H(1)	0.88(2)	P(3)-Fe(1)-P(1)	88.37(11)
N(2)-Fe(1)#1	2.034(9)	N(1)#1-N(1)-Fe(1)	118.6(2)
N(2)-H(2A)	0.92(2)	N(1)#1-N(1)-H(1)	116(6)
N(2)-H(2B)	0.91(2)	Fe(1)-N(1)-H(1)	123(6)
N(1)-Fe(1)-N(2)#1	81.2(3)	Fe(1)#1-N(2)-Fe(1)	98.3(4)
N(1)-Fe(1)-N(2)	82.2(3)	Fe(1)#1-N(2)-H(2A)	114(6)
N(2)#1-Fe(1)-N(2)	74.5(4)	Fe(1)-N(2)-H(2A)	119(6)
N(1)-Fe(1)-P(2)	97.4(2)	Fe(1)#1-N(2)-H(2B)	106(7)
N(2)#1-Fe(1)-P(2)	95.5(2)	Fe(1)-N(2)-H(2B)	120(6)
N(2)-Fe(1)-P(2)	169.9(3)	H(2A)-N(2)-H(2B)	99(9)
N(1)-Fe(1)-P(3)	90.3(3)		

Table A1.7. Crystal data and structure refinement for **2.5**

Identification code	08318	
Empirical formula	C110 H202 B2 Fe2 N4 O3 P6	
Formula weight	1947.90	
Temperature	100(2) K	
Wavelength	0.71073 Å	
Crystal system	Monoclinic	
Space group	C2/c	
Unit cell dimensions	a = 15.914(3) Å	α= 90°.
	b = 27.596(4) Å	β= 97.306(3)°.
	c = 25.488(4) Å	γ = 90°.
Volume	11103(3) Å^3	
Z	4	
Density (calculated)	1.165 Mg/m^3	
Absorption coefficient	0.397 mm^{-1}	
F(000)	4264	
Crystal size	0.25 x 0.22 x 0.20 mm^3	
Theta range for data collection	1.48 to 23.25°.	
Index ranges	-17<=h<=17, -30<=k<=30, -28<=l<=28	
Reflections collected	81105	
Independent reflections	7983 [R(int) = 0.1137]	
Completeness to theta = 23.25°	100.0 %	
Absorption correction	Semi-empirical from equivalents	
Max. and min. transmission	0.9248 and 0.9073	
Refinement method	Full-matrix least-squares on F^2	
Data / restraints / parameters	7983 / 2064 / 848	
Goodness-of-fit on F^2	1.265	
Final R indices [I>2sigma(I)]	R1 = 0.1303, wR2 = 0.3042	
R indices (all data)	R1 = 0.1471, wR2 = 0.3120	
Largest diff. peak and hole	0.878 and -0.876 e.Å^{-3}	

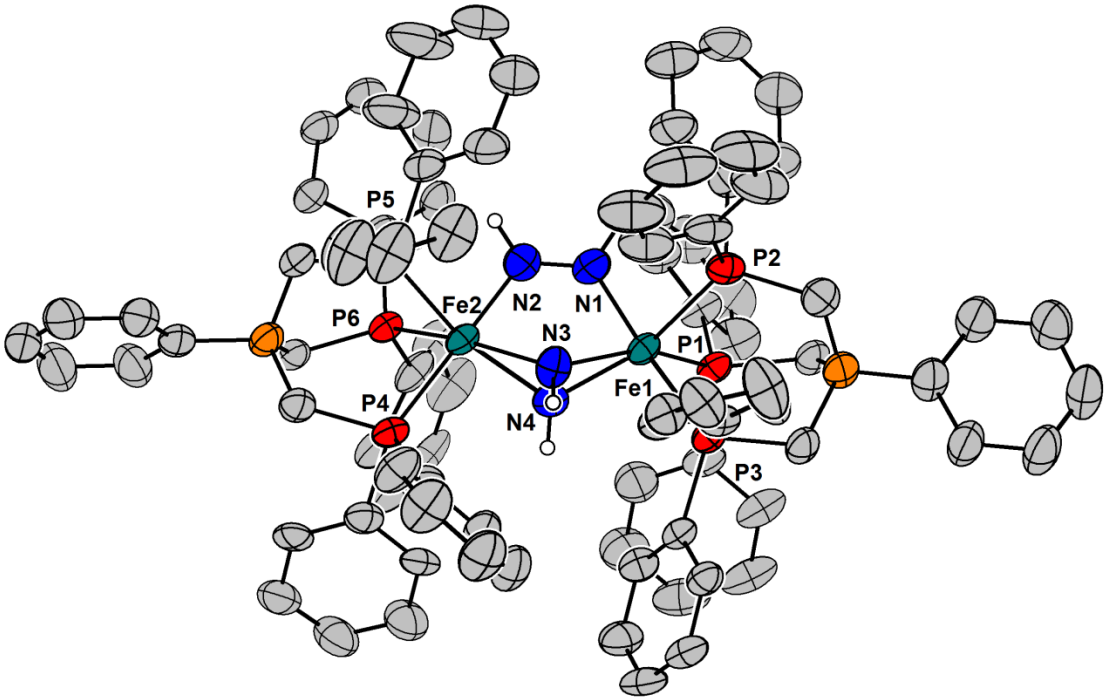

Figure A1.5. Displacement ellipsoid (50%) representation of **2.6**. Hydrogen atoms, solvent molecules, and the minor components of the disorder were removed for clarity.

Table A1.8. Select Bond lengths [Å] and angles [°] for **2.6**

Fe(1)-N(1)	1.884(4)	N(2)-Fe(2)-N(3)	81.78(17)
Fe(1)-N(4)	1.972(4)	N(2)-Fe(2)-N(4)	83.46(16)
Fe(1)-N(3)	1.980(4)	N(3)-Fe(2)-N(4)	42.97(15)
Fe(1)-P(2)	2.2480(13)	N(2)-Fe(2)-P(6)	91.93(13)
Fe(1)-P(1)	2.2641(13)	N(3)-Fe(2)-P(6)	156.66(11)
Fe(1)-P(3)	2.2950(12)	N(4)-Fe(2)-P(6)	114.16(11)
Fe(2)-N(2)	1.889(4)	N(2)-Fe(2)-P(5)	91.25(12)
Fe(2)-N(3)	1.975(4)	N(3)-Fe(2)-P(5)	113.04(12)
Fe(2)-N(4)	2.005(4)	N(4)-Fe(2)-P(5)	155.89(11)
Fe(2)-P(6)	2.2356(12)	P(6)-Fe(2)-P(5)	89.44(5)
Fe(2)-P(5)	2.2403(12)	N(2)-Fe(2)-P(4)	179.00(13)
Fe(2)-P(4)	2.2875(13)	N(3)-Fe(2)-P(4)	97.70(12)
N(1)-N(2)	1.281(5)	N(4)-Fe(2)-P(4)	96.75(11)
N(1)-H(1N)	0.929(18)	P(6)-Fe(2)-P(4)	88.88(5)
N(2)-H(2N)	0.919(18)	P(5)-Fe(2)-P(4)	88.17(5)
N(3)-N(4)	1.458(5)	N(2)-N(1)-Fe(1)	122.2(3)
N(3)-H(3N)	0.915(15)	N(2)-N(1)-H(1N)	119(3)
N(4)-H(4N)	0.878(15)	Fe(1)-N(1)-H(1N)	118(3)
N(1)-Fe(1)-N(4)	84.20(17)	N(1)-N(2)-Fe(2)	123.6(3)
N(1)-Fe(1)-N(3)	82.78(17)	N(1)-N(2)-H(2N)	126(3)
N(4)-Fe(1)-N(3)	43.30(15)	Fe(2)-N(2)-H(2N)	110(3)
N(1)-Fe(1)-P(2)	85.43(13)	N(4)-N(3)-Fe(2)	69.6(2)
N(4)-Fe(1)-P(2)	160.31(11)	N(4)-N(3)-Fe(1)	68.1(2)
N(3)-Fe(1)-P(2)	118.65(12)	Fe(2)-N(3)-Fe(1)	114.71(18)
N(1)-Fe(1)-P(1)	99.25(14)	N(4)-N(3)-H(3N)	110(2)
N(4)-Fe(1)-P(1)	107.62(11)	Fe(2)-N(3)-H(3N)	120.5(11)
N(3)-Fe(1)-P(1)	150.78(12)	Fe(1)-N(3)-H(3N)	119.4(11)
P(2)-Fe(1)-P(1)	90.54(5)	N(3)-N(4)-Fe(1)	68.6(2)
N(1)-Fe(1)-P(3)	168.08(14)	N(3)-N(4)-Fe(2)	67.4(2)
N(4)-Fe(1)-P(3)	100.61(11)	Fe(1)-N(4)-Fe(2)	113.75(17)
N(3)-Fe(1)-P(3)	93.21(11)	N(3)-N(4)-H(4N)	121(2)
P(2)-Fe(1)-P(3)	86.68(4)	Fe(1)-N(4)-H(4N)	123.4(10)
P(1)-Fe(1)-P(3)	89.74(4)	Fe(2)-N(4)-H(4N)	121.2(10)

Table A1.9. Crystal data and structure refinement for **2.6**

Identification code	08348	
Empirical formula	C108 H104 B2 Fe2 N4 P6	
Formula weight	1777.09	
Temperature	100(2) K	
Wavelength	0.71073 Å	
Crystal system	Triclinic	
Space group	P-1	
Unit cell dimensions	a = 13.5700(17) Å	α= 95.483(4)°.
	b = 13.8818(19) Å	β= 95.884(4)°.
	c = 28.049(5) Å	γ = 118.639(2)°.
Volume	4549.1(12) $Å^3$	
Z	2	
Density (calculated)	1.297 Mg/m^3	
Absorption coefficient	0.477 mm^{-1}	
F(000)	1864	
Crystal size	0.35 x 0.13 x 0.05 mm^3	
Theta range for data collection	1.48 to 26.08°.	
Index ranges	-16<=h<=16, -17<=k<=17, -34<=l<=34	
Reflections collected	75437	
Independent reflections	17915 [R(int) = 0.0773]	
Completeness to theta = 26.08°	99.2 %	
Absorption correction	Semi-empirical from equivalents	
Max. and min. transmission	0.9766 and 0.8510	
Refinement method	Full-matrix least-squares on F^2	
Data / restraints / parameters	17915 / 7915 / 1603	
Goodness-of-fit on F^2	1.037	
Final R indices [I>2sigma(I)]	R1 = 0.0676, wR2 = 0.1718	
R indices (all data)	R1 = 0.1172, wR2 = 0.2050	
Largest diff. peak and hole	1.045 and -0.510 $e.Å^{-3}$	

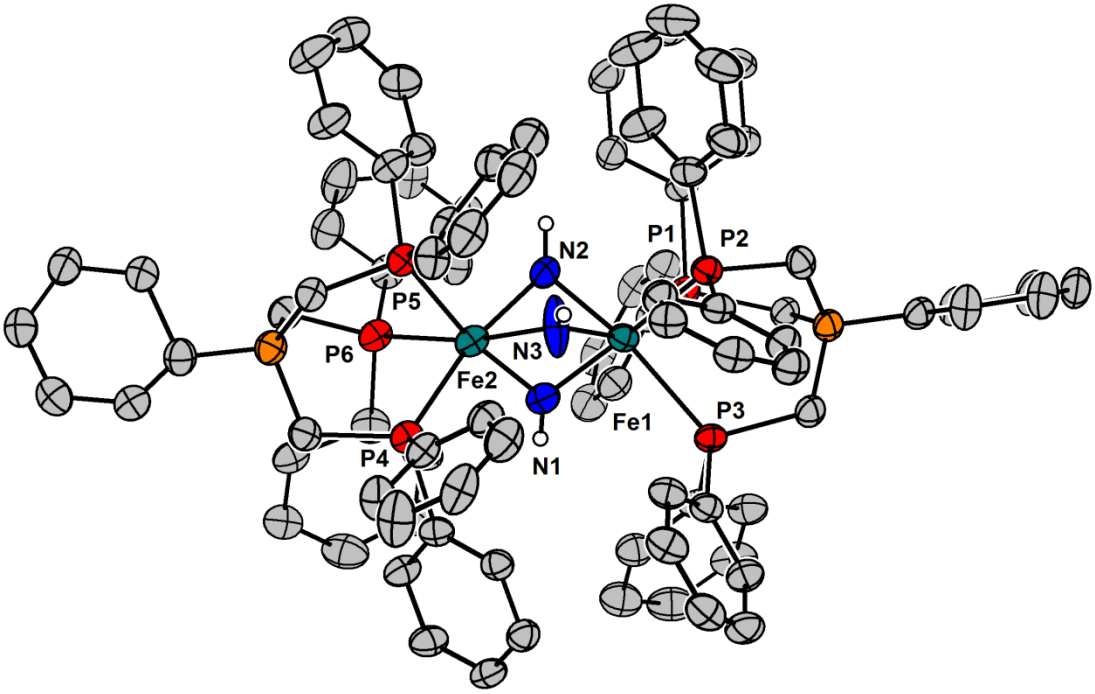

Figure A1.6. Displacement ellipsoid (50%) representation of **2.7**. Hydrogen atoms, solvent molecules, and the minor components of the disorder (ligand) were removed for clarity. The disorder in the two imido ligands is shown.

Table A1.10. Select bond lengths [Å] and angles [°] for **2.7**

Fe(1)-N(3)	1.794(9)	P(2)-Fe(1)-Fe(2)	123.68(3)
Fe(1)-N(2)	1.835(3)	P(1)-Fe(1)-Fe(2)	126.90(3)
Fe(1)-N(1)	1.858(3)	P(3)-Fe(1)-Fe(2)	129.03(3)
Fe(1)-P(2)	2.3278(9)	N(3)-Fe(2)-N(2)	49.6(4)
Fe(1)-P(1)	2.3332(9)	N(3)-Fe(2)-N(1)	75.1(4)
Fe(1)-P(3)	2.3707(9)	N(2)-Fe(2)-N(1)	79.59(15)
Fe(1)-Fe(2)	2.7392(7)	N(3)-Fe(2)-P(4)	108.3(4)
Fe(2)-N(3)	1.770(9)	N(2)-Fe(2)-P(4)	157.75(12)
Fe(2)-N(2)	1.804(4)	N(1)-Fe(2)-P(4)	98.30(10)
Fe(2)-N(1)	1.855(3)	N(3)-Fe(2)-P(5)	94.0(3)
Fe(2)-P(4)	2.3063(10)	N(2)-Fe(2)-P(5)	92.00(12)
Fe(2)-P(5)	2.3192(9)	N(1)-Fe(2)-P(5)	168.93(10)
Fe(2)-P(6)	2.3204(9)	P(4)-Fe(2)-P(5)	86.74(3)
N(1)-H(1N)	0.817(14)	N(3)-Fe(2)-P(6)	164.3(4)
N(2)-H(2N)	0.867(14)	N(2)-Fe(2)-P(6)	114.83(11)
N(3)-H(3N)	0.910(15)	N(1)-Fe(2)-P(6)	102.15(10)
N(3)-Fe(1)-N(2)	48.7(4)	P(4)-Fe(2)-P(6)	87.34(3)
N(3)-Fe(1)-N(1)	74.4(4)	P(5)-Fe(2)-P(6)	87.87(3)
N(2)-Fe(1)-N(1)	78.70(15)	N(3)-Fe(2)-Fe(1)	40.1(3)
N(3)-Fe(1)-P(2)	87.2(3)	N(2)-Fe(2)-Fe(1)	41.61(11)
N(2)-Fe(1)-P(2)	95.82(12)	N(1)-Fe(2)-Fe(1)	42.51(9)
N(1)-Fe(1)-P(2)	159.70(10)	P(4)-Fe(2)-Fe(1)	125.48(3)
N(3)-Fe(1)-P(1)	149.9(4)	P(5)-Fe(2)-Fe(1)	126.91(3)
N(2)-Fe(1)-P(1)	102.35(12)	P(6)-Fe(2)-Fe(1)	128.96(3)
N(1)-Fe(1)-P(1)	112.28(10)	Fe(2)-N(1)-Fe(1)	95.07(14)
P(2)-Fe(1)-P(1)	87.95(3)	Fe(2)-N(1)-H(1N)	132.4(12)
N(3)-Fe(1)-P(3)	120.7(4)	Fe(1)-N(1)-H(1N)	132.3(12)
N(2)-Fe(1)-P(3)	168.46(12)	Fe(2)-N(2)-Fe(1)	97.66(17)
N(1)-Fe(1)-P(3)	94.26(9)	Fe(2)-N(2)-H(2N)	133.2(12)
P(2)-Fe(1)-P(3)	87.66(3)	Fe(1)-N(2)-H(2N)	128.8(12)
P(1)-Fe(1)-P(3)	88.75(3)	Fe(2)-N(3)-Fe(1)	100.4(4)
N(3)-Fe(1)-Fe(2)	39.5(3)	Fe(2)-N(3)-H(3N)	130.9(14)
N(2)-Fe(1)-Fe(2)	40.73(11)	Fe(1)-N(3)-H(3N)	128.6(14)
N(1)-Fe(1)-Fe(2)	42.42(9)		

Table A1.11. Crystal data and structure refinement for **2.7**

Identification code	d8_09016	
Empirical formula	C105 H114 B2 Fe2 N2 P6	
Formula weight	1723.12	
Temperature	100(2) K	
Wavelength	1.54178 Å	
Crystal system	Monoclinic	
Space group	P2(1)/c	
Unit cell dimensions	a = 16.4689(4) Å	α= 90°.
	b = 14.2851(3) Å	β= 101.2670(10)°.
	c = 37.7006(8) Å	γ = 90°.
Volume	8698.5(3) Å^3	
Z	4	
Density (calculated)	1.316 Mg/m^3	
Absorption coefficient	4.103 mm^{-1}	
F(000)	3640	
Crystal size	0.30 x 0.20 x 0.07 mm^3	
Theta range for data collection	2.39 to 69.01°.	
Index ranges	-19<=h<=19, -17<=k<=17, -44<=l<=45	
Reflections collected	167430	
Independent reflections	15614 [R(int) = 0.0557]	
Completeness to theta = 69.01°	96.5 %	
Absorption correction	Semi-empirical from equivalents	
Max. and min. transmission	0.7622 and 0.3724	
Refinement method	Full-matrix least-squares on F^2	
Data / restraints / parameters	15614 / 6855 / 1537	
Goodness-of-fit on F^2	1.058	
Final R indices [I>2sigma(I)]	R1 = 0.0542, wR2 = 0.1292	
R indices (all data)	R1 = 0.0642, wR2 = 0.1354	
Largest diff. peak and hole	0.847 and -0.542 e.Å^{-3}	

Appendix 2: Supplementary Data for Chapter 3

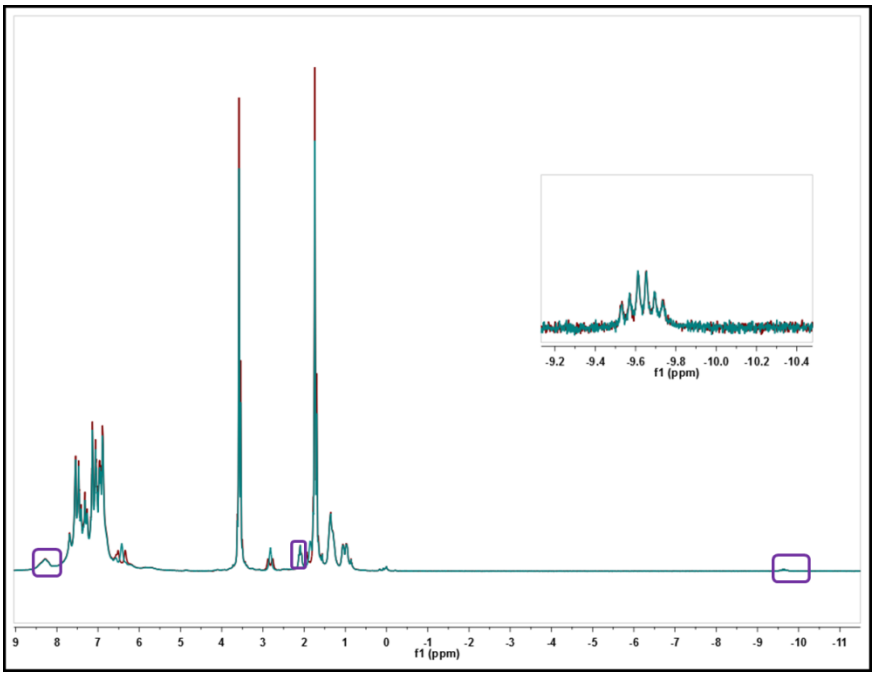

Figure A2.1. Overlay of ^{1}H (red) and $^{1}H\{^{31}P\}$ (blue) NMR (THF-d_8, -75 ^{o}C) spectrum of **3.1** prepared with $^{15}N_2H_4$. Peaks marked by a purple box are due to $[PhBP_3]Fe(CO)_2H$, with the inset indicating the hydride resonance of $[PhBP_3]Fe(CO)_2H$.

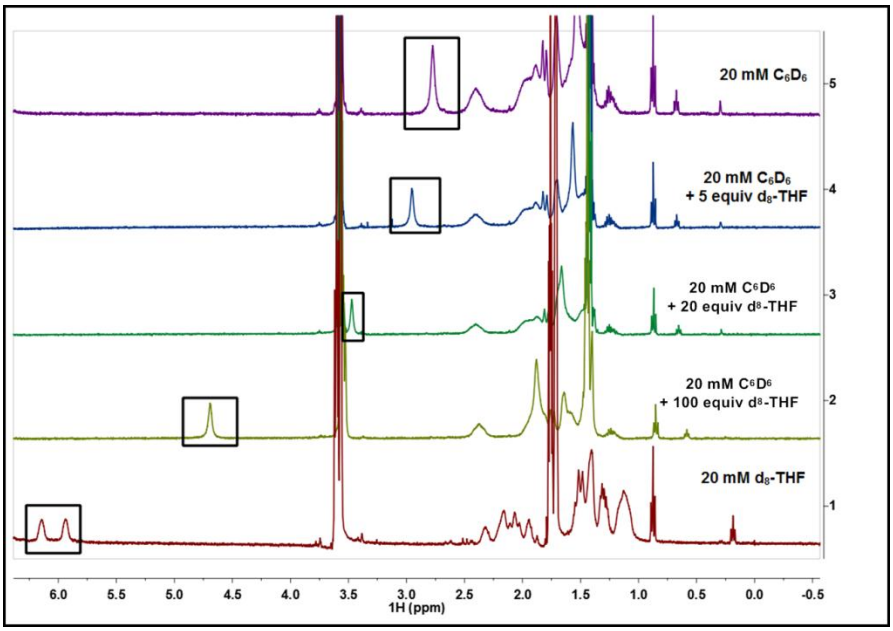

Figure A2.2. ^{1}H NMR spectra of **3.1** (22 ^{o}C) in various solvent ratios. The spectrum in THF-d_8 is ^{15}N-enriched. The NHH_{trans} resonance is shown in a black box, highlighting the effect of hydrogen-bonding to THF.

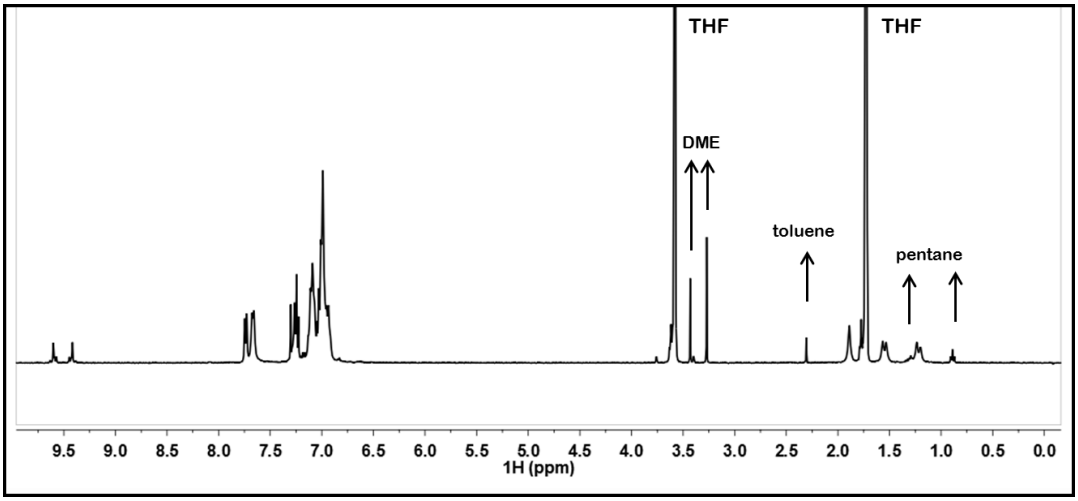

Figure A2.3. $^{1}H\{^{31}P\}$ NMR spectrum of ^{15}N-enriched **3.2** (THF-d_8)

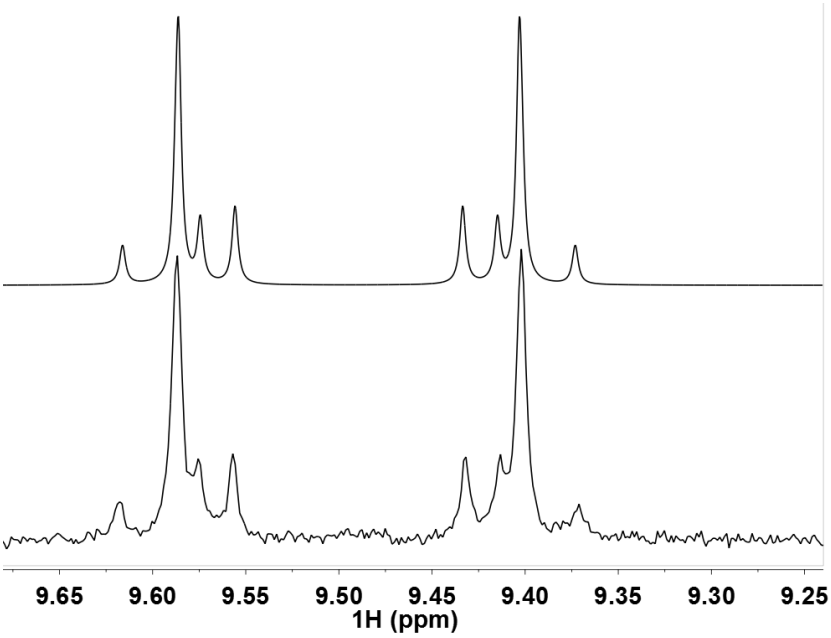

Figure A2.4. Simulation (top) and experimental (bottom) ^{1}H NMR spectrum of the N*H* proton in ^{15}N-enriched **3.2**. Fitting parameters: δ 9.494, $^{1}J_{NH}$ = -71.0 Hz, $^{2}J_{NH}$ = -2.1 Hz, $^{3}J_{HH}$ = 14.8 Hz, $^{1}J_{NN}$ = 9.5 Hz

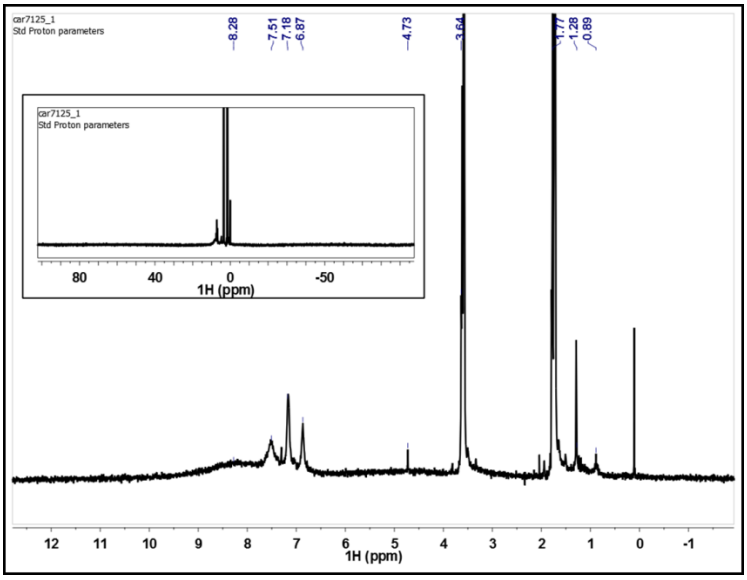

Figure A2.5. ^{1}H NMR spectrum of **3.3** (THF-d_8). The inset shows the same spectrum in a larger chemical shift window.

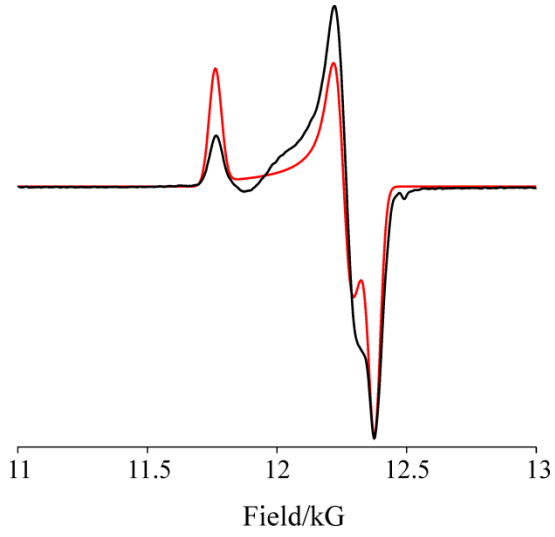

Figure A2.6. Two-pulse echo-detected EPR spectrum of **3.3** (red) and fit (black). *Experimental Conditions*: pulse length, π = 200 ns; microwave frequency, 35.003 GHz, repetition time, 20 ms; τ = 600 ns; 20 shots per point, temperature, 2 K. Spectrum was simulated with g = [2.125, 2.040, 2.120], and an anisotropic Gaussian linewidth of [55, 65, 45] G to account for the EPR linewidth contribution that is due to unresolved hyperfine couplings.

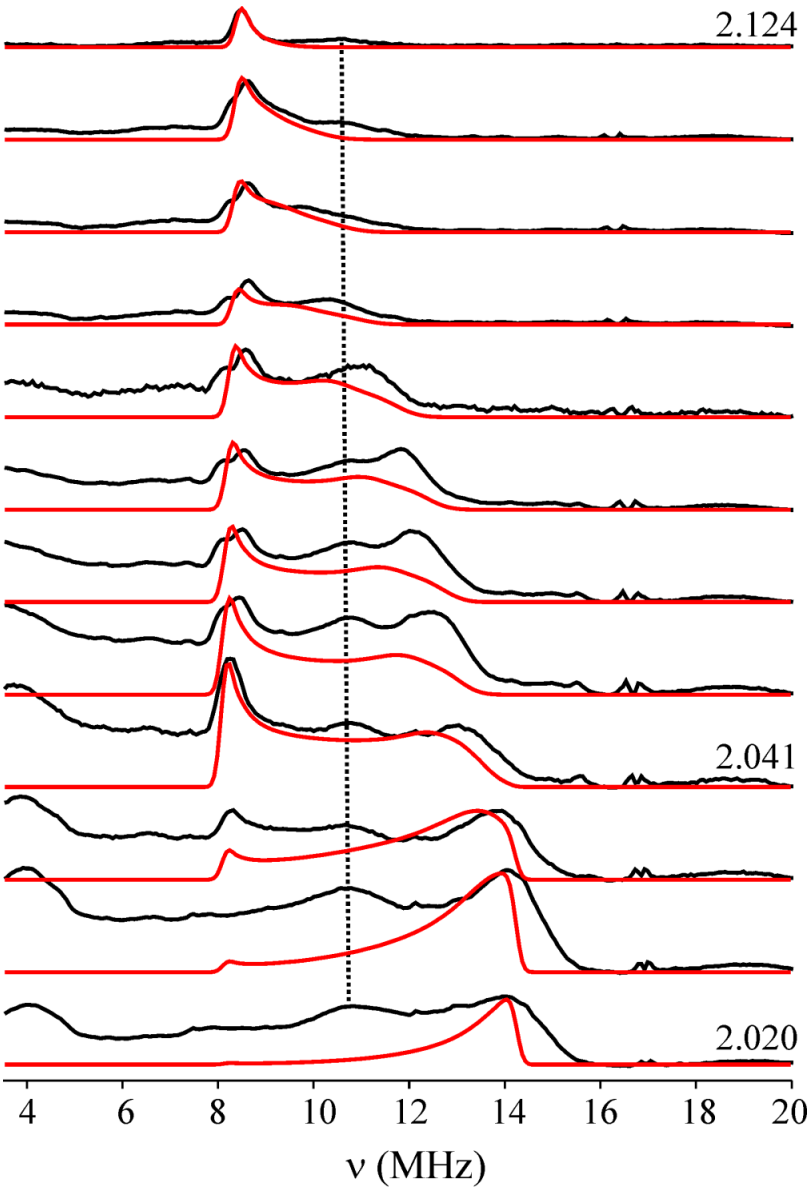

Figure A2.7. Davies ^{15}N pulsed ENDOR spectra from ^{15}N-**3.3**, 2D field-frequency pattern (black traces) with simulations (red traces). The spectra have been simulated using a single type of ^{15}N nucleus whose hyperfine tensor is rotated relative to **g** by 7^{o} around the N-N vector (g_1). The dotted black line corresponds to an ENDOR response from ^{31}P nuclei in **3.3**. *Experimental conditions*: microwave frequency, 34.922-34.983 GHz; π = 200 ns; τ = 600 ns; t_{rf} = 30 μs; repetition rate, 20 ms; RF randomly hopped. *Simulations*. g = [2.125, 2.040, 2.020] (g_1 = z); A = [6.7, 5.6, 17.8] MHz; (α,β,γ) = (7,5,0); microwave frequency, 34.983 GHz; EPR linewidth, 300 MHz; ENDOR linewidth, 0.25 MHz; the maximum simulation intensity is individually matched to the maximum ENDOR intensity at each field.

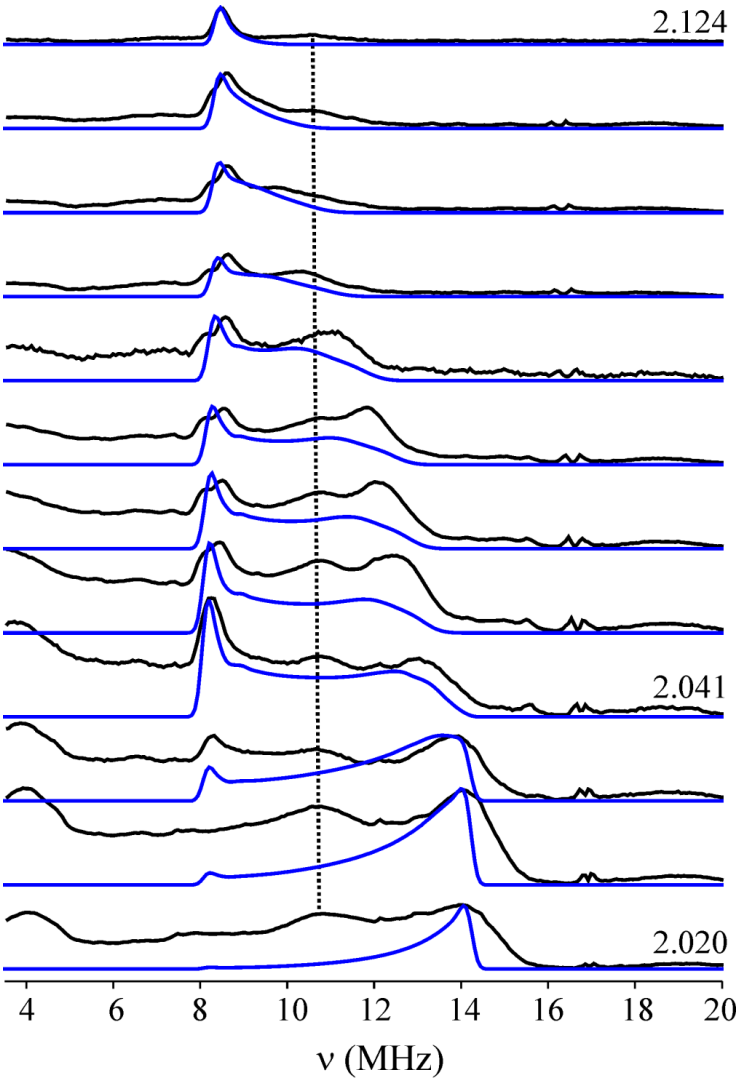

Figure A2.8. Davies ^{15}N pulsed ENDOR spectra from ^{15}N-**3.3**, 2D field-frequency pattern (black traces) with simulations (blue traces). The spectra have been simulated using a sum of two magnetically equivalent ^{15}N nuclei whose hyperfine tensors are rotated relative to **g** by 0^{o} and 15^{o} around the N-N vector (g_1). The dotted black line corresponds to an ENDOR response from ^{31}P nuclei in **3.3**. *Experimental conditions*: microwave frequency, 34.922-34.983 GHz; π = 200 ns; τ = 600 ns; t_{rf} = 30 μs; repetition rate, 20 ms; RF randomly hopped. *Simulations*. g = [2.125, 2.040, 2.020] (g_1 = z); A = [6.7, 5.6, 17.8] MHz; (α,β,γ) = (0,5,0:N1), (15,5,0:N2); microwave frequency, 34.983 GHz; EPR linewidth, 300 MHz; ENDOR linewidth, 0.25 MHz; the ENDOR intensity from N1 and N2 have been given equal weight in the summation; the maximum simulation intensity is individually matched to the maximum ENDOR intensity at each field.

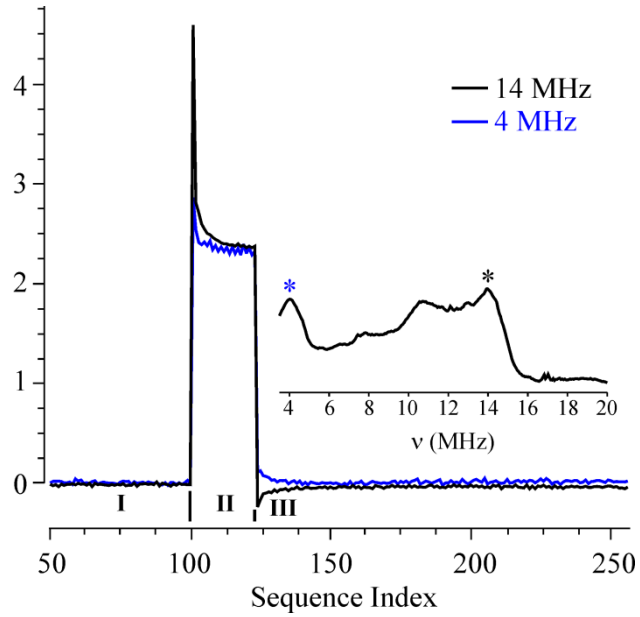

Figure A2.9. PESTRE spectra measured at the ν_+ (14 MHz; black) and ν_- (4 MHz; blue) frequencies from the ^{15}N ENDOR response at g_2 = 2.024 in ^{15}N-**3.3**. *Inset*. Davies ^{15}N ENDOR spectrum at g_2. The frequencies at which a PESTRE spectrum is acquired are denoted by stars. *Conditions*. PESTRE: microwave frequency, 34.974 GHz; π = 200 ns; τ = 600 ns; repetition rate, 25 ms; t_{rf} = 30 μs; RF frequency, 14 MHz (ν_+) and 4.0 MHz (ν_-); t_{mix} = 5 ms; ^{15}N ENDOR: π = 200 ns; τ = 600 ns; repetition rate, 20 ms; t_{rf} = 30 μs; RF frequency randomly hopped

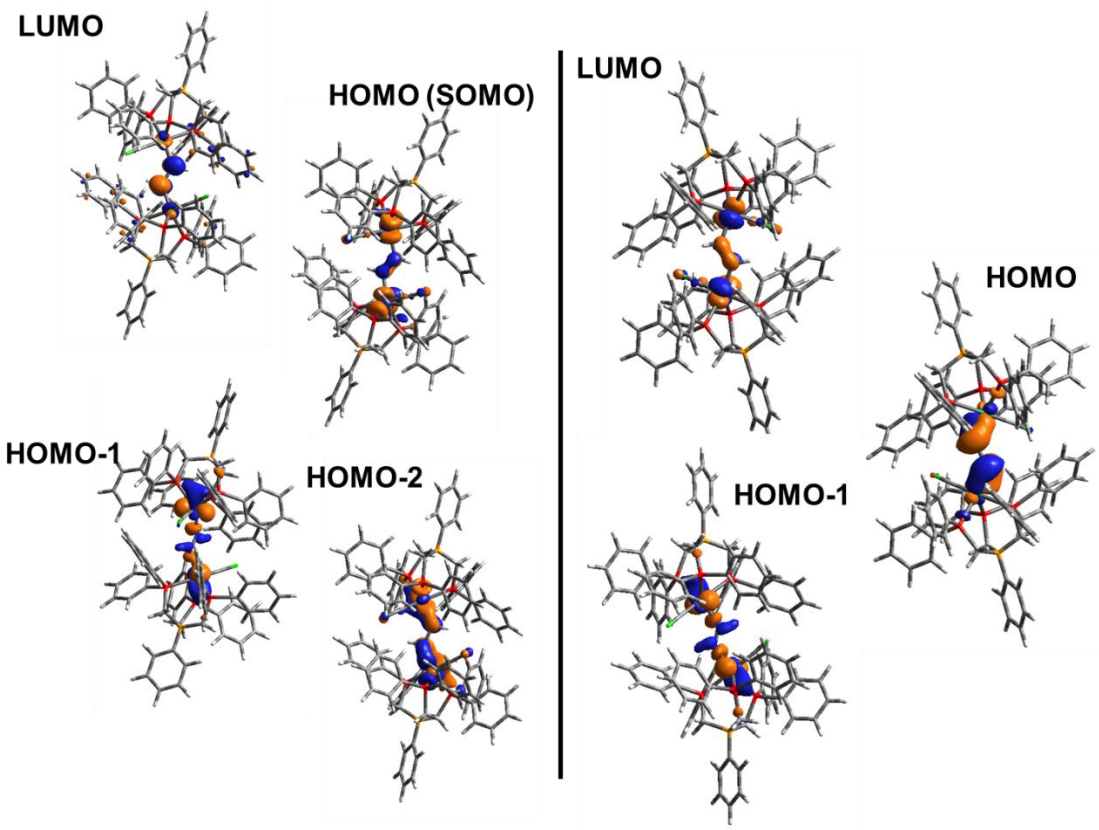

Figure A2.10. Isocontour plots (0.04) of the frontier orbitals of **3.3** (left; α spin) and **3.2** (right). The β orbitals for **3.3** were similar to the analogous α orbitals and are not shown. For the anion **3.3**, the energy difference between HOMO-1 and HOMO-2 is 0.67 kcal/mol (α) and 1.39 kcal/mol (β). The ordering of these orbitals is switched from that of the HOMO and HOMO-1 for **3.2**, in which the energy difference is 5.41 kcal/mol.

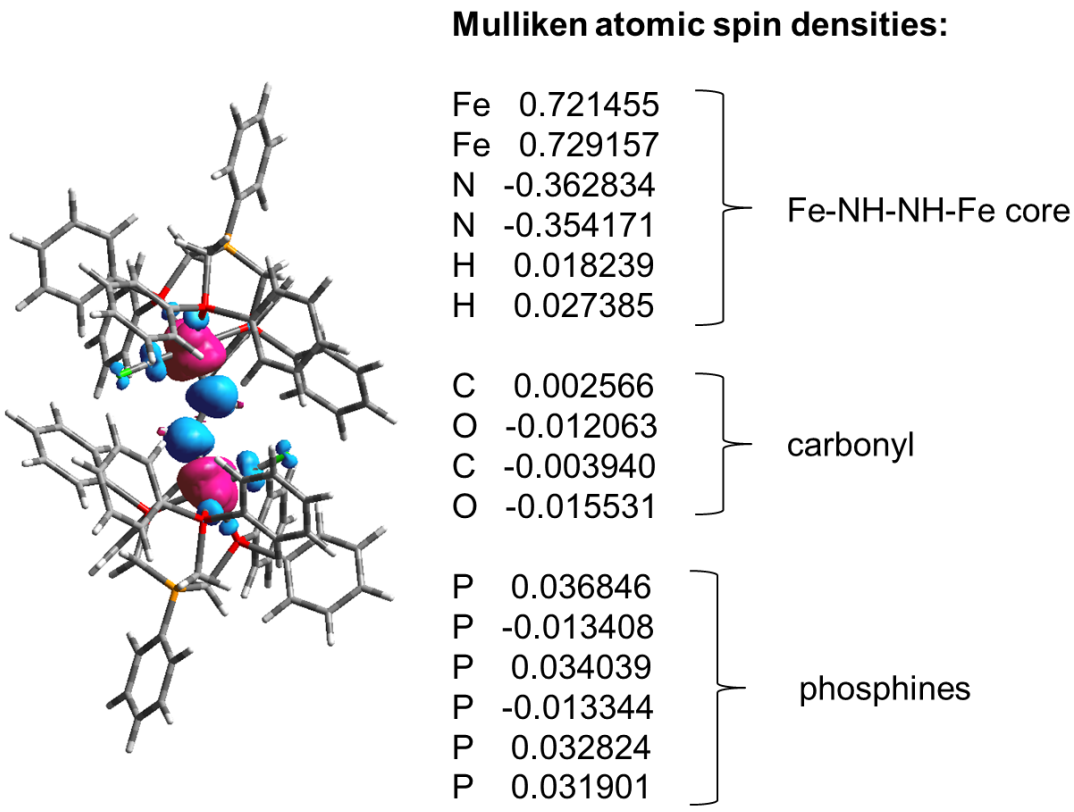

Figure A2.11. Isocontour plot (0.002) of the spin density of **3.3** with calculated densities listed. The remainder of the density (ca. 14 %) residing on the aryl rings of the ligands

Table A2.1. Select bond lengths [Å] and angles [°] for **3.1**

Fe(1)-C(46)	1.758(2)
Fe(1)-N(1)	1.991(2)
Fe(1)-N(2)	2.019(2)
Fe(1)-P(2)	2.2335(6)
Fe(1)-P(1)	2.2340(6)
Fe(1)-P(3)	2.3602(6)
C(46)-O(1)	1.155(3)
N(1)-N(2)	1.383(3)
C(46)-Fe(1)-N(1)	91.85(9)
C(46)-Fe(1)-N(2)	93.75(9)
N(1)-Fe(1)-N(2)	40.33(9)
C(46)-Fe(1)-P(2)	92.31(7)
N(1)-Fe(1)-P(2)	153.49(7)
N(2)-Fe(1)-P(2)	113.23(7)
C(46)-Fe(1)-P(1)	90.85(7)
N(1)-Fe(1)-P(1)	113.69(7)
N(2)-Fe(1)-P(1)	153.69(7)
P(2)-Fe(1)-P(1)	92.41(2)
C(46)-Fe(1)-P(3)	179.12(7)
N(1)-Fe(1)-P(3)	89.00(6)
N(2)-Fe(1)-P(3)	86.77(6)
P(2)-Fe(1)-P(3)	86.83(2)
P(1)-Fe(1)-P(3)	89.00(2)
O(1)-C(46)-Fe(1)	178.5(2)
N(2)-N(1)-Fe(1)	70.94(13)
N(1)-N(2)-Fe(1)	68.73(12)

Table A2.2. Crystal data and structure refinement for **3.1**

Identification code	d8_09026_1	
Empirical formula	C55 H53 B Fe N2 O P3	
Formula weight	917.56	
Temperature	100(2) K	
Wavelength	1.54178 Å	
Crystal system	Monoclinic	
Space group	P2(1)/c	
Unit cell dimensions	a = 22.3583(6) Å	α= 90°.
	b = 11.8150(3) Å	β= 97.956(2)°.
	c = 18.1214(6) Å	γ = 90°.
Volume	4740.9(2) $Å^3$	
Z	4	
Density (calculated)	1.286 Mg/m^3	
Absorption coefficient	3.823 mm^{-1}	
F(000)	1924	
Crystal size	0.40 x 0.22 x 0.07 mm^3	
Theta range for data collection	3.99 to 66.88°.	
Index ranges	-26<=h<=26, -14<=k<=14, -20<=l<=16	
Reflections collected	65781	
Independent reflections	8118 [R(int) = 0.0393]	
Completeness to theta = 66.88°	96.3 %	
Absorption correction	Multi-scan	
Max. and min. transmission	0.7757 and 0.3100	
Refinement method	Full-matrix least-squares on F^2	
Data / restraints / parameters	8118 / 1023 / 706	
Goodness-of-fit on F^2	1.082	
Final R indices [I>2sigma(I)]	R1 = 0.0391, wR2 = 0.1052	
R indices (all data)	R1 = 0.0436, wR2 = 0.1085	
Largest diff. peak and hole	0.968 and -0.348 $e.Å^{-3}$	

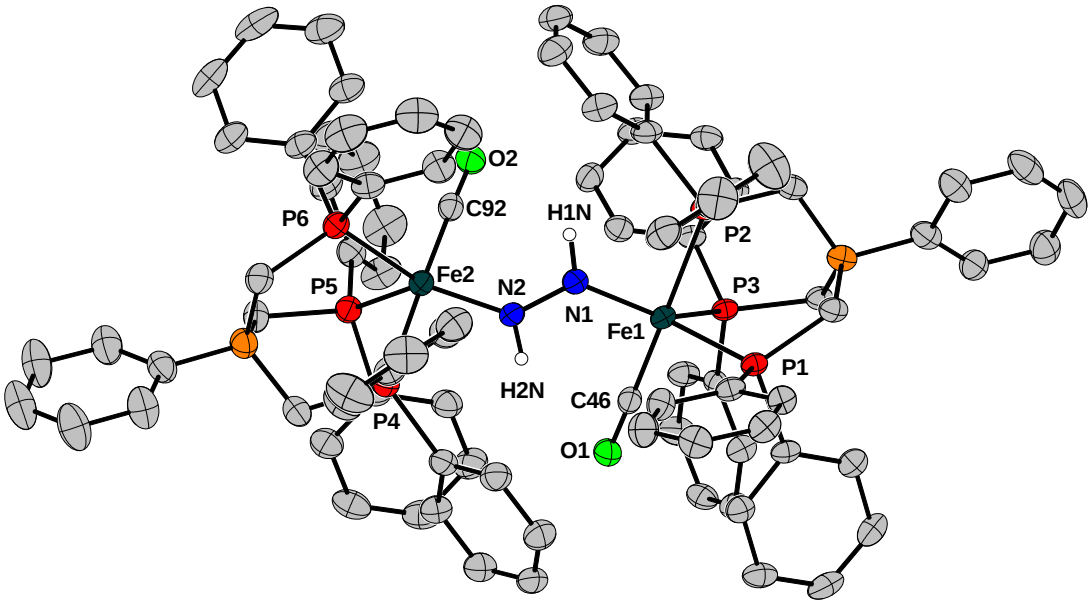

Figure A2.12. Displacement ellipsoid (50%) representation of **3.2**. Hydrogen atoms, minor components of disorder, and solvent molecules were removed for clarity.

Table A2.3. Select bond lengths [Å] and angles [°] for **3.2**

Fe(1)-C(46)	1.773(4)	N(1)-Fe(1)-P(2)	86.12(10)
Fe(1)-N(1)	1.824(3)	P(3)-Fe(1)-P(2)	89.77(4)
Fe(1)-P(3)	2.2109(10)	P(1)-Fe(1)-P(2)	87.25(4)
Fe(1)-P(1)	2.2383(10)	N(2)-N(1)-Fe(1)	130.0(2)
Fe(1)-P(2)	2.3248(10)	N(2)-N(1)-H(1N)	110(3)
N(1)-N(2)	1.362(4)	Fe(1)-N(1)-H(1N)	119(3)
N(1)-H(1N)	0.886(18)	O(1)-C(46)-Fe(1)	175.7(3)
C(46)-O(1)	1.147(4)	C(92)-Fe(2)-N(2)	92.40(15)
Fe(2)-C(92)	1.773(4)	C(92)-Fe(2)-P(5)	91.34(12)
Fe(2)-N(2)	1.841(3)	N(2)-Fe(2)-P(5)	127.96(10)
Fe(2)-P(5)	2.2156(11)	C(92)-Fe(2)-P(6)	93.55(11)
Fe(2)-P(6)	2.2481(10)	N(2)-Fe(2)-P(6)	139.54(10)
Fe(2)-P(4)	2.3140(11)	P(5)-Fe(2)-P(6)	91.87(4)
N(2)-H(2N)	0.873(18)	C(92)-Fe(2)-P(4)	178.40(12)
C(92)-O(2)	1.150(4)	N(2)-Fe(2)-P(4)	86.09(10)
C(46)-Fe(1)-N(1)	93.15(14)	P(5)-Fe(2)-P(4)	89.17(4)
C(46)-Fe(1)-P(3)	90.60(11)	P(6)-Fe(2)-P(4)	87.94(4)
N(1)-Fe(1)-P(3)	126.62(10)	N(1)-N(2)-Fe(2)	131.7(2)
C(46)-Fe(1)-P(1)	93.37(11)	N(1)-N(2)-H(2N)	106(3)
N(1)-Fe(1)-P(1)	140.66(10)	Fe(2)-N(2)-H(2N)	122(3)
P(3)-Fe(1)-P(1)	92.05(4)	O(2)-C(92)-Fe(2)	176.5(3)
C(46)-Fe(1)-P(2)	179.26(12)		

Table A2.4. Crystal data and structure refinement for **3.2**

Identification code	pm	
Empirical formula	C52 H48 B Fe N O P3	
Formula weight	862.48	
Temperature	100(2) K	
Wavelength	1.54178 Å	
Crystal system	Triclinic	
Space group	P-1	
Unit cell dimensions	a = 12.5497(3) Å	α= 87.989(2)°.
	b = 16.5501(4) Å	β= 76.110(2)°.
	c = 22.2784(5) Å	γ = 76.326(2)°.
Volume	4363.42(18) Å^3	
Z	4	
Density (calculated)	1.313 Mg/m^3	
Absorption coefficient	4.113 mm^{-1}	
F(000)	1804	
Crystal size	0.14 x 0.11 x 0.10 mm^3	
Theta range for data collection	2.04 to 65.10°.	
Index ranges	-14<=h<=14, -19<=k<=19, -26<=l<=26	
Reflections collected	85059	
Independent reflections	14565 [R(int) = 0.0639]	
Completeness to theta = 65.10°	97.8 %	
Absorption correction	Semi-empirical from equivalents	
Max. and min. transmission	0.6838 and 0.5967	
Refinement method	Full-matrix least-squares on F^2	
Data / restraints / parameters	14565 / 1506 / 1124	
Goodness-of-fit on F^2	1.072	
Final R indices [I>2sigma(I)]	R1 = 0.0556, wR2 = 0.1385	
R indices (all data)	R1 = 0.0713, wR2 = 0.1476	
Largest diff. peak and hole	1.027 and -0.670 e.Å^{-3}	

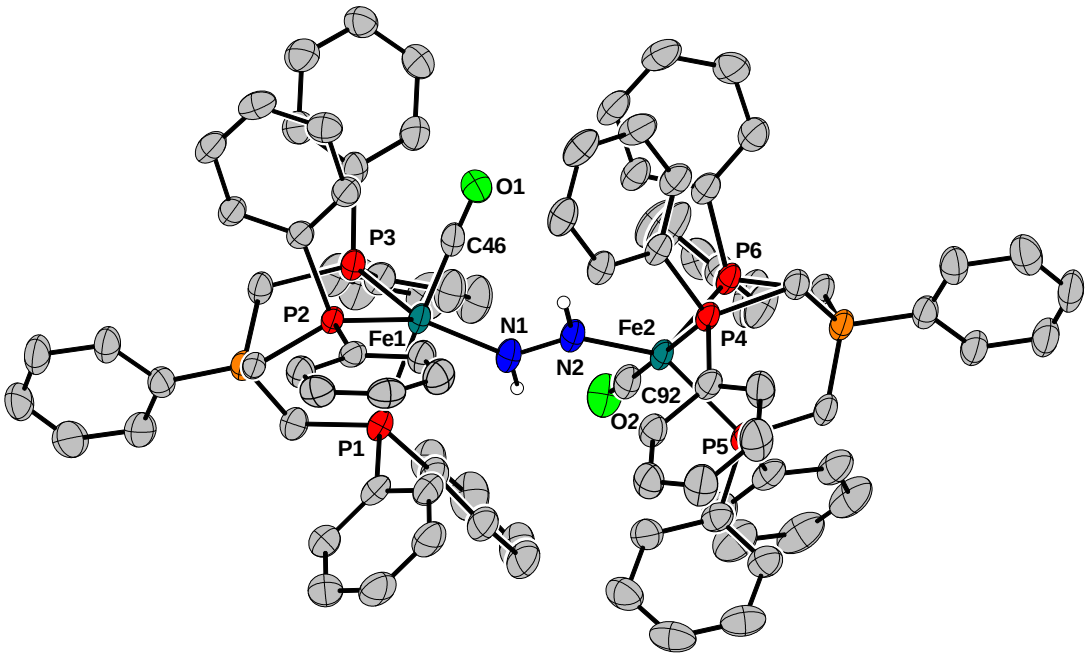

Figure A2.13. Displacement ellipsoid (50%) representation of **3.3**. Hydrogen atoms, the Na counter-cation, and solvent molecules were removed for clarity.

Table A2.5. Select bond lengths [Å] and angles [°] for **3.3**

Fe(1)-C(46)	1.750(3)	C(92)-Fe(2)-P(4)	178.68(10)
Fe(1)-N(1)	1.876(2)	N(2)-Fe(2)-P(4)	87.33(8)
Fe(1)-P(3)	2.2209(10)	P(6)-Fe(2)-P(4)	88.77(4)
Fe(1)-P(2)	2.2370(10)	P(5)-Fe(2)-P(4)	86.93(4)
Fe(1)-P(1)	2.3011(11)	N(1)-N(2)-Fe(2)	131.42(19)
N(1)-N(2)	1.342(3)	N(1)-N(2)-H(2N)	104(2)
N(1)-H(1N)	0.903(19)	Fe(2)-N(2)-H(2N)	124(2)
C(46)-O(1)	1.160(4)	O(2)-C(92)-Fe(2)	175.9(3)
Fe(2)-C(92)	1.753(3)		
Fe(2)-N(2)	1.884(2)		
Fe(2)-P(6)	2.2069(9)		
Fe(2)-P(5)	2.2268(12)		
Fe(2)-P(4)	2.2937(9)		
N(2)-H(2N)	0.899(19)		
C(92)-O(2)	1.155(4)		
C(46)-Fe(1)-N(1)	92.77(12)		
C(46)-Fe(1)-P(3)	91.08(9)		
N(1)-Fe(1)-P(3)	127.21(8)		
C(46)-Fe(1)-P(2)	93.64(9)		
N(1)-Fe(1)-P(2)	141.19(8)		
P(3)-Fe(1)-P(2)	90.89(3)		
C(46)-Fe(1)-P(1)	177.75(8)		
N(1)-Fe(1)-P(1)	85.27(9)		
P(3)-Fe(1)-P(1)	91.00(4)		
P(2)-Fe(1)-P(1)	87.21(4)		
N(2)-N(1)-Fe(1)	133.0(2)		
N(2)-N(1)-H(1N)	103(2)		
Fe(1)-N(1)-H(1N)	123(2)		
O(1)-C(46)-Fe(1)	176.3(2)		
C(92)-Fe(2)-N(2)	93.18(11)		
C(92)-Fe(2)-P(6)	89.94(10)		
N(2)-Fe(2)-P(6)	125.57(9)		
C(92)-Fe(2)-P(5)	93.45(10)		
N(2)-Fe(2)-P(5)	140.08(8)		
P(6)-Fe(2)-P(5)	93.76(4)		

Table A2.6. Crystal data and structure refinement for **3.3**

Identification code	car31	
Empirical formula	C48.23 H63.12 B0.67 Fe0.67 N0.67 Na0.33 O3.10 P2	
Formula weight	815.89	
Temperature	100(1) K	
Wavelength	0.73 Å	
Crystal system	Triclinic	
Space group	P-1	
Unit cell dimensions	a = 12.380(3) Å	α= 107.95(3)°.
	b = 22.750(5) Å	β= 92.56(3)°.
	c = 24.870(5) Å	γ = 101.30(3)°.
Volume	6493(2) Å^3	
Z	6	
Density (calculated)	1.252 Mg/m^3	
Absorption coefficient	0.360 mm^{-1}	
F(000)	2618	
Crystal size	0.17 x 0.15 x 0.07 mm^3	
Theta range for data collection	0.87 to 25.45°.	
Index ranges	-14<=h<=14, -27<=k<=27, -30<=l<=30	
Reflections collected	219105	
Independent reflections	21306 [R(int) = 0.0852]	
Completeness to theta = 25.45°	88.7 %	
Refinement method	Full-matrix least-squares on F^2	
Data / restraints / parameters	21306 / 5305 / 1964	
Goodness-of-fit on F^2	1.024	
Final R indices [I>2sigma(I)]	R1 = 0.0500, wR2 = 0.1353	
R indices (all data)	R1 = 0.0520, wR2 = 0.1370	
Extinction coefficient	0.0063(3)	
Largest diff. peak and hole	0.557 and -0.457 e.Å^{-3}	

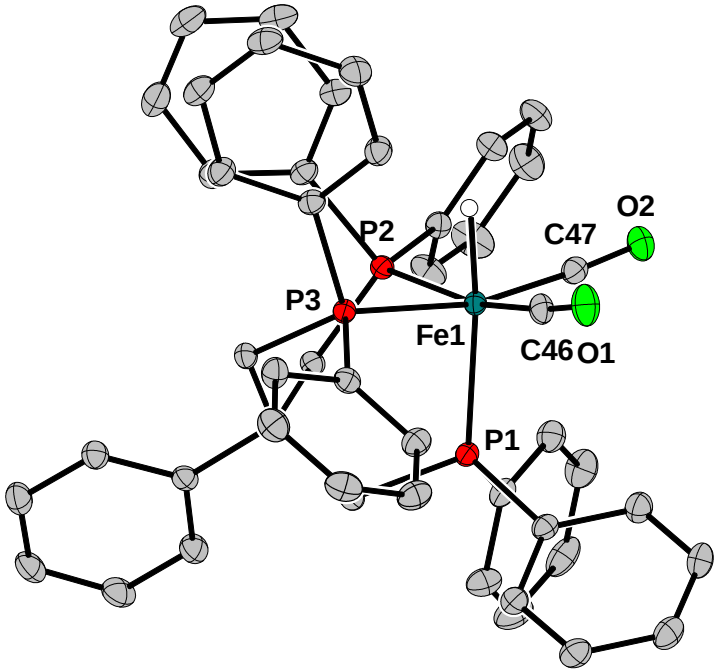

Figure A2.14. Displacement ellipsoid (50%) representation of **[PhBP$_3$]Fe(CO)$_2$H**. The hydride was located in the difference map, and refined. Other hydrogen atoms and solvent molecules were removed for clarity.

Table A2.7. Crystal data and structure refinement for **[$PhBP_3$]$Fe(CO)_2H$**

Identification code	07141
Empirical formula	C56 H51 B Fe O2 P3
Formula weight	915.54
Temperature	100(2) K
Wavelength	0.71073 A
Crystal system, space group	Triclinic, P-1
Unit cell dimensions	a = 11.0932(11) A alpha = 88.936(2) deg.
	b = 11.1987(11) A beta = 87.070(2) deg.
	c = 20.566(2) A gamma = 64.6150(10) deg.
Volume	2305.2(4) A^3
Z, Calculated density	2, 1.319 Mg/m^3
Absorption coefficient	0.474 mm^-1
F(000)	958
Crystal size	0.35 x 0.22 x 0.10 mm
Theta range for data collection	0.99 to 29.57 deg.
Limiting indices	-15<=h<=15, -15<=k<=15, -28<=l<=28
Reflections collected / unique	61011 / 12924 [R(int) = 0.0304]
Completeness to theta = 29.57	99.8 %
Absorption correction	Semi-empirical from equivalents
Max. and min. transmission	0.9541 and 0.8516
Refinement method	Full-matrix least-squares on F^2
Data / restraints / parameters	12924 / 0 / 572
Goodness-of-fit on F^2	1.066
Final R indices [I>2sigma(I)]	R1 = 0.0320, wR2 = 0.0802
R indices (all data)	R1 = 0.0393, wR2 = 0.0887
Largest diff. peak and hole	0.539 and -0.304 e.A^-3

Table A2.8. Select bond lengths [A] and angles [deg] for **[PhBP$_3$]Fe(CO)$_2$H**

Fe(1)-C(46)	1.7719(14)
Fe(1)-C(47)	1.7723(14)
Fe(1)-P(2)	2.2787(4)
Fe(1)-P(1)	2.2908(4)
Fe(1)-P(3)	2.2944(4)
Fe(1)-H(57)	1.42(2)
O(1)-C(46)	1.1478(17)
O(2)-C(47)	1.1494(16)
C(46)-Fe(1)-C(47)	89.26(6)
C(46)-Fe(1)-P(2)	167.93(5)
C(47)-Fe(1)-P(2)	92.61(4)
C(46)-Fe(1)-P(1)	100.23(5)
C(47)-Fe(1)-P(1)	100.99(4)
P(2)-Fe(1)-P(1)	91.128(13)
C(46)-Fe(1)-P(3)	89.81(4)
C(47)-Fe(1)-P(3)	166.98(4)
P(2)-Fe(1)-P(3)	85.684(14)
P(1)-Fe(1)-P(3)	91.958(14)
C(46)-Fe(1)-H(57)	84.9(8)
C(47)-Fe(1)-H(57)	83.0(8)
P(2)-Fe(1)-H(57)	83.5(8)
P(1)-Fe(1)-H(57)	173.5(8)
P(3)-Fe(1)-H(57)	84.0(8)
O(1)-C(46)-Fe(1)	174.35(13)
O(2)-C(47)-Fe(1)	173.88(12)

Appendix 3: Supplementary Data for Chapter 4

Supplementary Experimental Section

Reaction of [PhBP$^{Ph}_3$]Fe(η^2-N_2H_3) with *para*-benzoquinone. A solution of *para*-benzoquinone (0.0410 g, 0.379 mmol) in 4 mL THF was added dropwise to a solution of **4.5** (0.1897 mmol) in 10 mL THF at -78 ^oC. After stirring at -78 ^oC for one hour, the reaction was warmed to room temperature, and stirred an additional hour before the volatiles were removed. By ^1H NMR, several species were present. Triteration of the resulting residue with pentane, followed by THF extraction and layering of pentane afford crystals of {[PhBP$^{Ph}_3$]Fe}$_2$(μ-OArO). IR of the crude reaction mixture does not show any NH stretches.

Reaction of [PhBP$^{Ph}_3$]Fe(η^2-N_2H_3) with 3,5-ditbutyl,*ortho*-quinone. A solution of 3,5-di-^{t}butyl-*ortho*-quinone (0.0168 g, 0.0748 mmol) in 1 mL THF was added dropwise to a stirring solution of **4.5** (0.03741 mmol) in 3 mL THF at -78 ^oC. The reaction stirred overnight, during which it warmed to room temperature. The volatiles were removed, and the resulting solid was rinsed with pentane, extracted into THF, and filtered. The slow evaporation of pentane into the THF solution yielded purple crystals of [PhBP$^{Ph}_3$]Fe(OArO). ^1H NMR (C_6D_6, 300 MHz) δ 16.5, 11.4, 10.2, 5.9, 5.6, 4.5, 1.9, -4.2, -9.7 (bs), -9.9 (bs), -14.0 (bs). Evans Method (C_6D_6): 2.4 B.M. UV-vis (THF) λ_{max}, nm (ε, M^{-1} cm^{-1}): 563 (5300), 820 (4170).

Reaction of [PhBP$^{mter}_3$]Fe(η^2-N_2H_3) with *para*-benzoquinone. A solution of *para*-benzoquinone (0.0027 g, 0.0246 mmol) in 2 mL benzene was added to a stirring solution

of **4.1** (0.0246 mmol) in 2 mL benzene, and stirred for 1 h, during which the solution went from green to orange. The solution was filtered, and the volatiles were removed. The solids were extracted into DME, and layered with pentane to afford crystals of [PhBP$^{mter}_3$]Fe(OArOH (0.0231g, 60.4 %). ^{1}H NMR (C_6D_6, 300 MHz) δ 70.1, 37.9, 19.4, 18.7, 17.4, 8.7, 7.1, 6.8, 5.5, 3.5, -8.6, -12.3, -32.5.

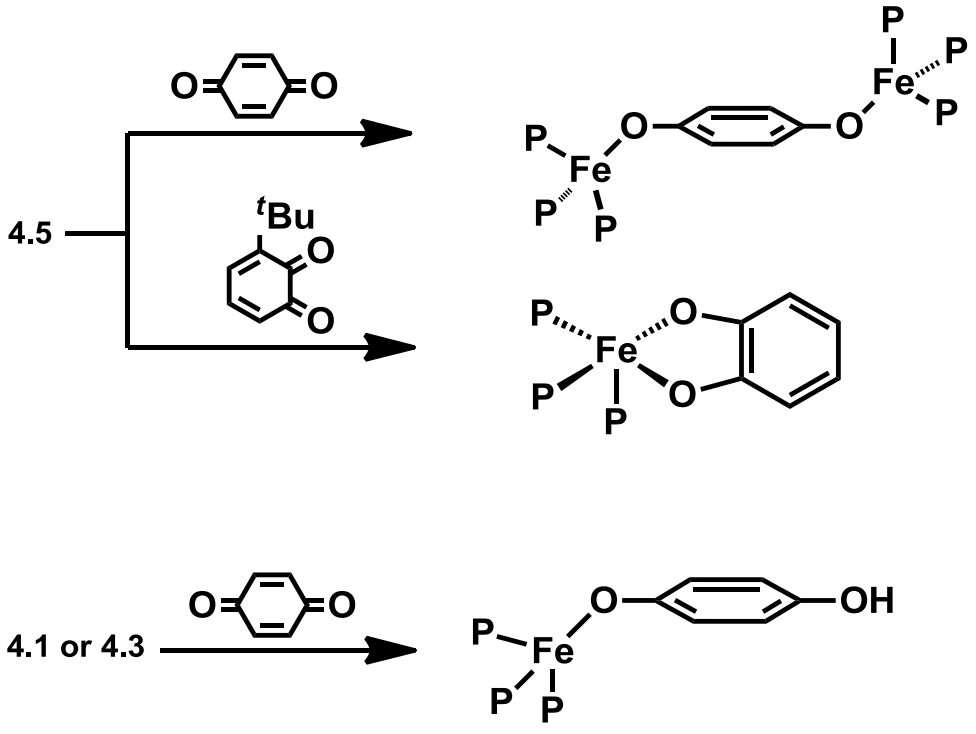

Scheme A3.1.

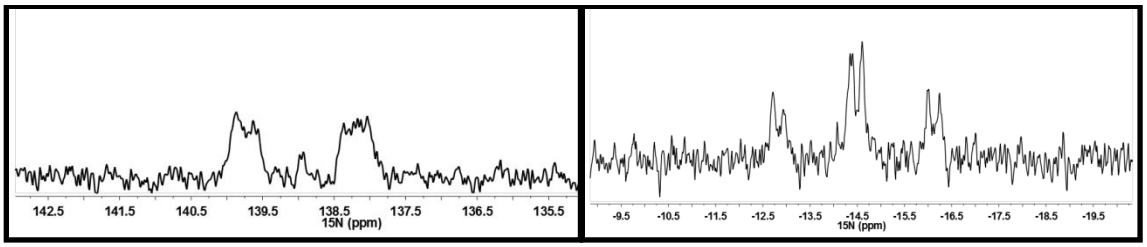

Figure A3.1. Closeup of the ^{15}N NMR spectrum of **4.1**, highlighting the NH and NN coupling (d_8-THF, -25 ^{o}C)

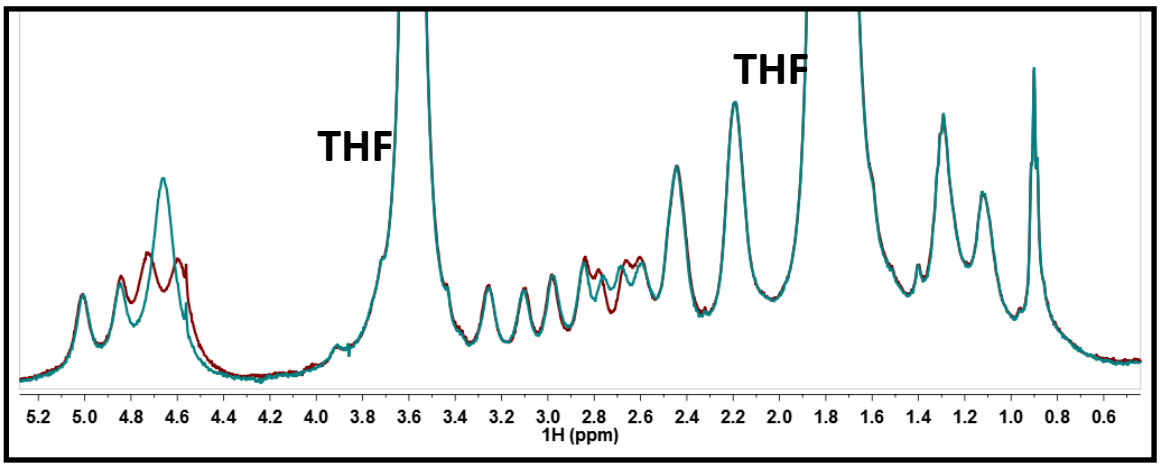

Figure A3.2. ^{1}H/1H{^{15}N, 47.4 ppm} NMR spectrum of **4.3** (d_8-THF, -40 ^{o}C)

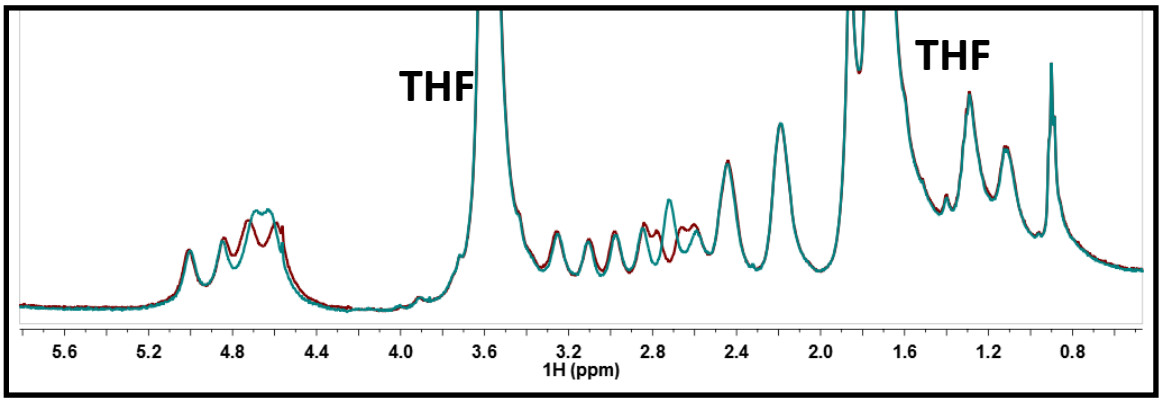

Figure A3.3. ^{1}H/1H{^{15}N, 40.8 ppm} NMR spectrum of **4.3** (d_8-THF, -40 ^{o}C)

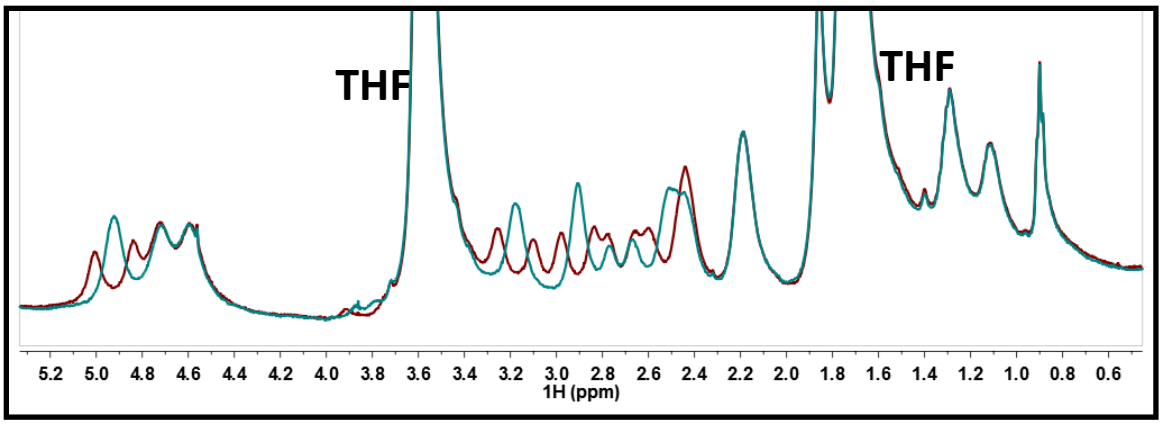

Figure A3.4. $^{1}H/1H\{^{15}N$, 23.0 ppm} NMR spectrum of **4.3** (d_8-THF, -40 ^{o}C)

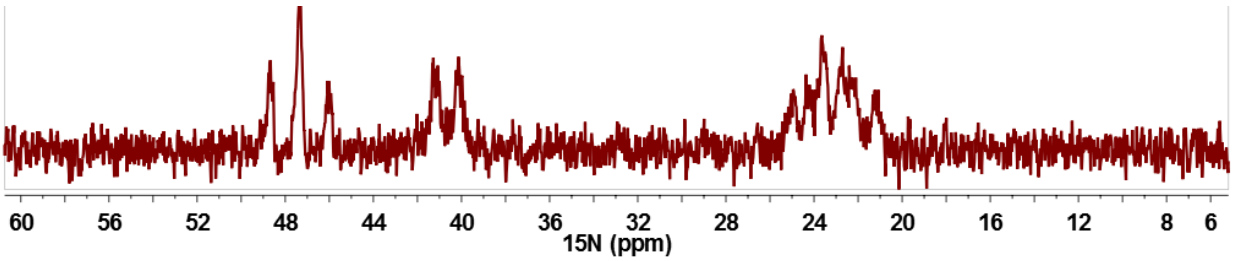

Figure A3.5. ^{15}N NMR spectrum of **4.3** (d_8-THF), -40 ^{o}C

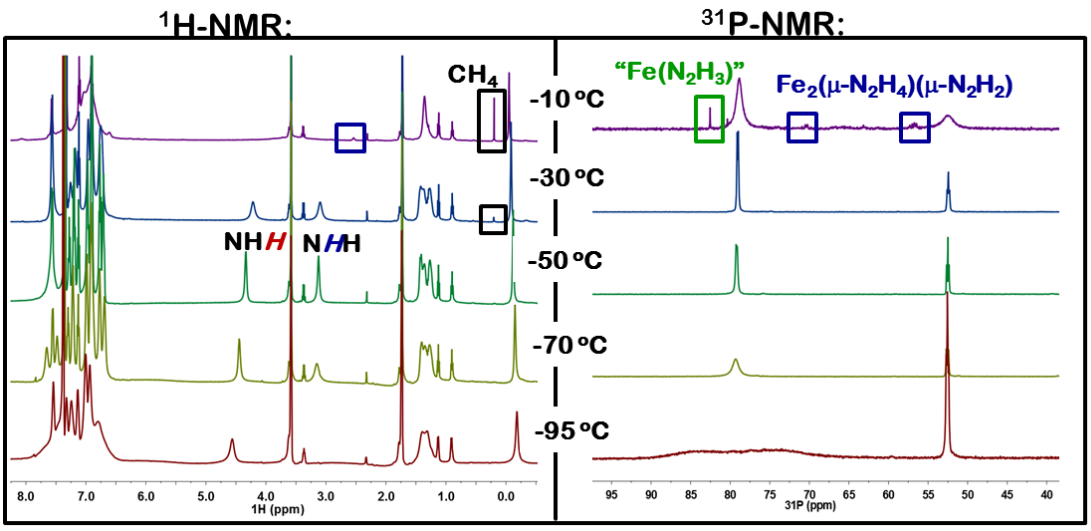

Figure A3.6. ^{1}H and ^{31}P NMR VT profile of **4.5** (d_8-THF). Peaks marked with an asterix correspond to $\{[PhBP^{Ph}_3]Fe\}_2(\mu\text{-}\eta^1\text{:}\eta^1\text{-}N_2H_4)(\mu\text{-}\eta^2\text{:}\eta^2\text{-}N_2H_2^{2-})$.

Table A3.1. Crystal data and structure refinement for [**PhBP$^{mter}_3$]FeCl**

Identification code	ccl68a	
Empirical formula	C234 H178 B2 Cl1.94 Fe1.94 P6 Tl0.06	
Formula weight	3386.59	
Temperature	100(2) K	
Wavelength	0.71073 Å	
Crystal system	Triclinic	
Space group	P-1	
Unit cell dimensions	a = 13.5781(10) Å	α= 75.466(2)°.
	b = 15.8816(11) Å	β= 80.341(2)°.
	c = 22.2863(16) Å	γ = 77.215(2)°.
Volume	4504.5(6) Å^3	
Z	1	
Density (calculated)	1.248 Mg/m^3	
Absorption coefficient	0.350 mm^{-1}	
F(000)	1770	
Crystal size	0.15 x 0.10 x 0.09 mm^3	
Theta range for data collection	1.47 to 25.02°.	
Index ranges	-15<=h<=15, -17<=k<=18, -26<=l<=26	
Reflections collected	19581	
Independent reflections	12901 [R(int) = 0.0605]	
Completeness to theta = 25.02°	81.2 %	
Absorption correction	Semi-empirical from equivalents	
Max. and min. transmission	1 and 0.747422	
Refinement method	Full-matrix least-squares on F^2	
Data / restraints / parameters	12901 / 1365 / 1173	
Goodness-of-fit on F^2	1.087	
Final R indices [I>2sigma(I)]	R1 = 0.0914, wR2 = 0.2151	
R indices (all data)	R1 = 0.1538, wR2 = 0.2460	
Largest diff. peak and hole	1.154 and -0.912 e.Å^{-3}	

Table A3.2. Crystal data and structure refinement for $Fe(NHNMe_2)$ (**4.2**)

Identification code	x	
Empirical formula	C47 H48 B Fe N2 P3	
Formula weight	800.44	
Temperature	100(2) K	
Wavelength	0.71073 Å	
Crystal system	Monoclinic	
Space group	P2(1)/n	
Unit cell dimensions	a = 13.294(3) Å	α= 90°.
	b = 22.458(5) Å	β= 94.24(3)°.
	c = 13.418(3) Å	γ = 90°.
Volume	3995.2(14) $Å^3$	
Z	4	
Density (calculated)	1.331 Mg/m^3	
Absorption coefficient	0.534 mm^{-1}	
F(000)	1680	
Crystal size	0.43 x 0.34 x 0.28 mm^3	
Theta range for data collection	1.77 to 29.57°.	
Index ranges	-18<=h<=18, -31<=k<=30, -18<=l<=18	
Reflections collected	83416	
Independent reflections	11169 [R(int) = 0.0547]	
Completeness to theta = 29.57°	99.5 %	
Absorption correction	Semi-empirical from equivalents	
Max. and min. transmission	0.7461 and 0.6786	
Refinement method	Full-matrix least-squares on F^2	
Data / restraints / parameters	11169 / 458 / 492	
Goodness-of-fit on F^2	1.050	
Final R indices [I>2sigma(I)]	R1 = 0.0395, wR2 = 0.0998	
R indices (all data)	R1 = 0.0509, wR2 = 0.1086	
Largest diff. peak and hole	0.621 and -0.300 $e.Å^{-3}$	

Table A3.3. Crystal data and structure refinement for $[PhBP^{mter}_3]Fe(NH_3)(N_2H_3)$ **(4.4)**

Identification code	car	
Empirical formula	C96.67 H100.67 B0.67 Fe0.67 N2 O4.67 P2	
Formula weight	1471.51	
Temperature	100(2) K	
Wavelength	1.54178 Å	
Crystal system	Monoclinic	
Space group	P2(1)/c	
Unit cell dimensions	a = 19.5253(4) Å	α= 90°.
	b = 21.1191(3) Å	β= 104.0950(10)°.
	c = 30.1301(6) Å	γ = 90°.
Volume	12050.3(4) $Å^3$	
Z	6	
Density (calculated)	1.217 Mg/m^3	
Absorption coefficient	1.841 mm^{-1}	
F(000)	4696	
Crystal size	0.33 x 0.29 x 0.20 mm^3	
Theta range for data collection	2.33 to 65.17°.	
Index ranges	-22<=h<=21, -24<=k<=24, -35<=l<=35	
Reflections collected	231415	
Independent reflections	20143 [R(int) = 0.0560]	
Completeness to theta = 65.17°	97.9 %	
Absorption correction	Semi-empirical from equivalents	
Max. and min. transmission	0.7097 and 0.5817	
Refinement method	Full-matrix least-squares on F^2	
Data / restraints / parameters	20143 / 6333 / 1933	
Goodness-of-fit on F^2	1.044	
Final R indices [I>2sigma(I)]	R1 = 0.0525, wR2 = 0.1405	
R indices (all data)	R1 = 0.0633, wR2 = 0.1496	
Largest diff. peak and hole	0.496 and -0.372 $e.Å^{-3}$	

Table A3.4. Crystal data and structure refinement for {[$PhBP^{Ph}_3$]Fe(N_2H_4)}{PF_6} (**4.6**)

Identification code	08257	
Empirical formula	C49.98 H54.85 B Cl0.25 F4.53 Fe N1.94 O1.25 P3.76	
Formula weight	980.52	
Temperature	100(2) K	
Wavelength	0.71073 Å	
Crystal system	Triclinic	
Space group	P-1	
Unit cell dimensions	a = 11.7898(9) Å	α= 73.970(2)°.
	b = 12.1629(10) Å	β= 79.3670(10)°.
	c = 18.5270(15) Å	γ = 74.2410(10)°.
Volume	2440.2(3) $Å^3$	
Z	2	
Density (calculated)	1.334 Mg/m^3	
Absorption coefficient	0.502 mm^{-1}	
F(000)	1021	
Crystal size	0.15 x 0.10 x 0.10 mm^3	
Theta range for data collection	1.15 to 29.13°.	
Index ranges	-16<=h<=16, -16<=k<=16, -25<=l<=25	
Reflections collected	50609	
Independent reflections	13080 [R(int) = 0.0637]	
Completeness to theta = 29.13°	99.7 %	
Absorption correction	Semi-empirical from equivalents	
Max. and min. transmission	0.9515 and 0.9285	
Refinement method	Full-matrix least-squares on F^2	
Data / restraints / parameters	13080 / 1894 / 793	
Goodness-of-fit on F^2	1.029	
Final R indices [I>2sigma(I)]	R1 = 0.0611, wR2 = 0.1754	
R indices (all data)	R1 = 0.0928, wR2 = 0.2001	
Largest diff. peak and hole	1.370 and -1.049 e.$Å^{-3}$	

Table A3.5. Crystal data and structure refinement for $[PhBP^{Ph}_3]Fe(OAc)(N_2H_4)$ (**4.7**)

Identification code	d8_10012	
Empirical formula	C55.50 H60 B Fe N2 O2 P3	
Formula weight	946.62	
Temperature	100(2) K	
Wavelength	1.54178 Å	
Crystal system	Triclinic	
Space group	P-1	
Unit cell dimensions	a = 12.74930(10) Å	α= 68.4530(10)°.
	b = 13.26200(10) Å	β= 69.9450(10)°.
	c = 17.4092(2) Å	γ = 64.3070(10)°.
Volume	2407.19(4) $Å^3$	
Z	2	
Density (calculated)	1.306 Mg/m^3	
Absorption coefficient	3.794 mm^{-1}	
F(000)	998	
Crystal size	0.34 x 0.13 x 0.02 mm^3	
Theta range for data collection	2.80 to 63.68°.	
Index ranges	-14<=h<=14, -15<=k<=15, -20<=l<=20	
Reflections collected	26019	
Independent reflections	7698 [R(int) = 0.0446]	
Completeness to theta = 63.68°	97.1 %	
Absorption correction	Semi-empirical from equivalents	
Max. and min. transmission	0.9280 and 0.3586	
Refinement method	Full-matrix least-squares on F^2	
Data / restraints / parameters	7698 / 1297 / 674	
Goodness-of-fit on F^2	1.030	
Final R indices [I>2sigma(I)]	R1 = 0.0389, wR2 = 0.0908	
R indices (all data)	R1 = 0.0505, wR2 = 0.0972	
Largest diff. peak and hole	0.529 and -0.265 e.$Å^{-3}$	

Table A3.6. Crystal data and structure refinement for $[PhBP^{Ph}_3]Fe(OAc)(NH_3)$ (**4.8**)

Identification code	x	
Empirical formula	C53 H50 B Fe N0 O2 P3	
Formula weight	878.50	
Temperature	100(2) K	
Wavelength	1.54178 Å	
Crystal system	Triclinic	
Space group	P-1	
Unit cell dimensions	a = 10.38700(10) Å	α= 98.0580(10)°.
	b = 11.73090(10) Å	β= 98.6680(10)°.
	c = 20.3455(2) Å	γ = 113.7440(10)°.
Volume	2187.35(4) $Å^3$	
Z	2	
Density (calculated)	1.334 Mg/m^3	
Absorption coefficient	4.123 mm^{-1}	
F(000)	920	
Crystal size	0.44 x 0.37 x 0.10 mm^3	
Theta range for data collection	2.25 to 65.11°.	
Index ranges	-11<=h<=12, -13<=k<=13, -23<=l<=23	
Reflections collected	42443	
Independent reflections	7294 [R(int) = 0.0294]	
Completeness to theta = 65.11°	97.6 %	
Absorption correction	Semi-empirical from equivalents	
Max. and min. transmission	0.6833 and 0.2642	
Refinement method	Full-matrix least-squares on F^2	
Data / restraints / parameters	7294 / 6 / 542	
Goodness-of-fit on F^2	1.032	
Final R indices [I>2sigma(I)]	R1 = 0.0313, wR2 = 0.0792	
R indices (all data)	R1 = 0.0324, wR2 = 0.0800	
Largest diff. peak and hole	0.565 and -0.300 $e.Å^{-3}$	

Table A3.7. Crystal data and structure refinement for {[$PhBP^{Ph}_3$]Fe(NH_3)(N_2H_4)}{PF_6} (**4.9**)

Identification code	09287	
Empirical formula	C49 H56 B F6 Fe N3 O P4	
Formula weight	1007.51	
Temperature	100(2) K	
Wavelength	0.71073 Å	
Crystal system	Triclinic	
Space group	P-1	
Unit cell dimensions	a = 11.7861(9) Å	α= 74.0540(10)°.
	b = 12.1742(9) Å	β= 79.4630(10)°.
	c = 18.5366(14) Å	γ = 74.3450(10)°.
Volume	2445.5(3) $Å^3$	
Z	2	
Density (calculated)	1.368 Mg/m^3	
Absorption coefficient	0.502 mm^{-1}	
F(000)	1048	
Crystal size	0.40 x 0.30 x 0.15 mm^3	
Theta range for data collection	1.15 to 26.73°.	
Index ranges	-14<=h<=14, -15<=k<=15, -23<=l<=23	
Reflections collected	54310	
Independent reflections	10397 [R(int) = 0.0395]	
Completeness to theta = 26.73°	100.0 %	
Absorption correction	Semi-empirical from equivalents	
Max. and min. transmission	0.9285 and 0.8245	
Refinement method	Full-matrix least-squares on F^2	
Data / restraints / parameters	10397 / 1773 / 755	
Goodness-of-fit on F^2	1.044	
Final R indices [I>2sigma(I)]	R1 = 0.0415, wR2 = 0.1082	
R indices (all data)	R1 = 0.0506, wR2 = 0.1169	
Largest diff. peak and hole	1.180 and -0.726 e.$Å^{-3}$	

Table A3.8. Crystal data and structure refinement for [PhBP$^{m\text{ter}}_3$]Fe(OAc)(NH_3) (**4.10**)

Identification code	car	
Empirical formula	C127 H115 B Fe N O6 P3	
Formula weight	1910.77	
Temperature	100(2) K	
Wavelength	1.54178 Å	
Crystal system	Orthorhombic	
Space group	P2(1)2(1)2(1)	
Unit cell dimensions	a = 14.2347(4) Å	α= 90°.
	b = 14.8690(4) Å	β= 90°.
	c = 49.9305(15) Å	γ = 90°.
Volume	10568.1(5) Å^3	
Z	4	
Density (calculated)	1.201 Mg/m^3	
Absorption coefficient	2.013 mm^{-1}	
F(000)	4032	
Crystal size	0.50 x 0.20 x 0.02 mm^3	
Theta range for data collection	1.77 to 66.69°.	
Index ranges	-16<=h<=15, -17<=k<=17, -59<=l<=59	
Reflections collected	207678	
Independent reflections	18700 [R(int) = 0.0757]	
Completeness to theta = 66.69°	100.0 %	
Absorption correction	Semi-empirical from equivalents	
Max. and min. transmission	0.9609 and 0.4327	
Refinement method	Full-matrix least-squares on F^2	
Data / restraints / parameters	18700 / 1623 / 1346	
Goodness-of-fit on F^2	1.147	
Final R indices [I>2sigma(I)]	R1 = 0.0542, wR2 = 0.1390	
R indices (all data)	R1 = 0.0612, wR2 = 0.1430	
Absolute structure parameter	0.014(5)	
Largest diff. peak and hole	0.682 and -0.329 e.Å^{-3}	

Table A3.9. Crystal data and structure refinement for {[$PhBP^{Ph}_3$]Fe(CO)(N_2H_4)}{PF_6} (**4.11**)

Identification code	car42	
Empirical formula	C50 H53 B F6 Fe N2 O2 P4	
Formula weight	1018.48	
Temperature	100(2) K	
Wavelength	0.71073 Å	
Crystal system	Triclinic	
Space group	P-1	
Unit cell dimensions	a = 11.7629(16) Å	α= 85.960(2)°.
	b = 14.444(2) Å	β= 77.814(2)°.
	c = 15.194(2) Å	γ = 72.853(2)°.
Volume	2411.1(6) $Å^3$	
Z	2	
Density (calculated)	1.403 Mg/m^3	
Absorption coefficient	0.511 mm^{-1}	
F(000)	1056	
Crystal size	0.10 x 0.07 x 0.03 mm^3	
Theta range for data collection	2.51 to 26.73°.	
Index ranges	-14<=h<=14, -18<=k<=18, -19<=l<=19	
Reflections collected	41794	
Independent reflections	10219 [R(int) = 0.0642]	
Completeness to theta = 26.73°	99.8 %	
Absorption correction	Semi-empirical from equivalents	
Max. and min. transmission	0.9848 and 0.9507	
Refinement method	Full-matrix least-squares on F^2	
Data / restraints / parameters	10219 / 892 / 708	
Goodness-of-fit on F^2	1.086	
Final R indices [I>2sigma(I)]	R1 = 0.0641, wR2 = 0.1321	
R indices (all data)	R1 = 0.0993, wR2 = 0.1461	
Largest diff. peak and hole	0.500 and -0.473 e.$Å^{-3}$	

Table A3.10. Crystal data and structure refinement for **[PhBP$^{Ph}_3$]Fe(OAc)**

Identification code	x	
Empirical formula	C53 H50 B Fe N0 O2 P3	
Formula weight	878.50	
Temperature	100(2) K	
Wavelength	1.54178 Å	
Crystal system	Triclinic	
Space group	P-1	
Unit cell dimensions	a = 10.38700(10) Å	α= 98.0580(10)°.
	b = 11.73090(10) Å	β= 98.6680(10)°.
	c = 20.3455(2) Å	γ = 113.7440(10)°.
Volume	2187.35(4) Å^3	
Z	2	
Density (calculated)	1.334 Mg/m^3	
Absorption coefficient	4.123 mm^{-1}	
F(000)	920	
Crystal size	0.44 x 0.37 x 0.10 mm^3	
Theta range for data collection	2.25 to 65.11°.	
Index ranges	-11<=h<=12, -13<=k<=13, -23<=l<=23	
Reflections collected	42443	
Independent reflections	7294 [R(int) = 0.0294]	
Completeness to theta = 65.11°	97.6 %	
Absorption correction	Semi-empirical from equivalents	
Max. and min. transmission	0.6833 and 0.2642	
Refinement method	Full-matrix least-squares on F^2	
Data / restraints / parameters	7294 / 6 / 542	
Goodness-of-fit on F^2	1.032	
Final R indices [I>2sigma(I)]	R1 = 0.0313, wR2 = 0.0792	
R indices (all data)	R1 = 0.0324, wR2 = 0.0800	
Largest diff. peak and hole	0.565 and -0.300 e.Å^{-3}	

Table A3.11. Crystal data and structure refinement for **[PhBP$^{Ph}_3$]Fe(OArO)**

Identification code	09298_14	
Empirical formula	C63.16 H69.63 B Fe N0 O2.84 P3	
Formula weight	1033.76	
Temperature	100(2) K	
Wavelength	0.71073 Å	
Crystal system	Monoclinic	
Space group	P2(1)/c	
Unit cell dimensions	a = 10.4739(9) Å	α= 90°.
	b = 48.182(4) Å	β= 109.8440(10)°.
	c = 11.3434(9) Å	γ = 90°.
Volume	5384.6(8) Å^3	
Z	4	
Density (calculated)	1.275 Mg/m^3	
Absorption coefficient	0.415 mm^{-1}	
F(000)	2189	
Crystal size	0.45 x 0.30 x 0.15 mm^3	
Theta range for data collection	1.69 to 27.10°.	
Index ranges	-13<=h<=13, -61<=k<=61, -14<=l<=14	
Reflections collected	102031	
Independent reflections	11890 [R(int) = 0.0601]	
Completeness to theta = 27.10°	99.9 %	
Absorption correction	Semi-empirical from equivalents	
Max. and min. transmission	0.9403 and 0.8352	
Refinement method	Full-matrix least-squares on F^2	
Data / restraints / parameters	11890 / 1016 / 723	
Goodness-of-fit on F^2	1.173	
Final R indices [I>2sigma(I)]	R1 = 0.0550, wR2 = 0.1190	
R indices (all data)	R1 = 0.0654, wR2 = 0.1239	
Largest diff. peak and hole	0.690 and -0.353 e.Å^{-3}	

Table A3.12. Crystal data and structure refinement for {**[PhBP$^{Ph}_3$]Fe}$_2$(OArO)**

Identification code	d8_09057	
Empirical formula	C52 H51 B Fe O2 P3	
Formula weight	867.50	
Temperature	100(2) K	
Wavelength	1.54178 Å	
Crystal system	Monoclinic	
Space group	P2(1)/c	
Unit cell dimensions	a = 10.12850(10) Å	α= 90°.
	b = 39.1720(5) Å	β= 111.1960(10)°.
	c = 11.76110(10) Å	γ = 90°.
Volume	4350.58(8) Å^3	
Z	4	
Density (calculated)	1.324 Mg/m^3	
Absorption coefficient	4.137 mm^{-1}	
F(000)	1820	
Crystal size	0.40 x 0.20 x 0.05 mm^3	
Theta range for data collection	2.26 to 65.07°.	
Index ranges	-11<=h<=11, -46<=k<=46, -13<=l<=13	
Reflections collected	40077	
Independent reflections	7392 [R(int) = 0.0465]	
Completeness to theta = 65.07°	99.8 %	
Absorption correction	Semi-empirical from equivalents	
Max. and min. transmission	0.8198 and 0.2884	
Refinement method	Full-matrix least-squares on F^2	
Data / restraints / parameters	7392 / 618 / 532	
Goodness-of-fit on F^2	1.048	
Final R indices [I>2sigma(I)]	R1 = 0.0378, wR2 = 0.0930	
R indices (all data)	R1 = 0.0425, wR2 = 0.0955	
Largest diff. peak and hole	0.516 and -0.287 e.Å^{-3}	

Table A3.13. Crystal data and structure refinement for **[PhBP$^{mter}_3$]Fe(OArOH)**

Identification code	d8_10022	
Empirical formula	C127 H104 B Fe N0 O4 P3	
Formula weight	1853.67	
Temperature	100(2) K	
Wavelength	1.54178 Å	
Crystal system	Triclinic	
Space group	P-1	
Unit cell dimensions	a = 14.9321(3) Å	α= 83.028(2)°.
	b = 16.5020(4) Å	β= 81.3610(10)°.
	c = 21.5928(6) Å	γ = 67.6940(10)°.
Volume	4854.6(2) Å^3	
Z	2	
Density (calculated)	1.268 Mg/m^3	
Absorption coefficient	2.158 mm^{-1}	
F(000)	1948	
Crystal size	0.45 x 0.30 x 0.28 mm^3	
Theta range for data collection	2.07 to 63.72°.	
Index ranges	-17<=h<=17, -14<=k<=18, -25<=l<=25	
Reflections collected	92126	
Independent reflections	15678 [R(int) = 0.0318]	
Completeness to theta = 63.72°	97.8 %	
Absorption correction	Semi-empirical from equivalents	
Max. and min. transmission	0.5833 and 0.4434	
Refinement method	Full-matrix least-squares on F^2	
Data / restraints / parameters	15678 / 2139 / 1342	
Goodness-of-fit on F^2	1.028	
Final R indices [I>2sigma(I)]	R1 = 0.0411, wR2 = 0.1079	
R indices (all data)	R1 = 0.0450, wR2 = 0.1110	
Largest diff. peak and hole	0.510 and -0.298 e.Å^{-3}	

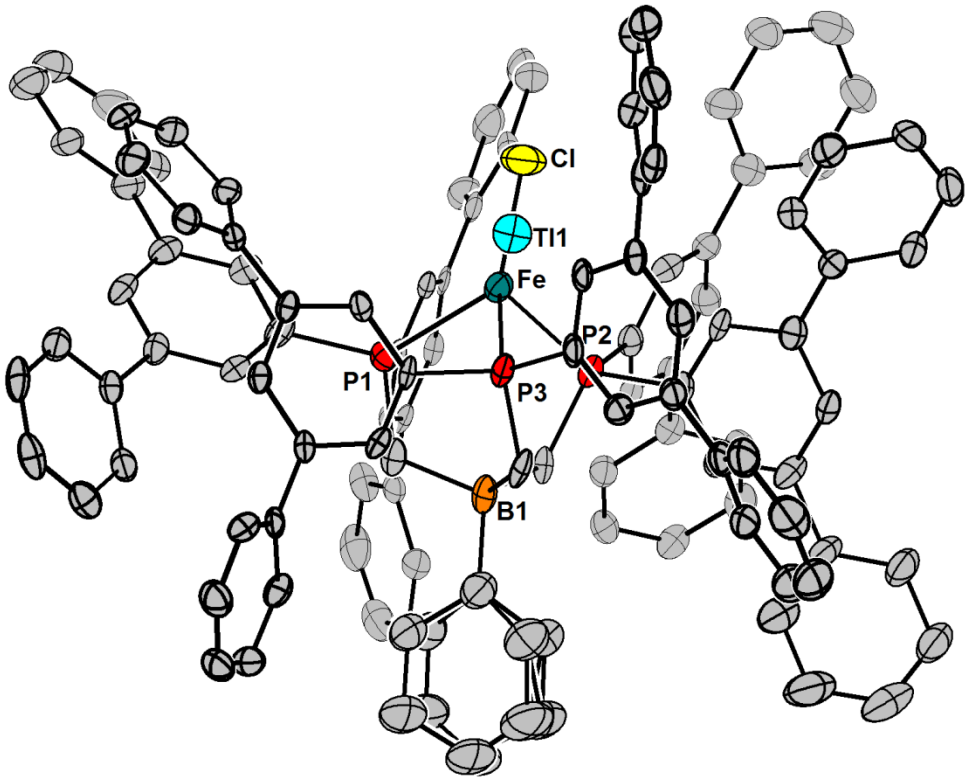

Figure A3.7. Solid-state structure (50% displacement ellipsoids) of [PhBP$^{mter}_{3}$]FeCl, with the disordered atoms shown. Select bond lengths [Å] and angles [°] for [PhBP$^{mter}_{3}$]FeCl: Fe-Cl 2.202(2), Fe-P(3) 2.408(2), Fe-P(2) 2.427(2), Fe-P(1) 2.456(2), Cl-Fe-P(3) 127.61(9), Cl-Fe-P(2) 115.54(9), P(3)-Fe-P(2) 91.21(7), Cl-Fe-P(1) 127.49(9), P(3)-Fe-P(1) 91.91(8), P(2)-Fe-P(1) 93.25(8)

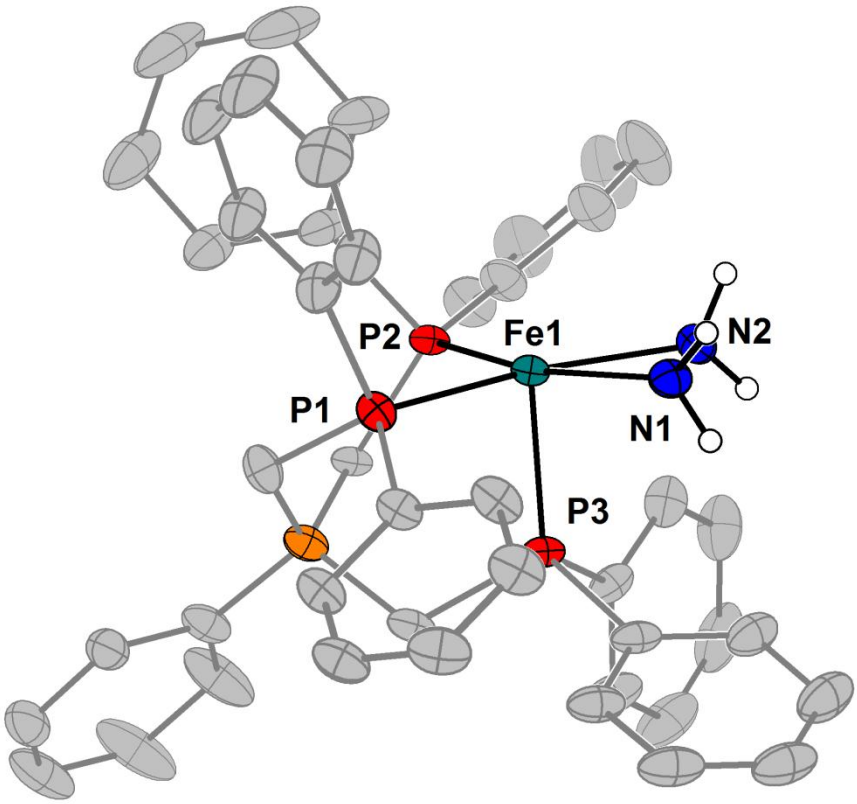

Figure A3.8. Solid-state structure (50% displacement ellipsoids) of {[PhBP$^{Ph}_3$]Fe(η^2-N_2H_4)}{PF_6}, **4.6**. Hydrogen atoms, solvent molecules, the PF_6^- counteranion, and minor components of disorder have been removed for clarity. The hydrogen atoms that coordinate the hydrazine were located in the difference map, were refined semi-freely, and are shown.

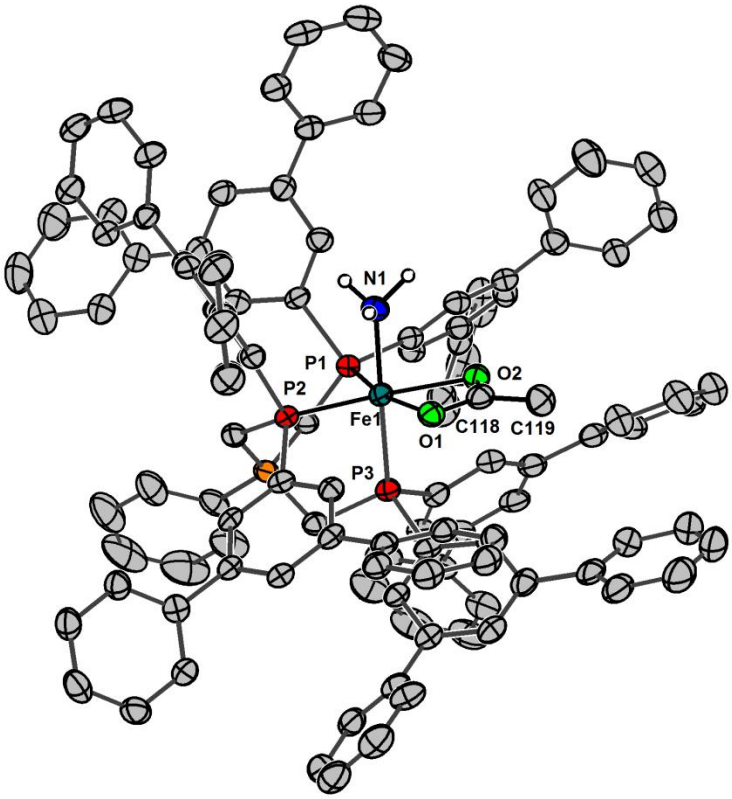

Figure A3.9. Solid-state structure (50% displacement ellipsoids) of [PhBP$^{m\text{ter}}_3$]Fe(NH_3)(OAc), **4.10**. Hydrogen atoms and solvent molecules have been removed for clarity.

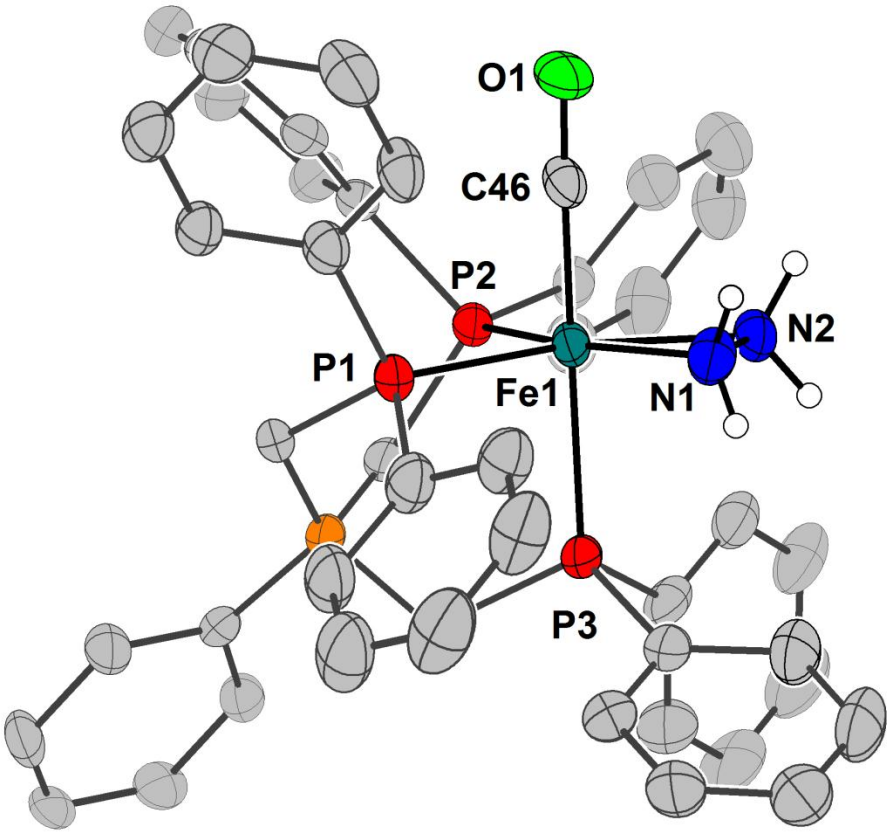

Figure A3.10. Solid-state structure (50% displacement ellipsoids) of {[$PhBP^{Ph}_3$]Fe(CO)(η^2-N_2H_4)}{PF_6}, **4.11**. Hydrogen atoms, solvent molecules, the PF_6^- counteranion, and minor components of disorder have been removed for clarity. The hydrogen atoms that coordinate the hydrazine were located in the difference map, were refined semi-freely, and are shown. Select bond lengths (Å) for **4.11**: Fe(1)-C(46) 1.772(4),Fe(1)-N(1) 1.984(3), Fe(1)-N(2) 2.005(3)

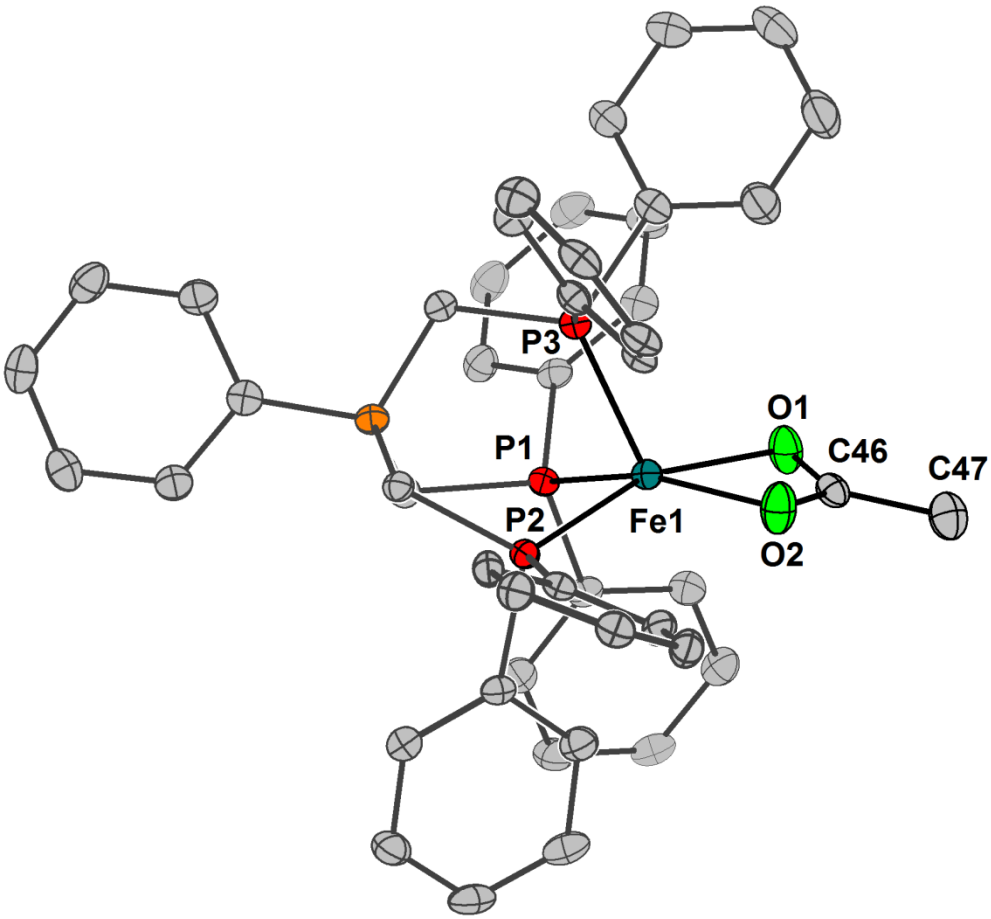

Figure A3.11. Solid-state structure (50% displacement ellipsoids) of [PhBP$^{Ph}_{3}$]Fe(OAc). Hydrogen atoms and solvent molecules have been removed for clarity.

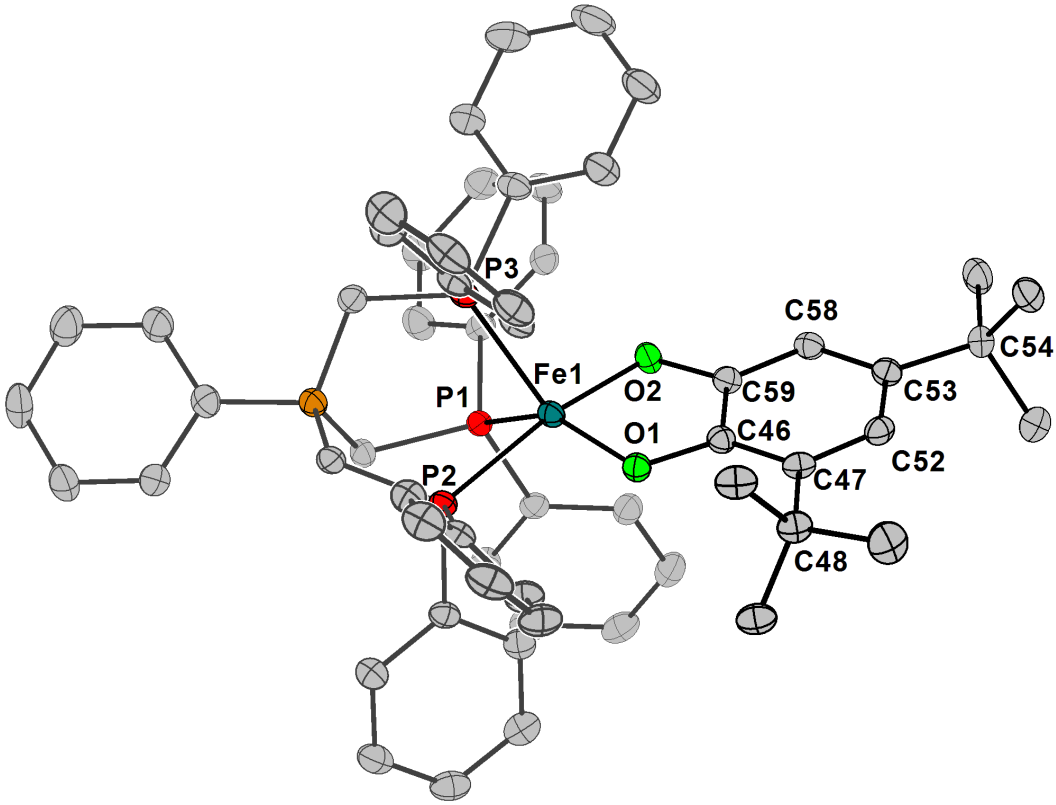

Figure A3.12. Solid-state structure (50% displacement ellipsoids) of [PhBP$^{Ph}_3$]Fe(κ^2-OArO). Hydrogen atoms and solvent molecules have been removed for clarity. Select bond distances (Å): Fe1-O1 1.876(2), Fe1-O2 1.856(2), Fe1-P1 2.2782(7), Fe1-P2 2.3376(7), Fe1-P3 2.2458, O1-C46 1.357(3), O2-C59 1.347(3), C46-C47 1.412(3), C47-C52 1.392(4), C52-C53 1.408(4), C53-C58 1.384(4), C59-C59 1.400(4), C59-C46 1.401(3)

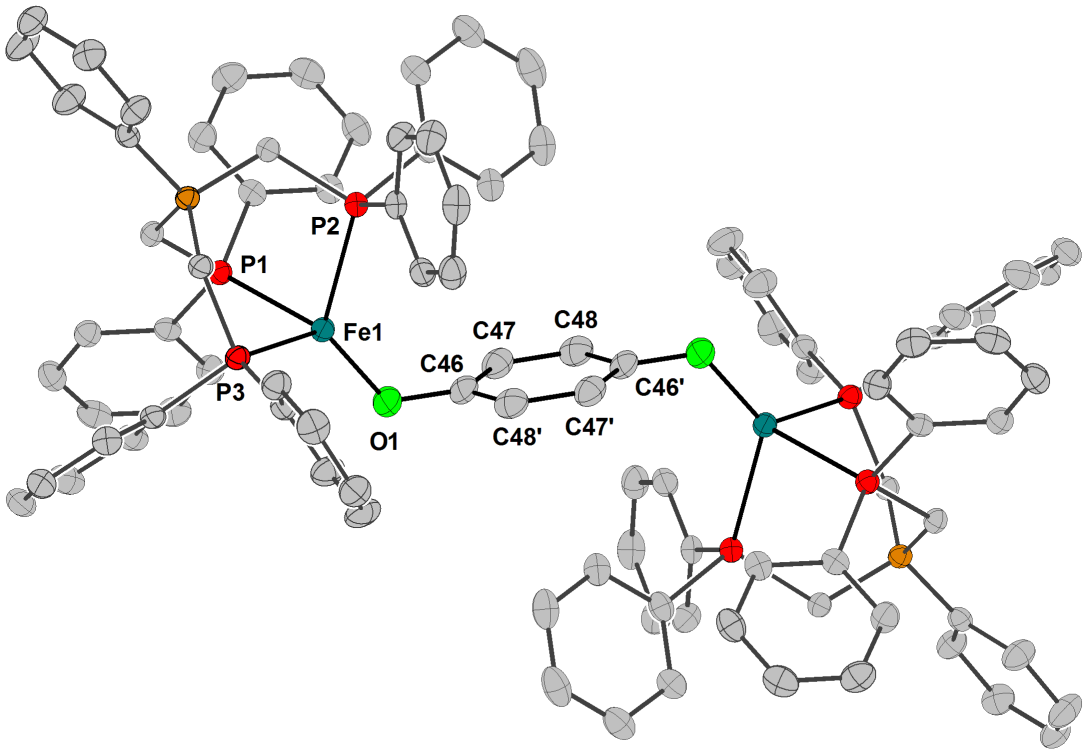

Figure A3.13. Solid-state structure (50% displacement ellipsoids) of {[PhBP$^{Ph}_3$]Fe}$_2$(OArO). Hydrogen atoms and solvent molecules have been removed for clarity. Select bond distances (Å) and angles (deg): Fe1-O1 1.871(2), Fe1-P1 2.4345(6), Fe1-P2 2.4573(6), Fe1-P3 2.4374(6), O1-C46 1.356(3), C46-C47 1.393(3), C47-C48 1.401(3), C46-C48' 1.391(3), Fe1-O1-C46 120.9(1), P1-Fe1-P2 91.15(2), P1-Fe1-P3 92.55(2), P2-Fe1-P3 91.69(2), P1-Fe1-O1 119.69(6), P2-Fe1-O1 128.31(5), P3-Fe1-O1 123.78(6)

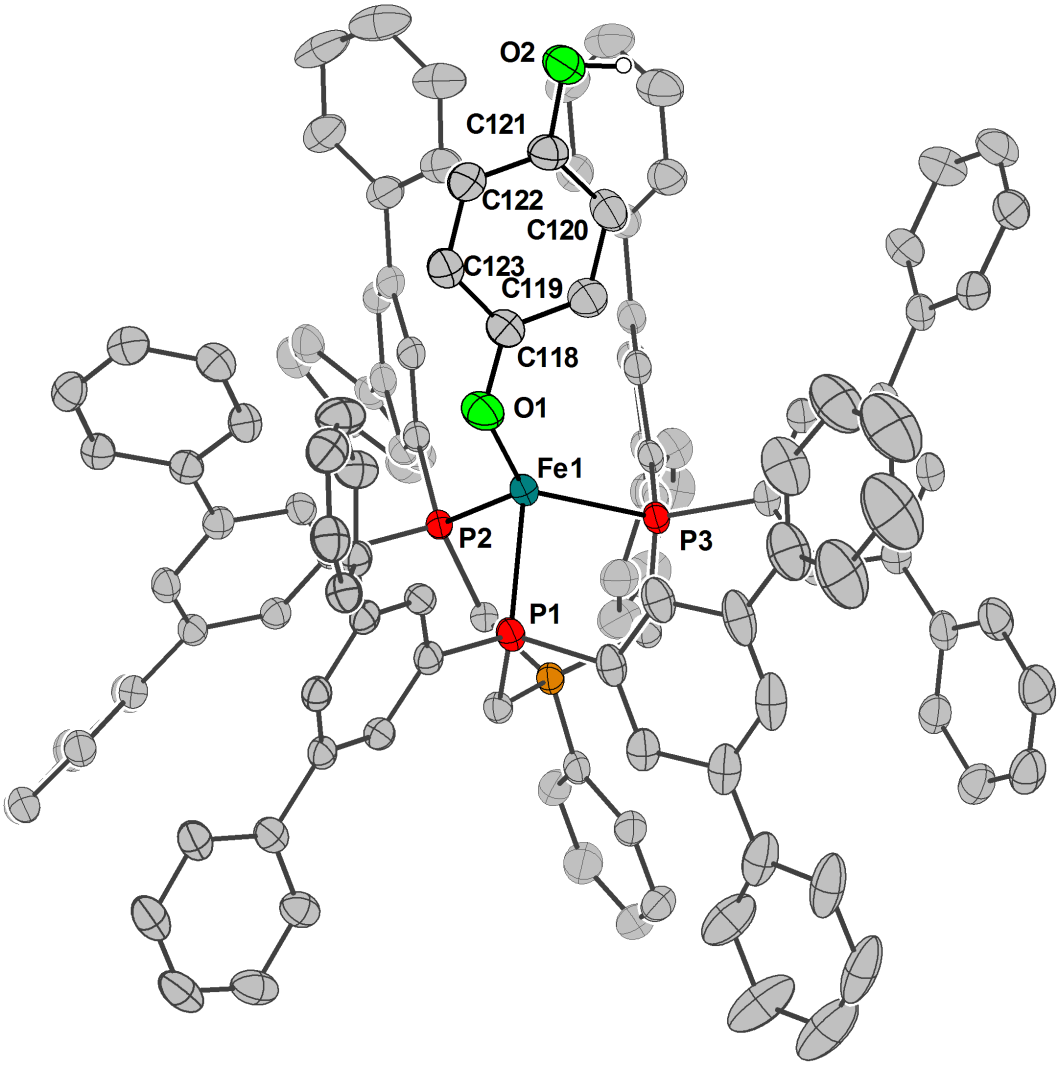

Figure A3.14. Solid-state structure (50% displacement ellipsoids) of [PhBP$^{mter}_3$]Fe(OArOH). Hydrogen atoms and solvent molecules have been removed for clarity. The acidic OH proton was located in the difference map, and is shown. Select bond distances (Å) and angles (deg): Fe1-P1 2.3966(6), Fe1-P2 2.4280(5), Fe1-P3 2.4315(5), Fe1-O1 1.858(2), O1-C118 1.327(3), C118-C119 1.393(3), C119-C120 1.395(3), C120-C121 1.382(3), C121-C122 1.383(3), C122-C123 1.377(3), C123-C118 1.401(3), C121-O2 1.380(3), P1-Fe1-P2 92.15(2), P1-Fe1-P3 95.29(2), P1-Fe1-O1 110.04(5), P2-Fe1-P3 89.84(2), P2-Fe1-O1 120.24(6), P3-Fe1-O1 138.53(5)

Appendix 4: Supplementary Data for Chapter 5

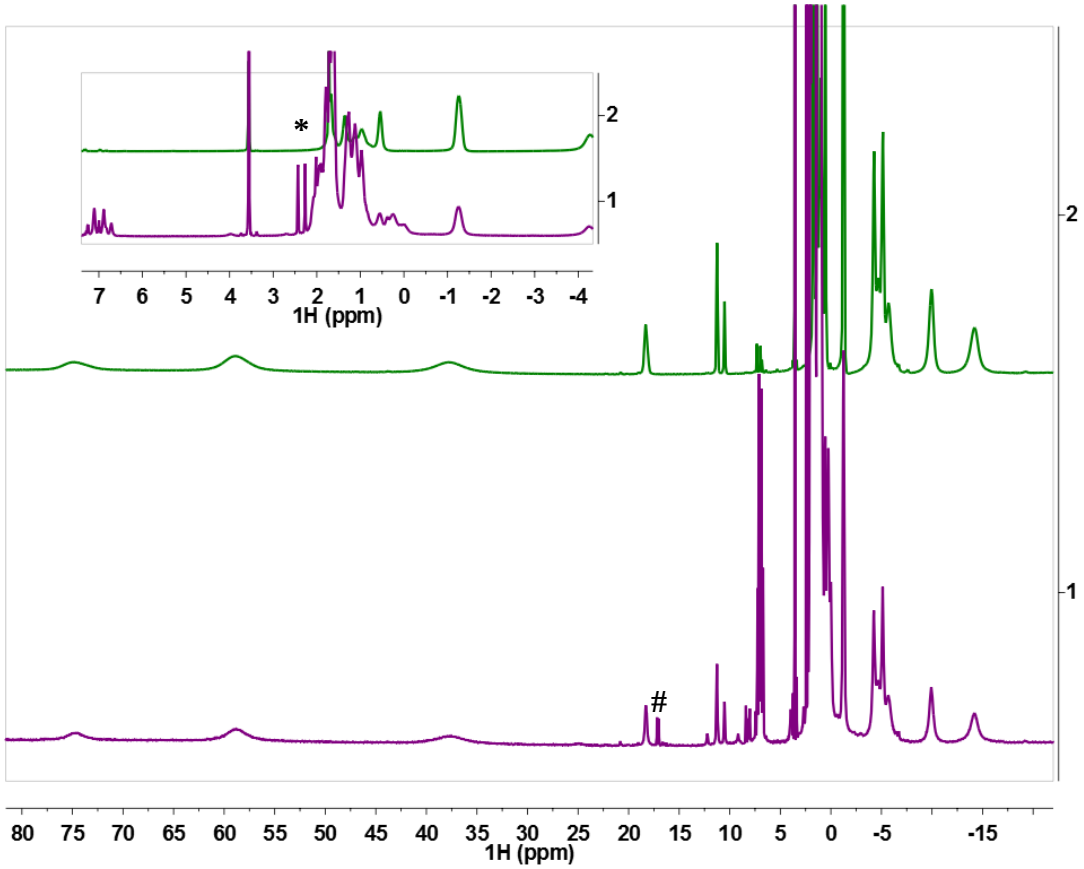

Figure A4.1. ^{1}H NMR spectrum (THF-d_8, 0 ^{o}C) of 5.1 (top) and ^{15}N-**5.3** (bottom). The bottom spectrums shows resonances ascribed to **5.1** (paramagnetic) and **5.3** (*, inset). At this temperature, ^{15}N-**5.4** (#) forms from ^{15}N-**5.3**.

Table A4.1. Crystal data and structure refinement for $\{[PhBP^{CH2Cy}_3]Fe(OAc)\}_2(\mu\text{-}N_2)$ (**5.2**)

Identification code	car	
Empirical formula	C118 H210 B2 Fe2 N2 O7 P6	
Formula weight	2088.02	
Temperature	100(2) K	
Wavelength	1.54178 Å	
Crystal system	Triclinic	
Space group	P-1	
Unit cell dimensions	a = 14.1982(3) Å	α= 114.5230(10)°.
	b = 15.5521(3) Å	β= 107.3310(10)°.
	c = 15.6310(3) Å	γ = 91.1740(10)°.
Volume	2956.03(10) Å^3	
Z	1	
Density (calculated)	1.173 Mg/m^3	
Absorption coefficient	3.132 mm^{-1}	
F(000)	1140	
Crystal size	0.42 x 0.18 x 0.02 mm^3	
Theta range for data collection	3.17 to 65.08°.	
Index ranges	-13<=h<=16, -18<=k<=18, -18<=l<=18	
Reflections collected	47273	
Independent reflections	9717 [R(int) = 0.0750]	
Completeness to theta = 65.08°	96.3 %	
Absorption correction	Semi-empirical from equivalents	
Max. and min. transmission	0.9400 and 0.3529	
Refinement method	Full-matrix least-squares on F^2	
Data / restraints / parameters	9717 / 1253 / 774	
Goodness-of-fit on F^2	1.036	
Final R indices [I>2sigma(I)]	R1 = 0.0603, wR2 = 0.1484	
R indices (all data)	R1 = 0.0767, wR2 = 0.1584	
Largest diff. peak and hole	1.413 and -0.466 e.Å^{-3}	

Table A4.2. Crystal data and structure refinement for $\{[PhBP^{CH2Cy}{}_3]Fe(OAc)\}_2(\mu\text{-}N_2H_2)$ (**5.4**)

Identification code	caltech1	
Empirical formula	C118 H196 B2 Fe2 N2 O4 P6	
Formula weight	2025.91	
Temperature	100(2) K	
Wavelength	1.54178 Å	
Crystal system	Monoclinic	
Space group	P2(1)/c	
Unit cell dimensions	a = 18.2270(6) Å	α= 90°.
	b = 19.7406(8) Å	β= 90.833(3)°.
	c = 31.1376(12) Å	γ = 90°.
Volume	11202.5(7) Å^3	
Z	4	
Density (calculated)	1.201 Mg/m^3	
Absorption coefficient	3.273 mm^{-1}	
F(000)	4408	
Crystal size	0.23 x 0.22 x 0.05 mm^3	
Theta range for data collection	2.42 to 61.16°.	
Index ranges	-20<=h<=16, -22<=k<=22, -35<=l<=34	
Reflections collected	61591	
Independent reflections	16995 [R(int) = 0.1394]	
Completeness to theta = 61.16°	98.7 %	
Max. and min. transmission	0.8535 and 0.5135	
Refinement method	Full-matrix least-squares on F^2	
Data / restraints / parameters	16995 / 4641 / 2417	
Goodness-of-fit on F^2	1.097	
Final R indices [I>2sigma(I)]	R1 = 0.1323, wR2 = 0.2979	
R indices (all data)	R1 = 0.2062, wR2 = 0.3338	
Largest diff. peak and hole	1.073 and -1.932 e.Å^{-3}	

Table A4.3. Crystal data and structure refinement for $[PhBP^{CH2Cy}{}_3]Fe(OAc)(NH_3)$ (**5.5**)

Identification code	car	
Empirical formula	C68 H110 B Fe N O2 P3	
Formula weight	1133.14	
Temperature	100(2) K	
Wavelength	0.71073 Å	
Crystal system	Monoclinic	
Space group	P(2)1/n	
Unit cell dimensions	a = 14.5464(9) Å	α= 90°.
	b = 27.6742(18) Å	β= 112.1960(10)°.
	c = 17.3460(11) Å	γ = 90°.
Volume	6465.4(7) $Å^3$	
Z	4	
Density (calculated)	1.164 Mg/m^3	
Absorption coefficient	0.350 mm^{-1}	
F(000)	2468	
Crystal size	0.25 x 0.16 x 0.10 mm^3	
Theta range for data collection	2.11 to 29.57°.	
Index ranges	-20<=h<=20, -38<=k<=38, -23<=l<=24	
Reflections collected	121842	
Independent reflections	18141 [R(int) = 0.0988]	
Completeness to theta = 29.57°	100.0 %	
Max. and min. transmission	0.9658 and 0.9175	
Refinement method	Full-matrix least-squares on F^2	
Data / restraints / parameters	18141 / 633 / 695	
Goodness-of-fit on F^2	1.010	
Final R indices [I>2sigma(I)]	R1 = 0.0440, wR2 = 0.0964	
R indices (all data)	R1 = 0.0859, wR2 = 0.1169	
Largest diff. peak and hole	0.506 and -0.480 $e.Å^{-3}$	

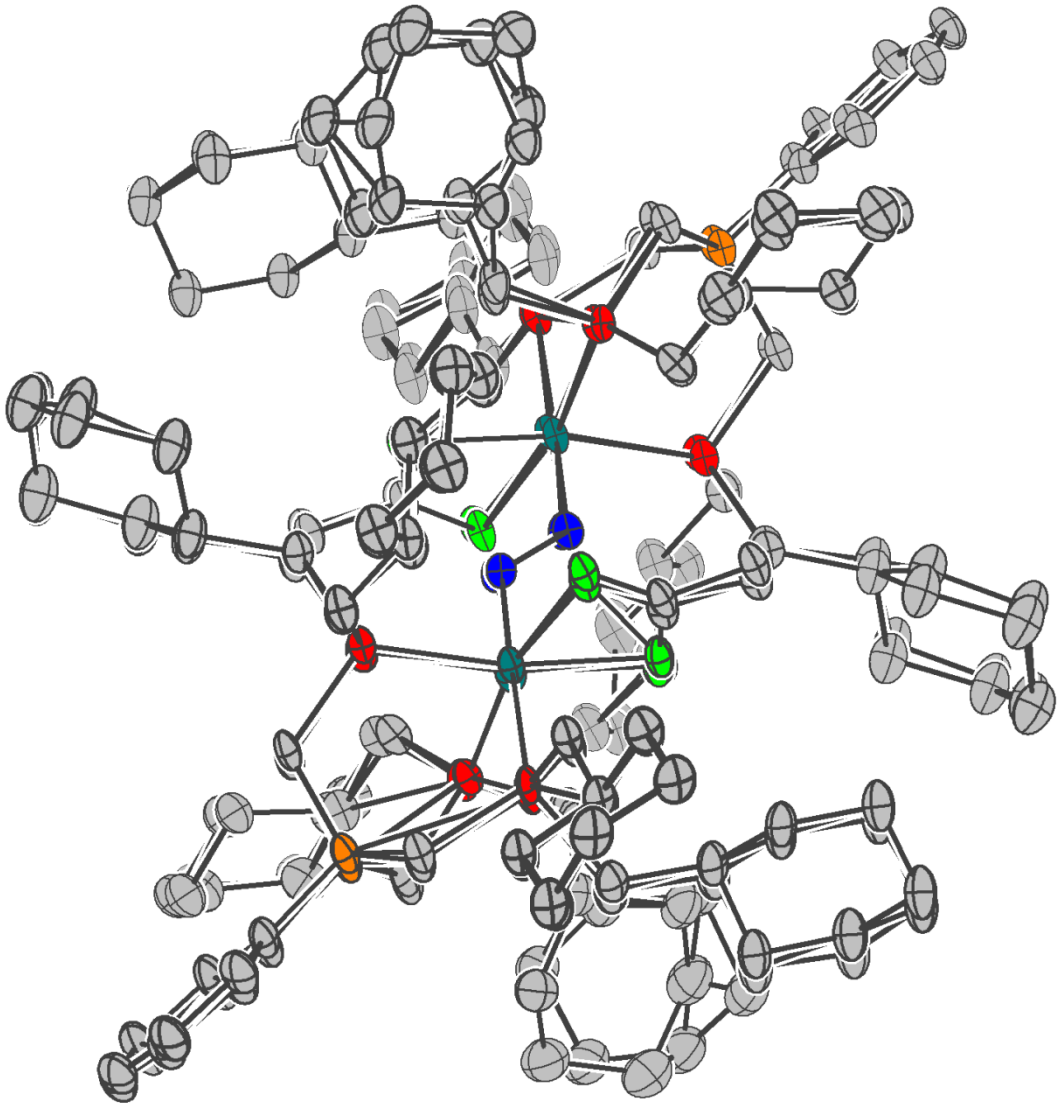

Figure A4.2. Displacement ellipsoid (50 %) representation of **5.4** viewed along the b axis. Hydrogen atoms and disordered benzene molecules have been omitted for clarity.

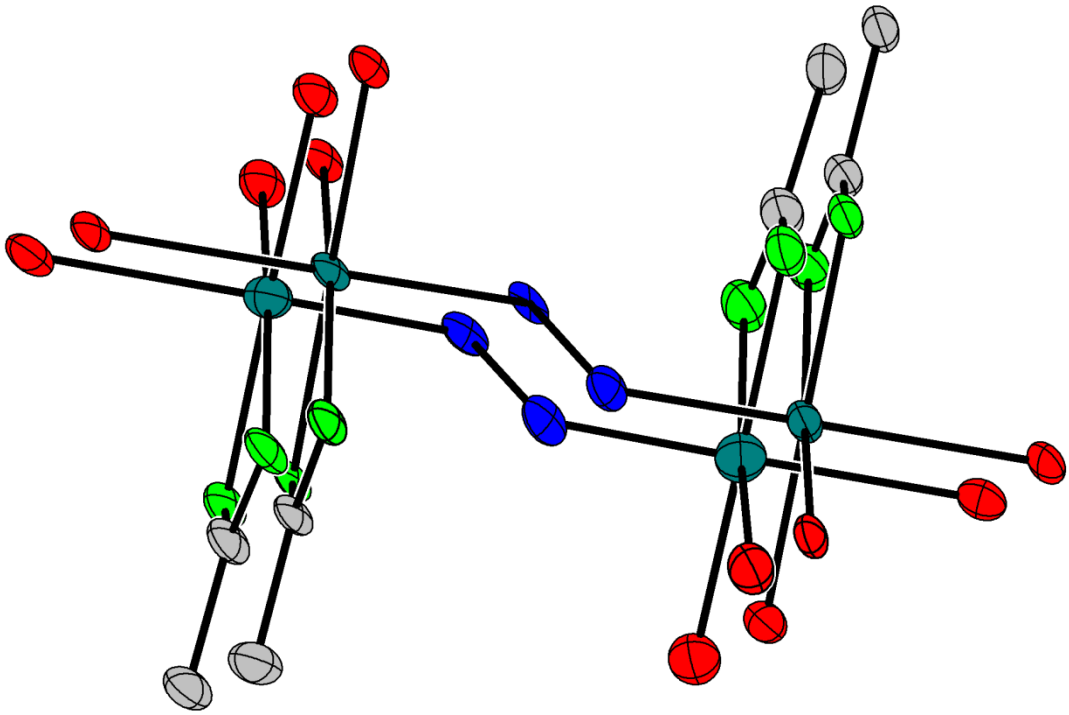

Figure A4.3. Displacement ellipsoid (50%) representation of the core atoms of **5.4**

Appendix 5: Supplementary Data for Chapter 6

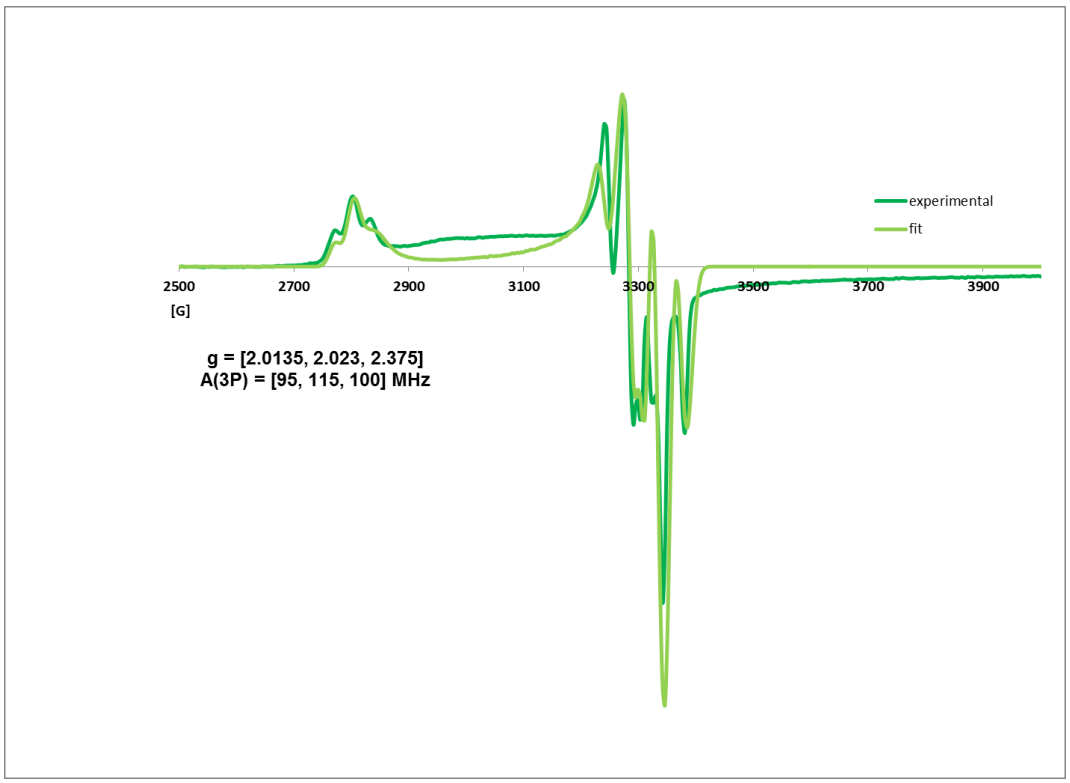

Figure A5.1. X-band EPR spectrum of **6.1** (Gauss) recorded at 4K in a MeCy glass (experimental dark green; fit lime green).

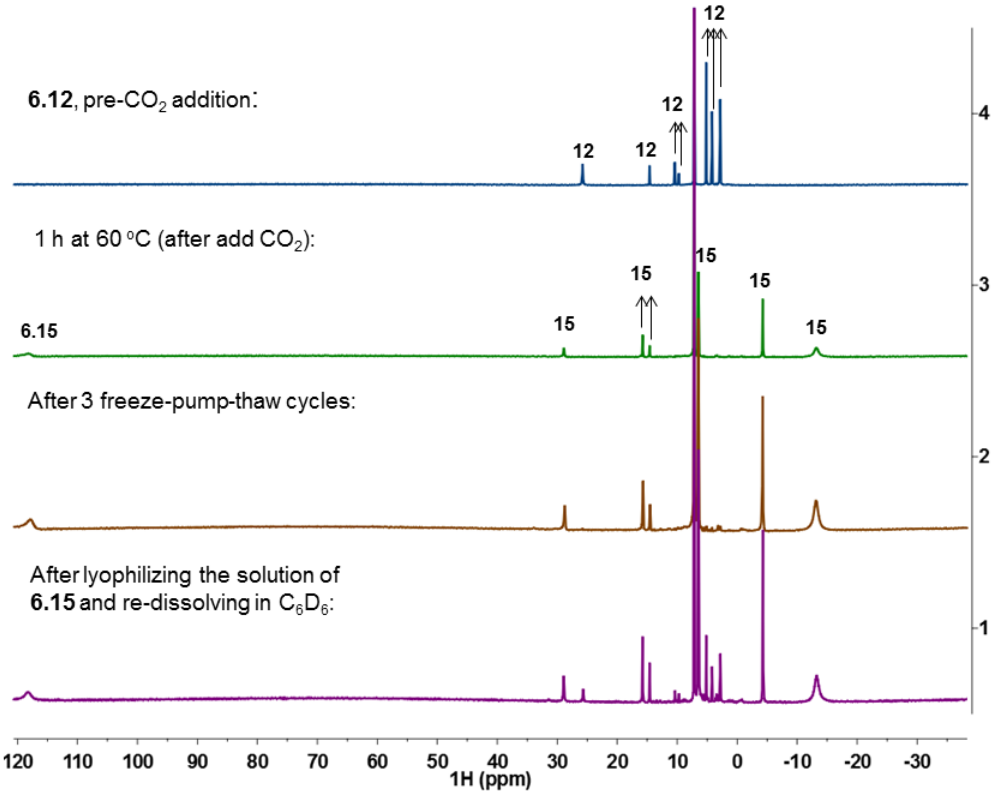

Figure A5.2. ^{1}H NMR profile (C_6D_6) of the reaction between **6.12** and CO_2.

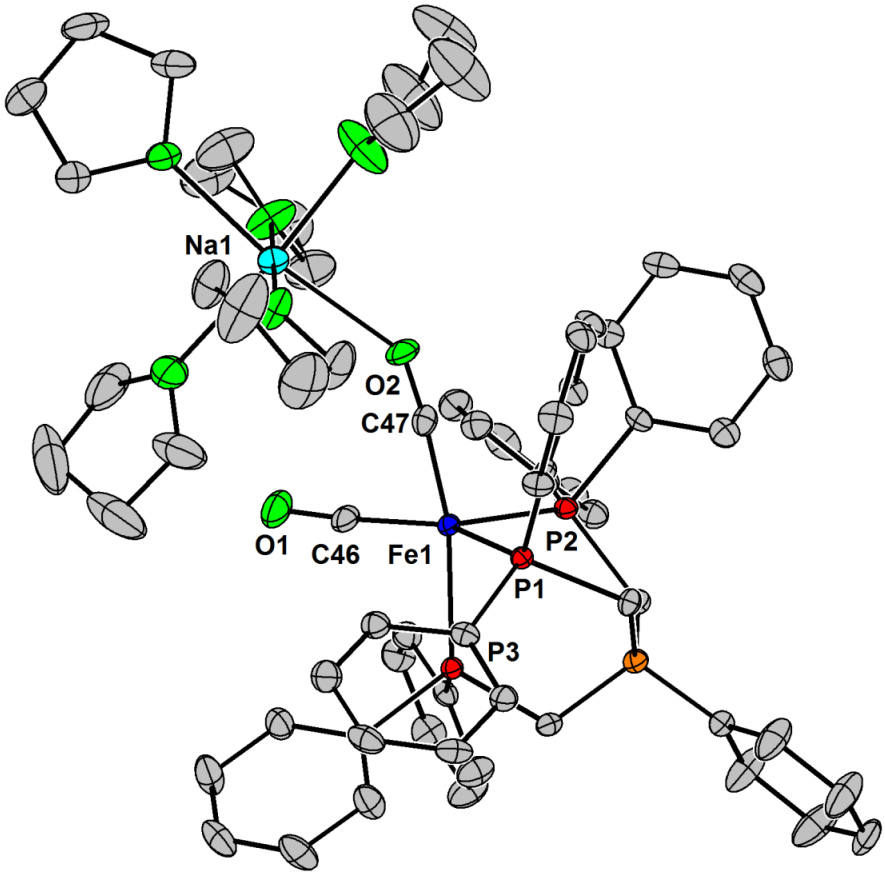

Figure A5.3. 50% thermal ellipsoid representation of {[PhBP$^{Ph}_3$]Fe(CO)$_2$}{Na(THF)$_5$} (**6.14**). Hydrogen atoms have been removed for clarity. Selected bond distances (Å) and angles (deg.) for 6.13: Fe1-P1 2.2158(8), Fe1-P2 2.2116(8), Fe1-P3 2.2663(8), Fe1-C47 1.750(3), Fe1-C46 1.752(3), C46-O1 1.162(4), C47-O2 1.158(3), O2-Na12.501(2), C47-Fe1-C46 82.7(1), C47-Fe1-P2 103.9(1), C46-Fe1-P2 121.6(1), C47-Fe1-P1 93.75(9), C46-Fe1-P1 143.7(1), P2-Fe1-P1 94.35(3), C47-Fe1-P3 167.4(1), C46-Fe1-P3 89.30(9), P2-Fe1-P3 88.50(3), P1-Fe1-P3 86.97(3)

Table A5.1. Crystal data and structure refinement for {[PhBP$^{CH2Cy}{}_3$]Fe}$_2$(μ-η^5:η^5-6,6'-bicyclohexadienyl) (**6.5**)

Identification code	global	
Empirical formula	C118 H206 B2 Fe2 O P6	
Formula weight	1959.97	
Temperature	100(2) K	
Wavelength	0.71073 Å	
Crystal system	Monoclinic	
Space group	C2/c	
Unit cell dimensions	a = 28.3106(8) Å	α= 90°.
	b = 21.7915(7) Å	β= 126.5720(10)°.
	c = 22.8536(7) Å	γ = 90°.
Volume	11323.1(6) Å^3	
Z	4	
Density (calculated)	1.150 Mg/m^3	
Absorption coefficient	0.388 mm^{-1}	
F(000)	4296	
Crystal size	0.60 x 0.40 x 0.33 mm^3	
Theta range for data collection	1.29 to 27.08°.	
Index ranges	-35<=h<=35, -26<=k<=22, -28<=l<=28	
Reflections collected	41539	
Independent reflections	11211 [R(int) = 0.1119]	
Completeness to theta = 27.08°	90.0 %	
Absorption correction	None	
Max. and min. transmission	0.8828 and 0.8007	
Refinement method	Full matrix least-squares on F^2	
Data / restraints / parameters	11211 / 1152 / 722	
Goodness-of-fit on F^2	1.997	
Final R indices [I>2sigma(I)]	R1 = 0.1005, wR2 = 0.1613	
R indices (all data)	R1 = 0.1524, wR2 = 0.1666	
Largest diff. peak and hole	0.619 and -0.586 e.Å^{-3}	

Table A5.2. Crystal data and structure refinement for {[PhBP$^{CH2Cy}{}_3$]Fe}$_2$(μ-η^5:η^5-azobenzene) (**6.6**)

Identification code	global	
Empirical formula	C124 H208 B2 Cl4 Fe2 N2 O2 P6	
Formula weight	2219.86	
Temperature	100(2) K	
Wavelength	0.71073 Å	
Crystal system	Monoclinic	
Space group	P2(1)/c	
Unit cell dimensions	a = 22.7338(16) Å	α= 90°.
	b = 15.5757(11) Å	β= 110.2880(10)°.
	c = 17.6503(13) Å	γ = 90°.
Volume	5862.1(7) Å^3	
Z	2	
Density (calculated)	1.258 Mg/m^3	
Absorption coefficient	0.472 mm^{-1}	
F(000)	2404	
Crystal size	0.40 x 0.35 x 0.10 mm^3	
Theta range for data collection	1.62 to 24.95°.	
Index ranges	-25<=h<=25, -16<=k<=18, -20<=l<=19	
Reflections collected	38965	
Independent reflections	9196 [R(int) = 0.0902]	
Completeness to theta = 24.95°	89.6 %	
Absorption correction	None	
Max. and min. transmission	0.9543 and 0.8338	
Refinement method	Full matrix least-squares on F^2	
Data / restraints / parameters	9196 / 5918 / 764	
Goodness-of-fit on F^2	2.946	
Final R indices [I>2sigma(I)]	R1 = 0.1009, wR2 = 0.1747	
R indices (all data)	R1 = 0.1743, wR2 = 0.1813	
Largest diff. peak and hole	1.313 and -0.633 e.Å^{-3}	

Table A5.3. Crystal data and structure refinement for $\{[PhBP^{iPr}_3]Fe\}_2(\mu\text{–}O)$ (**6.10**)

Identification code	cmt20	
Empirical formula	C54 H106 B2 Fe2 O P6	
Formula weight	1090.53	
Temperature	100(2) K	
Wavelength	0.71073 Å	
Crystal system	Monoclinic	
Space group	P2(1)	
Unit cell dimensions	a = 14.199(4) Å	α= 90°.
	b = 14.985(5) Å	β= 103.184(5)°.
	c = 14.939(5) Å	γ = 90°.
Volume	3094.6(17) $Å^3$	
Z	2	
Density (calculated)	1.170 Mg/m^3	
Absorption coefficient	0.657 mm^{-1}	
F(000)	1180	
Crystal size	0.41 x 0.36 x 0.07 mm^3	
Theta range for data collection	1.40 to 25.97°.	
Index ranges	-16<=h<=16, -18<=k<=18, -18<=l<=18	
Reflections collected	26177	
Independent reflections	10115 [R(int) = 0.1890]	
Completeness to theta = 25.97°	90.1 %	
Max. and min. transmission	0.9554 and 0.7743	
Refinement method	Full-matrix least-squares on F^2	
Data / restraints / parameters	10115 / 337 / 610	
Goodness-of-fit on F^2	0.941	
Final R indices [I>2sigma(I)]	R1 = 0.0990, wR2 = 0.2319	
R indices (all data)	R1 = 0.1678, wR2 = 0.2737	
Absolute structure parameter	-0.02(4)	
Largest diff. peak and hole	1.582 and -0.640 e.$Å^{-3}$	

Table A5.4. Crystal data and structure refinement for $\{[PhBP^{Ph}_3]Fe\}_2(\mu\text{–}O)$ (**6.12**)

Identification code	07148	
Empirical formula	C102 H94 B2 Fe2 O P6	
Formula weight	1654.91	
Temperature	100(2) K	
Wavelength	0.71073 Å	
Crystal system	Tetragonal	
Space group	I -4 2 d	
Unit cell dimensions	a = 33.2834(6) Å	α= 90°.
	b = 33.2834(6) Å	β= 90°.
	c = 16.7509(6) Å	γ = 90°.
Volume	18556.4(8) $Å^3$	
Z	8	
Density (calculated)	1.185 Mg/m^3	
Absorption coefficient	0.462 mm^{-1}	
F(000)	6928	
Crystal size	0.40 x 0.30 x 0.30 mm^3	
Theta range for data collection	1.83 to 25.61°.	
Index ranges	-40<=h<=40, -40<=k<=40, -20<=l<=20	
Reflections collected	124894	
Independent reflections	8762 [R(int) = 0.0396]	
Completeness to theta = 25.61°	99.9 %	
Absorption correction	Semi-empirical from equivalents	
Max. and min. transmission	0.8738 and 0.8367	
Refinement method	Full-matrix least-squares on F^2	
Data / restraints / parameters	8762 / 4119 / 1002	
Goodness-of-fit on F^2	1.117	
Final R indices [I>2sigma(I)]	R1 = 0.0554, wR2 = 0.1516	
R indices (all data)	R1 = 0.0596, wR2 = 0.1557	
Absolute structure parameter	0.017(18)	
Largest diff. peak and hole	0.761 and -0.260 $e.Å^{-3}$	

Table A5.5. Crystal data and structure refinement for {[$PhBP^{Ph}_3$]Fe$(CO)_2$}{Na$(THF)_5$} (**6.14**)

Identification code	car25_p31	
Empirical formula	C67 H81 B1 Fe1 Na1 O7 P3	
Formula weight	1180.88	
Temperature	293(2) K	
Wavelength	0.71073 Å	
Crystal system	Hexagonal	
Space group	p3(1)	
Unit cell dimensions	a = 13.1184(19) Å	α= 90°.
	b = 13.1184(19) Å	β= 90°.
	c = 31.059(6) Å	γ = 120°.
Volume	4628.9(13) $Å^3$	
Z	3	
Density (calculated)	1.271 Mg/m^3	
Absorption coefficient	0.382 mm^{-1}	
F(000)	1878	
Crystal size	? x ? x ? mm^3	
Theta range for data collection	1.79 to 28.43°.	
Index ranges	-17<=h<=17, -17<=k<=17, -40<=l<=41	
Reflections collected	38888	
Independent reflections	13916 [R(int) = 0.0591]	
Completeness to theta = 28.43°	93.7 %	
Absorption correction	None	
Refinement method	Full-matrix least-squares on F^2	
Data / restraints / parameters	13916 / 1 / 741	
Goodness-of-fit on F^2	1.077	
Final R indices [I>2sigma(I)]	R1 = 0.0465, wR2 = 0.1123	
R indices (all data)	R1 = 0.0524, wR2 = 0.1160	
Absolute structure parameter	-0.010(11)	
Largest diff. peak and hole	0.735 and -0.416 e.$Å^{-3}$	

Table A5.6. Crystal data and structure refinement for $\{[PhBP^{Ph}_3]Fe\}_2(\mu\text{-}\eta^2\text{:}\eta^1\text{-}CO_3)$ (**6.15**)

Identification code	car4195	
Empirical formula	C108 H116 B2 Fe2 O6.50 P6	
Formula weight	1837.15	
Temperature	100(2) K	
Wavelength	1.54178 Å	
Crystal system	Triclinic	
Space group	P-1	
Unit cell dimensions	a = 13.7605(4) Å	α= 96.6650(10)°.
	b = 16.3419(4) Å	β= 106.7190(10)°.
	c = 22.5111(6) Å	γ = 103.4890(10)°.
Volume	4622.3(2) Å^3	
Z	2	
Density (calculated)	1.320 Mg/m^3	
Absorption coefficient	3.943 mm^{-1}	
F(000)	1936	
Crystal size	0.46 x 0.17 x 0.03 mm^3	
Theta range for data collection	2.09 to 50.44°.	
Index ranges	-13<=h<=13, -16<=k<=16, -21<=l<=19	
Reflections collected	28804	
Independent reflections	9102 [R(int) = 0.1079]	
Completeness to theta = 50.44°	93.8 %	
Max. and min. transmission	0.8909 and 0.2642	
Refinement method	Full-matrix least-squares on F^2	
Data / restraints / parameters	9102 / 3956 / 1373	
Goodness-of-fit on F^2	0.917	
Final R indices [I>2sigma(I)]	R1 = 0.0603, wR2 = 0.1388	
R indices (all data)	R1 = 0.0949, wR2 = 0.1502	
Largest diff. peak and hole	1.061 and -0.382 e.Å^{-3}	